



ISSN 1343-2230

CNS-REP-92
March, 2014

Annual Report 2012

Center for Nuclear Study,
Graduate School of Science, the University of Tokyo

Editors

Shinsuke Ota

Yuko Soma

Center for Nuclear Study

CNS Reports are available from:

Wako-Branch at RIKEN

Center for Nuclear Study,

Graduate School of Science, the University of Tokyo

2-1 Hirosawa, Wako

351-0198, Japan

Tel: +81-48-464-4191

Fax: +81-48-464-4554

Annual Report 2012

Center for Nuclear Study,
Graduate School of Science, the University of Tokyo

Preface

This is the annual report of the Center for Nuclear Study (CNS), Graduate School of Science, the University of Tokyo, for the fiscal year 2012 (April 2012 through March 2013). In the CNS, during this period, a large number of scientific activities in various fields of nuclear physics have been carried out and a wide variety of fruitful results have been obtained. This report presents a report of such activities. Some highlights of the report are mentioned here.

The NUSPEQ (NUclear SPectroscopy for Extreme Quantum system) group studies exotic structures in high-isospin and/or high-spin states in nuclei. The CNS GRAPE (Gamma-Ray detector Array with Position and Energy sensitivity) is a major apparatus for high-resolution in-beam gamma-ray spectroscopy. Missing mass spectroscopy using the SHARAQ is going to start as another approach on exotic nuclei. In 2012, the following progress has been made.

Analysis of α inelastic scattering data from nuclei in the island of inversion, which was taken by using GRAPE, has progressed. Experiments of searching new isomers by using ^{238}U and ^{124}Xe primary beams from SRC were performed and the analysis of the obtained data is in progress. The double-charge exchange reaction $^4\text{He}(^8\text{He}, ^8\text{Be})4n$ at 200 A MeV was measured for investigating the tetra-neutron system, which is now analyzing. In-beam spectroscopy of neutron-rich Ca isotopes was performed by using ^{70}Zn primary beam at RIBF. The fusion reaction $^{26}\text{Mg}(^{18}\text{O}, 2\alpha n)$ reaction was measured at the Tandem ALTO facility in Orsay for searching super deformed states in ^{35}S . The readout system of 14 detectors of the CNS GRAPE was upgraded, where digital pulse data taken by sampling ADCs are analyzed by FPGAs on boards.

The nuclear astrophysics group is studying astrophysical reactions particularly at high temperature phenomena, such as supernovae and X-ray bursts, using the low-energy beam separator, CRIB. In 2012, the operation of CRIB scheme was renewed after the retirement of Prof. Kubono. The $^{17}\text{F}+p$ resonant scattering experiment proposed by IMP (Lanzhou) group was performed, and it was the first experiment under the new scheme. The preparation for the approved ^{16}N alpha-decay measurement is in progress, and the development of the active target (GEM-MSTPC) including gating grid system and the ^{16}N beam production test were carried out. The production test of ^{44}Ti beam, which is one of the heaviest beams produced ever at CRIB, was performed and we had a good prospect for producing the beam at 10^4 pps order. We also had two test beamtimes of the industrial application of the RI beam at CRIB in collaboration with RIKEN.

One of the major tasks of the accelerator group is the AVF upgrade project that includes development of ion source, improvement in operation of the AVF cyclotron of RIKEN and the transport to the CRIB. Development of ECR heavy ion sources is to provide a new HI beams, higher and stable beams of metallic ions, and to improve the control system. The HyperECR and the SuperECR provides all the beams for the AVF cyclotron and support not only CRIB experiments but also a large number of RIBF experiments. New ion-source beam diagnosis and monitoring system are being developed, where a new method of beam emittance method and a plasma spectrometry are applied.

The SHARAQ group performed two physics experiments. One was a search for tetra-neutron states via the $^4\text{He}(^8\text{He}, ^8\text{Be})$ reaction. The exothermicity of the $(^8\text{He}, ^8\text{Be})$ reaction is advantageous in populating the fragile tetra-neutron states from the ^4He target. The energy needed in the target excitation is almost completely compensated by the positive Q-value in the projectile. The other was an $^{14,22,24}\text{O}(p, 2p)$ reaction experiment, which was designed to exploit the systematics of spin-orbit splitting of oxygen isotopes following our subsequent study of the $^{18}\text{O}(p, 2p)$ reaction at RCNP. The polarized proton target was introduced to SHARAQ for the first time and was operated successfully. The data analyses for these experiments are currently underway.

Main goal of the quark physics group is to understand the properties of hot and dense nuclear matter created by colliding heavy nuclei at relativistic energies. The group has been involved in the PHENIX experiment at Relativistic Heavy Ion Collider (RHIC) at Brookhaven National Laboratory, and in the ALICE experiment at Large Hadron Collider (LHC) at CERN.

In PHENIX, the group has been concentrating on the physics analysis involving leptons and photons. The main topics are; J/ψ production in ultra-peripheral Au+Au collisions, direct photon production using the virtual-gamma method, and heavy quark production using electrons from semi-leptonic decay.

In ALICE, the group has been involved in the installation/commissioning of the Transition Radiation Detector (TRD), and has started R&D for GEM based Time Projection Chamber (TPC) readout system in this year.

The group also has significant contribution to the data analysis in ALICE. The main physics topics are; Chiral magnetic effect using multi-particle azimuthal angular correlation, parton energy loss in the medium using neutral pions, and production mechanism of low-mass dilepton production in Pb-Pb collisions.

The group has also been working for the FoCal (forward calorimeter) for future ALICE upgrade. Significant progress has been made for the R&D of ASIC readout electronics in 2012.

R&D of gas electron multiplier (GEM) and related techniques has been continuing. A topic in 2012 was the development of GEM with insulator made of glass (glass-GEM).

In a project of active target development launched as an intergroup collaboration in 2009, two types of active target have been developed. Technical developments such as a capability of gating operation of GEM and the operation of GEM with low-pressure deuterium are undergoing. A pilot experiment with 14O beam for CAT was performed.

The nuclear theory group has been promoting the RIKEN-CNS collaboration project on large-scale nuclear structure calculations since 2001 and maintaining its parallel computing clusters. Based on this experience, we participated in activities of HPCI Strategic Programs for Innovative Research (SPIRE) Field 5 "The origin of matter and the universe" since 2011. The SPIRE project aims at the comprehensive understanding of the origin and structure of matter and the universe utilizing K computer. We started using K computer since September 2012 for the Monte Carlo Shell Model calculations. We mainly studied exotic nuclear structure of nickel isotopes and *ab initio* calculations of light nuclei.

In March 2013, our research activities since the last CNS review in 2005 were reviewed by the international review committee appointed by the dean of the Graduate School of Science, the University of Tokyo. The committee members were Prof. T. Kishimoto, Prof. S. Gales, Prof. S. Nagamiya, Prof. T. Noro, and Prof. K. Langanke. We appreciate the committee for the precise and thoughtful review report. We are encouraged to find that the short- and mid-term plans of CNS groups were deemed well defined. On the other hand, the committee advised us to concentrate the present diverse projects to fewer ones, while maintaining individual independency. Discussion of the future project has been started accordingly.

The 11th CNS International Summer School (CNSSS12) has been organized in September 2012 with many invited lecturers including three foreign distinguished physicists. There were 104 participants including 9 lecturers from 7 countries mainly from Asia.

Along the radiation-map project, the CNS continues measurements of radioactivities in soils taken around the Fukushima Daiichi Nuclear Power Plant for study of the depth profiles and their long-range propagation. About 600 samples taken in early summer and early winter were measured in the CNS.

Finally, I thank Ms. Y. Asakawa, Mr. H. Yoshimura and other administrative and technical staff members for their heartfelt contributions throughout the year.

Takaharu Otsuka
Director of CNS



Table of Contents

1a. Experimental Nuclear Physics: Low and Intermediate Energies

Spectroscopy of neutron-rich nuclei around ^{32}Mg via α inelastic scattering	3
<i>T. Fujii, S. Ota, S. Shimoura, N. Aoi, E. Takeshita, S. Takeuchi, H. Suzuki, H. Baba, T. Fukuchi, T. Fukui, Y. Hashimoto, E. Ideguchi, K. Ieki, N. Iwasa, H. Iwasaki, S. Kanno, Y. Kondo, T. Kubo, K. Kurita, T. Minemura, S. Michimasa, T. Motobayashi, T. Murakami, T. Nakabayashi, T. Nakamura, J. Niikura, T. Okumura, T. Onishi, H. Sakurai, M. Shinohara, D. Suzuki, M. Suzuki, M. Tamaki, K. Tanaka, Y. Togano, and Y. Wakabayashi</i>	
Study of high spin states in ^{35}S	5
<i>S. Go, E. Ideguchi, R. Yokoyama, M. Kobayashi, K. Kisamori, S. Michimasa, S. Shimoura, M. Niikura, A. Yagi, H. Nishibata, I. Matea, D. Suzuki, D. Verney, F. Azaiez, M. Sugawara, M. Koizumi, Y. Toh, T. Shizuma, A. Kimura, H. Harada, Y. Furutaka, S. Nakamura, F. Kitatani, Y. Hatsukawa.</i>	
In-beam Gamma-ray Spectroscopy of $^{38,40,42}\text{Si}$	7
<i>M. Matsushita S. Takeuchi, N. Aoi, P. Doornenbal, J. Lee, K. Li, T. Motobayashi, H. Scheit, D. Steppenbeck, H. Wang, H. Baba, D. Bazin, L. C�aceres, H. Crawford, P. Fallon, R. Gernh�user, J. Gibelin, S. Go, S. Gr�vy, C. Hinke, C. R. Hoffman, R. Hughes, E. Ideguchi, D. Jenkins, N. Kobayashi, Y. Kondo, R. Kriicken, T. Le Bleis, G. Lee, A. Matta, S. Michimasa, T. Nakamura, S. Ota, M. Petri, T. Sako, H. Sakurai, S. Shimoura, K. Steiger, K. Takahashi, M. Takechi, Y. Togano, R. Winkler, and K. Yoneda</i>	
In-beam γ -ray spectroscopy of ^{53}Ca and ^{54}Ca	9
<i>D. Steppenbeck, S. Takeuchi, N. Aoi, P. Doornenbal, M. Matsushita H. Wang, H. Baba, N. Fukuda, S. Go J. Lee, K. Matsui, S. Michimasa T. Motobayashi, D. Nishimura, H. Sakurai, Y. Shiga, P.-A. S�oderstr�m, T. Sumikama, H. Suzuki, R. Taniuchi, J. J. Valiente-Dob�n and K. Yoneda</i>	
Observation of new isomers in neutron-rich Tb isotopes	11
<i>R. Yokoyama, D. Kameda, T. Kubo, N. Inabe, N. Fukuda, S. Go, T. Fujii, E. Ideguchi, H. Takeda, H. Suzuki, K. Yoshida, K. Kusaka, K. Tanaka, Y. Yanagisawa, M. Ohtake, H. Sato, Y. Shimizu, H. Baba, M. Kurokawa, D. Nishimura, T. Ohnishi, N. Iwasa, A. Chiba, T. Yamada, H. Nishibata, K. Ieki, D. Murai, S. Momota, Y. Sato, J. Hwang, S. Kim, O. B. Tarasov, D. J. Morrissey, B. M. Sherrill, and G. Simpson</i>	
Spectroscopy of single-particle states in oxygen isotopes via the (\bar{p},pN) reaction with polarized protons	13
<i>S. Kawase, T. Uesaka, S. Shimoura, K. Yako, S. Ota, S. Michimasa, H. Tokieda, H. Miya, T. L. Tang, K. Kisamori, M. Takaki, Y. Kubota, C. S. Lee, R. Yokoyama, T. Fujii, M. Kobayashi, M. Sasano, J. Zenihiro, H. Matsubara, M. Dozono, J. Lee, H. Sakai, T. Kubo, K. Yoshida, N. Inabe, Y. Yanagisawa, H. Takeda, K. Kusaka, N. Fukuda, D. Kameda, H. Suzuki, T. Kawahara, T. Wakui, S. Sakaguchi, T. Noro, T. Wakasa, J. Yasuda, T. Fukunaga, Y. Maeda, W. Y. Kim, S. H. Hwang, S. Stepanyan, A. Obertelli, A. Galindo-Uribarri, E. Padilla-Rodal, and D. Beaumel</i>	
Measurement of the $^8\text{He}(p,n)^8\text{Li}$ reaction at intermediate energy in inverse kinematics	15
<i>M. Kobayashi, K. Yako, S. Shimoura, M. Dozono, S. Kawase, K. Kisamori, Y. Kubota, C.S. Lee, S. Michimasa, H. Miya, S. Ota, H. Sakai, M. Sasano and M. Takaki</i>	
Missing-mass spectroscopy of the $4n$ system by exothermic double-charge exchange reaction $^4\text{He}(^8\text{He}, ^8\text{Be})4n$	17
<i>K. Kisamori, S. Shimoura, H. Miya, M. Assie, H. Baba, T. Baba, D. Beaumel, M. Dozono, T. Fujii, N. Fukuda, S. Go, F. Hammache, E. Ideguchi, N. Inabe, M. Ito, D. Kameda, S. Kawase, T. Kawabata, M. Kobayashi, Y. Kondo, T. Kubo, Y. Kubota, M. Kurata-Nishimura, C. S. Lee, Y. Maeda, H. Matsubara, S. Michimasa, K. Miki, T. Nishi, S. Noji, S. Ota, S. Sakaguchi, H. Sakai, Y. Sasamoto, M. Sasano, H. Sato, Y. Shimizu, A. Stolz H. Suzuki, M. Takaki, H. Takeda, S. Takeuchi, A. Tamii, L. Tang, H. Tokieda, M. Tsumura, T. Uesaka, K. Yako, Y. Yanagisawa and R. Yokoyama</i>	
Study of spin-isospin responses via exothermic charge exchange reaction $(^8\text{He}, ^8\text{Li}^*(1^+))$	19

H. Miya, S. Shimoura, K. Kisamori, M. Assié, H. Baba, T. Baba, D. Beaumel, M. Dozono, T. Fujii, N. Fukuda, S. Go, F. Hammache, E. Ideguchi, N. Inabe, M. Ito, D. Kameda, S. Kawase, T. Kawabata, M. Kobayashi, Y. Kondo, T. Kubo, Y. Kubota, C. S. Lee, Y. Maeda, H. Matsubara, S. Michimasa, K. Miki, T. Nishi, M. Kurata-Nishimura, S. Ota, H. Sakai, S. Sakaguchi, M. Sasano, H. Sato, Y. Shimizu, H. Suzuki, A. Stolz, M. Takaki, H. Takeda, S. Takeuchi, A. Tamii, H. Tokieda, M. Tsumura, T. Uesaka, K. Yako, Y. Yanagisawa, and R. Yokoyama

Search for a double Gamow-Teller giant resonance with heavy-ion double charge exchange ($^{12}\text{C}, ^{12}\text{Be}(0_2^+)$) reaction . 21

M. Takaki, H. Matsubara, T. Uesaka, S. Shimoura, N. Aoi, M. Dozono, T. Hashimoto, T. Kawabata, S. Kawase, K. Kisamori, M. Kobayashi, C.S. Lee, Y. Maeda, S. Michimasa, K. Miki, H. Miya, S. Ota, S. Sakaguchi, M. Sasano, T. Suzuki, K. Takahisa, T.L. Tang, A. Tamii, H. Tokieda, K. Yako and J. Zenihiro

Charge-exchange (p,n) reaction in inverse-kinematics with isomer beams: Toward feasibility test on the isomer $^{52}\text{Fe}(12^+)$ 23

K. Yako, M. Kobayashi and H. Sakai

Quasi-elastic scattering of the proton drip line nucleus ^{17}F on ^{12}C at 60MeV 25

G. L. Zhang, C. L. Zhang, H. Q. Zhang, C. J. Lin, D. Y. Pang, X. K. Wu, H. M. Jia, G. P. An, Z. D. Wu, X. X. Xu, F. Yang, Z. H. Liu, S. Kubono, H. Yamaguchi, S. Hayakawa, D. N. Binh, Y. k. Kwon, N. Iwasa, M. Mazzocco, M. La Commara, M. Romoli, and C. Signorini

Investigation for the resonant scattering of $^{17}\text{F}+p$ 27

J. Hu, J. J. He, S. W. Xu, H. Yamaguchi, P. Ma, D. Kahl, J. Su, H. W. Wang, T. Nakao, Y. Wakabayashi, J. Y. Moon, T. Teranishi, H. S. Jung, T. Hashimoto, A. Chen, D. Irvine, and S. Kubono

1b. Experimental Nuclear Physics: PHENIX Experiment at BNL-RHIC and ALICE Experiment at CERN-LHC

First Three-Year Operation of the LHC-ALICE experiment and Activities of CNS 31

T. Gunji, H. Hamagaki, Y. L. Yamaguchi, S. Sano, Y. Hori, T. Tsuji, S. Hayashi, K. Terasaki

Measurement of dielectron in $\sqrt{s_{NN}} = 5.02$ TeV p+Pb collision at LHC 33

S. Hayashi, for the ALICE Collaboration

Heavy-quark measurement in p+p collisions at $\sqrt{s_{NN}} = 200\text{GeV}$ 35

R. Akimoto, Y. Akiba, H. Asano, T. Gunji, T. Hachiya, H. Hamagaki, M. Kurosawa, M. Shimomura (for the PHENIX Collaboration)

Measurement of J/ψ photo-production in ultra-peripheral Au+Au collisions at $\sqrt{s_{NN}}=200\text{GeV}$ using the PHENIX detector 37

A. Takahara, H. Hamagaki, T. Gunji, Z. Conesa del Valle, Y. Akiba, M. Chiu, J. Nystrand, S. White, K. Skjerdal, E. T. Atomssa for the PHENIX collaboration

2. Accelerator and Instrumentation

Ion back flow study for the ALICE GEM-TPC upgrade	41
<i>Y.L. Yamaguchi, H. Hamagaki, and T. Gunji, on behalf of the ALICE-TPC group</i>	
Study of Ion Back Flow Suppression with Thick COBRA GEM	43
<i>K. Terasaki, H. Hamagaki, T. Gunji, and Y.L. Yamaguchi</i>	
Performance test of the wide-dynamic-range ASIC for W+Si calorimeter	45
<i>S. Hayashi, H. Hamagaki, T. Gunji, M. Tanaka, and H. Ikeda</i>	
The design and development of SOI pixel detector for radiation monitor	47
<i>Y. Sekiguchi, H. Hamagaki, T. Gunji, Y. Arai, T. Imamura, T. Ohmoto, and A. Iwata</i>	
Performance evaluation of CAT through the measurement of $d(^{14}\text{O},d)$ reaction	49
<i>S. Ota, H. Tokieda, A. Corsi, M. Dozno, J. Gibelin, T. Gunji, H. Hamagaki, T. Kawabata, S. Kawase, S. Kubono, Y. Kubota, C.S. Lee, Y. Maeda, H. Matsubara, Y. Matsuda, S. Michimasa, T. Nakao, T. Nishi, A. Obertelli, K. Okochi, H. Otsu, T. Ryan, C. Santamaria, M. Sasano, M. Takaki, Y. Tanaka, T. Uesaka, K. Yako, H. Yamaguchi, J. Zenihiro, E. Takada</i>	
Measurements of Gas Gain of Gas Electron Multiplier with 1-atm Deuterium Gas	51
<i>H. Tokieda, S. Ota, M. Dozono, C. S. Lee, and T. Uesaka</i>	
Properties of Thick-GEM in Low Pressure Deuterium for Low Pressure Gaseous Active Target	53
<i>C. S. Lee, S. Ota, H. Tokieda and T. Uesaka</i>	
Algorithms for Active Target Data Analysis	55
<i>D. Kahl, T. Hashimoto, S. Kubono, S. Ota, and H. Yamaguchi</i>	
Ion-optical study of SHARAQ for high-resolution spectroscopy	57
<i>S. Michimasa, M. Takaki, M. Dozono, T. Nishi, S. Go, H. Baba, A. Stolz, S. Ota, K. Yako, H. Matsubara, H. Miya, H. Tokieda, S. Kasase, K. Kisamori, R. Yokoyama, T. Fujii, Y. Kubota, C.S. Lee, M. Kobayashi, T. Kawabata, T. Baba, M. Tsumura, R.G.T. Zegers, E. Ideguchi, H. Takeda, Y. Yanagisawa, T. Kubo, N. Inabe, N. Fukuda, D. Kameda, H. Suzuki, Y. Shimizu, H. Sato, T. Ichihara, H. Sakai, T. Uesaka, S. Shimoura for the SHARAQ collaboration</i>	
Polarized proton target in SHARAQ04 experiment	59
<i>T.L. Tang, S.H. Hwang, T. Kawahara, T. Wakui, S. Sakaguchi, S. Kawase, T. Uesaka</i>	
Performance test of high-granularity neutron detector with neutron beams in CYRIC	61
<i>Y. Kubota, M. Sasano, T. Uesaka, M. Dozono, M. Itoh, S. Kawase, M. Kobayashi, C. S. Lee, H. Matsubara, H. Miya, S. Ota, K. Sekiguchi, T. Taguchi, T. L. Tang, H. Tokieda and T. Wakui</i>	
Beam simulation of AVF cyclotron injection line for efficient beam transportation	63
<i>S. Watanabe, Y. Ohshiro, S. Yamaka, H. Yamaguchi, S. Shimoura, Y. Kotaka, M. Kase, K. Hatanaka, A. Goto, W. Yotaka, T. Mitsumoto</i>	
Development of intense ^7Be and ^{22}Na beam for wear diagnostic application	65
<i>A. Yoshida, A. Nakao, T. Kambara, R. Uemoto, H. Uno, H. Yamaguchi, T. Nakao, and D. Kahl</i>	
Radioactive Beam Production of ^{44}Ti	67
<i>H. Ishiyama, H. Yamaguchi, Y.X. Watanabe, D. Kahl, Y. Hirayama, T. Nakao, N. Imai, Y.H. Kim, M. Mukai, M. Oyaizu, H. Miyatake, S.C. Jeong, Y. Wakabayashi, T. Hashimoto, P. Lee, G.W. Kim, and T. Komatsubara</i>	
Plasma Spectroscopy for Hyper-ECR Ion Source	69
<i>H. Muto, Y. Ohshiro, S. Yamaka, S. Watanabe, M. Oyaizu, S. Kubono, H. Yamaguchi, M. Kase, T. Hattori and S. Shimoura</i>	

3. Theoretical Nuclear Physics

Rotational stabilization in exotic and heavy nuclear synthesis	73
<i>Y. Iwata</i>	
E1 strength in calcium isotopes in view of shell-model calculations	75
<i>N. Shimizu, S. Ebata, M. Honma</i>	
The behavior of PDR and E1 polarizability with respect to neutron skin-thickness	77
<i>S. Ebata and T. Nakatsukasa</i>	
Shape transitions in exotic Si and S isotopes and tensor-force-driven Jahn-Teller effect	79
<i>Y. Utsuno, T. Otsuka, B. A. Brown, M. Honma, T. Mizusaki, and N. Shimizu</i>	
Shell-model calculation of the high-spin states in neutron-rich Cr isotopes	81
<i>T. Togashi, N. Shimizu, Y. Utsuno and T. Otsuka</i>	
Cluster structure in Monte Carlo shell model	83
<i>T. Yoshida, N. Shimizu, T. Abe and T. Otsuka</i>	

4. Other Activities

Laboratory exercise for undergraduate students	87
<i>S. Ota, K. Yako, M. Niikura, M. Kobayashi, K. Matsui, H. Sakurai, and S. Shimoura</i>	

Appendices

Symposium, Workshop, Seminar, PAC and External Review	91
CNS Reports	93
Publication List	94
Talks and Presentations	100
Personnel	108

Experimental Nuclear Physics: Low and Intermediate Energies

Spectroscopy of neutron-rich nuclei around ^{32}Mg via α inelastic scattering

T. Fujii, S. Ota, S. Shimoura, N. Aoi^b, E. Takeshita^a, S. Takeuchi^a, H. Suzuki^b, H. Baba^a, T. Fukuchi^c, T. Fukui^d, Y. Hashimoto^e, E. Ideguchi, K. Ieki^f, N. Iwasa^g, H. Iwasaki^h, S. Kanno^a, Y. Kondo^b, T. Kubo^a, K. Kurita^f, T. Minemura^a, S. Michimasa, T. Motobayashi^a, T. Murakami^d, T. Nakabayashi^e, T. Nakamura^e, M. Niikura^b, T. Okumura^e, T. Onishi^b, H. Sakurai^a, M. Shinohara^e, D. Suzuki^b, M. Suzuki^b, M. Tamaki, K. Tanaka^a, Y. Togano^f, and Y. Wakabayashiⁱ

Center for Nuclear Study, Graduate School of Science, University of Tokyo

^aRIKEN (The Institute of Physical and Chemical Research)

^bDepartment of Physics, University of Tokyo

^cDepartment of Physics, Osaka University

^dDepartment of Physics, Kyoto University

^eDepartment of Physics, Tokyo Institute Technology

^fDepartment of Physics, Rikkyo University

^gDepartment of Physics, Tohoku University

^hInstitut de Physique Nucléaire, IN2P3-CNRS, 91406 Orsay, France

ⁱDepartment of Physics, Kyusyu University

The ^{32}Mg nucleus and several neutron-rich ($N=20$) nuclei around ^{32}Mg have attracted much interest. The nature of these nuclei is very different from that of other nuclei which are near the β stability line. Especially, the ^{32}Mg nucleus has been mainly watched, because of its large $B(E2; 0_{g.s.}^+ \rightarrow 2_1^+)$. The ^{31}Na nucleus and the ^{30}Ne nucleus have anomalous nature like the ^{32}Mg nucleus. These nuclei have been called island of inversion. On the other hand, the nature of the ^{34}Si nucleus is similar to that of stable $N=20$ magic nuclei. It means the ^{34}Si nucleus is out of the island of inversion. The ^{33}Al nucleus is the nucleus between ^{34}Si and ^{32}Mg . This nucleus is thought to be near or on the border of island of inversion. More studies about the ^{33}Al nucleus and the systematics on $N=20$ nuclei are expected to develop an understanding of island of inversion. In the present work, we discuss the differential cross section of ^{32}Mg and ^{33}Al with α -inelastic scattering. α -inelastic scattering is considered as a best tool for investigating the isoscalar multipole excitation since the α particle is a $T=0, S=0$ probe. Using this probe and cocktail beam, we can study the deformation of nuclear matter systematically around $N=20$ region.

The experiment was performed at RIKEN. A 63 MeV/nucleon ^{40}Ar beam from the ring cyclotron was fragmented in a 1 mm-thick carbon target. The fragmentation products were separated by RIKEN projectile fragmentation separator, RIPS [1]. A particle identification was accomplished by measuring the energy loss in a silicon detector and time-of-flight (TOF). The TOF was obtained from the timing information of RF-signal and a plastic detector at the third focal plane. The secondary ^{32}Mg beam bombarded a liquid helium target. The γ ray detector Array with Energy and Position sensitivity (GRAPE [2]) was positioned around the reaction target to detect the γ rays from the excited states populated in the reaction. Each segment of GRAPE has position sensitivity of about 3 mm FWHM. Doppler shift of γ ray from outgoing particle moving at $\beta \sim 0.26$ can be corrected, by using the interaction point of the γ rays in GRAPE, reaction position, the angle of outgoing particle and the velocity of the outgoing particle, which is measured as described below. For the identifica-

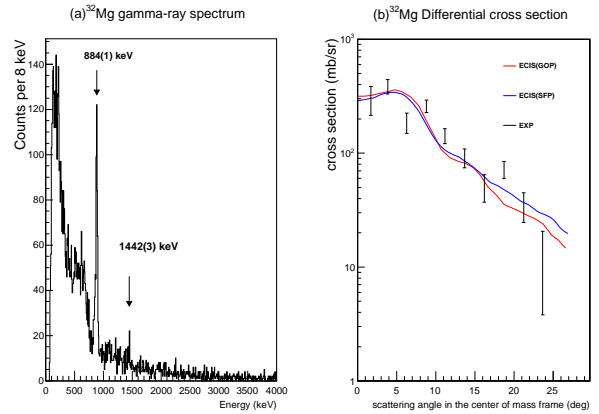


Figure 1. (a) Doppler corrected γ ray spectrum for the $^{32}\text{Mg}(\alpha, \alpha')^{32}\text{Mg}$ reaction. One clear peak positions at 884 (1) keV. There is a small peak around 1436 keV. This peak corresponds to $4_1^+ \rightarrow 2_1^+$. (b) The differential cross section of $^{32}\text{Mg}(\alpha, \alpha')^{32}\text{Mg}$ reaction. The black dots are experimental data. The red (blue) curve is the result of coupled channel calculation with Global Optical Potential (Single Folding Potential).

tion of outgoing particles, TOF-Spectrometer [3] was used. The TOF was obtained from the timing information of two plastic scintillators. The flight length between them is 386 cm, which is long enough to separate each nucleus. Superconducting Triplet Quadrupole magnets (STQ) [3] was used in order to focus the outgoing particles the energy loss was measured by silicon detectors. For the purpose of mass identification, NaI Wall [4] was positioned at the end of the beam line, and it enabled us to measure the total energy of outgoing particles. The positions of incoming and scattered particles were measured with PPACs. Three of them were placed upstream of the target, and two was placed downstream. By these PPACs we could obtain the reaction position in the target and the scattering angle.

The γ ray spectrum after doppler-shift correction is shown in Fig. 1 (a). To obtain this spectrum, we selected the

event which the beam particle and scattered particle were both considered to be ^{32}Mg . We can see a clear peak at 887 keV which corresponds to de-excitation from the first excited 2^+ state at 885 keV to the ground state of ^{32}Mg .

Selecting the events correspond to individual excitations by this spectrum and using the information of scattering angle measured by PPACs, the differential cross section is going to be obtained. To obtain the differential cross section, we considered some corrections. First, for correction of the number of scattering particle, we considered the loss of transfer in TOF-spectrometer and non-sensitive region of NaI-Wall. For ^{32}Mg , we used the data only upstream of TOF-Spectrometer to avoid this correction. The particle identification of scattered ^{32}Mg was enough good although we used limited data. Second, we reduce the γ ray yield by 5.4 (4)% because the angular distribution of γ ray concentrates to forward angle and GRAPE doesn't cover 4π around the target. We estimated the angular distribution of emitted γ ray using ECIS97 [5] code. We used this angular distribution for GEANT4 simulation and got the correction factor 5.4 (4)%. Finally, the differential cross section of the excitation from 0^+ ground state to first excited 2^+ state for ^{32}Mg was reduced by 26 (8)% for the correction of feeding from the higher excited state. Because 885 keV γ ray is emitted not only the excitation from 0^+ ground state to first 2^+ state but also the excitation from 0^+ state to some highly excitations with their de-excitations pass the first 2^+ state. To obtain the correction factor 26 (8)%, we calculated the differential cross section from ground state to first 4^+ state, that exists at 1436 keV. And then, we multiply that cross section by 2, for all the excitations with their de-excitations pass the first 2^+ state. The factor 2 is estimated for the experiment of proton inelastic scattering on ^{32}Mg .

We compared the obtained cross section data with the calculated one using ECIS97 [5] code. About ^{32}Mg , we used the single folding model for coupled channel calculation. The comparison is shown in Fig. 1 (b). From comparison, we obtained ground state quadrupole deformation parameter $\beta_2 = 0.40$ (3). This is slightly small compared to proton-inelastic scattering [6] and coulex [7], but it is consistent within the error.

The γ ray spectrum for α inelastic scattering on ^{33}Al is shown in Fig. 2 (a). There are two clear peaks at 746 keV and 1436 keV. And the differential cross section for α inelastic scattering on ^{33}Al is shown in Fig. 2 (b). We made this figure considering that 746 keV γ ray corresponds to the transition from the ground state of ^{33}Al to the first excited state of ^{33}Al . But there is not enough statistics, so more detailed research is hoped.

References

- [1] T. Kubo et al., Nucl. Instr. Meth. B 70, 309 (1992).
- [2] S. Shimoura, Nuclear Instruments and Methods in Physics Research Section A 525, 188 (2004).
- [3] N. Aoi et al., RIKEN Accel. Prog. Rep. 38, 176 (2005).
- [4] T. Tamaki et al., CNS-REP 59, 76 (2003).
- [5] J. Raynal, coupled-channel code ECIS97 (unpublished).
- [6] S. Takeuchi et al., Phys. Rev. C 79, 054319 (2009).
- [7] T. Motobayashi et al., Phys.Lett.B 346, 9 (1995).

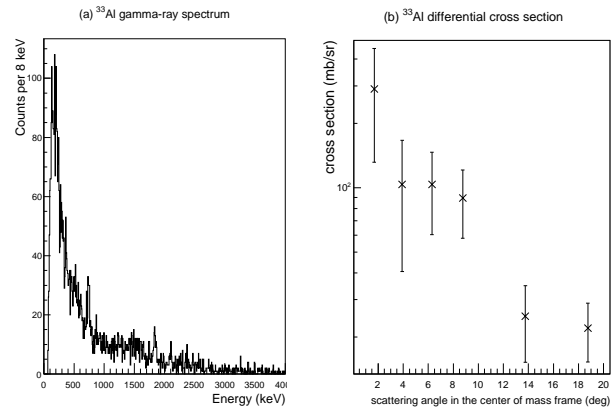


Figure 2. (a) Doppler corrected γ ray spectrum for the $^{33}\text{Al}(\alpha, \alpha')^{33}\text{Al}$ reaction. One clear peak positions at 746 (3) keV. There is another peak at 1436 (4) keV. (b) The differential cross section of $^{32}\text{Al}(\alpha, \alpha')^{33}\text{Al}$ reaction. The Black dots is experimental data.

Study of high spin states in ^{35}S

S. Go, E. Ideguchi^a, R. Yokoyama, M. Kobayashi, K. Kisamori, S. Michimasa, S. Shimoura, M. Niikura^b, A. Yagi^c, H. Nishibata^c, I. Matea^d, D. Suzuki^d, D. Verney^d, F. Azaiez^d, M. Sugawara^e, M. Koizumi^f, Y. Toh^f, T. Shizuma^f, A. Kimura^f, H. Harada^f, Y. Furutaka^f, S. Nakamura^f, F. Kitatani^f, Y. Hatsukawa^f.

Center for Nuclear Study, Graduate School of Science, University of Tokyo

^aResearch Center for Nuclear Physics, Osaka University

^bDepartment of Physics, University of Tokyo

^cDepartment of Physics, Osaka University

^dInstitute de Physique Nucléaire d'Orsay

^eDepartment of Physics, Chiba Institute of Technology

^fJapan Atomic Energy Agency

Since the finding of superdeformed (SD) band in ^{152}Dy [1], SD structures in various mass regions have been systematically studied. Recently SD rotational bands in the mass $A \sim 40$ region have been discovered in ^{36}Ar [2], ^{40}Ar [3] and ^{40}Ca [4]. The occurrence of SD structures in this region is related to the existence of large energy gaps of deformed single particle energies. Woods-Saxon single particle diagram (see Fig. 4 of Ref [4]) shows the gaps at $\beta_2 \sim 0.5$ in $Z = 18$ and $\beta_2 \sim 0.6$ in $Z = 20$. The diagram also shows candidates of the SD nuclei, $\beta_2 \sim 0.6$ in $Z = 16$. The existence of the SD band in ^{32}S ($Z = 16$) was predicted for a long time [5], but the SD structure has not been observed yet. Neutron-rich sulfur isotopes were also predicted as the candidates of SD nuclei by Skyrme-Hartree-Fock calculation and the SD local minimum in ^{36}S appears due to the combination of the large gap in $Z = 16$ and $N = 20$ [6]. Accordingly, the high spin study of the neutron-rich sulfur isotopes has the importance to clarify the SD structure in $Z = 16$. About the high spin state in ^{35}S , the excited levels up to 7.18 MeV were found and the multiplicities of each γ -ray transition were studied in our previous study [7, 8]. To clarify the high spin levels and to investigate the collective structure in ^{35}S , we have performed the in-beam γ -ray spectroscopy experiment.

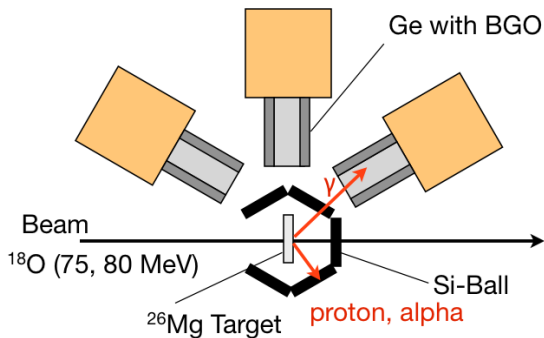


Figure 1. Schematic view of experimental setup. 13 Ge detectors with BGO Compton suppressor shield were used to measure the gamma-ray. Protons and alpha particles evaporated from the compound nuclei were measured by the Si-Ball.

The experiment was performed at the tandem accelerator facility of Institute de Physique Nucléaire d'Orsay (IPN Orsay). Figure 1 shows the schematic view of experimental

setup. High spin states of ^{35}S was produced by the fusion evaporation reaction $^{26}\text{Mg}(^{18}\text{O}, 2\alpha)^{35}\text{S}$ at an ^{18}O beam energy of 75 and 80 MeV. A thin ^{26}Mg self-supporting target was used. γ -rays were measured by the ORGAM array

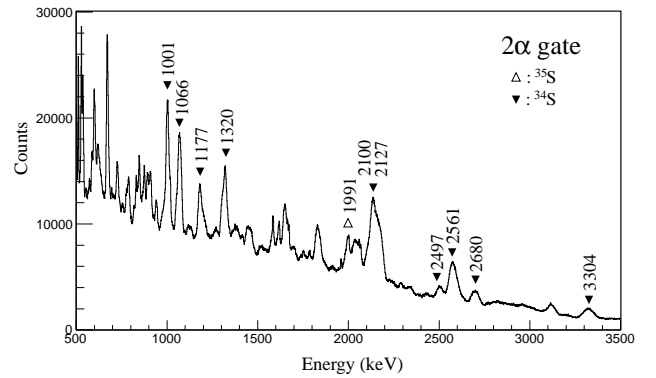


Figure 2. Gamma-ray spectrum obtained by gating the events with two alpha particles. The lowest transition related to ^{35}S at 1.991 MeV [14] was also observed. Strong peaks related to ^{34}S [12], which had the largest cross section in two alpha channel estimated by the CASCADE calculation [13], were observed in the spectrum.

comprised of the EUROGAM coaxial germanium detectors with the BGO Compton suppressor shield [9]. The 13 detectors were placed at 3 different angles, 46° (3 Ge's), 90° (5 Ge's), and 133° (5 Ge's). The ΔE of charged particle from compound nuclei were measured by Si-Ball [10], a 4π array consisting of 11 Si detectors of $170 \mu\text{m}$ thickness. The most forward Si detector was segmented into 5 sections and the second forward detectors were segmented into 2 sections. Total 20 channels ΔE information were used to select the multi-charged evaporation channels. The Trigger rate of particle- γ - γ was averagely 2.5 kcps. The multi-event-data-readout system [11] was employed to measure in the high rate condition.

The γ -ray spectrum was obtained by gating the events with two alpha particles and correcting the Doppler effect of the gamma-rays (See Fig. 2). The lowest transition related to ^{35}S at 1.991 MeV [12] was observed, and γ - γ coincidence analysis have been performed by gating on the events with the 1.991 MeV γ -ray (See Fig. 3). The transitions reported in the previous study [7,8] were observed. To

find the new levels in ^{35}S , the improvement of Doppler-shift correction by considering the recoil effect of the evaporated particles by using the information from Si-Ball will be performed.

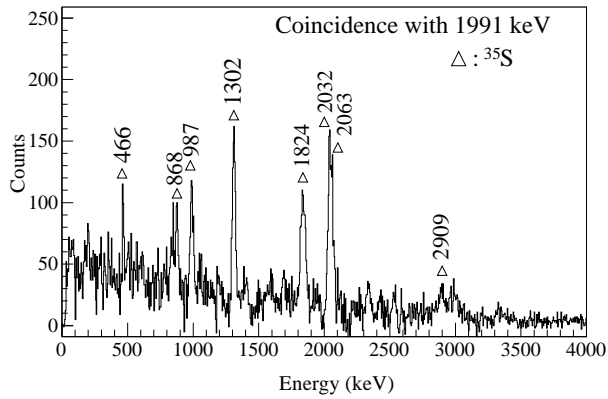


Figure 3. Gamma-ray spectrum gating the 1991 keV transition of ^{35}S . The peaks reported in previous study [7,8] were observed.

References

- [1] P. J. Twin *et al.*, Phys. Rev. Lett **57**, (1986) 7.
- [2] C. E. Swensson *et al.*, Phys. Lett. **85**, (2000) 2693.
- [3] E. Ideguchi *et al.*, Phys. Lett. B **686**, (2010) 18.
- [4] E. Ideguchi *et al.*, Phys. Rev. Lett. **87**, (2001) 222501.
- [5] I. Ragnarsson *et al.*, Phys. Rep. **45**, (1978) 1.
- [6] T. Inakura *et al.*, Nucl. Phys. A **728**, (2003) 52.
- [7] E. Ideguchi *et al.*, CNS Ann. Rep. 2009 (2010) 23.
- [8] E. Ideguchi *et al.*, CNS Ann. Rep. 2010 (2011) 5.
- [9] C. W. Beausang *et al.*, Nucl. Instr. Meth. A **313** (1992) 37.
- [10] T. Kuroyanagi *et al.*, Nucl. Instr. Meth. A **316** (1992) 289.
- [11] H. Baba *et al.*, Nucl. Instr. Meth. A **616** (2010) 65.
- [12] A. Guichard *et al.*, Phys. Rev. C **12** (1975) 4.
- [13] P. Mason *et al.*, Phys. Rev. C **71** (2005) 014316.
- [14] O. B. Tarasov and D. Bazin, Nucl. Instr. Meth. B **204** (2003) 174.

In-beam γ -ray spectroscopy of $^{38,40,42}\text{Si}$

M. Matsushita S. Takeuchi^a N. Aoi^b P. Doornenbal^a J. Lee^a K. Li^c T. Motobayashi^a H. Scheit^d
D. Steppenbeck H. Wang^c H. Baba^a D. Bazin^e L. Caceres^f H. Crawford^g P. Fallon^g
R. Gernhäuser^h J. Gibelinⁱ S. Go S. Grévy^f C. Hinke^h C. R. Hoffman^j R. Hughes^k E. Ideguchi^b
D. Jenkins^l N. Kobayashi^m Y. Kondoⁿ R. Krücken^o T. Le Bleis^h G. Leeⁿ A. Mattaⁱ S. Michimasa
T. Nakamuraⁿ S. Ota M. Petri^d T. Sakoⁿ H. Sakurai^a S. Shimoura K. Steiger^h K. Takahashiⁿ
M. Takechi^p Y. Toganoⁿ R. Winkler^d and K. Yoneda^a

Center for Nuclear Study, Graduate School of Science, University of Tokyo, RIKEN Campus, Wako, Saitama 351-0198, Japan.

^aRIKEN Nishina Center, Wako, Saitama 351-0198, Japan.

^bRCNP, Osaka University, Mihogaoka, Ibaraki, Osaka 567-0047, Japan.

^cState Key Laboratory of Nuclear Physics and Technology, Peking University, Beijing 100871, People's Republic of China.

^dInstitut für Kernphysik, Technische Universität Darmstadt, 64289 Darmstadt, Germany.

^eNational Superconducting Cyclotron Laboratory, Michigan State University, East Lansing, Michigan 48824, USA.

^fGrand Accélérateur National d'Ions Lourds, CEA/DSM-CNRS/IN2P3, F-14076 Caen Cedex 5, France.

^gLawrence Berkeley National Laboratory, Berkeley, California 94720, USA.

^hPhysik Department, Technische Universität München, D-85748 Garching, Germany.

ⁱInstitut de Physique Nucléaire, IN2P3-CNRS, Université de Paris Sud, F-91406 Orsay, France.

^jPhysics Division, Argonne National Laboratory, Argonne, Illinois 60439, USA.

^kDepartment of Physics, University of Richmond, Richmond, Virginia 23173, USA.

^lPhysics Department, University of York, Heslington, York YO10 5DD, United Kingdom.

^mDepartment of Physics, University of Tokyo, Bunkyo, Tokyo 113-0033, Japan.

ⁿDepartment of Physics, Tokyo Institute of Technology, Meguro, Tokyo 152-8551, Japan.

^oTRIUMF, 4004 Wesbrook Mall, Vancouver, Canada.

^pExtreme Matter Institute EMMI and Research Division, GSI Helmholtzzentrum, 64291 Darmstadt, Germany.

^qLos Alamos National Laboratory, Los Alamos, NM 87545, USA.

Excited states in the nuclei $^{38,40,42}\text{Si}$ have been studied using in-beam γ -ray spectroscopy following multi-nucleon removal reactions to investigate the systematics of excitation energies along the $Z=14$ isotopic chain [1]. The $N=28$ isotope, ^{42}Si , is regarded as a magic nucleus in the traditional shell model, because a large energy gap exists at $N=28$ and $Z=14$ due to the $f_{7/2} - f_{5/2}$ and $d_{5/2} - d_{3/2}$ spin-orbit splitting, respectively. The disappearance of the spherical shell closure together with a large deformation, however, has been suggested for ^{42}Si from the observation of a low energy 2_1^+ state [2]. Several experiments have been performed so far [3, 4, 5], but no experimental data have been reported on higher-lying state, such as 4_1^+ state, which will provide valuable information on the nature of the collectivity and/or shell evolution.

In order to study these states, we performed in-beam γ -ray spectroscopy of $^{38,40,42}\text{Si}$ with multi-nucleon removal reactions. Experiment was carried out at the RI Beam Factory accelerator complex operated by the RIKEN Nishina Center and CNS, University of Tokyo. The ^{40}S and ^{44}S beams were produced by a projectile fragmentation reaction of the ^{48}Ca primary beam with a typical intensity of around 70 pA. The primary beam bombarded a 15 mm-thick rotating Be target placed in the F0 focal plane of the in-flight RI beam separator BigRIPS [6] at 345 MeV/nucleon. The energy and intensity of the secondary ^{40}S (^{44}S) beam was approximately 210 MeV/nucleon (210 MeV/nucleon) and around 4×10^4 particles per second (pps) (6×10^4 pps), respectively. The secondary beams bombarded a reaction tar-

get of 2.54 g/cm²-thick C located at the F8 focal plane in the ZeroDegree Spectrometer [7], which was employed to analyze the reaction products ^{38}Si and $^{40,42}\text{Si}$ produced by the multi nucleon removal reaction of ^{40}S and ^{44}S , respectively. De-excitation γ -rays were detected in coincidence with each reaction by the DALI2 γ -ray spectrometer [8]. Owing to high detection efficiency of γ -ray spectrometer and the intense secondary beams, several γ -ray lines were observed for the first time.

The Doppler-shift corrected γ -ray energy spectra obtained for ^{38}Si , ^{40}Si and ^{42}Si are shown in Fig. 1. As shown in Fig. 1 (c), the $2_1^+ \rightarrow 0_{g.s.}^+$ transition in ^{42}Si previously observed at 770(19) keV [2] was measured at 742(8) keV with high statistics, whereas three γ -ray transitions with energies of 1431(11), 2032(9) and 2357(15) keV were obtained for the first time. With an analysis on γ - γ coincidence and intensity for each peak, the 1431-keV γ -ray lines was found out to feed the 2_1^+ state directly from a higher-lying excited state. This 1431-keV γ -ray line was tentatively assigned to the $4_1^+ \rightarrow 2_1^+$ transition in ^{42}Si based on the known tendency that yrast states, including the 2_1^+ and 4_1^+ states, are preferentially populated in nucleon removal reactions [9, 10, 11]. Similar analysis was also performed to data obtained for ^{38}Si and ^{40}Si . The 1168(22)- and 1539(16) keV γ -ray lines, as shown in Fig. 1 (a) and (b), were obtained as the most probable candidates for the $4_1^+ \rightarrow 2_1^+$ transitions in ^{38}Si and ^{40}Si , respectively.

The isotopic dependence of the excitation energy of 4_1^+ - and 2_1^+ states for $^{34-42}\text{Si}$ are shown together with their ratio

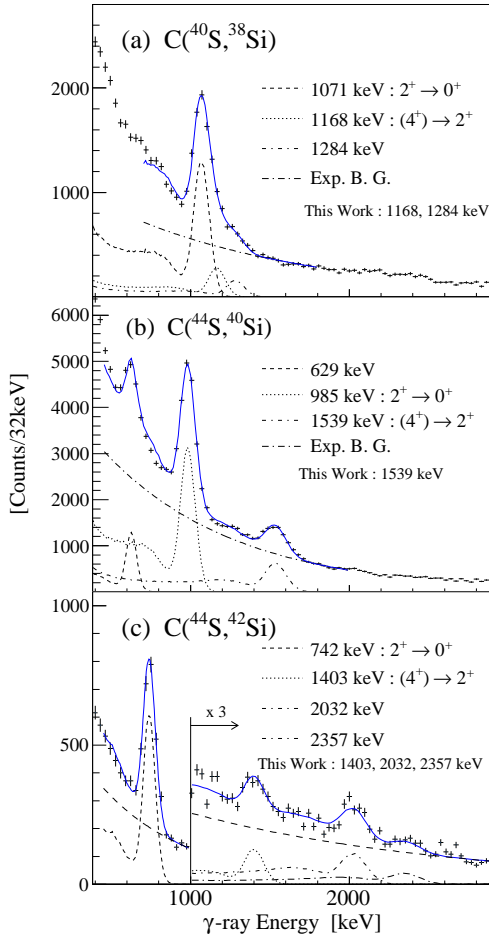


Figure 1. Doppler-shift corrected γ -ray energy spectra obtained in coincidence with (a) $C(^{40}\text{S}, ^{38}\text{Si})$, (b) $C(^{44}\text{S}, ^{40}\text{Si})$ and (c) $C(^{44}\text{S}, ^{42}\text{Si})$ reactions.

$R_{4/2}$ in Fig. 2, where the systematic properties of Si isotopes show large deviations toward $N=28$ from those of Ca isotopes which clearly demonstrate the magic behavior at the both of $N=20$ and 28 . The $R_{4/2}$ ratio for ^{36}Si and ^{38}Si are close to the vibrational limit (2.00), whereas it increases to 2.56(5) at ^{40}Si , indicating a deviation from the spherical shape at $N=26$. In the case of the $N=28$ isotope ^{42}Si , the $R_{4/2}$ ratio further increases to 2.93(5) despite the neutron magic number $N=28$. From the present study, a rapid development of deformation toward the $N=28$ isotope ^{42}Si was experimentally established, and the possibility of a magic nature of ^{42}Si was excluded. The present results are in good agreement with the prediction of the shell model calculation using SDPF-MU effective interaction [12, 13], which suggests the tensor force between neutron and proton plays a significant role in the structure of ^{42}Si .

References

- [1] S. Takeuchi *et al.*: Phys. Rev. Lett. **109**, 182501 (2012).
- [2] B. Bastin *et al.*: Phys. Rev. Lett. **99**, 022503 (2007).
- [3] R.W. Ibbotson *et al.*: Phys. Rev. Lett. **80**, 2081 (1998).
- [4] C.M. Campbell *et al.*: Phys. Rev. Lett. **97**, 112501 (2006).
- [5] C.M. Campbell *et al.*: Phys. Lett. B **652**, 169 (2007).
- [6] T. Kubo : Nucl. Instrum. Methods Phys. Res., Sect. B

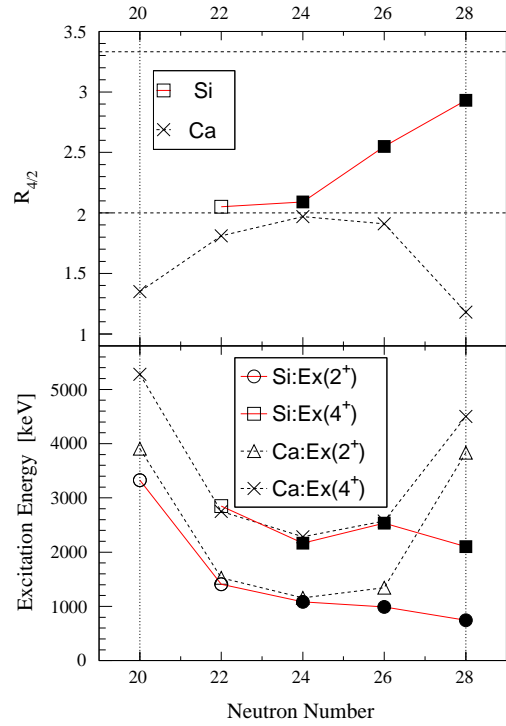


Figure 2. The energy of 2_1^+ - and 4_1^+ state (bottom panel), and its ratio (upper panel) of Si isotopes are compared with Ca isotopes. Filled symbols are results obtained from the present study. The horizontal lines at $R_{4/2}=2.00$ and 3.33 indicate the vibrational and rotational limits, respectively. The vertical lines at the neutron magic number $N=20$ and 28 are intended to guide the eye.

204, 97 (2003).

- [7] Y. Mizoi *et al.*: RIKEN Accel. Prog. Rep. **38**, 297 (2005).
- [8] S. Takeuchi *et al.*: RIKEN Accel. Prog. Rep. **36**, 148 (2003).
- [9] M. Bellegruic *et al.*: Phys. Scr. **T88**, 122 (2000).
- [10] K. Yoneda *et al.*: Phys. Lett. B **499**, 233 (2001).
- [11] P. Fallon *et al.*: Phys. Rev. C **74**, 041302 (2010).
- [12] T. Otsuka *et al.*: Nucl. Phys. A **805**, 127c (2008).
- [13] Y. Utsuno *et al.*: Phys. Rev. C **86**, 051301 (2012).

In-beam γ -ray spectroscopy of ^{53}Ca and ^{54}Ca

D. Steppenbeck, S. Takeuchi^a, N. Aoi^b, P. Doornenbal^a, M. Matsushita H. Wang^a, H. Baba^a, N. Fukuda^a, S. Go J. Lee^a, K. Matsui^c, S. Michimasa T. Motobayashi^a, D. Nishimura^d, H. Sakurai^{a,c}, Y. Shiga^e, P.-A. Söderström^a, T. Sumikama^f, H. Suzuki^a, R. Taniuchi^c, J. J. Valiente-Dobón^g and K. Yoneda^a

Center for Nuclear Study, Graduate School of Science, University of Tokyo

^aRIKEN Nishina Center for Accelerator-Based Science

^bResearch Center for Nuclear Physics, Osaka University

^cDepartment of Physics, University of Tokyo

^dDepartment of Physics, Tokyo University of Science

^eDepartment of Physics, Rikkyo University

^fDepartment of Physics, Tohoku University

^gIstituto Nazionale di Fisica Nucleare, Laboratori Nazionali di Legnaro

Over the past few decades, the evolution of nuclear shell structure in exotic, neutron-rich nuclei has attracted much attention on both the experimental and theoretical fronts. Recent noteworthy examples include the onset of a new neutron magic number at $N = 16$ in exotic oxygen isotopes [1, 2] and the disappearance of the traditional $N = 28$ shell gap in ^{42}Si [3, 4].

In the neutron-rich fp shell, the onset of a new subshell closure at $N = 32$ was highlighted by structural characteristics along the Ca [5, 6], Ti [7, 8] and Cr [9, 10] isotopic chains, which are reproduced well by several shell-model effective interactions, such as the GXPF1A [11] and KB3G [12] Hamiltonians. In the framework of tensor-force-driven shell evolution [13], the onset of the $N = 32$ subshell closure is a direct consequence of a sizable $\nu p_{3/2}-\nu p_{1/2}$ gap, which presents itself as the $\nu f_{5/2}$ orbital shifts up in energy relative to the $\nu p_{3/2}-\nu p_{1/2}$ spin-orbit partners due to a weakening of the attractive proton-neutron $\pi f_{7/2}-\nu f_{5/2}$ interaction as protons are removed from the $\pi f_{7/2}$ orbital. An important manifestation in the case of the GXPF1A Hamiltonian is the prediction of a large subshell gap at $N = 34$ since the $\nu f_{5/2}$ orbital lies sufficiently high in energy above the $\nu p_{1/2}$ orbital in that interaction. On the other hand, the KB3G effective interaction indicates no shell closure at $N = 34$ for Ca. In fact, it has already been shown that no significant $N = 34$ subshell gap exists along the Ti [8, 14] or Cr [9, 10] isotopic chains, and, therefore, the size of the energy gap in

^{54}Ca is an important structural characteristic that requires experimental input. Moreover, the single-particle states of ^{53}Ca may also reflect the nature of the $N = 34$ closure.

In the present work, the structures of ^{53}Ca and ^{54}Ca were investigated using in-beam γ -ray spectroscopy at the RIKEN Radioactive Isotope Beam Factory to address this issue. A primary beam of ^{70}Zn at 345 MeV/u was delivered to the BigRIPS separator [15], where a radioactive beam containing ^{55}Sc and ^{56}Ti was delivered to a 10-mm-thick Be reaction target located at the 8th focal plane. The typical intensity of the primary beam was ~ 60 pA. The DALI2 γ -ray detector array [16], consisting of 186 NaI(Tl) detectors, was used to measure γ -ray transitions from nuclear excited states populated via nucleon knockout reactions. The reaction products were identified with the ZeroDegree spectrometer [15] using standard $B\rho$ -TOF- ΔE techniques (see, for example, Ref. [17]). A particle identification plot for the Ca isotopic chain measured in the present study is provided in Fig. 1.

Several new γ rays have been identified in the present work for ^{54}Ca and ^{53}Ca . Doppler-corrected γ -ray energy spectra measured in coincidence with these two isotopes are displayed in Figs 2(a) and (b), respectively. In the case of ^{54}Ca , all three transitions, with peak energies of 1184(24), 1656(20) and 2043(19) keV, are reported in the present study for the first time. The 2043(19)-keV peak is assigned as the transition from the first 2^+ state to the 0^+ ground state based on the γ -ray relative intensities and systematics of even-even nuclei. For ^{53}Ca , the 1753(15)-keV transition is reported here for the first time, while the line at 2227(19) keV is consistent in energy with a transition previously measured at 2221(1) keV in a β -decay study of ^{53}K [18].

The results of the present study provide the first direct experimental evidence for a significant $N = 34$ subshell closure in exotic Ca isotopes.

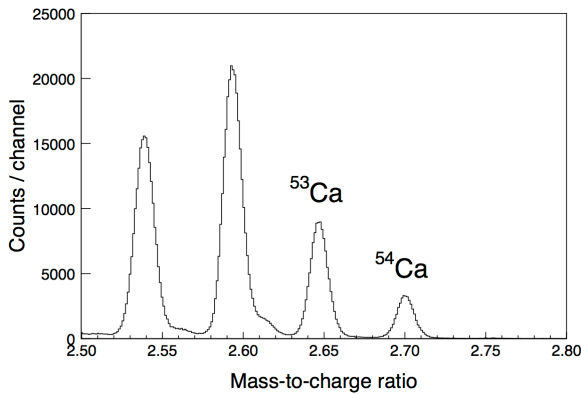


Figure 1. Particle identification (A/q) for the Ca isotopic chain measured with the ZeroDegree spectrometer [15].

References

- [1] R. Kanungo *et al.* Phys. Rev. Lett. **102** (2009) 152501.
- [2] C. R. Hoffman *et al.* Phys. Lett. B **672** (2009) 17.
- [3] B. Bastin *et al.* Phys. Rev. Lett. **99** (2007) 022503.
- [4] S. Takeuchi *et al.* Phys. Rev. Lett. **109** (2012) 182501.
- [5] A. Huck *et al.* Phys. Rev. C **31** (1985) 2226.

- [6] A. Gade *et al.* Phys. Rev. C **74** (2006) 021302(R).
 [7] R. V. F. Janssens *et al.* Phys. Lett. B **546** (2002) 55.
 [8] D.-C. Dinca *et al.* Phys. Rev. C **71** (2005) 041302(R).
 [9] J. I. Prisciandaro *et al.* Phys. Lett. B **510** (2001) 17.
 [10] A. Bürger *et al.* Phys. Lett. B **622** (2005) 29.
 [11] M. Honma, T. Otsuka, B. A. Brown and T. Mizusaki. Eur. Phys. J. A **25** (2005) s01, 499.
 [12] A. Poves *et al.* Nucl. Phys. A **694** (2001) 157.
 [13] T. Otsuka, T. Suzuki, R. Fujimoto, H. Grawe and Y. Akaishi. Phys. Rev. Lett. **95** (2005) 232502.
 [14] S. N. Liddick *et al.* Phys. Rev. Lett. **92** (2004) 072502.
 [15] T. Kubo *et al.* Prog. Theor. Exp. Phys. (2012) 03C003.
 [16] S. Takeuchi, T. Motobayashi, H. Murakami, K. Demichi and H. Hasegawa. RIKEN Accel. Prog. Rep. **36** (2003) 148.
 [17] T. Ohnishi *et al.* J. Phys. Soc. Jpn. **77** (2008) 083201.
 [18] F. Perrot *et al.* Phys. Rev. C **74** (2006) 014313.

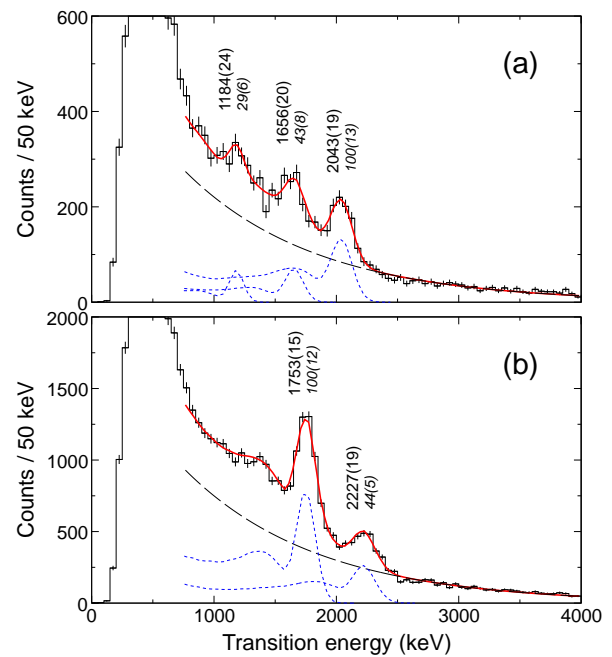


Figure 2. (Colour) Doppler-corrected γ -ray energy spectra for (a) ^{54}Ca and (b) ^{53}Ca deduced in the present work. The short dashed lines are GEANT4 simulations. Transition energies are given in keV and γ -ray relative intensities are indicated by italic font.

Observation of new isomers in neutron-rich Tb isotopes

R. Yokoyama, D. Kameda^A, T. Kubo^A, N. Inabe^A, N. Fukuda^A, S. Go, T. Fujii, E. Ideguchi², H. Takeda^A, H. Suzuki^A, K. Yoshida^A, K. Kusaka^A, K. Tanaka^A, Y. Yanagisawa^A, M. Ohtake^A, H. Sato^A, Y. Shimizu^A, H. Baba^A, M. Kurokawa^A, D. Nishimura^{A1}, T. Ohnishi^A, N. Iwasa^B, A. Chiba^B, T. Yamada^B, H. Nishibata^C, K. Ieki^D, D. Murai^D, S. Momota^E, Y. Sato^F, J. Hwang^F, S. Kim^F, O. B. Tarasov^G, D. J. Morrissey^G, B. M. Sherrill^G, and G. Simpson^H

Center for Nuclear Study, Graduate School of Science, University of Tokyo

^A*RIKEN, Nishina Center*

^B*Department of Physics Tohoku University*

^C*Department of Physics, Osaka University*

^D*Department of Physics, Rikkyo University*

^E*School of Environmental Science and Engineering, Kochi University of Technology*

^F*Department of Physics and Astronomy, Seoul National University*

^G*National Superconducting Cyclotron Laboratory Michigan State University*

^H*LPSC-IN2P3*

In rare earth nuclei with $Z = 60 - 66$, it is known that there is a sudden onset of large quadrupole prolate deformation at $N = 88 - 90$. This can be assumed from the systematics of the excitation energy of the first 2^+ state ($E(2^+)$) and the ratio of the energies of the 4^+ and 2^+ states ($E(4^+)/E(2^+)$) of even-even nuclei. $E(2^+)$ of $Z = 56-66$ nuclei shows clear decrease at $N = 88-90$ while $E(4^+)/E(2^+)$ gets closer to the value 3.33 as the neutron number increases [1]. Theoretically, the deformation is expected to proceed to $N = 104$ mid-shell. However, little has been known about the excited states of such neutron-rich nuclides in $Z \sim 60$ region. Recently, it has been reported that the first 2^+ energies of $Z = 70$ and 72 even-even nuclei have their minimum point at $N = 104$ mid-shell. However, isotopes with smaller proton number seem to have at least local minimum at $N = 98$. This may indicate an unusual change in structure at $N = 98$. Data of this region are not sufficient to have detailed discussion. It is, thus, interesting to examine how the nuclear shapes and shell structure change in the further neutron-rich side.

There had been experimental difficulties in the production and identification of such neutron-rich nuclei. In-flight fission of the ^{238}U beam at the RI Beam Factory (RIBF) in RIKEN enables us to produce the beams of highly neutron-rich isotopes with a wide range of atomic numbers. This novel means provides us with rare opportunity to study the neutron-rich rare-earth nuclei far from stability, which have been unexplored so far.

The neutron-rich $Z \sim 60$ nuclei were produced by in-flight fission of 345 MeV/nucleon ^{238}U beam at the RI Beam Factory in RIKEN Nishina Center. The fission fragments were separated and identified in the BigRIPS in-flight separator [3]. Delayed γ rays were measured in two different separator settings. One centers $Z = 64$ nuclei and the other does $Z = 59$ nuclei. The primary ^{238}U beam was bombarded to the production target (made of Be with 4.93 mm thick for higher Z setting, and 3.96 mm thick for lower Z setting) placed at the F0 focal plane. The energy and the intensity of the primary beam were 345 MeV/nucleon and 0.31 p nA respectively. The produced RI beams were identi-

fied event-by-event by their proton numbers (Z) and mass-to-charge ratio (A/Q). These quantities were obtained by the measurement of the magnetic rigidity ($B\rho$), time of flight (TOF), and energy loss (ΔE). The TOF was obtained by the time difference between plastic scintillation counters at F3 and F7. Detailed explanation of the particle identification at the BigRIPS is shown in [4]. In addition, a total kinetic energy (TKE) detector was installed at the F12 focal plane, at the end of the BigRIPS beamline. This is to identify ions with different atomic charge states, which becomes important for $Z > 60$ elements. The TKE detector consists of 14 layers of Si detectors and is designed to stop all ions of interest. The ΔE is also obtained from this detector. A set of PPACs was also installed just before the TKE detector, as a tracker of the ions implanted to the TKE detector. The γ rays from the ions stopped at F12 were detected by four clover-type HPGe detectors placed around the TKE detector. A clover-type Ge detector consists of four crystals which are to improve the signal-to-noise ratio by adding back Compton-scattered events in the neighboring crystals.

To search for new isomers, energies, half lives and relative intensities of the γ rays from each isotope were examined by gating on the RI in the PID. In order to reduce the background from beam irradiation, the γ events from 500 to 200 ns or closer to the timing of the beam implantation were excluded. Half-lives are obtained by likelihood fitting of a timing spectrum of each γ ray with a function with an exponential function with a constant background. Relative intensities of the γ rays were obtained for the isotopes which had two or more γ rays observed. In order to obtain the relative intensities, relative detection efficiencies of γ rays were estimated by Monte Carlo simulation using Geant4. The relative intensities of 56 γ rays of 21 known isotopes obtained in this study are consistent with their known level schemes.

We have systematically observed new isomers in neutron-rich Tb isotopes, ^{165}Tb , ^{166}Tb , ^{167}Tb and ^{168}Tb . Total number of the beam fragments were 1.3×10^5 , 1.5×10^5 , 1.2×10^5 and 6.0×10^4 respectively in 58 hours. Energy spectra and decay curves are shown in Fig.1. We have constructed the level schemes of these two nuclei from the

¹present address: Department of Physics, Tokyo University of Science

²present address: RCNP, Osaka University

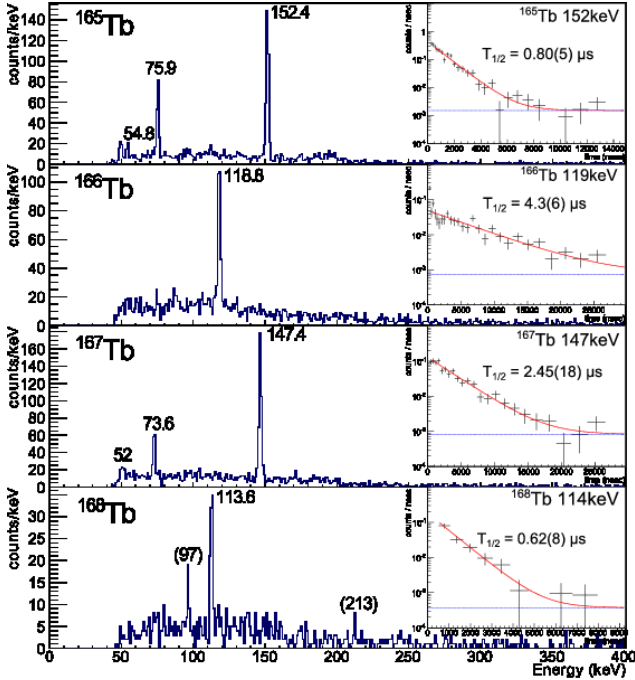


Figure 1. γ -ray energy spectra and decay curves for 165 – 168 Tb isomers. γ -ray energies are shown in the spectra. Energies of the weak peaks are labeled in parenthesis. K_{β} X-ray emitted after the internal conversions are observed in 165 Tb and 167 Tb. The red curves drawn in the decay curves show the fitting functions, and the blue lines show the constant component of the functions. The time window is gated up to 7 μ s for 165 Tb, 20 μ s for 166 Tb, 15 μ s for 167 Tb and 5 μ s for 168 Tb.

observed spectra and systematics of the lighter Tb isotopes. The level schemes are shown in Fig.2. The γ rays around ~ 50 and ~ 75 keV are tentatively assigned to be cascading γ rays of the first and second excited state of the ground-state rotational band by comparing with those of the less neutron-rich odd-mass Tb isotopes. [6, 7] Spin and parity (J^{π}) of the ground states of 165 Tb and 167 Tb have been estimated to be $3/2^{+}$ from the systematics of the ground-state bands in the lighter Tb isotopes. [8] J^{π} of the first and second excited states are assigned based on this argument on the ground state. The strong peaks at 152.4 and 147.4keV in 165 Tb and 167 Tb respectively are assigned as an isomeric transition as shown in Fig.2. The 75.9keV and 73.6keV γ rays could be assigned as a doublet from the energy sum and intensity balance. Similar isomeric states were not previously reported in the lighter Tb isotopes. However, it is known that the excitation energy of the $7/2^{-}$ intrinsic state which is characterized by the $7/2[523]$ orbit gradually goes down as neutron number increases from 92 to 98. [6, 7] Based on this systematics, we interpret that the isomer of 165 Tb and 167 Tb is generated by the $7/2[523]$ orbit which is expected to appear in such a low lying level of 165 Tb and 167 Tb.

From the γ -ray energies of the $7/2^{+} \rightarrow 5/2^{+}$ and $5/2^{+} \rightarrow 3/2^{+}$ decays of 165 Tb and 167 Tb, moment of inertia ($J^{(1)}$) values are obtained. In Fig.3, systematics of $J^{(1)}/A^{5/3}$ values of Tb isotopes are plotted. This graph shows that the deformation of the ground state becomes larger as the number of neutron increases. There is a local maximum at $N = 98$ just as neighbouring even- Z isotopes, Gd and Dy [5]. Further examination is in progress.

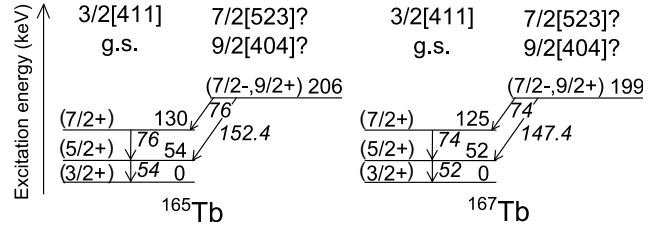


Figure 2. Level schemes for 165 Tb and 167 Tb that are obtained for the first time in this study.

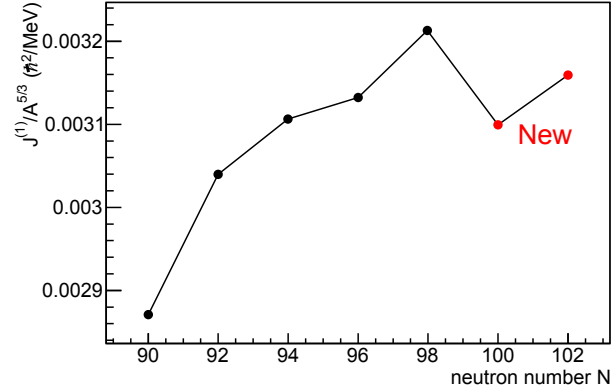


Figure 3. Systematics of the moment of inertia ($J^{(1)}$) values divided by $5/3$ power of each mass number A . The $J^{(1)}$ values are obtained from the γ -ray energy of the first excited state of the ground-state band [6, 7]. Points at $N = 100$ and 102 colored in red are newly obtained in this study.

References

- [1] R. F. Casten *et al.*: Phys. Rev. Lett. 47, 1433 (1981)
- [2] P. Moller and J. R. Nix, Atomic Dat. and Nucl. Dat. Tables 59, 185 (1995)
- [3] T. Kubo, Nucl. Instr. Meth. B 204, 97 (2003)
- [4] T. Ohnishi *et al.*: J. Phys. Soc. Japan 79, 073201 (2010)
- [5] E.F. Jones *et al.*: Eur. Phys. J. A 25, 467 (2005)
- [6] P. Garrett *et al.*: Nucl. Phys. A550, 1 (1992)
- [7] G. Winter *et al.*: Nucl. Phys. A176, 609 (1971)
- [8] R. C. Greenwood *et al.*: Phys. Rev. C 27, 1266 (1983)

Spectroscopy of single-particle states in oxygen isotopes via the (\vec{p}, pN) reaction with polarized protons

S. Kawase, T. Uesaka,^a S. Shimoura, K. Yako, S. Ota, S. Michimasa, H. Tokieda, H. Miya,^a T. L. Tang, K. Kisamori,^a M. Takaki, Y. Kubota,^a C. S. Lee,^a R. Yokoyama, T. Fujii, M. Kobayashi, M. Sasano,^a J. Zenihiro,^a H. Matsubara,^a M. Dozono,^a J. Lee,^a H. Sakai,^a T. Kubo,^a K. Yoshida,^a N. Inabe,^a Y. Yanagisawa,^a H. Takeda,^a K. Kusaka,^a N. Fukuda,^a D. Kameda,^a H. Suzuki,^a T. Kawahara,^b T. Wakui,^c S. Sakaguchi,^d T. Noro,^d T. Wakasa,^d J. Yasuda,^d T. Fukunaga,^d Y. Maeda,^e W. Y. Kim,^f S. H. Hwang,^f S. Stepanyan,^f A. Obertelli,^g A. Galindo-Uribarri,^h E. Padilla-Rodal,ⁱ and D. Beaume^j

Center for Nuclear Study, Graduate School of Science, University of Tokyo

^aRIKEN (The Institute of Physical and Chemical Research)

^bDepartment of Physics, Toho University

^cCyclotron and Radioisotope Center, Tohoku University

^dDepartment of Physics, Kyushu University

^eDepartment of Physics, University of Miyazaki

^fDepartment of Physics and Energy Sciences, Kyungpook National University, Korea
^gCEA Saclay, France

^hOak Ridge National Laboratory, USA

ⁱInstituto de Ciencias Nucleares, Universidad Nacional Autónoma de México, México

^jInstitut de Physique Nucléaire d'Orsay, France

The spin-orbit coupling has an important part in building the nuclear structure. It is so strong in nuclei, unlike atomic system, that it can shuffle the level sequences with different principal quantum numbers, or in different major shells. Our goal is to elucidate how the spin-orbit splitting, which is a direct measure of the strength of the spin-orbit coupling and is defined as a single-particle energy difference of spin-doublet, changes as a function of nucleon number in Oxygen isotopes. To this end, the (\vec{p}, pN) reaction is an effective spectroscopic tool because of its property of selectively populating single-hole states. One can determine the spin-parity of single-hole states in nuclei from the momentum dependence of the cross section and the vector analyzing power without model dependence [1].

Beam energy was chosen to be around 260 MeV/u by using a momentum slit at the F1 focal plane. Particle identification was carried out by using time of flight (TOF) information between the F3-FH9 focal planes and light output information of the plastic scintillator at FH9. The beam momentum was obtained from the x-position at the F6 focal plane by using a position sensitive parallel-plate avalanche counter (PPAC) [2]. The beam bombarded a polarized proton target [3, 4] with a thickness of ~ 100 mg/cm² placed at the S0 focal plane of the SHARAQ beam line. The target chamber was installed between the magnet coils and cooled down by liquid nitrogen to keep the polarization of the target (see Fig. 2). A schematic overview of the setup is shown in Fig. 1. Two low-pressure multiwire drift chambers (LP-MWDCs) [5, 6] were used to track beam particles to determine the reaction point on the target. Two sets of detectors were symmetrically placed on both sides of the beam-line to detect the two nucleons scattered through the (p, pN) reaction. For scattered protons, two multiwire drift chambers (MWDCs) [7] and two plastic scintillators were used to measure the scattering angle and the TOF, respectively. For neutrons, a pair of neutron hodoscopes consisting of 20 plastic scintillators each were used. The residual nuclei were analyzed by the quadrupole and dipole magnets, and detected by the plastic scintillator and the two MWDCs located downstream of the target.

In addition, a carbon target (~ 130 mg/cm²) was placed 15 cm downstream of the polarized target to simultaneously evaluate the background due to the carbon contained in the polarized target. The events in the carbon target were identified by the hit pattern of four plastic scintillators located right beside the carbon target. For the measurement of polarization of the target, the data for proton beam were also taken.

The proton separation energy is obtained from the scat-

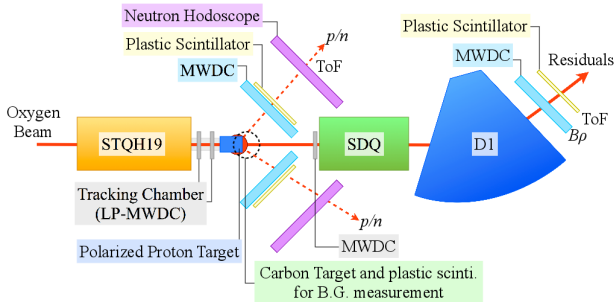


Figure 1. Schematic overview of the setup of the SHARAQ04 experiment.

We performed the SHARAQ04 experiment at RIKEN RIBF to measure single-particle spectra and to determine spin-orbit splitting between $1p$ spin-doublet in $^{14,22-24}\text{O}$. The beam including oxygen isotopes was produced via the projectile fragmentation of a primary ^{48}Ca beam that was accelerated up to 345 MeV/u by the SRC, and then achromatically transported into the high-resolution beam-



Figure 2. Polarized target chamber installed at the S0 focal plane.

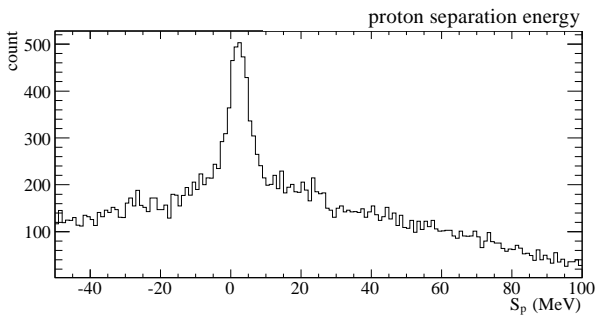


Figure 3. Separation energy spectrum for pp elastic scattering.

tering angles and the momenta of scattered protons:

$$S_p = -m_p(\gamma - 1) - \gamma(T_1 + T_2) + \beta\gamma(P_{1\parallel} + P_{2\parallel}) - \frac{|\vec{q}|^2}{2m_R},$$

where m_p is the proton mass, m_R is the mass of residual nucleus, γ is the Lorentz factor of the beam particle, T_1 and T_2 are the kinetic energies of scattered protons in laboratory system, $P_{1\parallel}$ and $P_{2\parallel}$ are the components of the momenta of the scattered protons parallel to the beam, and \vec{q} is the momentum transfer. The momenta of scattered particles were determined from TOF measurements. Figure 3 shows the separation energy spectrum for the proton beam. The peak at 0 MeV corresponds to pp elastic scattering. The background is due to accidental coincidences and also from the proton knockout reaction in surrounding materials and in carbon nuclei contained in the polarized target. Gates on reaction points are not set in the analysis of the runs with the proton beam because of the lack of information on beam tracks. This lack of information is due to the low efficiency of LP-MWDC for protons.

The analysis for oxygen isotopes is in progress.

References

- [1] G. Jacob, Th. A. J. Maris *et al.*: Nucl. Phys. A, **257**, 517 (1976).
- [2] H. Kumagai *et al.*: Nucl. Instrum. Methods Phys. Res. **A470**, 562 (2001).
- [3] T. Wakui *et al.*: Nucl. Instrum. Methods Phys. Res. **A550**, 521 (2005).

- [4] S. Kawase *et al.*: CNS Ann. Rep. 2011 (2012) 26.
- [5] A. Saito *et al.*: CNS Ann. Rep. 2006 (2007) 67.
- [6] H. Miya *et al.*: CNS Ann. Rep. 2011 (2012) 65.
- [7] H. Okamura *et al.*: Nucl. Instrum. Methods Phys. Res. **A406**, 78 (1998).

Measurement of the ${}^8\text{He}(p,n){}^8\text{Li}$ reaction at intermediate energy in inverse kinematics

M. Kobayashi, K. Yako, S. Shimoura, M. Dozono^a, S. Kawase, K. Kisamori, Y. Kubota, C.S. Lee, S. Michimasa, H. Miya, S. Ota, H. Sakai^a, M. Sasano^a and M. Takaki

Center for Nuclear Study, Graduate School of Science, University of Tokyo
^aRIKEN Nishina Center

1. Introduction

Charge-exchange (p,n) measurements at intermediate energies ($E > 100$ MeV) are recognized as a powerful tool to study the spin-isospin responses of nuclei [1]. In particular, Gamow-Teller (GT) transitions, which are characterized by an angular momentum transfer of $\Delta L = 0$, a spin transfer of $\Delta S = 1$ and an isospin transfer of $\Delta T = 1$ between the initial and final nuclei, have been the subject of intense studies. A facility for (p,n) measurements in inverse kinematics was constructed at SHARAQ to extend the scope of spin-isospin studies to unstable nuclei [2].

In this study, we focus on a neutron-rich nucleus ${}^8\text{He}$, which has the largest neutron to proton ratio ($N/Z = 3$) among all bound nuclei. It is expected to have a five-body $\alpha + 4n$ structure [3] and various configurations of these valence neutrons are proposed [4, 5].

A fundamental study on the structure of ${}^8\text{He}$ is its β -decay, where the Q -value is 10.7 MeV. Figure 1 shows the energy diagram related to GT transitions from ${}^8\text{He}$ to ${}^8\text{Li}$. Herein, it is noted that there are limitations in β -decay studies. We can only access the states within the Q -window. In addition, the observed intensities of the transition to higher-lying levels are strongly suppressed because the phase space factor of a β -decay decreases as excitation energy increases. In contrast to β -decay, charge-exchange reactions, such as (p,n) reactions, do not suffer from the Q -value limitation and can be used to study transitions to highly excited states, covering the whole GT resonance. GT strength $B(\text{GT})$ is extracted by using the proportionality relationship between GT strength and differential cross section at momentum transfer $q = 0$. So far, no measurements of charge exchange reactions for ${}^8\text{He}$ have been carried out.

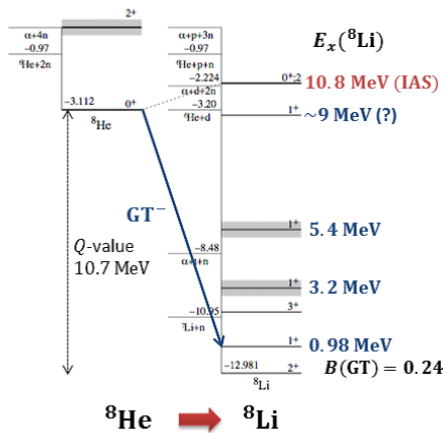


Figure 1. Energy levels in ${}^8\text{Li}$ related to the GT transitions from ${}^8\text{He}$. The isobaric analog state of the ${}^8\text{He}$ ground state is also shown ($E_x = 10.8$ MeV).

2. Experimental Method

In April 2012, we performed a measurement for the ${}^8\text{He}(p,n){}^8\text{Li}$ reaction as the second (p,n) measurement in inverse kinematics at RIBF. It was carried out as a parasite experiment on the missing mass spectroscopy of the tetra-neutron system via the ${}^4\text{He}({}^8\text{He}, {}^8\text{Be})4n$ reaction.

The setup in this experiment is shown in Fig. 2. A primary ${}^{18}\text{O}$ beam of 230A MeV was used to bombard a Be target of 20 mm thickness, yielding a secondary ${}^8\text{He}$ beam of 190A MeV by projectile fragmentation. A typical intensity of the ${}^8\text{He}$ beam was 2 Mcps. Secondary targets of polyethylene ($(\text{CH}_2)_n$) and carbon (C), with thicknesses of 0.39 and 0.46 g/cm², respectively, were employed. Runs with the C target were for evaluating the carbon contribution in the $(\text{CH}_2)_n$ target.

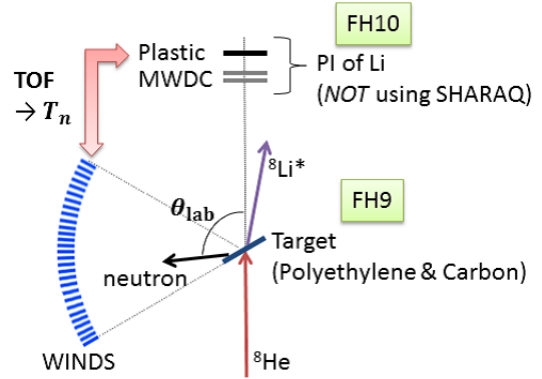


Figure 2. Experimental setup of the inverse kinematics ${}^8\text{He}(p,n)$ measurement. θ_{lab} was determined by the location of the scintillator bar in which the scattered neutron was detected. TOF was measured between the downstream plastic scintillator and the WINDS.

In this experiment, missing mass spectroscopy was employed. The excitation energy (E_x) of ${}^8\text{Li}$ and the scattering angle in the center-of-mass system (θ_{cm}) were constructed from the kinetic energy (T_n) and the scattering angle in the laboratory system (θ_{lab}) of a neutron produced by the (p,n) reaction. T_n was determined by measuring the neutron time-of-flight (TOF), for which the time references were taken from the plastic scintillator placed 10 m downstream from the secondary target and the neutron detector array (WINDS) [2], surrounding the target at a distance of 180 cm. θ_{lab} was determined by the location of the scintillator bar in which the scattered neutron was detected. In this measurement, the scattering angle region $73.5^\circ \leq \theta_{\text{lab}} \leq 108^\circ$ is covered by using a part of the scintillator bars of WINDS.

3. Results

We focus on the decay channels to Li isotopes from excited states in ${}^8\text{Li}$. The Li isotopes were tagged by using the energy-loss information of downstream detectors (a plastic scintillator and MWDCs) as shown in Fig. 2.

Figure 3 shows a preliminary spectrum of the neutrons from the ${}^8\text{He}(p,n){}^8\text{Li}$ reaction with tagging of the Li isotopes. Two loci are clearly observed in this figure. The locus at low excitation energy is most likely to be the 1^+ state at 0.98 MeV. This state has been observed in previous β -decay studies and its GT transition strength is $B(\text{GT}) = 0.24$ [6]. A region with a large transition strength is observed at around $E_x \sim 8$ MeV. So far, no excited states which decay to Li isotopes at around $E_x \sim 8$ MeV have been observed. The observed state is a candidate of the Gamow-Teller state. In order to clarify the nature of this state, the angular distribution of the differential cross sections will be analyzed. In addition, GT strength distribution for the transition to ${}^8\text{Li}$ will be extracted. Further analysis is currently in progress.

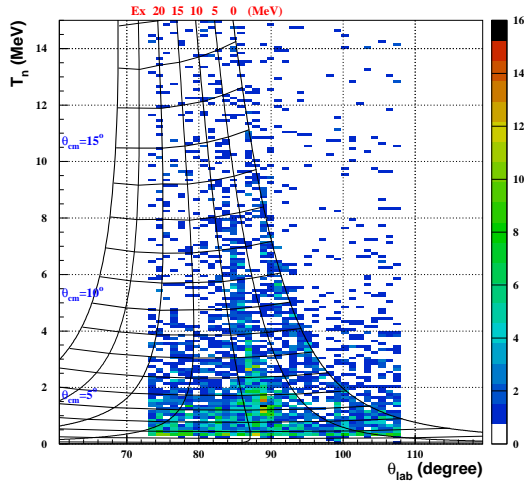


Figure 3. The preliminary neutron spectrum of the ${}^8\text{He}(p,n){}^8\text{Li}$ reactions as the function of the kinetic energy (T_n) and the scattering angle in the laboratory system (θ_{lab}). The vertical and horizontal curves indicate the correlation between T_n and θ_{lab} for the different values of excitation energies (E_x) of ${}^8\text{Li}$ and scattering angles in the center-of-mass system (θ_{cm}), respectively.

References

- [1] T.N. Taddeucci *et al.*, Nucl. Phys. A **469**, 125 (1987).
- [2] K. Yako *et al.*, CNS-REP-**90**, 67 (2013).
- [3] I. Tanihata *et al.*, Phys. Lett. B **289**, 261 (1992).
- [4] M.V. Zhukov, A.A. Korshennikov, and M.H. Smedberg, Phys. Rev. C **50**, R1 (1994).
- [5] K. Hagino, N. Takahashi, and H. Sagawa, Phys. Rev. C **77**, 054317 (2008).
- [6] F.C. Barker, E.K. Warburton, Nucl. Phys. A **487** (1988) 269.

Missing-mass spectroscopy of the $4n$ system by exothermic double-charge exchange reaction ${}^4\text{He}({}^8\text{He}, {}^8\text{Be})4n$

K. Kisamori, S. Shimoura, H. Miya, M. Assie^a, H. Baba^b, T. Baba^c, D. Beaumel^a, M. Dozono^b, T. Fujii, N. Fukuda^b, S. Go, F. Hammache^a, E. Ideguchi^d, N. Inabe^b, M. Ito^e, D. Kameda^b, S. Kawase, T. Kawabata^c, M. Kobayashi, Y. Kondo^f, T. Kubo^b, Y. Kubota, M. Kurata-Nishimura^b, C. S. Lee, Y. Maeda^g, H. Matsubara, S. Michimasa, K. Miki^d, T. Nishi^h, S. Nojiⁱ, S. Ota, S. Sakaguchi^j, H. Sakai^b, Y. Sasamoto, M. Sasano^b, H. Sato^b, Y. Shimizu^b, A. Stolz^a, H. Suzuki^b, M. Takaki, H. Takeda^b, S. Takeuchi^b, A. Tamii^d, L. Tang, H. Tokieda, M. Tsumura^c, T. Uesaka^b, K. Yako, Y. Yanagisawa^b and R. Yokoyama

Center for Nuclear Study, Graduate School of Science, University of Tokyo
^aIPN, Orsay, France

^bRIKEN (The Institute of Physical and Chemical Research)

^cDepartment of Physics, Kyoto University

^dResearch Center Nuclear Physics, Osaka University

^eCyclotron and Radioisotope Center, Tohoku University

^fDepartment of Physics, Tokyo Institute of Technology

^gFaculty of Engineering, University of Miyazaki

^hDepartment of Physics, University of Tokyo

ⁱNational Superconducting Cyclotron Laboratory, Michigan State University, USA

^jFaculty of Sciences, Kyushu University

Multi-neutron systems in nuclei have attracted considerable attention on both the experimental and theoretical perspectives ever since candidates of bound tetra-neutron system were reported [1]. While later theoretical papers using ab-initio calculations [2] suggest that bound tetra-neutron cannot exist, the possibility of the tetra-neutron system forming a resonance state is still an open and fascinating question.

We performed missing-mass spectroscopy of the $4n$ system via the exothermic double-charge exchange reaction ${}^4\text{He}({}^8\text{He}, {}^8\text{Be})4n$. The experiment was carried out at the RI Beam Factory (RIBF) at RIKEN using the SHARAQ spectrometer and liquid He target system. In order to produce the $4n$ system with a small momentum transfer less than 20 MeV/c, the secondary beam of ${}^8\text{He}$ having a large internal energy was used at 190 A MeV. To obtain the missing-mass spectrum, we measured momentum of the ${}^8\text{He}$ beam with the High-Resolution Beamline and momentum of two alpha particles, which were the decay products of the ${}^8\text{Be}$ ejectile, with the SHARAQ spectrometer. If the spectrum has a resonance peak above the $4n$ threshold, it can be directly compared with theoretical predictions and information on the relevant interaction in the tetra-neutron system, such as the $T=3/2$ three-body force, can be obtained. Another interest is the possible correlations in sub-systems, such as di-neutron correlations in the four-body scattering state.

A schematic picture of the experimental setup is shown in Fig. 1. Figure 1 shows the experimental setup. A primary beam of ${}^{18}\text{O}$ of 230 A MeV bombarded a target of 20-mm-thick Be at BigRIPS-F0 to produce the ${}^8\text{He}$ secondary beam. The typical ${}^8\text{He}$ beam intensity was 2×10^6 Hz. The ${}^8\text{He}$ beam was transported in High-Resolution-Achromatic mode to a liquid He target with thickness of 120 mg/cm² at the SHARAQ-S0. The momentum of ${}^8\text{He}$ was measured by Multi Wire Drift Chambers (MWDCs) at BigRIPS-F6. The SHARAQ spectrometer was operated to have a momentum

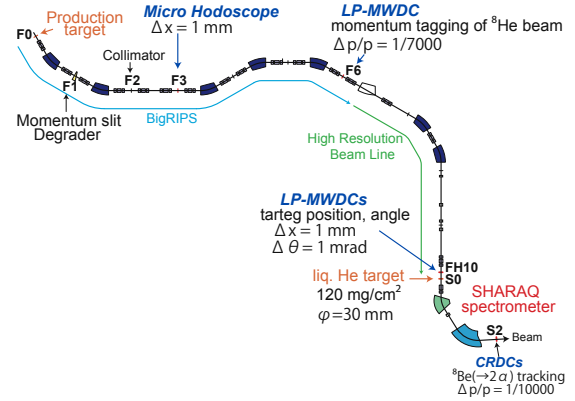


Figure 1. Setup of the experiment.

acceptance about $\pm 2.5\%$ (considering momentum distribution $\pm 0.74\%$ of the two-alpha, and $\pm 1\%$ of the beam), and effective solid angle 4.3 msr, and satisfy momentum resolution 1/10000, which gives about 1 MeV missing-mass resolution. A Cathode Readout Drift Chamber (CRDC), which has no dead space and large effective area, was used as the detector for two-particle tracking [3].

In the present analysis, a method for treating multi-hits in MWDCs under high beam rate condition was developed in order to achieve a large yield. At focal plane CRDC, ${}^8\text{Be}$ can be identified by measuring the invariant mass of the coincident two-alpha particle with a good signal-to-noise ratio. Figure 2 shows a track of two-alpha particle of a candidate of the $4n$ event at CRDC. We identify about a few hundreds of events as candidates of $4n$ events, but still have to eliminate the background.

References

- [1] F. Marques *et al.*, Phys. Rev. C **65**, 044006 (2002)
- [2] S. Pieper, Phys. Rev. Lett. **90**, 252501 (2003)
- [3] K. Kizamori *et al.*, CNS Ann. Rep. 2010 (2012)

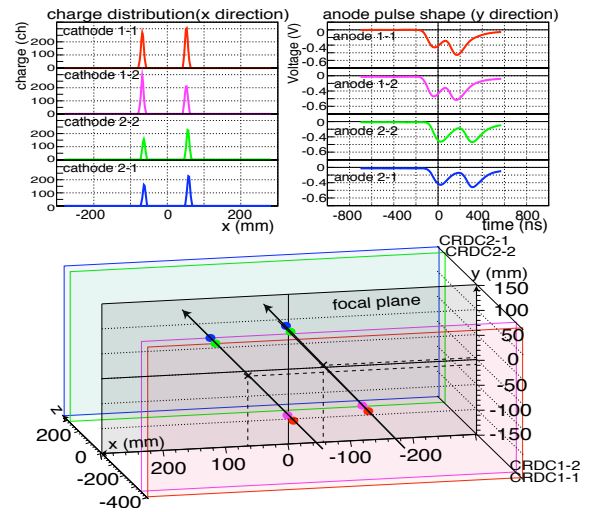


Figure 2. The sample of an event snapshot. The vertical and horizontal positions of charged particles are determined by the center of the distribution of induced charges on the cathode pads and by measuring the drift time of electrons in the drift plane, respectively

Study of spin-isospin responses via exothermic charge exchange reaction (^8He , $^8\text{Li}^*(1^+)$)

H. Miya, S. Shimoura, K. Kisamori, M. Assié^a, H. Baba^b, T. Baba^c, D. Beaumel^b, M. Dozono^b,
T. Fujii, N. Fukuda^b, S. Go, F. Hammache^b, E. Ideguchi^d, N. Inabe^b, M. Ito^e, D. Kameda^b,
S. Kawase, T. Kawabata^c, M. Kobayashi, Y. Kondo^f, T. Kubo^b, Y. Kubota, C. S. Lee, Y. Maeda^g,
H. Matsubara^b, S. Michimasa, K. Miki^d, T. Nishi^h, M. Kurata-Nishimura^b, S. Ota, H. Sakai^b,
S. Sakaguchiⁱ, M. Sasano^b, H. Sato^b, Y. Shimizu^b, H. Suzuki^b, A. Stolz^j, M. Takaki, H. Takeda^b,
S. Takeuchi^b, A. Tamii^d, H. Tokieda, M. Tsumura^c, T. Uesaka^b, K. Yako, Y. Yanagisawa^b,
and R. Yokoyama

Center for Nuclear Study, Graduate School of Science, the University of Tokyo

^a*Institut de Physique Nucléaire, Orsay, France*

^b*RIKEN (The Institute of Physical and Chemical Research)*

^c*Department of Physics, Kyoto University*

^d*Research Center for Nuclear Physics, Osaka University*

^e*Cyclotron and Radioisotope Center, Tohoku University*

^f*Department of Physics, Tokyo Institute of Technology*

^g*Department of Applied Physics, University of Miyazaki*

^h*Department of Physics, the University of Tokyo*

ⁱ*Department of Physics, Kyushu University*

^j*National Superconducting Cyclotron Laboratory, Michigan State University, USA*

We performed an experiment study of the exothermic charge-exchange (CE) reaction (^8He , $^8\text{Li}^*(1^+)$) at the RIKEN RIBF facility by using the BigRIPS, the High-Resolution beamline, and the SHARAQ spectrometer. [1] Missing mass spectra for ^4He , $^{12}\text{C}(^8\text{He}, ^8\text{Li}^*(1^+))$ at the beam energy of 190 MeV/nucleon were measured. In this experiment, the spin-isospin response of a spin-dipole transition occurring as the result of a CE reaction induced with radioactive isotope beams was studied. In order to identify $^8\text{Li}^*(1^+)$, we used the 980-keV γ -ray corresponding to the $1^+ \rightarrow 2^+$ transition in ^8Li . The coincident detection of ^8Li and the 980-keV γ -ray can be considered clear evidence of the occurrence of the CE reaction. In this article, we report on the relevant experimental procedures and preliminary analysis.

Figure 1 shows the schematic view of the BigRIPS, the High-Resolution Beamline, and the SHARAQ spectrometer. A ^8He beam at 190 MeV/nucleon was produced via the projectile fragmentation reaction of the ^{18}O beam at 230 MeV/nucleon with a Be target at F0. The intensity of ^8He was approximately 2×10^6 cps at S0, where the secondary targets of solid ^{12}C and ^4He were installed. The target thicknesses of ^{12}C and liquid ^4He were 45 mg/cm^2 and 120 mg/cm^2 , respectively. The liquid ^4He target was made using the CRYPTA system. [2] The beam trajectory was measured by μ hodoscope [3] and low-pressure multi-wire drift chambers [4] (LP-MWDCs) in the BigRIPS and the High-Resolution Beamline. The μ hodoscope was installed at F3 to measure beam position whose spot size is as small as 1 cm (FWHM). The LP-MWDCs were placed at F6, FH9, and S0. The momentum of ^8He was measured at F6, which is the momentum dispersive focal plane. At S0, the beam position and incident angle into the targets were determined. The scattered ^8Li was momentum analyzed with the SHARAQ spectrometer and detected by cathode readout drift chambers [5] at S2. The 980-keV γ -rays emit-

ted from ^8Li were detected by the NaI(Tl) detector array (DALI2 [6]) located near the secondary target.

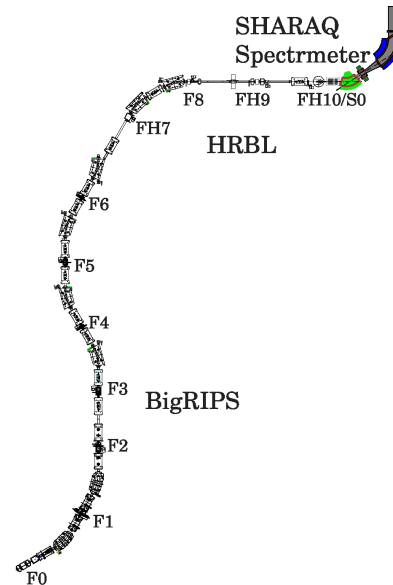


Figure 1. Schematic view of BigRIPS, High-Resolution Beamline, and SHARAQ Spectrometer.

Figure 2 shows the momentum correlation between ^8He and ^8Li in the $^{12}\text{C}(^8\text{He}, ^8\text{Li})^{12}\text{B}$ reaction. The horizontal and vertical axes represent the horizontal positions of ^8He at F6 and of ^8Li at S2, respectively. Since the slope of the dashed line corresponds to the correlation of the dispersions at F6 (7.2 m) and S2 (5.8 m), the momentum spread at the S2 is canceled by tagging the momentum at F6. Therefore, the missing mass can be deduced.

In order to identify ${}^8\text{Li}^{1+}$, the emitted γ -rays were analyzed. Since the γ -rays energy are affected by the Doppler effects, the energy are corrected by using the incident angle to the NaI crystals and the velocity of the projectile. Figure 3 shows a Doppler-corrected spectrum measured by DALI2 for the ${}^{12}\text{C}$ target. The 980-keV γ -ray of ${}^8\text{Li}^{1+}$ was clearly observed.

Further analysis is now in progress.

References

- [1] T. Uesaka *et al.*: Prog. Theor. Exp. Phys. 2012 (2012) 03C007.
- [2] H. Ryuto *et al.*: Nucl. Instr. Meth. A 555, 1-5 (2005).
- [3] S. Ota *et al.*: CNS Ann Rep. 2011 (2013).
- [4] H. Miya *et al.*: CNS Ann Rep. 2011 (2013).
- [5] K. Kisamori *et al.*: CNS Ann Rep. 2011 (2013).
- [6] T. Takeuchi *et al.*: RIKEN Accel Prog. Rep. **36**, 148 (2003).

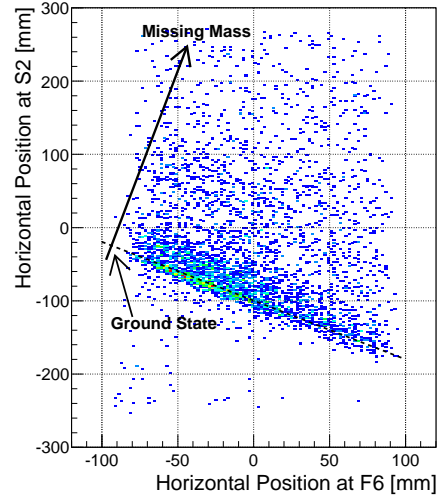


Figure 2. Momentum correlation between ${}^8\text{He}$ and ${}^8\text{Li}$ in ${}^{12}\text{C}({}^8\text{He}, {}^8\text{Li}){}^{12}\text{B}$.

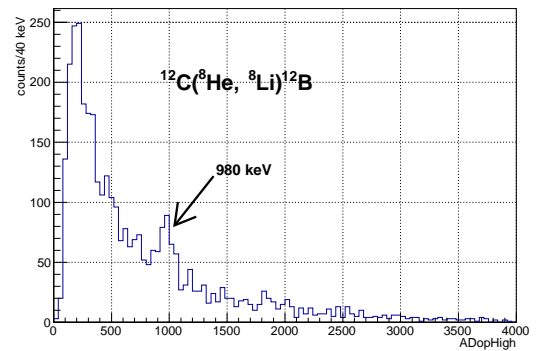


Figure 3. Doppler-corrected γ -ray spectrum of ${}^{12}\text{C}({}^8\text{He}, {}^8\text{Li}){}^{12}\text{B}$ obtained by DALI2.

Search for a double Gamow-Teller giant resonance with heavy-ion double charge exchange ($^{12}\text{C}, ^{12}\text{Be}(0_2^+)$) reaction

M. Takaki, H. Matsubara^a, T. Uesaka^a, S. Shimoura, N. Aoi^b, M. Dozono^a, T. Hashimoto^b, T. Kawabata^c, S. Kawase, K. Kisamori, M. Kobayashi, C.S. Lee, Y. Maeda^d, S. Michimasa, K. Miki^b, H. Miya, S. Ota, S. Sakaguchi^e, M. Sasano^a, T. Suzuki^b, K. Takahisa^b, T.L. Tang, A. Tamii^b, H. Tokieda, K. Yako and J. Zenihiro^b

Center for Nuclear Study, Graduate School of Science, University of Tokyo

^a*RIKEN (The Institute of Physical and Chemical Research)*

^b*Research Center for Nuclear Physics, Osaka University*

^c*Department of Physics, Kyoto University*

^d*Department of Applied Physics, Miyazaki University*

^e*Department of Physics, Kyushu University*

One of the most interesting features in atomic nuclei is the variety of spin and isospin responses. For example, the Gamow-Teller (GT) transition, which is characterized by $\Delta L = 0$, $\Delta S = 1$, and $\Delta T = 1$ and induced by the transition operator $\sigma\tau$, is the simplest spin-isospin response within one-phonon excitations, and has been well studied [1]. In contrast, the data on multi-phonon excitations have been scarce. The double GT giant resonance (DGTGR) is the most basic mode among two-phonon excitation modes, which consists of two successive GT excitations and induced by the operator $\sigma\tau\sigma\tau$ [2, 3, 4]. Discovery of the DGTGR is an essential step in extending research of the spin-isospin responses to multi-phonon world.

Another obvious interest of DGTGR lies in its relevance to the neutrino physics; the DGT transition is induced by the same transition operator as the $\beta\beta$ -decay, i.e. $\sigma\tau\sigma\tau$. If $\beta\beta$ -decay experiments conducted world-wide such as the CANDLES project [5] observe the neutrino-less mode of this decay, the $0\nu\beta\beta$ decay, it would give a direct evidence that the neutrinos are Majorana particles. Here, a calculation of the nuclear matrix element $M^{0\nu}$ is needed to deduce a quantity of interest from the observed lifetime. Such calculation is tested by using the experimentally observed half-life of the other mode of this decay, the $2\nu\beta\beta$ decay, because the $0\nu\beta\beta$ and $2\nu\beta\beta$ decays have the same initial and final states. Despite of the importance of the understanding the $2\nu\beta\beta$ decay, this process is very much complicated by detail of nuclear structures and highly suppressed [6, 7]; most of the DGT strength is pushed up to highly excited states in the DGTGR.

In this report, we propose a new probe, a pn -type heavy-ion double charge exchange (HIDCX) reaction for $\beta^-\beta^-$ DGT processes studies. HIDCX reactions are unique spectroscopic tools which induce two-phonon excitations with transferring spin and isospin by two units.

In July 2011, We performed the $^{12}\text{C}(^{18}\text{O}, ^{18}\text{Ne})^{12}\text{Be}$ experiment at 80 MeV/nucleon at RCNP, Osaka University and found that the reaction has a large cross section of 800 nb/sr at 0° [8]. This unexpectedly large cross section indicates that the matrix elements for the transition from the $^{12}\text{C}(0_{g.s.}^+)$ to the $^{12}\text{Be}(0_2^+)$ state is large. Probably this is because all of the initial $^{12}\text{C}(0_{g.s.}^+)$, intermediate $^{12}\text{B}(1_{g.s.}^+)$ and final $^{12}\text{Be}(0_2^+)$ states are dominated by $0\hbar\omega$ configuration [9, 10, 11, 12, 13]. Such condition is hardly satisfied if another stable nucleus is used as a projectile. This leads us

to a new idea to use the ($^{12}\text{C}, ^{12}\text{Be}(0_2^+)$) reaction as a tool to investigate $\beta^-\beta^-$ DGT processes.

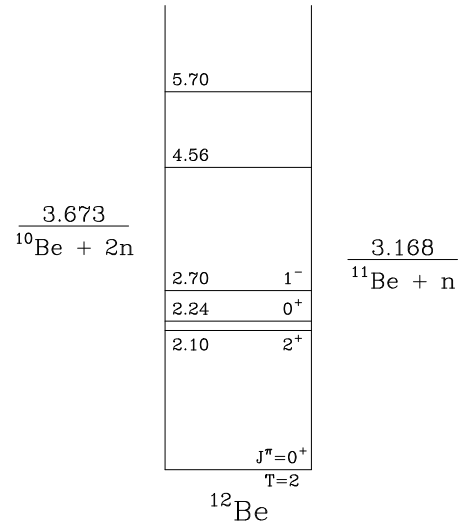


Figure 1. Level scheme of ^{12}Be up to 5.7 MeV.

Another advantage of this probe is that the $^{12}\text{Be}(0_2^+)$ state is identified with a delayed γ -ray coincidence method, as mentioned in the following. The delayed γ -ray coincidence method works to tag the transition in the projectile from the initial $^{12}\text{C}(0_{g.s.}^+)$ to the final $^{12}\text{Be}(0_2^+)$ state. The $^{12}\text{Be}(0_2^+)$ state will be identified by detecting the γ -ray with the energies of 140 keV, 511 keV and 2.11 MeV at the focal plane of the GR spectrometer. The outgoing ^{12}Be particles are momentum analyzed with the GR spectrometer. A fraction of 71% among the $^{12}\text{Be}(0_2^+)$ particles at the 0_2^+ state going into the spectrometer reach to the focal plane before the de-excitation with a half life of 331 ns [11]. The ^{12}Be nuclei going through the GR spectrometer are stopped by a thick plastic scintillator at the end of the spectrometer. Then, the emitted γ -rays are detected by using NaI γ -ray detectors. The NaI detectors surround the plastic stopper.

The Ring Cyclotron facility at RCNP in combination with the Grand Raiden (GR) spectrometer provide the opportunity for the HIDCX ($^{12}\text{C}, ^{12}\text{Be}(0_2^+)$) reaction studies. Prior to the DGTGR experiment, we plan to perform a pilot experiment to optimize focal plane detectors (vertical drift chambers and plastic scintillators), delayed γ -ray detectors

and data acquisition (DAQ) system for the ($^{12}\text{C}, ^{12}\text{Be}(0_2^+)$) measurement at RCNP. Background level of γ -rays around focal plane should be known. For this pilot experiment, we will employ the cross section measurement for the $^{18}\text{O}(^{12}\text{C}, ^{12}\text{Be}(0_2^+))^{18}\text{Ne}$ reaction at 100 MeV/nucleon by using the H_2^{18}O ice target [14]. This reaction is same as our previous $^{12}\text{C}(^{18}\text{O}, ^{18}\text{Ne})^{12}\text{Be}$ reaction measurement, while the projectile and the target are swapped. After establishment of this method, we will apply the method to the $\beta\beta$ -decay nuclei such as ^{48}Ca .

[14]T. Kawabata *et al.*, Nucl. Instrum. Methods A **459**, 171 (2001).

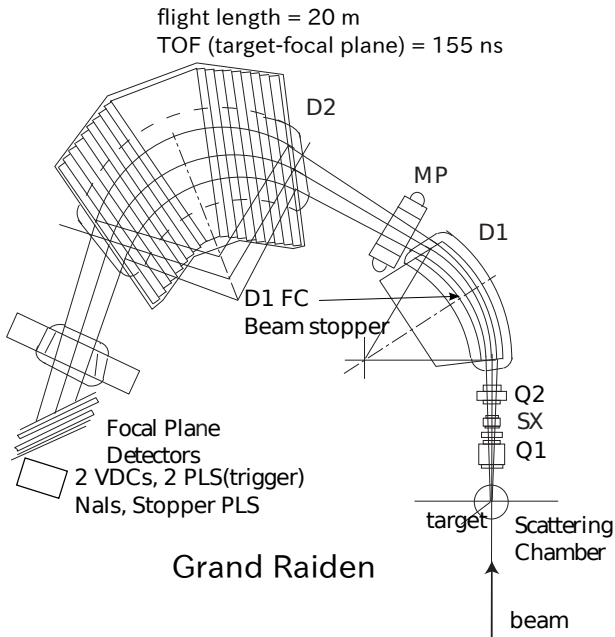


Figure 2. Schematic drawing of the setup for the ($^{12}\text{C}, ^{12}\text{Be}(0_2^+)$) experiment.

References

- [1] M. Ichimura, H. Sakai, and T. Wakasa, Progress in Particle and Nuclear Physics **56**, 446 (2006).
- [2] D. C. Zheng, L. Zamick, and N. Auerbach, Phys. Rev. C **40**, 936 (1989).
- [3] N. Auerbach, L. Zamick, and D. Zheng, Annals of Physics **192**, 77 (1989).
- [4] D. C. Zheng, L. Zamick, and N. Auerbach, Annals of Physics **197**, 343 (1990).
- [5] T. Kishimoto, International Journal of Modern Physics E **18**, 2129 (2009).
- [6] K. Yako *et al.*, Phys. Rev. Lett. **103**, 012503 (2009).
- [7] M. Horoi, S. Stoica, and B. A. Brown, Phys. Rev. C **35**, 034303 (2007).
- [8] M. Takaki *et al.*, CNS annual report (2011).
- [9] F.C. Barker, J. Phys. G **2**, L45 (1976).
- [10] A. Navin *et al.*, Phys. Rev. Lett. **85**, 266 (2000).
- [11] S. Shimoura *et al.*, Physics Letters B **560**, 31 (2003); *ibid* **654**, 87 (2007).
- [12] H. Fortune and R. Sherr, Phys. Rev. C **74**, 024301 (2006).
- [13] R. Meharchand *et al.*, Phys. Rev. Lett **108**, 122501 (2012).

Charge-exchange (p, n) reaction in inverse-kinematics with isomer beams: Toward feasibility test on the isomer $^{52}\text{Fe}(12^+)$

K. Yako, M. Kobayashi and H. Sakai^a

Center for Nuclear Study, Graduate School of Science, University of Tokyo
^aRIKEN Nishina Center

Radioactive ion (RI) beams allow experimental study of *exotic* nuclei whose neutron and proton numbers are unbalanced, extending the horizon of the nuclear physics in terms of isospin. An outstanding aspect of RI beams is nuclear isomers, i.e. excited metastable states of nuclei. Since the metastability of isomers originates essentially from structural differences (shape, spin, etc.) from the nearby lower excited states, they give additional dimensions to study of nuclear structure.

So far the studies on the isomeric states are performed by producing the isomer via reactions and then by subsequent observation of de-excitations via γ -, β -, particle-decay or fission-decay. If we are able to carry out a reaction study with an isomer target (a target nucleus in isomeric state), it may open up a new field of an exotic structure such as states with a very high spin built on an unique spin or shape pertinent to the isomeric state.

The 12^+ isomer in ^{52}Fe , locating at $E_x = 6.96$ MeV and has the half-life of $T_{1/2} = 45.9$ s, is considered to be the seniority 4 state (two proton and two neutrons) in $f_{7/2}$ orbit which couple to the maximum angular momentum of 12. This 12^+ state is interesting, because the fact that the 12^+ state lying lower than the 10^+ state can be considered as a feature of high- j aligned n - p system where the n - p quadrupole interaction is strong. We are aiming at using an isomer as the starting point of spin-isospin excitations, such as the Gamow-Teller (GT) and Spin-Dipole (SD) giant resonances (GRs) by the $^{52}\text{Fe}^{\text{iso}}(p, n)^{52}\text{Co}^*$ reaction at 160–200A MeV.

The energy diagrams for the GTGR and SDGR transitions from the ground state (g.s.) 0^+ and 12^+ isomer state in ^{52}Fe , respectively, are shown in Figure 1. Since nothing is known for those transitions, the GT and SD strength distributions (mean energy, width, total strength) may provide interesting information.

In this report, we review the following key elements of the isomer beam experiment: (1) isomer production rate, (2) tagging the isomeric state by mass measurement, and (3) luminosity and ejectile detection.

Isomer production rate (isomer ratio)

There are several studies on the isomer ratio in unstable beams [1, 2, 3, 4]. It depends on the reaction, fragmentation, few nucleon pickup / stripping or fission. The isomer ratio, defined as the ratio of number of ions in the isomeric state to that of in the g.s., is in general 10–30%.

It is necessary to know the 12^+ isomer ratio of the ^{52}Fe beam prior to make a specific proposal to NP-PAC at RIBF. The measurement could be done in typically less than few hours. Since the 12^+ isomer in ^{52}Fe is considered to be four-hole ($2p2n$) state in $f_{7/2}$ shell orbital, there might be some advantage to start with reactions with removal of four or more nucleons such as, $^{58}\text{Ni} \rightarrow ^{52}\text{Fe}^{\text{iso}} + 2p4n$, $^{64}\text{Zn} \rightarrow ^{52}\text{Fe}^{\text{iso}} + 4p8n$ or possibly $^{56}\text{Fe} \rightarrow ^{52}\text{Fe}^{\text{iso}} + 4n$. Note that the production of the 12^+ isomer beam by fragmentation of

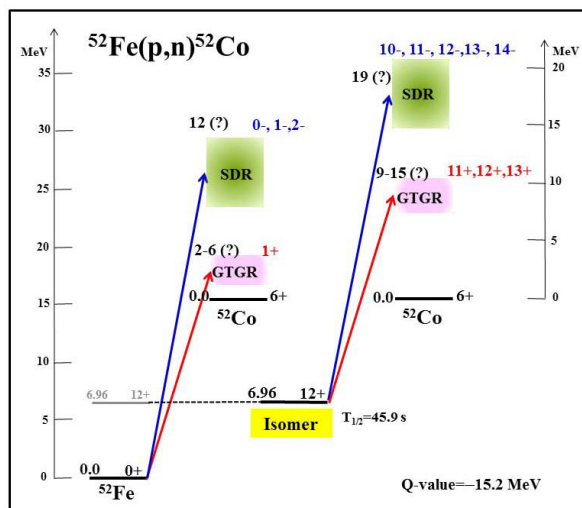


Figure 1. Energy diagrams for the $^{52}\text{Fe}(p, n)^{52}\text{Co}$ reaction from the ground state and from the 12^+ isomer state, respectively.

^{58}Ni with 1A GeV on a ^9Be target was made at FRS of GSI and an isomer ratio of $\geq 10\%$ was reported [5]. We also note that RIBF has developed an intense Zn beam for the element synthesis of $Z = 113$, which can be used to provide the primary beam for the present isomer (p, n) measurement.

Tagging the isomer by mass

The isomers in the beam are selected event-by-event based on mass difference. The particle mass m is obtained from the momentum p and the velocity β by using the relation of $p = m\gamma\beta$. The mass dispersion dm can be written as

$$\frac{dm}{m} = \sqrt{\left(\frac{dp}{p}\right)^2 + \gamma^4 \left(\frac{d\beta}{\beta}\right)^2}, \quad (1)$$

where dp and $d\beta$ are the momentum- and velocity- dispersions, respectively. The isomer with an excitation energy of E_x of can be discriminated if the condition

$$\frac{dm}{m} \leq \frac{E_x}{m} \quad (2)$$

is satisfied.

The high momentum resolution beam line leading to the SHARAQ magnetic spectrometer is the unique facility enabling the discrimination above at RIBF. Here, the momentum resolution has already achieved to 1/7,500 and it is possible to double the resolution by tuning the beam line or closing the momentum-defining slit F2 with some cost of intensity.

The velocity is obtained from the time-of-flight (TOF) measurement. The distance L between the F3 slit and the target position of SHARAQ is about 100 m (See Figure 2). The velocity of particle is determined by $\beta = L/tc$ and its

relative uncertainty $d\beta$ is $d\beta/\beta = \Delta t/t$, where Δt is the uncertainty in the flight time. A set of diamond detectors will be used for the time pick-up. A prototype is being developed [6] and a resolution of $\Delta t = 35$ ps has been achieved. Thus the overall time resolution from the start and stop diamond detectors is about 50 ps.

Assuming the isomer beam energy of 160A MeV ($\beta = 0.52$, $\gamma = 1.27$ and $t = 640$ ns), the condition above becomes $dm/m = 1.3 \times 10^{-4}$. This system would allow the separation of $^{52}\text{Fe}^{\text{iso}}(12^+)$ since $E_x/m = 6.96 \text{ MeV}/(51.948 \times 931.5 \text{ MeV}) = 1.44 \times 10^{-4}$ satisfies the condition (2).

Luminosity and ejectile detection

The (p,n) measurement is performed in the inverse kinematics by using a liquid hydrogen target and neutron detector array, called WINDS [7]. A typical experiment is 5-day beamtime with 5×10^5 counts/s secondary beam on a 14 mm-thick target [8]. Since the beam intensity of the isomeric state is about an order of magnitude weaker than that of g.s., the reduction might be partially compensated by use of a thicker target to keep a beam time in an affordable length.

It should be noted that both transitions from the g.s. and the isomer state are measured simultaneously. This allows a direct comparison of the excitation spectra with minimum systematic uncertainties.

In summary, the (p,n) measurement on isomeric $^{52}\text{Fe}(12^+)$ is technically feasible. Whether the experiment can be carried out in an affordable beamtime depends on the intensity and purity of the isomer beam, which can be studied separately.

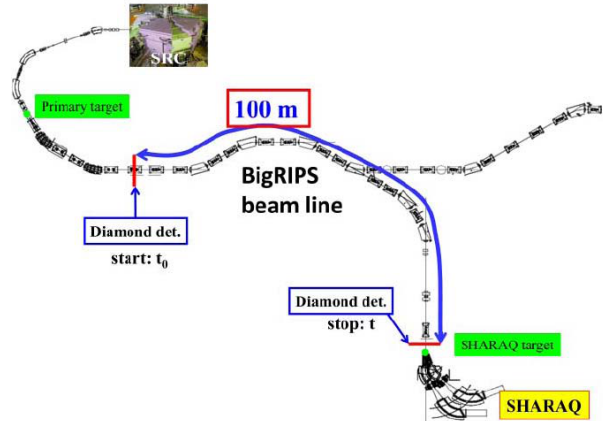


Figure 2. The layout of the facility. The flight path length for the analysis of the isomer beam is 100 m.

References

- [1] B.M. Young *et al.*, Phys. Lett. B **311** (1993) 22.
- [2] R. Grzywacz *et al.*, Phys. Lett. B **355** (1995) 439.
- [3] M. Pfützner *et al.*, Nucl. Instrum. and Methods B **444** (1998) 32.
- [4] M. Fukuda, HIMAC experiment. private communication.
- [5] A. Gadea *et al.*, experimental proposal to GSI.
- [6] S. Michimasa *et al.*, Nucl. Instrum. and Methods B **317** (2013) 710.
- [7] K. Yako *et al.*, CNS Ann. Rep. 2011 55.
- [8] K. Yako *et al.*, CNS Ann. Rep. 2011 22.

Quasi-elastic scattering of the proton drip line nucleus ^{17}F on ^{12}C at 60 MeV

G. L. Zhang^{a,b}, C. L. Zhang^{a,c}, H. Q. Zhang^a, C. J. Lin^a, D. Y. Pang^b, X. K. Wu^d, H. M. Jia^a, G. P. An^a, Z. D. Wu^a, X. X. Xu^a, F. Yang^a, Z. H. Liu^a, S. Kubono^e, H. Yamaguchi^e, S. Hayakawa^e, D. N. Binh^e, Y. k. Kwon^f, N. Iwasa^g, M. Mazzocco^h, M. La Commara^{i,j}, M. Romoli^j, and C. Signorini^h

^aChina Institute of Atomic Energy, Beijing 102413, China

^bSchool of Physics and Nuclear Energy Engineering, Beihang University, Beijing 100191, China

^cParticle Astrophysics Center, Institute of High Energy Physics, Chinese Academy of Sciences, Beijing 100039, China

^dInstitute for Standardization of Nuclear Industry, Beijing 100091, China

^eCenter of Nuclear Study, University of Tokyo, Japan

^fRIKEN (Department of Physics, Chung-Ang University, Seoul 156-756, South Korea)

^gDepartment of Physics, Tohoku University, Aoba, Sendai, Miyagi 980-8578, Japan

^hDipartimento di Fisica, Università di Padova and Istituto Nazionale di Fisica Nucleare-Sezione di Padova, via F. Marzolo 8, I-35131 Padova, Italy

ⁱDipartimento di Scienze Fisiche, Università di Napoli, via Cinthia, I-80126 Napoli, Italy

^jIstituto Nazionale di Fisica Nucleare-Sezione di Napoli, via Cinthia, I-80126 Napoli, Italy

The nuclear reactions induced by the nuclei near or at the drip line are research topics of current interest. ^{17}F is a proton drip line nucleus with 601 keV binding energy of its valence proton. Owing to its special character and importance in astronomy, ^{17}F itself as well as the reactions induced by this projectile have attracted much attentions. Many experiments with ^{17}F as projectile have been performed in recent years [1, 2, 3, 4, 5, 6, 7, 8]. The fusion cross sections of $^{17}\text{F} + ^{208}\text{Pb}$ were measured at energies near and below the Coulomb barrier [1]. No enhancement has been observed. This may reflect the fact that the measured breakup cross section is too small to influence the fusion probability [1, 2]. The interaction cross section of ^{17}F with ^{208}Pb has also been measured [3] and the corresponding rms radius has been extracted. No anomaly was found [4]. Elastic scattering angular distributions of $^{17}\text{F} + ^{208}\text{Pb}$ were measured at 170 MeV [5], 98 MeV and 120 MeV [6], and 90.4 MeV [7], respectively. Precise data were obtained for the elastic scattering of ^{17}F on ^{12}C and ^{14}N at 10 MeV/nucleon [8]. The data for elastic scattering of ^{17}F on ^{58}Ni were also published recently [9].

It is well established that information of optical model potential (OMP) can be extracted from elastic scattering data. The radioactive nuclei loosely bound like ^{17}F tend to be easily broken up during their collisions with target nuclei through the excitation of the core-valence nucleon system into continuum states. As a consequence, in the extraction of optical potential, the couplings of the breakup and/or transfer channels with the elastic channel should be carefully taken into account [10, 11]. On the other hand, from the optical-model analysis of the elastic scattering at energies near Coulomb barrier, the total reaction cross sections can be deduced and the breakup effects may be examined [12, 13]. Thus, studies of elastic scattering induced by light loosely bound exotic nuclei are of particular interest.

The experiment was performed at the low-energy radioisotope beam separator (CRIB) of the Center of Nuclear Study (CNS), University of Tokyo. The CRIB was the first extensive low-energy in-flight RIB separator; detailed information could be found in Ref. [14]. The primary beam of 101 MeV ^{16}O was provided to bombard a deuteron gas target which is contained by two Havar windows, to pro-

duce radioactive beam ^{17}F by the $d(^{16}\text{O}, n)^{17}\text{F}$ reaction. The energy of ^{17}F produced at gas target center was decreased to 60 MeV when after passing through the Havar foils and two Parallel Plate Avalanche Counters (PPAC) upstream of the secondary target. The thickness of the ^{12}C target was $435 \mu\text{g}/\text{cm}^2$. The experimental setups are shown in Figure 1. The position of ^{17}F on ^{12}C target was determined by

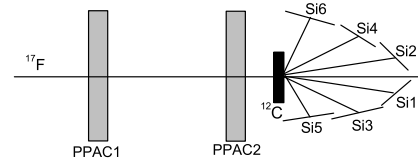


Figure 1. Schematic view of the experimental setup.

duce the signals from the two position-sensitive PPACs set in the beam line. Six sets of ΔE -E detector telescopes were used. The angle range covered corresponded to $\theta_{lab} = 5^\circ - 80^\circ$. These detectors were symmetrically positioned with respect to the beam axis in order to efficiently measure the events of ^{17}F elastic scattering. Thin ΔE detectors (DSSD, $65 \mu\text{m}$ thickness, each side 16 strips, the strip width 3 mm and the strip span 0.1 mm) were placed in front of $300 \mu\text{m}$ -thick E detectors (SSD). The experimental quasi-elastic scattering angular distribution of the 60 MeV ^{17}F on ^{12}C target is shown in Figure 2, in which the error bars represent the statistical uncertainties.

We make an optical model fitting of the $^{17}\text{F} + ^{12}\text{C}$ quasi-elastic scattering data based on the OMP parameters of the $^{16}\text{O} + ^{12}\text{C}$ system at 56.5 MeV. The detailed information was shown in Ref. [15]. Optical model calculations are shown and compared with experimental data in Figure 2. One can see that these parameters can reproduce our experimental data reasonably well. The results of the OM calculation for ^{16}O elastic scattering on ^{12}C at 56.5 MeV with the above parameters are also shown in Figure 2 for comparison. We evaluate the coupling effect to the elastic channel from the inelastic channel to the first 2^+ state of ^{12}C . The resulting elastic scattering cross sections were depicted as the dashed

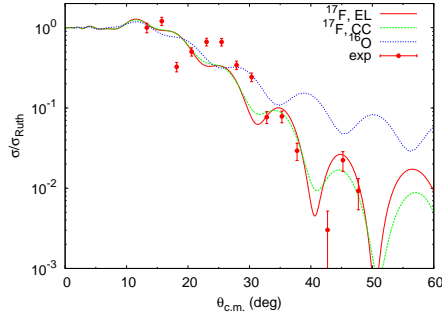


Figure 2. Experimental data of angular distributions of the cross sections for the ^{17}F quasi-elastic scattering from ^{12}C at 60 MeV and their comparisons with: i) single-channel optical model calculations (EL, solid curve), ii) coupled channel calculation including the first 2^+ state of ^{12}C (CC, dashed curve), and iii) ^{16}O elastic scattering from ^{12}C at 56.5 MeV (dotted curve). See the text for details.

curve in Figure 2. One sees that the inelastic scattering channel has visible coupling effects to the elastic channel, but it does not improve the description to the experimental data.

We have examined the coupling effects of the breakup channels to the elastic and inelastic channels with the CDCC method. The detailed information can be seen Ref. [15]. The results of the CDCC calculations for elastic and inelastic scattering cross sections are shown in Figure 2. We can conclude that the inelastic scattering cross sections to the first excited state of ^{17}F are negligible compared to those of the ground state and the small differences between calculations with and without couplings to continuum states indicate that the breakup effects to the elastic and inelastic scattering channels are small.

It is difficult to clarify and assess if the fusion cross sections are enhanced or hindered in the reactions induced by weakly bound nuclei at the energies near and below the Coulomb barrier. We used Shorto *et al* proposal [16] with a universal function $F(x)$ to classify this effect. This method eliminates the geometrical and static effects, and keeps only dynamic effects. In order to explore the breakup effects systematically, we selected some systems of weakly and tightly bound projectile interacting with ^{12}C target [17].

From Figure 3 we can see that except for ^4He and ^{12}C , all of $F(x)$ s follow the same trend described by the universal function $F_0(x)$ in spite of the differences in the structure, binding energy and reaction mechanism. It is particularly interesting to note that the $F(x)$ s of proton-halo nuclei ^{17}F , ^8B and two-neutron-halo nucleus ^6He have similar trend, this indicates that the breakup channels do not have important contribution to the total cross section for these weakly bound projectiles bombarding on ^{12}C target. For ^4He and ^{12}C projectiles on the ^{12}C target the values of $F(x)$ do not exactly follow the universal function $F_0(x)$. Because of the tightly bound for ^4He and ^{12}C , the other reaction channels should give a small contribution to the total reaction cross sections. According to Ref. [17], we select $0.6F_0(x)$ to fit those of $^4\text{He}+^{12}\text{C}$ and $^{12}\text{C}+^{12}\text{C}$ systems. It means that the reduced cross sections for $^4\text{He}+^{12}\text{C}$ and $^{12}\text{C}+^{12}\text{C}$ systems are 40% lower than the other systems.

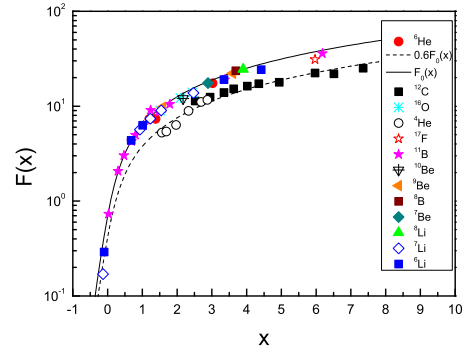


Figure 3. The total reaction functions $F(x)$ for different systems with weakly and tightly bound projectiles on ^{12}C target together with $^{17}\text{F}+^{12}\text{C}$ system data from this work. The solid and dashed lines represent $F_0(x)$ and $0.6F_0(x)$ which are explained in the text, respectively.

References

- [1] K. E. Rehm *et al.*, Phys. Rev. Lett. **81**(1998) 3341.
- [2] J. F. Liang *et al.*, Phys. Lett. B **491** (2000) 23.
- [3] A. Ozawa, T. Suzuki and I. Tanihata, Nucl. Phys. A **693** (2001) 32.
- [4] H. Kitagawa, N. Tajima and H. Sagawa, Z. Phys. A **358** (1997) 381.
- [5] J. F. Liang *et al.*, Phys. Rev. C **65** (2002) 051603.
- [6] J. F. Liang *et al.*, Phys. Rev. C **67** (2003) 044603.
- [7] M. Romoli *et al.*, Phys. Rev. C **69** (2004) 064614.
- [8] J. C. Blackmon *et al.*, Phys. Rev. C **72** (2005) 034606.
- [9] M. Mazzocco *et al.*, Phys. Rev. C **82** (2010) 054604.
- [10] E. F. Aguilera *et al.*, Phys. Rev. Lett. **84** (2000) 5058.
- [11] J. J. Kolata *et al.*, Phys. Rev. C **57** (1998) 6(R).
- [12] K. Kalita *et al.*, Phys. Rev. C **73** (2006) 024609.
- [13] A. Barioni *et al.*, Phys. Rev. C **84** (2011) 014603.
- [14] Y. Yanagisawa *et al.*, Nucl. Instrum. Methods A **539**, 74 (2005).
- [15] G. L. Zhang *et al.*, Eur. Phys. J. A **48** (2012) 65.
- [16] J. Shorto *et al.*, Phys. Lett. B **678** (2009) 77.
- [17] J. C. Zamora *et al.*, Phys. Rev. C **84** (2011) 034611.

Investigation for the resonant scattering of $^{17}\text{F}+p$

J. Hu^a, J. J. He^a, S. W. Xu^a, H. Yamaguchi, P. Ma^a, D. Kahl, J. Su^b, H. W. Wang^c, T. Nakao, Y. Wakabayashi^d, J. Y. Moon^e, T. Teranishi^f, H. S. Jung^e, T. Hashimoto^g, A. Chen^h, D. Irvine^h, and S. Kubono^d

Center for Nuclear Study, Graduate School of Science, the University of Tokyo

^aInstitute of Modern Physics, Lanzhou, China

^bChina Institute of Atomic Energy, Beijing, China

^cShanghai Institute of Applied Physics, Shanghai, China

^dNishina Center, RIKEN, Japan

^eDepartment of Physics, Chung-Ang University, Korea

^fDepartment of Physics, Kyushu University, Japan

^gRCNP, Osaka University, Japan

^hDepartment of Physics & Astronomy, McMaster University, Canada

X-ray bursts [1] have been considered as probably an important source for the production of proton-rich nuclei via the high temperature rp-process [2], and the $^{14}\text{O}(\alpha, p)^{17}\text{F}$ reaction is thought to be one of the crucial stellar reactions during the ignition phase. By far, its reaction rate is still uncertain. Therefore, the studies of this reaction are of great nuclear astrophysical importance to understand the energy generation and nucleosynthesis in the explosive stellar environments.

The reaction $^{14}\text{O}(\alpha, p)^{17}\text{F}$ is mainly resonant, and its reaction rate depends on the properties of those excited states above the α threshold in the compound nucleus ^{18}Ne . In this work, the properties in ^{18}Ne have been studied using the resonant elastic and inelastic scattering of $^{17}\text{F}+p$ with a ^{17}F beam bombarding a thick H_2 gas target. The experimental goal was to determine the spin-parities and proton partial widths for those states above the proton threshold in ^{18}Ne .

The experiment was performed using the CNS radioactive ion beam separator (CRIB) [3], installed by the Center for Nuclear Study (CNS), University of Tokyo, in the RIKEN Accelerator Research Facility. A primary beam of $^{16}\text{O}^{6+}$ was accelerated up to 6.6 AMeV by the AVF cyclotron ($K = 70$) with an average intensity of 560 enA. The primary beam bombarded a liquid-nitrogen-cooled D_2 gas target where a secondary beam of ^{17}F was produced via the $^{16}\text{O}(d, n)^{17}\text{F}$ reaction in inverse kinematics. The D_2 gas at 120 Torr and 90 K was confined in a small cell with a length of 80 mm whose entrance and exit windows were made of 2.5 μm thick Havar foils. The ^{17}F beam was separated by the CRIB separator using the in-flight method. The ^{17}F beam, with a mean energy of 61.9 ± 0.5 MeV and an average intensity of 2.5×10^5 pps, was then delivered to F3 experimental chamber and bombarded a thick H_2 gas target in which the beam was stopped.

The setup at F3 experimental chamber is shown in Figs. 1. The beam purity can be up to 98% after passing through a Wien-filter, which significantly purifies the secondary beam. Two PPACS (Parallel Plate Avalanche Counters) were used for measuring time and two-dimensional position information of the beam particles. The beam profile on the secondary target was also monitored by the PPACS during the data acquisition. The beam particles were identified in an event-by-event mode by using the abscissa signal of PPACa, and the TOF between PPACa and the RF signal

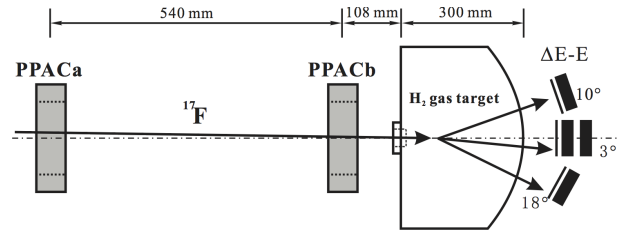


Figure 1. Schematic diagram of the experimental setup at F3 chamber.

provided by the cyclotron. Figs. 2 shows the particle identification before the secondary target. The H_2 gas target was

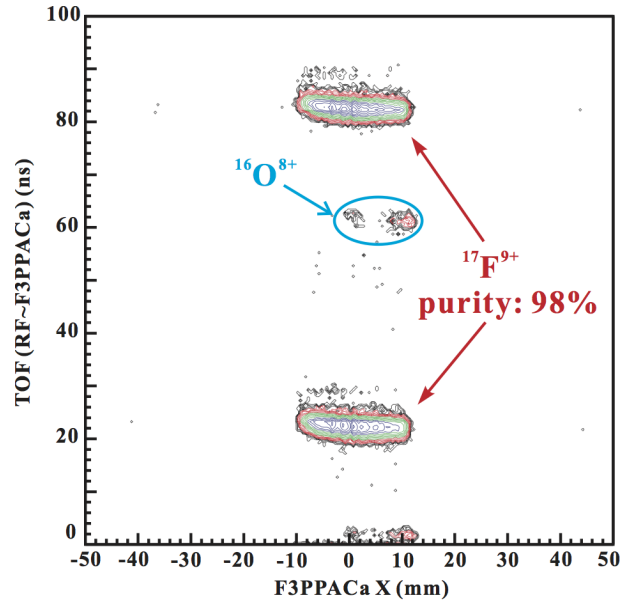


Figure 2. Identification plot for the beam particles before target.

at 600 Torr, housed in a 300-mm-radius semi-cylindrical shape chamber. The beam entrance window is sealed with a 2.5- μm -thick Havar foil, and the beam exit window with a 25- μm -thick aluminized Mylar foil. Compared with the solid polyethylene $(\text{CH}_2)_n$ target, the gas target is free from background contribution from C. The recoiled light particles were measured by using three sets of ΔE -E Si telescopes at averaged angles of $\theta_{lab} \approx 3^\circ$, 10° and 18° , respectively. At $\theta_{lab} \approx 3^\circ$, the telescope consisted of a 65-

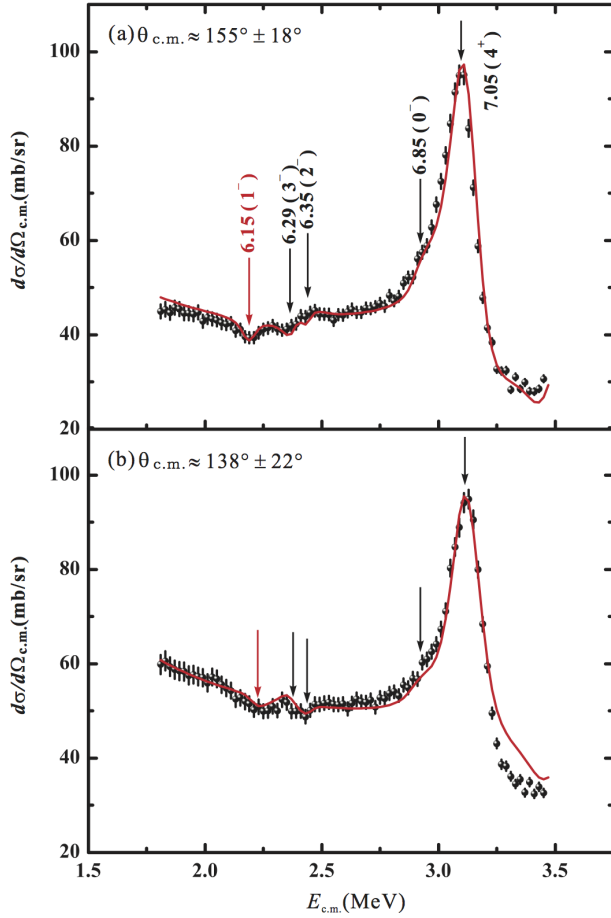


Figure 3. The c.m. differential cross-sections for elastically scattered protons produced by bombarding a thick H_2 gas target with 61.9 MeV ^{17}F particles at scattering angles of (a) $\theta_{c.m.} \approx 155^\circ \pm 18^\circ$ and (b) $\theta_{c.m.} \approx 138^\circ \pm 22^\circ$. The curves represent the R -matrix fits to the data.

μm -thick W1-type double-sided-strip (16×16 strips) silicon detector and two $1500\text{-}\mu\text{m}$ -thick MSX25-type pad detectors, and the third Si detector was used to veto the high-energy protons which were produced from the upper stream of the scattering chamber. The setup of the telescopes at other angles were very similar to the one at $\theta_{lab} \approx 3^\circ$, but without the third Si pad detector. The recoiled particles were clearly identified by using the ΔE - E method.

The energy calibration for the silicon detectors was performed by using a standard triple α source. In order to correct the pulse height defect, energy calibration for protons was performed with the proton beams at various energies. In addition, an Ar gas at 120 Torr filled in the secondary gas target chamber, was used in a separate run for evaluating the background contribution from the upper stream of the beam line.

The excitation function of $^{17}\text{F}+p$ elastic scattering cross sections at different scattering angle regions are shown in Figs. 3(a)–(b). Several resonances were clearly observed. In order to determine the resonant parameters of observed resonances, the multichannel R -matrix calculations [4] that include the energies, widths, spins, angular momenta, and interference sign for each candidate resonance have been performed. A channel radius of $R = 4.464\text{fm}$ ($= 1.25 \times (1 + 17^{1/3})\text{fm}$) appropriate for the $^{17}\text{F}+p$ system has been utilized in the present R -matrix calculation. The ground-state spin-parity configurations of ^{17}F and proton are $5/2^+$

and $1/2^+$. Thus, there are two possible spins in the elastic channel, *i.e.*, $s = 2, 3$.

Five resonances, *i.e.*, at $E_x = 6.15, 6.29, 6.35, 6.85,$ and 7.05 MeV, have been analyzed and most probable fitting curves are shown in Figs. 3. It shows that the fitting results at different scattering angle regions are consistent with each other. A more comprehensive analysis and the inclusion of α particle information is in progress.

References

- [1] W.H.G. Lewin, J.V. Paradijs and R.E. Taam, *Space Science Reviews* **62** (1993) 223.
- [2] R.K. Wallace and S.E. Woosley, *Astrophys. J. Suppl.* **45** (1981) 389.
- [3] Y. Yanagisawa *et al.*, *Nucl. Instr. Meth.* **539** (2005) 74.
- [4] A.M. Lane and R.G. Thomas, *Rev. Mod. Phys.* **30** (1958) 257.

**Experiment Nuclear Physics: PHENIX
Experiment at BNL-RHIC and ALICE
Experiment at CERN-LHC**

First Three-Year Operation of the LHC-ALICE experiment and Activities of CNS

T. Gunji, H. Hamagaki, Y. L. Yamaguchi, S. Sano Y. Hori, T. Tsuji, S. Hayashi, K. Terasaki

Center for Nuclear Study, Graduate School of Science, University of Tokyo, Japan

1. Introduction

The first three-year operation of the Large Hadron Collider (LHC) was over on February 2013. The LHC's first three-year running has seen major advances in particle and nuclear physics, including the discovery of a new particle like Higgs boson in $p-p$ collisions and the discovery of a new state of hot and dense medium by smashing the heavy nuclei at highest colliding energies. The LHC now begins its first long shutdown (2013-2015). After consolidation and maintenance work of CERN's accelerator apparatus are done, the LHC will provide top energy $p-p$ collisions at $\sqrt{s}=14$ TeV and Pb-Pb collisions at $\sqrt{s_{NN}}=5.5$ TeV. ALICE (A Large Ion Collider Experiment) is very different in both design and purpose from the other experiments at the LHC. Its main aim is to study the physics of strongly interacting matter at extremely high energy densities, where the formation of a new phase of matter composed of deconfined quarks and gluon, is expected.

2. Detector setup of the ALICE Experiment

The ALICE experiment consists of a larger number of detectors [1]. Central barrel detectors measuring hadrons, electrons and photons at $|\eta| \leq 0.9$ are composed of an Inner Tracking System (ITS) of high-resolution silicon detectors, a cylindrical Time-Projection Chambers (TPC), a Transition Radiation Detectors and a Time-Of-Flight (TOF) detector. A single arm detectors of lead-scintillator ElectroMagnetic Calorimeter (EMCal), a lead-tungsten crystal calorimeter (PHOS), and a ring imaging Cherenkov hodoscope (HMPID) complement the central barrel of ALICE. The forward muon arm consists of a complex of absorbers, a dipole magnet, and tracking and triggering muon chambers. Several smaller detectors (T0, V0, ZDC, FMD, PMD) are also installed at forward rapidity in ALICE for the global event characterization and trigger.

3. Recorded Luminosity by LHC-ALICE

The ALICE experiment has collected wealthy data in $p-p$, Pb-Pb, and p -Pb collisions. The data collected with $p-p$ collisions at $\sqrt{s}=7$ TeV in 2010 and 2011 consist of a minimum-bias data sample with integrated luminosity of 16 nb^{-1} and rare triggered event based on EMCal, PHOS and MUON detectors with integrated luminosity of 5 pb^{-1} . The recorded luminosity of heavy-ion collisions at the center-of-mass energy per nucleon ($\sqrt{s_{NN}}$) of 2.76 TeV in 2010 and 2011 are $10 \mu\text{b}^{-1}$ and $143 \mu\text{b}^{-1}$, respectively. In 2013, ALICE recorded p -Pb collisions at $\sqrt{s_{NN}}=5.02$ TeV with integrated luminosity of 32 nb^{-1} .

4. Selected Results from Pb-Pb collisions

Charged particle multiplicity and transverse energy density in Pb-Pb collisions were measured [2]. Assuming that the formation time of the medium is $\sim 1 \text{ fm}/c$, Bjorken energy density of $\sim 16 \text{ GeV}/\text{fm}^3$ is largely exceeding the critical energy density and the density is $\times 2.5$ larger than at RHIC. Figure 1 shows photon spectrum in 0-40% cen-

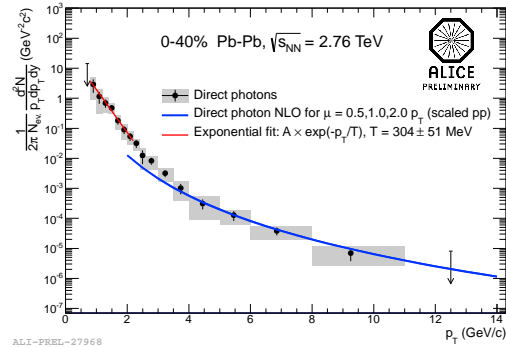
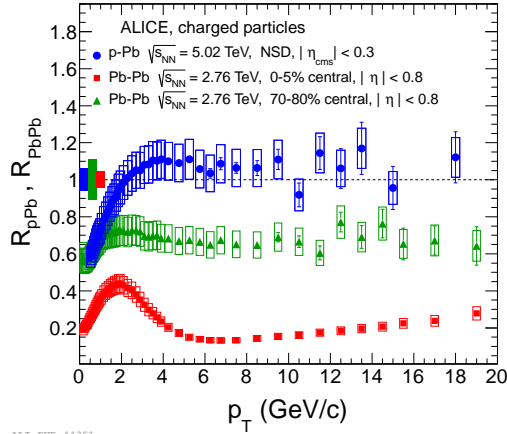


Figure 1. Photon spectrum in central Pb-Pb collisions (0-40% centrality of collisions) [3]

tral Pb-Pb collisions [3]. For $p_T \geq 4 \text{ GeV}/c$, the measured spectrum agrees with that for photons from initial hard scattering. For lower p_T , the spectrum has an exponential shape and magnitude is significantly larger than the contribution from hard scattering. This enhancement is possibly due to the radiation of photons from the medium. The inverse slope parameter, $T_{\text{LHC}} = 304 \pm 51 \text{ MeV}$, is larger than the value observed in Au-Au at RHIC.

Figure 2 shows the nuclear modification factor (R_{AA}), defined as a ratio of the particle spectrum in heavy-ion collision to that in $p-p$, scaled by the number of binary nucleon-nucleon collisions, for inclusive charged hadrons as a function of p_T in p -Pb (circle), peripheral Pb-Pb collisions (square), and central Pb-Pb collisions (triangle) [4]. R_{pPb} is consistent with unity for $p_T \geq 2 \text{ GeV}/c$, demonstrating that the strong suppression observed in central Pb-Pb collisions is not due to initial state effects such as gluon saturation, Cronin effect, or initial state energy loss, but rather the final state effects such as the energy loss of high energetic partons in the medium.

The azimuthal distribution of particles in the plane perpendicular to the beam direction is sensitive to the properties of the medium. When nuclei collide at non-zero impact parameter, the geometrical overlap region is anisotropic and anisotropy in spatial geometry is converted into a momentum anisotropy of the particles. The dumping of the spatial anisotropy and building up the momentum anisotropy depend on initial conditions, quantum fluctuations, EoS, temperature, and transport properties like viscosity to entropy ratio (η/s). The azimuthal anisotropy is usually characterized by the Fourier coefficients as $v_n = \langle \cos[n(\phi - \Psi_n)] \rangle$, where ϕ is the azimuthal angle of the particle, Ψ_n is the n -th order of harmonics of the angle of the initial state spatial plane. Figure 3 shows the harmonics v_2 , v_3 , v_4 , and v_5 as a function of p_T for 30-40% of central collisions [5]. The results are compared to hydrodynamic predictions using Glauber initial conditions for different values of η/s . It is observed that at low p_T , the different p_T dependence of v_2 and v_3 is described well by the predictions. However, $v_2(p_T)$ is better described by $\eta/s=0$, while $\eta/s=0.08$



ALICE-PUB-44351

Figure 2. the nuclear modification factor (R_{AA}) for inclusive charged hadrons as a function of p_T in p -Pb (circle), peripheral Pb-Pb collisions (square), and central Pb-Pb collisions (triangle) [4].

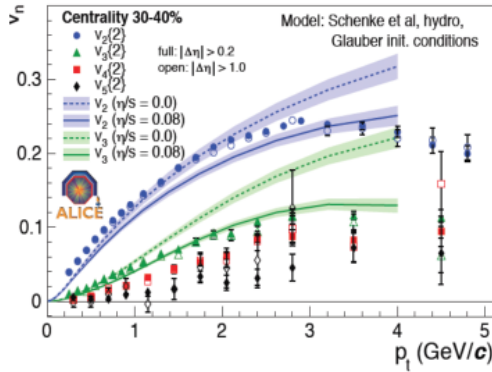


Figure 3. The harmonics of the particle azimuthal anisotropy, v_2 , v_3 , v_4 , and v_5 , as a function of transverse momentum for the 30-40% of central collisions [5]

gives a better description for $v_3(p_T)$. Moreover, the magnitude depends on the initial conditions. For instance, when MC-KNL model is employed, which is based on the gluon saturation, $\eta/s \sim 0.16$ describes experimental results.

5. Activities of CNS in ALICE

The CNS group has contributed detector commissioning, detector calibration, physics data analysis, and R&D of the ALICE detector upgrade. CNS has activities for the commissioning of the TRD and the development of the TRD slow control system [6] and for the calibration and performance evaluation of the TPC [7]. Leading efforts for the Forward Calorimeter (FoCAL) upgrade have been conducted [8]. In recent years, CNS started strong involvement of the ALICE GEM-TPC upgrade [9]. This upgrade enables to take 50kHz minimum-bias Pb-Pb collisions, which is $\times 100$ larger rate than the current data taking rate. In the data analysis, multiplicity dependence of the production of the multi-strangeness hadrons in p - p collisions has been investigated and collective phenomena in high multiplicity are observed [10]. Charge dependent mixed harmonics particle correlation in Pb-Pb collisions has been studied [11]. Path length dependence of parton energy loss in Pb-Pb collisions are being investigated to understand the detailed mechanisms of the energy loss in the medium [12]. Dielectron analysis is also on-going to study the virtual photon production and to study the correlation of heavy quark pro-

duction in Pb-Pb and p -Pb collisions [13].

6. Summary and Outlook

The first three-year running of the LHC-ALICE experiment reveals the formation of strongly interacting matter (small η/s) in heavy-ion collisions. The medium is hotter and denser compared to the medium created at RHIC. Further analysis to study the medium properties are underway. CNS group has a major contribution to the ALICE experiment in terms of detector commissioning, detector calibration, physics data analysis, and detector upgrades which will be continued extensively in the future.

References

- [1] ALICE Collaboration, Physics Performance Report Vol. 1 J. Phys. **G 30** (2003) 1517.
- [2] T. Gunji *et al.* CNS Annual Report 2010.
- [3] M. Wilde *et al.* (for the ALICE Collaboration), arXiv:1210.5958
- [4] B. Abelev *et al.* (for the ALICE Collaboration), arXiv:1210.4520
- [5] K. Aamodt *et al.* (for the ALICE Collaboration), Phys. Rev. Lett. **107**, 032301 (2011)
- [6] T. Gunji *et al.* CNS Annual Report 2007; T. Gunji *et al.* CNS Annual Report 2008.
- [7] S. Sano *et al.* CNS Annual Report 2009; Y. Hori *et al.* CNS Annual Report 2010.
- [8] T. Gunji *et al.* CNS Annual Report 2008; Y. Hori *et al.* CNS Annual Report 2009; T. Tsuji *et al.* CNS Annual Report 2010; S. Hayashi *et al.*, CNS Annual Report 2010
- [9] Y. L. Yamaguchi *et al.* CNS Annual Report 2012; K. Terasaki *et al.* CNS Annual Report 2012,
- [10] S. Sano *et al.* CNS Annual Report 2010
- [11] Y. Hori *et al.* CNS Annual Report 2012
- [12] T. Tsuji *et al.* CNS Annual Report 2011; T. Tsuji *et al.* CNS Annual Report 2012
- [13] T. Gunji *et al.* CNS Annual Report 2011; S. Hayashi *et al.* CNS Annual Report 2012

Measurement of dielectron in $\sqrt{s_{NN}} = 5.02$ TeV p+Pb collision at LHC

S. Hayashi, for the ALICE Collaboration

Center for Nuclear Study, Graduate School of Science, University of Tokyo

1. Introduction

Electron-positron pairs (dielectrons) are one of the excellent probes for studying of the properties of the matter created in high energy heavy ion collisions (QGP) since they can provide direct information of the dense medium without a strong interaction at penetrating the dense medium. In particular, at the intermediate mass region ($1.1 < M_{ee} < 2.5$ GeV/ c^2), the primary source is semi-leptonic decays of correlated open charm mesons. Heavy-quarks (charm and bottom) are mainly produced by gluon fusion and splitting in the initial stage of collisions and experience the full history of the collisions. Therefore the yield and the azimuthal correlation in this mass region are sensitive to the thermalization and energy loss of charm quarks in the medium [1].

p -Pb collisions are suitable to investigate initial state nuclear effects for high energy heavy ion collisions since QGP cannot be created in p -Pb collisions. At the LHC energy, small Bjorken- x regions ($10^{-4} < x < 10^{-3}$) become accessible at midrapidity, where x is the longitudinal momentum fraction of partons in the nucleon, nuclear matter effects are expected not to be negligible. The gluon density becomes extremely high and is possibly saturated at the small x region since the saturation scale $Q_s^2 \sim A^{1/3}x^{0.3}$ is expected a few GeV $^2/c^2$ at LHC, where A is the mass number. The saturation scale at LHC is expected a few GeV/ c . The charm quark mass is low compared with the saturation scale at LHC. Therefore correlated charmed pairs are expected to be affected by gluon saturation [2].

At LHC-ALICE, two different electron triggers with the Transition Radiation Detector (TRD) are available as well as the minimum bias trigger for the dielectron analysis. One is the single electron trigger with an electron identification cut for $p_T > 3$ GeV/ c . The other is the quarkonium trigger with a tighter electron cut compared with single electron trigger for $p_T > 2$ GeV/ c . During the 2013 run, 130M minimum bias events, 16M single electron trigger events, and 11M quarkonium trigger events for $\sqrt{s_{NN}} = 5.02$ TeV p -Pb collisions were taken at LHC-ALICE. The number of minimum bias equivalent events for TRD triggered events is 2.6B events. As a first step of the analysis for correlated heavy quarks pairs, the raw spectrum of the dielectron from hadronic sources was determined. In this report, the current status of the dielectron analysis for p -Pb collisions at LHC-ALICE is reported.

2. Electron identification

In the central barrel of the ALICE detector, charged tracks are reconstructed by the Inner Tracking System (ITS) and the Time Projection Chamber (TPC) [3]. The strength of the magnetic field at ALICE is 0.5 T and charged tracks with $p_T > 0.2$ GeV/ c can be reconstructed. Electrons are identified by dE/dx in TPC and TOF information. TOF is essential to remove contaminations of kaons, protons and deuterons up to 2 GeV/ c , although the TOF matching efficiency is low due to the large segment size of TOF. The hadron contaminations can be reduced less than 1% up to 3 GeV/ c by the TOF information. Figure 1 shows dE/dx

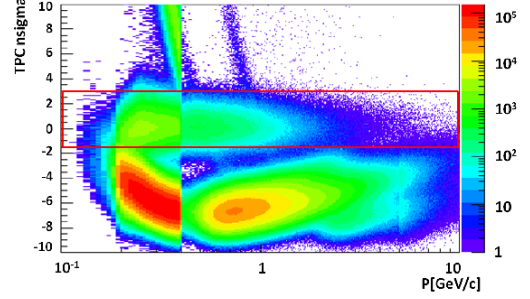


Figure 1. TPC dE/dx after TOF inclusion cut for the minimum bias trigger. The tracks inside the frame are selected as an electron candidate.

in TPC as a function of momentum for electrons after the TOF inclusion cut. Electrons can be clearly separated from hadrons. The tracks inside the frame in Fig. ?? are selected as the electron candidates. Figure 2 shows single electron p_T distributions for the minimum bias trigger and the TRD single electron trigger. The open symbols and the closed symbols show the spectrums for the TRD triggered data and the minimum bias data, respectively. The circular symbols mean the spectrums for electrons and the square symbols means the spectrums for positrons. The difference of the acceptance by changing the polarity of the magnetic field during the 2013 run is considered as one of the reasons for the difference between electrons and positrons for TRD triggered data.

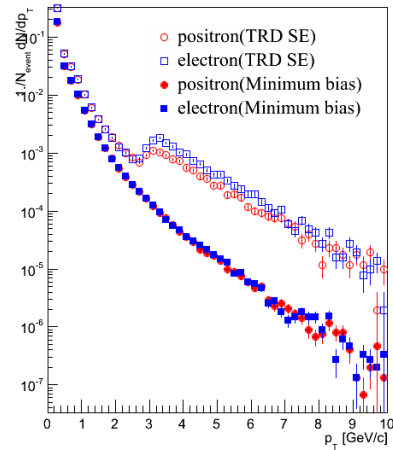


Figure 2. Single electron p_T distributions for the minimum bias trigger and the TRD single electron trigger.

3. Extraction of the raw dielectron spectrum

Signal extraction is made only for the minimum bias data because the available statistics for the TRD triggered data is not yet sufficient. All electrons and positrons are combined in the same event. Most of pairs are combinatorial and the

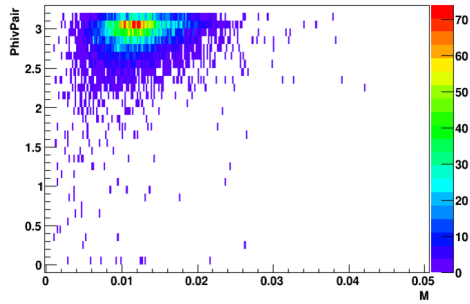


Figure 3. Phiv vs invariant mass of conversion pairs for Monte Carlo data.

signal fraction is very small. Combinatorial pairs and conversion pairs by the detector material should be removed for signal extraction.

Photon conversion pairs have a typical geometrical distribution. Phiv is defined as the angle between the pair plane and the direction of magnetic field. Electrons from hadronic source are distributed uniformly with respect to the magnetic field. On the other hand, the photon conversion pairs are localized at $\text{phiv} = \pi$ in the small mass region as shown in Fig. 3. Therefore, most of conversion pairs can be rejected by applying the phiv and mass cut.

To extract the signal, the combinatorial background should be subtracted from foreground dielectron pairs. For background estimation, like-sign pairs in the same events and the mixed events technique are used. Since the acceptance depends on the charge sign, acceptance correction is required. The pairs from mixed events are combinatorial and contains acceptance effects. Therefore the acceptance correction factor is defined as

$$R = \frac{N_{+-}|_{mix} + N_{-+}|_{mix}}{N_{++}|_{mix} + N_{--}|_{mix}} \quad (1)$$

where $N_{++}|_{mix}$, $N_{--}|_{mix}$ and $N_{+-}|_{mix}$, $N_{-+}|_{mix}$ are like-sign pairs and unlike-sign pairs in mixed events, respectively. The estimated combinatorial background is defined as

$$N_{CB} = 2R\sqrt{N_{++}N_{--}} \quad (2)$$

where N_{++} , N_{--} are like-sign pairs in the same event.

Figure 4 shows the dielectron spectrum after background subtraction. This is not corrected by the detection efficiency. The vector mesons and J/ψ peaks can be seen clearly. Figure 5 shows the signal-to-background ratio (S/B) of the dielectron spectrum. The S/B ratio is almost consistent with that of the pp data [4].

4. Summary and Outlook

The dielectron spectrum after background subtraction in p -Pb collisions was determined successfully with the ALICE detector. Compared with p - p collisions, the consistent S/B was obtained. The analysis for the TRD triggered data is on going. We are going to calculate the detection efficiency and determine the invariant cross section. Cocktail calculation will be carried out to estimate the contribution of hadronic sources. The multiplicity dependence and p_T distribution will be studied. Furthermore, the azimuthal angle correlation will be calculated and discussed on the nuclear matter effects at LHC.

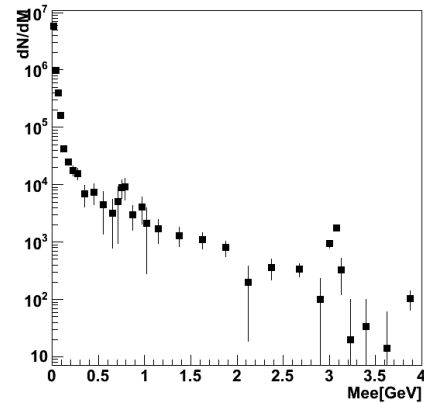


Figure 4. The dielectron spectrum after background subtraction for the minimum bias trigger.

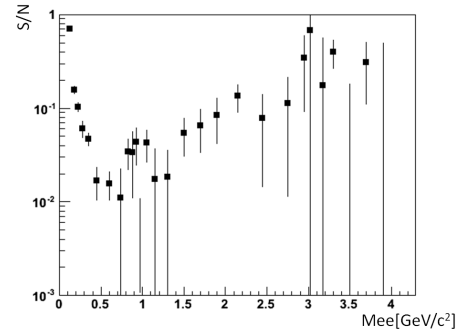


Figure 5. Signal to background ratio for the minimum bias trigger.

References

- [1] X. Zhu *et al.*: Phys. Rev. Lett 100, 152301 (2008).
- [2] L. D. McLerran and R. Venugopalan Phys. Rev. D 49 2233 (1994).
- [3] F. Carminati *et al.*, J. Phys. G: Nucl. Part. Phys. 30 1517 1763 (2004).
- [4] Markus K. Koehler: arXiv:1302.2049 (2013).

Heavy-quark measurement in $p + p$ collisions at $\sqrt{s} = 200$ GeV

R. Akimoto, Y. Akiba^{a,b}, H. Asano^c, T. Gunji, T. Hachiya^a, H. Hamagaki, M. Kurosawa^b,
M. Shimomura^d (for the PHENIX Collaboration)

Center for Nuclear Study, Graduate School of Science, University of Tokyo

^a*RIKEN (The Institute of Physical and Chemical Research)*

^b*RIKEN BNL Research Center, USA*

^c*Department of Physics, Kyoto University*

^d*Iowa State University*

1. Introduction

Heavy quarks (charm and bottom) are suitable probes to study the interactions between quarks and gluons in the quark-gluon plasma (QGP). Heavy quarks are created mainly by initial hard scatterings and their initial states are expected to be well evaluated by a perturbative QCD calculation. Therefore, the change of the properties of heavy quarks due to passing through the QGP can be clearly evaluated from their final states. By evaluating the changes of charm and bottom respectively, their behaviors inside the QGP can be evaluated precisely, and thus, the evaluation of the changes is helpful for the study of the QGP properties.

There are three methods to evaluate the yields of charmed and bottomed hadrons; one is a full reconstruction with all decay products from the hadronic decay, another is the analysis of the correlation between the electron and the hadron from the semi-leptonic decay, and the other is a measurement of the distance of the closest approach (DCA) of the track of a heavy-quark electron¹ to the beam collision vertex. The yields of charmed and bottomed hadrons can be evaluated from the difference in their distributions since the width of the DCA distribution depends on the lifetime and those of bottomed hadrons are considerably longer than those of charmed hadrons. The DCA analysis has the advantages of the good S/N ratio even in heavy-ion collisions and large branching ratio. The measurement of charmed hadrons has been made via the full reconstructions from the hadronic decays [1]. However, the measurement of bottomed hadrons with the hadronic decays is difficult due to a large hadronic background in central Au+Au collision events and their small branching ratios. The ratio of the electrons from charmed hadrons and those from bottomed hadrons was evaluated by the correlation analysis in $p + p$ collision events [2, 3], but it is also difficult to be performed in Au+Au collision events due to a large background. Therefore, the DCA analysis is the most suitable method to evaluate the yields of charmed and bottomed hadrons.

In this report, the contribution of electrons from bottomed hadrons in heavy-quark electrons determined by the DCA analysis is reported. $p + p$ collision events with $\sqrt{s} = 200$ GeV taken in 2011 and 2012 was analyzed.

2. DCA analysis

Electrons are mainly grouped into two by their sources; non-photonic and photonic electrons. Non-photonic electrons are those from weak decays, which include decays of heavy quarks and kaons. Photonic electrons are those from photon conversions and Dalitz decays of neutral mesons. In

addition, the fake tracks, which hits created by other tracks are associated with, are included in the measured electron sample.

The yields of the electrons from charmed and bottomed hadrons were evaluated by using the distribution of the charge \times DCA_{XY} (c-DCA_{XY})². The contributions of other sources than decays of heavy quarks were subtracted from the distribution. Then, the subtracted distribution was decomposed to charm and bottom contributions by fitting it with the shapes of their c-DCA_{XY} distributions. The shapes were evaluated by single-track Monte Carlo simulation. The simulated shapes were convoluted with a Gaussian whose RMS is equal to the c-DCA_{XY} resolution, which was evaluated by fitting the c-DCA_{XY} distribution of hadrons. The resolutions are listed in Table 1. The simulated tracks were generated by PYTHIA [4]. The production fractions of charmed and bottomed hadrons were tuned to match the measured values [5,6]. Only the large c-DCA_{XY} region was used for the fitting since the difference of the distributions of charm and bottom is clear at the region. Only the positive side of the distribution was used when p_T is less than 2 GeV/c. The electrons from photon conversion produce a large background at that p_T region, and the c-DCA_{XY} of the electron from photon conversion mainly distributes at negative side. Therefore, the S/N ratio can be improved by using only positive side of the distribution.

transverse momentum	c-DCA _{XY} resolution
1.0 - 1.5 GeV	142 \pm 5 μ m
1.5 - 2.0 GeV	139 \pm 5 μ m
2.0 - 2.5 GeV	138 \pm 5 μ m
2.5 - 3.0 GeV	137 \pm 5 μ m
3.0 - 4.0 GeV	138 \pm 5 μ m
4.0 - 5.0 GeV	140 \pm 5 μ m

Table 1. c-DCA_{XY} resolution as a function of transverse momentum.

The shapes of photonic electrons were evaluated by single-track simulation considering detector effects. The yields of photonic electrons and the electrons from kaon decays were calculated from the measured cross section [7, 8]. The shape and the yield of the fake tracks was evaluated by the c-DCA_{XY} distribution for the tracks with a large DCA along the Z-direction.

An isolation cut was applied to reject photonic electrons. A track was rejected by the cut when a hit was found around the hits associated to the track. Opening angles of the electrons from photon conversions and Dalitz decays are very

¹ The electron from decay of a heavy quark is called a heavy-quark electron.

² DCA_{XY} is the DCA in the XY-plane. The XY-plane is defined as the plane perpendicular to the beam axis and the Z-direction is defined as the direction along the beam axis.

small. On the other hands, opening angles of the decay products of heavy quarks are large due to large q -value. Therefore the isolation cut can improve the S/N ratio.

3. Result

Figure 1 shows the c - DCA_{XY} distribution of electrons with $p_T = 2.0 - 2.5$ GeV/c. The symbols indicate the measured counts and the associated bars indicate statistical errors. The dash-dot and the dash lines indicate the distributions of electrons from charmed and bottomed hadrons, respectively. The dot line indicates the distribution of electrons from other sources. The solid line indicates the sum of the distributions. The fitting result well reproduces the measured data.

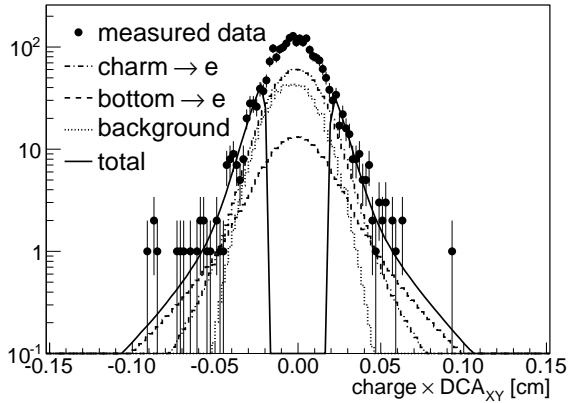


Figure 1. The c - DCA_{XY} distribution of electrons with $p_T = 2.0 - 2.5$ GeV/c. The symbols indicate the measured counts. The dash-dot and the dash lines indicate the distributions of electrons from charmed and bottomed hadrons, respectively.

Figure 2 shows the bottom fraction in heavy-quark electrons as a function of p_T of heavy-quark electrons. The circles indicate the preliminary result from the DCA analysis. The triangles and stars indicate the results evaluated by the PHENIX and the STAR experiments, respectively, from the correlation between the electrons and the hadrons from heavy-quark decays. [2,3] The solid line indicates the result of fixed order plus next-to-leading order (FONLL) calculation at rapidity $y = 0$, and the dashed lines indicate the boundaries of the error band for the calculation. [9] The bars and squares denote statistical and systematic errors, respectively. The present result with the DCA analysis is consistent with the published results, and the bottom fraction for the electrons with lower p_T can be evaluated by the analysis.

4. Summary and outlooks

The bottom fraction in heavy-quark electrons was evaluated successfully from the DCA analysis for the $p + p$ collision data. The result is consistent with the published results and the FONLL calculation is consistent with all of the results, and the bottom fraction for the electrons with lower p_T can be evaluated by the analysis.

The evaluation of Au+Au collision data is in progress.

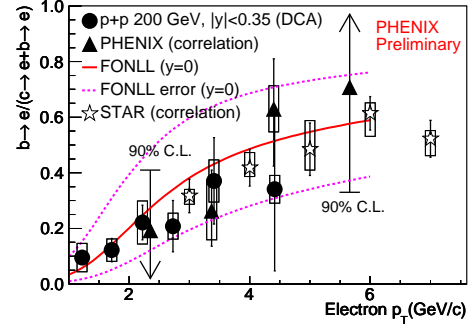


Figure 2. The bottom fraction in heavy-quark electrons as a function of p_T . The circles indicate the preliminary result from the DCA analysis. The triangles and stars indicate the results evaluated by the PHENIX and the STAR experiments, respectively, from the correlation analysis. The solid line indicates the result of FONLL calculation at rapidity $y = 0$, and the dashed lines indicate the boundaries of the error band for the calculation.

References

- [1] R. Bala *et al.*, for the ALICE Collaboration, arXiv:1208.4243.
- [2] A. Adare *et al.*, Phys. Rev. Lett. **103**, 082002 (2009).
- [3] M. M. Aggarwal *et al.*, Phys. Rev. Lett. **105**, 202301 (2010).
- [4] <http://home.thep.lu.se/~torbjorn/Pythia.html>
- [5] E. Lohrmann, arXiv:1112.3757.
- [6] R. Aaij *et al.*, for the LHCb Collaboration, Phys. Rev. D **85**, 032008 (2012).
- [7] S. S. Adler *et al.*, for the PHENIX Collaboration, Phys. Rev. Lett. **91**, 241803 (2003).
- [8] A. Adare *et al.*, for the PHENIX Collaboration, Phys. Rev. C **83**, 064903 (2011).
- [9] M. Cacciari *et al.*, Phys. Rev. Lett. **95**, 122001 (2005).

Measurement of J/ψ photo-production in ultra-peripheral Au+Au collisions at $\sqrt{s_{NN}}=200\text{GeV}$ using the PHENIX detector

A. Takahara, H. Hamagaki, T. Gunji, Z. Conesa del Valle^a, Y. Akiba^b, M. Chiu^c, J. Nystrand^d, S. White^e, K. Skjerdal^d, E. T. Atomssa^c for the PHENIX collaboration

Center for Nuclear Study, Graduate School of Science, University of Tokyo

^aCERN

^bRIKEN BNL

^cStony Brook University

^dDepartment of Physics, Lund University

^eBrookhaven National Laboratory

1. Introduction

We present the measurements of the photo-production of J/ψ in ultra-peripheral Au+Au collisions at $\sqrt{s_{NN}} = 200$ GeV at RHIC. An Ultra-Peripheral Collision (UPC) is a collision in which an impact parameter is greater than the sum of nuclear radii. The measurement of J/ψ in UPC serves as a considerable role for determining the gluon density in nuclei at the small Bjorken x (~ 0.01) region, where the gluon density is expected to be suppressed due to the gluon shadowing effect and has not been constrained by theoretical calculations [1, 2, 3].

In 2010, PHENIX collected an integrated luminosity of $656 \pm 25 \mu\text{b}^{-1}$ in Au+Au collisions. The J/ψ photo-production in UPC as a function of transverse momentum p_T and rapidity y has been established by using data taken in 2010.

2. Data analysis

The definition of the UPC trigger at forward rapidity is 1 or more neutron detection at both sides of ZDC, no hit on BBC and muons candidate measured by the muon spectrometer. The reason of neutron tagging by both ZDCs is to determine the collision vertex in the beam going direction. The events having only two muon tracks in forward rapidity are selected.

The hadron suppressor (Cu+Fe shield, 40 cm) are set in front of the PHENIX muon arms. Therefore, the dimuon efficiency of PHENIX muon arms strongly depends on pair p_T .

For background subtraction and determination of the J/ψ yield, the invariant mass distribution is divided into several p_T ranges. Figure 1 shows dimuons invariant mass spectrum in positive rapidity at $p_T < 0.5$ GeV/c with the fitting function. The fitting function is a combination of a modified exponential function for the continuum background associated with Three Gaussians. Three Gaussians correspond to J/ψ , its tail, and $\psi(2s)$. The ratio of J/ψ to $\psi(2s)$ is fixed to 7% that is the value of HERA $\gamma p \rightarrow J/\psi$ dimuon measurement [5]. Because of a small statistics, the shapes of other two Gaussians of J/ψ and its tail are fixed to those in the 2009 $p+p$ data (Figure 2). The background sources from the $\gamma\gamma$ and the most peripheral collisions are expected. Centrality is a pseudo parameter defined by BBC and ZDC which corresponds to an impact parameter. Impact parameter b , the distance between two nuclei, 0 and $2R$ (the radius of nuclei) corresponds to centrality 100 and 0, respectively. Due to BBC efficiency, the most peripheral region of $93 < \text{centrality} < 100$ considered to be triggered by the UPC trigger.

Figure 3 shows the comparison of the multiplicity distributions at central rapidity in UPC events and $p+p$ collisions, where the event has dimuon pair with the invariant mass from 2.7 to 3.5 GeV/ c^2 . Figure 3 shows even $p+p$ collisions, 72% of J/ψ candidate events have one or more track(s) in central arm. From the ratio, contamination from most peripheral J/ψ is estimated as 2.8 events. The expected invariant mass spectrum with the most peripheral contamination is shown in Fig 4. Three most peripheral events wrongly get mixed in with the dimuon UPC events.

3. result

The J/ψ invariant cross section is determined by corrections of the detection and trigger efficiencies. Figure 6 shows the preliminary results of the p_T distribution of the J/ψ cross section in UPC, where circle, triangle and square symbols correspond to the cross sections at mid-rapidity with one neutron tagged by ZDC, $-2.2 < y < -1.2$ and $1.2 < y < 2.2$ with two neutron tagged at both sides of ZDC, respectively. From Fig. 7, The cross section at mid-rapidity in low p_T is very large compared to that at forward-rapidity. This is due to the dominance of the coherent J/ψ production at low p_T in mid-rapidity, while the incoherent production is dominant at forward rapidity.

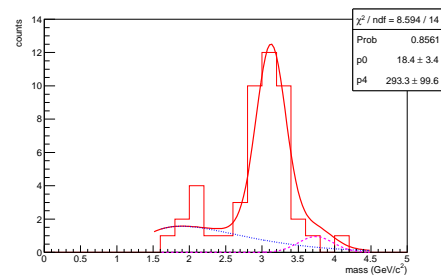


Figure 1. 2010 North arm (dimuon) invariant mass yields.

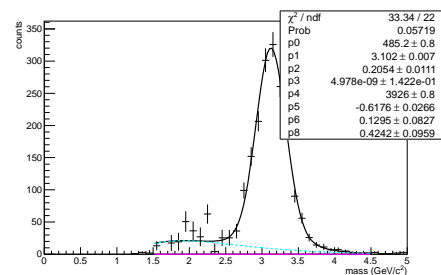


Figure 2. 2009 North arm (dimuon) invariant mass yields.

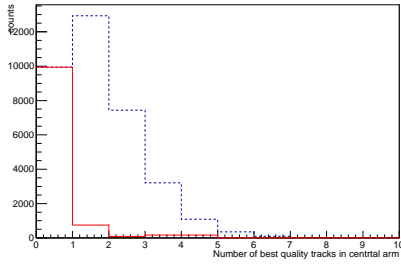


Figure 3. Comparison between multiplicity distribution for central rapidity in UPC and p+p(ncoll=1, dot line) collisions with dielectron with the invariant mass between 2.7 and 3.5 GeV/c^2

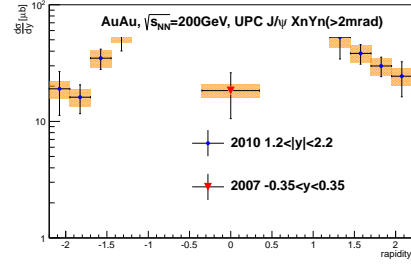


Figure 7. PHENIX 2010 RUN UPC J/ψ $\frac{d^2\sigma}{dy}$ distribution background in detail.

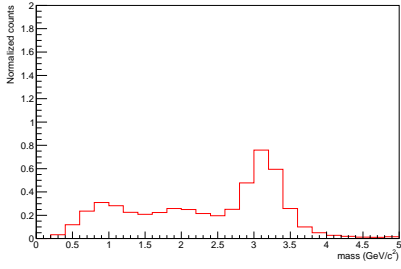


Figure 4. Expected contamination from most peripheral

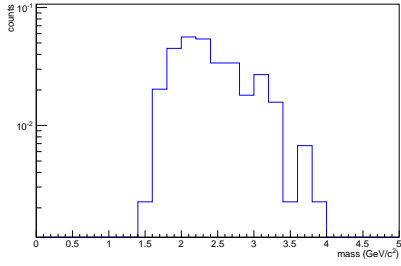


Figure 5. expected contamination form $\gamma\gamma$

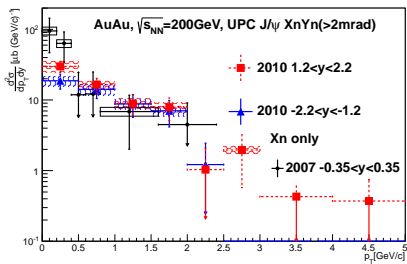


Figure 6. PHENIX 2010 dimuon (tringle and square) and 2007 dielectron(circle) UPC J/ψ $\frac{d^2\sigma}{dp_T dy}$. Dielectron distribution has significant significant entries in low p_T , which cannot be seen at forward rapidity.

Figure 7 shows the cross section as a function of y , where both side neutrons are tagged. The comparison with the theoretical calculations is underway.

4. Summary and Outlook

The J/ψ production in UPC has been estimated by using 2010 data. As same as HERA $\gamma p \rightarrow J/\psi$ measurement, the bacground contribution can't be explained by $\gamma\gamma$ process. The statistics is too low to discuss the origin of the

References

- [1] G. Baur, K. Hencken, D. Trautmann, S. Sadovsky, Y. Kharlov, Phys. Rept. **364** (2002) 359-450.
- [2] C. A. Bertulani, S. R. Klein, J. Nystrand, Ann. Rev. Nucl. Part. Sci. **55** (2005) 271-310.
- [3] A. J. Baltz, *et al.*, Physics Report **458** (2008) 1-171
- [4] J. Nystrand, Nucl. Phys. A **752**(2005)470c; A.J. Baltz, S.R. Klein, J. Nystrand, Phys. Rev. Lett. **89** (2002) 012301; S.R. Klein, J. Nystrand, Phys. Rev. C **60**(1999)014903.
- [5] S. Chekanov *et al.*, Eur. Phys. J. C **24**,(2002) 345-360

Accelerator and Instrumentation

Ion back flow study for the ALICE GEM-TPC upgrade

Y.L. Yamaguchi, H. Hamagaki, and T. Gunji, on behalf of the ALICE-TPC group

Center for Nuclear Study, Graduate School of Science, University of Tokyo

1. Introduction

The Time Projection Chamber (TPC) is one of the main tracking detectors at the ALICE experiment. The ALICE-TPC upgrade is scheduled in 2018 to precisely measure rare probes such as heavy quarks, thermal di-leptons and direct photons in a wide-ranging p_T region. In order to realize these measurements with 50 kHz Pb-Pb collisions expected after 2019, TPC is required a downtime-less readout with preserving the current resolutions of dE/dx and momentum in addition to improvement of vertex and momentum resolutions by the Inner Tracking System (ITS) upgrade. The current TPC employs proportional wires for signal amplification and a gating grid is used to prevent ion back flow (IBF) to the drift region since IBF brings on field distortion in the drift region. Thus, the current readout rate is limited by the operation rate of the gating grid.

A replacement of proportional wires with Gas Electron Multipliers (GEMs) [1] is a possible solution to realize a continuous readout without a downtime due to the gating grid since GEM has an intrinsic capability of IBF blocking. A typical GEM consists of a $50 \mu\text{m}$ insulator foil coated by $5 \mu\text{m}$ metal layers at both sides and $70 \mu\text{m}$ holes are regularly aligned with a $140 \mu\text{m}$ pitch. When an electron cascade is induced by a strong electric field inside a hole, ions generated with electrons move along lines of electric force due to their low mobility and some of them are finally absorbed by the GEM electrode. For the GEM-based TPC, less than 0.25% of IBF is required with gain of 2000 in Ne/CO₂ (90%/10%) to realize a downtime-less readout.

The development of the GEM-TPC has been proceeded as one of the major ALICE upgrade projects, and extensive R&D efforts are being made. We have charge on investigating an optimal condition for GEMs to achieve the required IBF value through both measurements and simulations. In this report, the current status of the IBF study as a part of the GEM-TPC upgrade project for ALICE is reported.

2. IBF study

2.1. Measurement setup

A schematic view of the IBF measurement setup is shown in Fig. 1. The measurements were conducted with a triple GEM stack configuration to suppress IBF effectively. A drift plane is mounted 80 or 3 mm above the top GEM. The transfer regions between the neighboring GEMs (T1, T2) and the induction region between the bottom GEM and readout pads are 2 mm. High voltages were supplied to the drift plane and GEM electrodes via individual channels. The field in the drift region, E_d was kept at 0.4 kV/cm during the measurements. X-rays were injected from the top of the chamber and the X-ray beam source is Amptek Mini-X tube with a Ag target. The electron and ion currents were monitored by the floating ammeters attached with the readout pads and the drift plane, respectively. The currents at the GEM electrodes were also monitored to confirm if the electron current sum is canceled out by the ion current sum. The Ar/CO₂ (70%/30%) mixture gas was flushed into the chamber with about 300 ml/hr. IBF is calculated by $(I_d - I_0)/I_p$, where $I_{d,p}$ indicate currents at the drift plane and pads, re-

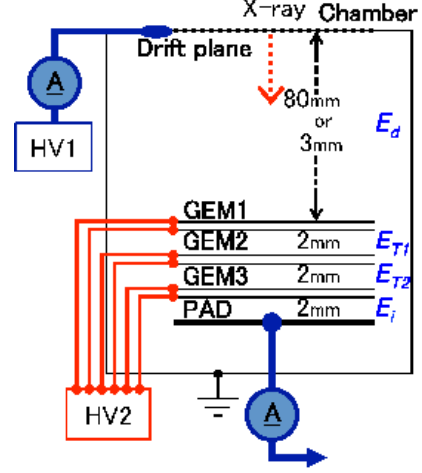


Figure 1. A schematic view of the IBF measurement setup.

spectively. I_0 is the primary ion current.

2.2. Rate dependence of IBF with different drift lengths

First, the X-ray rate dependence of IBF was explored. During the measurements, the voltage difference of GEMs, ΔV_{GEM} was kept at 360 V with the effective gain of about 10^4 and the electric fields in the transfer and induction regions, $E_{T1,T2,i}$ were 3.0, 3.5 and 5.0 kV/cm, respectively. The X-ray rate was varied using several filters to cover a wide range of the pad current, and the beam spot at the top GEM surface was estimated 0.9 cm in diameter.

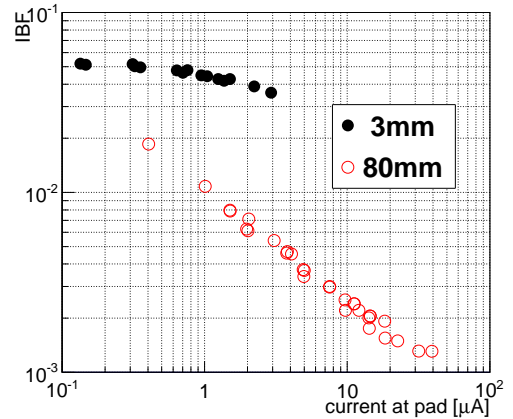


Figure 2. The X-ray rate dependence of IBF as a function of the current at the pads with 3 mm and 80 mm drift lengths.

Figure 2 shows the X-ray rate dependence of IBF as a function of the current at the pads with 3 mm and 80 mm drift lengths. The closed and open symbols show the results with 3 mm and 80 mm drift lengths, respectively. The results show the clear X-ray rate dependence of IBF possibly due to the space charge effect. Surprisingly they also show the different behaviors with 3 mm and 80 mm drift lengths, *i.e.* IBF with 80 mm drift length is much smaller and has steeper rate dependence compared to that with 3 mm drift length.

Only the difference between 3 mm and 80 mm drift length data is the space charge density in the drift region. The simulation using Garfield++ [2] was made for qualitative understanding of the space charge effect on IBF. A single GEM was simulated by varying a drift length with a static charge density and the fields above and below the GEM are 0.4 and 3.0 kV/cm, respectively. The simulated space charge density, ρ dependence of IBF with 3 mm and 80 mm drift lengths is shown in Fig. 3. The closed and open symbols

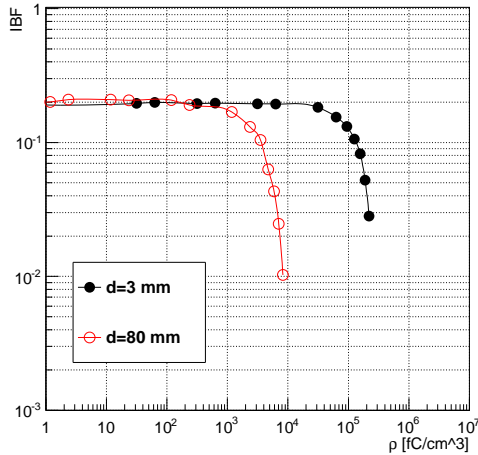


Figure 3. The space charge density dependence of IBF.

indicate 3 mm and 80 mm results, respectively. IBF drops dramatically at $\rho = 10^3$ fC/cm³ with 80 mm drift while IBF with 3 mm drift can keep flat until $\rho = 3 \times 10^4$ fC/cm³. Considering the ion velocity in Ar/CO₂ (70%/30%), the space charge densities for the measured data correspond to $\rho \sim 10^4 - 10^5$ and $10^3 - 10^4$ with 3 mm and 80 mm drift lengths, respectively. The space charge enhances ion blocking with 80 mm drift length, not with 3 mm drift length. The space charge effect does not matter with the actual ALICE experimental condition because of a small ρ .

2.3. Hole alignment

Another important achievement of the simulation study is quantitative evaluation of the hole alignment effect on IBF. If hole positions are mis-aligned between the neighboring GEMs, some lines of electric force from a hole of the lower GEM terminate at the bottom electrode of the upper GEM. Thus, the ion absorption efficiency at the bottom electrode depends on the degree of hole alignment between GEMs. A triple GEM stack was simulated with Ne/CO₂ (90%/10%) and $E_{d,T2,i}$ are 0.4, 0.5, 4.0 kV/cm, respectively. The hole alignment between GEM1 and GEM2 was varied with $E_{T1} = 1, 2, 4$ kV/cm and the holes of GEM2 and GEM3 were perfectly aligned. Figure 4 shows the IBF variation with different hole alignments between GEM1 and GEM2 for $E_{T1} = 1, 2, 4$ kV/cm. The distance between holes is defined as a distance between hole centers of GEM1 and GEM2 projected to the GEM plane. The square, open and closed circle symbols show the results with $E_{T1} = 1, 2, 4$ kV/cm, respectively. IBF can be improved with a larger hole distance for $E_{T1} > 1$ kV/cm. With the complete mis-alignment, IBF reaches more than 10 times better for $E_{T1} = 4$ kV/cm than that for $E_{T1} = 1$ kV/cm.

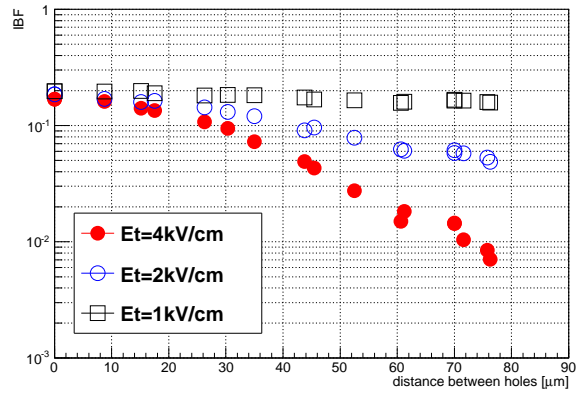


Figure 4. The IBF variation with different hole alignments between GEM1 and GEM2.

3. Summary and outlooks

The IBF suppression capability of GEM has been investigated through both measurements and simulations as a part of the ALICE GEM-TPC upgrade project. A better IBF and stronger X-ray rate dependence of IBF were observed with a larger drift length for ions. It was figured out by the simulation that the space charge density in the drift region enhances ion blocking more with a larger drift length. The hole mis-alignment of the neighboring GEMs can lead to better IBF with higher than 1 kV/cm since the ion absorption efficiency at the bottom electrode becomes higher due to increase of lines of electric force terminating at the bottom electrode from holes of the lower GEM.

Intensive efforts for development of the GEM-TPC are being made including development of an exotic GEM [3] specially designed for better IBF suppression than the standard GEM. The required IBF will be achieved with the optimal condition of GEMs.

References

- [1] F. Sauli, Nucl. Instr. and Meth. A **386**, 531 (1997).
- [2] Garfield++: <http://garfieldpp.web.cern.ch/garfieldpp/>.
- [3] K. Terasaki, *et al.*, CNS Annual Report (2013)

Study of ion back flow suppression with thick COBRA GEM

K. Terasaki, H. Hamagaki, T. Gunji, and Y.L. Yamaguchi

Center for Nuclear Study, Graduate School of Science, University of Tokyo

1. Introduction

Ion Back Flow (IBF) causes severe performance limitations for tracking detectors such as the Time Projection Chamber (TPC), especially under high rate and high multiplicity conditions because it distorts the electric field in the drift space and consequently leads to a worse position resolution. A typical solution for the problem is adopting a gating grid operation. Although the gating grid prevents IBF, it limits a readout rate due to a dead time. ALICE-TPC [1] is planning to record Pb-Pb collisions continuously at the rate of 50 kHz after the long shutdown of LHC in 2018. The requirement of IBF is less than 0.25% at gain ~ 2000 in Ne/CO₂ (90/10). One possible solution to meet the requirement is the Gas Electron Multiplier (GEM), which is a type of micro pattern gaseous detectors because GEM has a good IBF blocking capability.

The structure of a standard GEM is a 50- μm -thick insulator sandwiched by 5- μm -thick copper foils with 70 $\mu\text{m}\phi$ holes in 140 μm pitch. When high voltage is applied between GEM electrodes, an electron avalanche occurs owing to the high electric field inside holes. Ions going to the drift region can be blocked by the GEM electrodes. Furthermore, a multi-layer structure can make IBF suppression more efficiently. We have developed COBRA GEM [2], which is specially designed to achieve better IBF suppression compared to a standard GEM. Its performance is being studied for application to the GEM-based TPC. In this report, the current status of development of COBRA GEM is described.

2. Thick COBRA GEM

Figure 1 shows a microphotograph of the COBRA GEM surface and a schematic view of a cross section. It was originally developed by F.D. Amaro *et al.* [3]. COBRA GEM is characterized by a double electrode pattern on both sides. By creating a voltage difference between these two COBRA electrodes, ΔV_{gap} , ions can be efficiently absorbed. We define $\Delta V_{\text{gap}} \equiv V_{\text{in}} - V_{\text{out}}$, where $V_{\text{in,out}}$ are the voltages applied to inner and outer COBRA electrodes, respectively. Illustrations of ion absorption at the COBRA electrodes calculated by Garfield [4] are given in Fig. 2. The left and right panels of Fig. 2 show the results for $\Delta V_{\text{gap}} = 100$ and

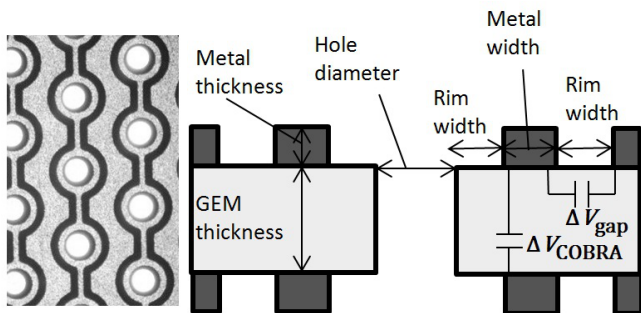


Figure 1. A microphotograph of COBRA GEM surface (left). Cross-section drawing of COBRA GEM (right).

calculated by Garfield [4] are given in Fig. 2. The left and right panels of Fig. 2 show the results for $\Delta V_{\text{gap}} = 100$ and

Table 1. The geometries of COBRA GEMs.

Insulator thickness (μm)	Hole pitch (mm)	Hole Diameter (μm)	Rim width (μm)	Metal width (μm)
200	0.5	150	50	50
400	1.0	300	100	100

300 V at $\Delta V_{\text{GEM}} = 1200$ V, where ΔV_{GEM} is the voltage between upper and lower electrodes. Ions are generated below the COBRA GEM structure and drift upward. At $\Delta V_{\text{gap}} = 100$ V, a large number of ions still flow into the drift space. On the other hand, most of ions passing through the hole are absorbed by the outer COBRA electrode at $\Delta V_{\text{gap}} = 300$ V because more electric lines of force go toward the outer COBRA electrode.

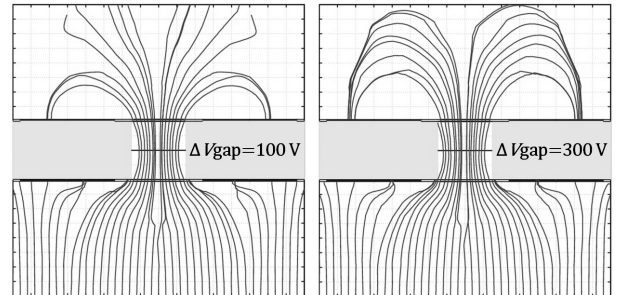


Figure 2. Illustrations of ion absorption at the COBRA electrodes calculated by Garfield. Ions drift upward from the bottom of the figures.

In collaboration with SciEnergy Co., Ltd. [5], we have developed prototype COBRA GEMs with two different thickness; 200 and 400 μm -thick. The geometries of them are given in Table 1. The glass epoxy laminate (FR5) is employed as an insulator, and 6 μm -thick copper layers cover in an active area of $3 \times 3 \text{ cm}^2$. The holes were pierced by a drill and the patterns on the COBRA electrodes were produced by a wet etching technique.

3. Measurement Setup

Figure 3 shows a schematic view of the measurement setup. The chamber is filled up with Ar/CO₂ (70/30) or Ne/CO₂ (90/10) at atmospheric pressure and the X-ray beam is injected perpendicular to the surface of COBRA GEM. The induction length between the multiplication region and the $3 \times 3 \text{ cm}^2$ readout pad is 2 mm. The electric fields in the drift and induction regions, $E_{d,i}$ are 0.4 kV/cm and 3 kV/cm, respectively. In the single COBRA configuration (Fig. 3(a)), we put one COBRA GEM in multiplication region and set 3 mm for the drift length between the mesh and the multiplication region. The measurements with the stack configuration (Fig. 3(b)) were also carried out. Two standard GEMs were placed below the 400 μm -thick COBRA GEM in the multiplication region and the drift length was extended to 7 mm. The electric field in the transfer region between the COBRA GEM and the upper standard GEM, E_{t1} is 0.4 kV/cm, and that between the

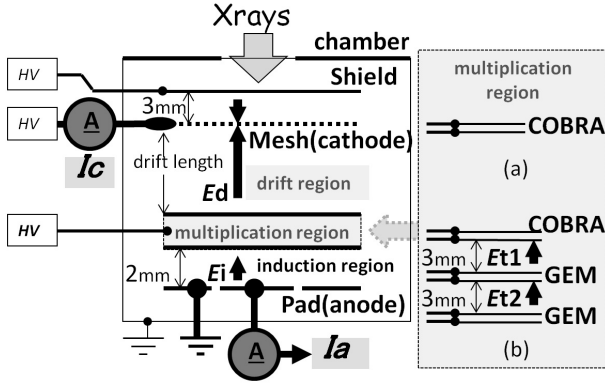


Figure 3. A schematic view of the measurement setup: (a) the single COBRA configuration, (b) the stack configuration.

standard GEMs, E_{i2} is 1.0 kV/cm.

4. Results

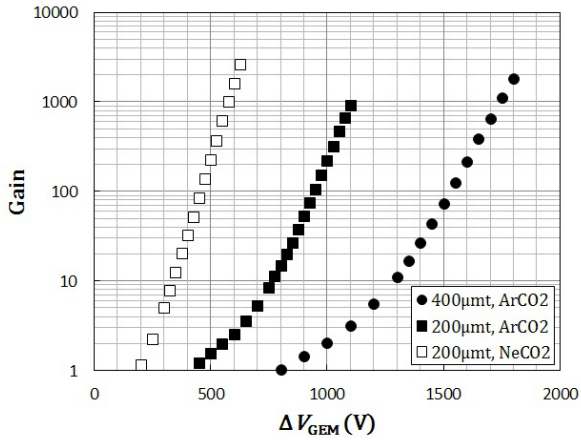


Figure 4. The gain as a function of ΔV_{GEM} for the 200- μm -thick and 400- μm -thick COBRA GEMs with Ar/CO₂ (70/30) and Ne/CO₂ (90/10).

Figure 4 shows the gain with the single COBRA configuration as a function of ΔV_{GEM} . Open and closed squares represent the data for 200- μm -thick COBRA GEM with Ne/CO₂ (90/10) and Ar/CO₂ (70/30), respectively. Closed circles show the 400- μm -thick COBRA GEM data with Ar/CO₂ (70/30). The gain of single COBRA GEM increases exponentially as ΔV_{GEM} increases and can reach more than 10^3 . It is consistent with the result with a 400- μm -thick GEM [6]. It indicates the proper multiplication of electrons.

Figure 5 shows the gain and IBF with the stack configuration as a function of ΔV_{gap} . We define $(\text{IBF}) \equiv (I_c - I_c^0)/I_a$, where I_c and I_a are the electric currents at the mesh and the pad due to ion and electron flows, respectively. I_c^0 is the primary ion current. ΔV_{GEM} of the COBRA GEM and each standard GEM are kept at 1200 and 425 V during this measurement. The tube current is the electric current of the X-ray tube, proportional to the X-ray rate. Open and closed circles represent the results with 0.3 mA and 3 mA tube currents, respectively. IBF can be more suppressed with a higher ΔV_{gap} . IBF improves by a factor of 10 compared to the result with a triple-standard-GEM stack of $\sim 2\%$ IBF at gain ~ 2000 . It indicates that the voltage difference between two COBRA GEM electrodes encourages ion absorption as expected by the simulation. It also shows that

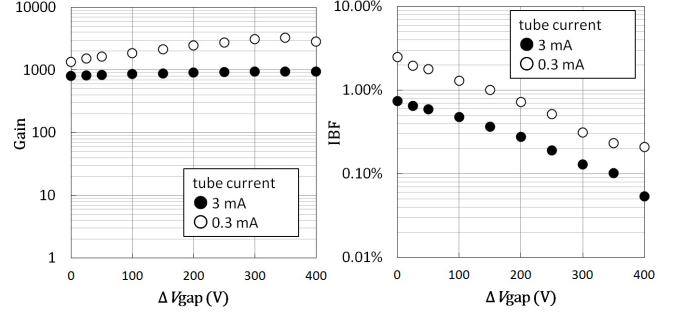


Figure 5. The gain and IBF as a function of ΔV_{gap} of 3 mA tube current (closed) and of 0.3 mA tube current (open).

there is a rate dependence and a higher rate leads more IBF suppression.

5. Summary and outlooks

We have successfully developed COBRA GEMs with two different geometries. The gain with the single COBRA GEM configuration reached to more than 10^3 and the COBRA GEM achieved 10 times better IBF suppression compared to the standard GEM. The optimization for IBF suppression are being studied. We are going to evaluate gain stability and energy resolution. In addition, we are developing a 100- μm -thick COBRA GEM without rim.

References

- [1] ALICE (A Large Ion Collider Experiment, CERN): F. Carminati *et al.*, J. Phys. G: Nucl. Part. Phys. **30** (2004) 1517-1763.
- [2] J.F.C.A. Veloso *et al.*, Nucl. Instr. and Meth. A **639** (2011) 134-136.
- [3] F. D. Amaro *et al.*, JINST **5** (2010) P10002.
- [4] Garfield (simulation of gaseous detectors) web page <http://garfield.web.cern.ch/garfield/>.
- [5] SciEnergy Co., Ltd. <http://www.scienergy.jp/>.
- [6] C. Shalem *et al.*, Nucl. Instr. and Meth. A **558** (2006) 475.

Performance test of the wide-dynamic-range ASIC for W+Si calorimeter

S. Hayashi, H. Hamagaki, T. Gunji, M. Tanaka^{a,c}, and H. Ikeda^{b,c}

Center for Nuclear Study, Graduate School of Science, University of Tokyo

^a High Energy Accelerator Research Organization

^b Japan Aerospace Exploration Agency

^c Open Source Consortium of Instrumentation

1. Introduction

ALICE is one of the experiments at CERN-LHC and it is dedicated for relativistic heavy-ion collisions. The study of the parton distribution function (PDF) in nuclei is essential to determine the initial condition of relativistic heavy-ion collisions. Since the bulk properties like the shear viscosity η/s depend on the initial condition of collisions [1], investigation of the initial state of collisions is crucial for studying the properties of the matter created in relativistic high energy collisions. However there are still large uncertainties regarding the gluon PDF at small values of Bjorken- x ($10^{-5} < x < 10^{-3}$) and the small momentum transfer scale Q^2 (\sim a few GeV^2). x is the longitudinal momentum fraction carried by partons inside a nucleon. In such a small x and small Q^2 region, the gluon density is expected to be extremely high and eventually to be saturated [2]. For $2 \rightarrow 2$ parton scattering like gluon Compton scattering, the incoming partons' x is determined by the transverse momentum and the rapidity of the outgoing partons. When the outgoing particles are measured at the same rapidity y , $x \sim x_T e^{-y}$ can be accessed, where $x_T = 2p_T/\sqrt{s}$.

Installation of the electromagnetic calorimeter covering $3.3 < \eta < 5.0$ (FOCAL) in the ALICE experiment is currently under consideration. FOCAL is intended to measure prompt γ , π^0 up to a transverse momentum of 50 GeV/c , and jets covering the range of $10^{-5} < x < 10^{-3}$ and $Q^2 = 1\text{--}1000 \text{ GeV}^2$. At high p_T , high granularity is required to separate prompt γ from π^0 because the opening angle of 2γ from a high $p_T \pi^0$ is very small and showers are merged. FOCAL consists of three longitudinal segments and each segment has seven layers of W + Si pad modules. More detailed design of FOCAL is described in Ref. [3].

The signal from the Si pad is summed up longitudinally at each segment. The front-end circuits for FOCAL are needed to cover a wide dynamic range since FOCAL is assumed to measure both MIP and the energy of γ up to 500 GeV . To cope with such a wide dynamic range, the front-end ASIC with different gain current conveyors has been developed. The integrated dynamic range of the ASIC is 5×10^3 . In this report, the basic performance of the ASIC fabricated for FOCAL is described.

2. Fabrication of CALFE01 chip

Parameter	Value
Dynamic range	50 fC - 200 pC
ENC	$< 3 \times 10^4 e^-$
Cross talk	$< 1 \%$
Trigger generation	$< 650 \text{ ns}$ from collisions

Table 1. Requirements of front-end circuits for FOCAL

The main requirements of the readout for FOCAL are summarized in Table 1. The dynamic range of the signal

varies from 50 fC to 200 pC and our ASIC is designed to cope with a wide dynamic range of the order of 10^4 . Furthermore FOCAL has to generate an event trigger within 650 ns. As shown in Fig. 1, the first stage of our ASIC is composed of a current conveyor with four different gain outputs (1/512, 8/512, 64/512, and 256/512) [4]. Another output with a gain of 128/512 is used to generate a fast trigger. Equivalent Noise Charge (ENC) corresponds to 2.19×10^4 in the SPICE simulation. The detail study with the SPICE simulator is described in Ref. [5].

The ASIC also contains shaping amplifiers, analog memory cells (AMC), analog buffer and multiplexer for the serial readout. Designing and simulation studies were carried out in the collaboration with the OpenIT project [6]. The

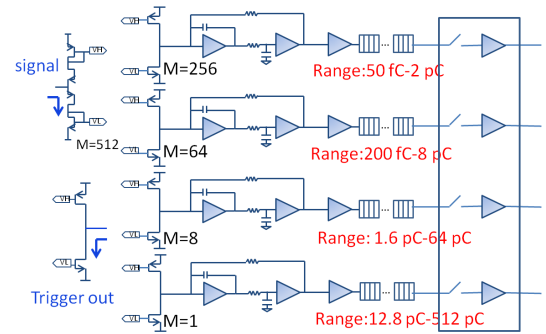


Figure 1. The schematic of one readout channel for FOCAL.

prototype chip (CALFE01) which has 6 readout channels was fabricated with $0.25 \mu\text{m}$ technology by UMC company. The power consumption of the ASIC is 15 mW for the analog part and 1.5 mW for the digital part per channel, respectively.

3. Performance test for CALFE01

The basic performance test of CALFE01 such as linearity and uniformity was carried out with a test board for CALFE01. The test board has a QFP socket for CALFE01 and FPGA for the operation of the digital part. Figure 2 shows the transient response of the trigger output port for the input charge of 200 pC. The output was terminated with a 50Ω resistance. The rising time of the output pulse was 10 ns equal to that of the input pulse. A good time response which fulfills the fast trigger generation was obtained. Figures 3 shows the channel dependence of nonlinearity at the shaper output in the chip. Although the variation was wider for a smaller input charge, the averaged nonlinearity was about 1% or less for all measured range. Uniformity of the 30 channels from 5 chips corresponding to 1σ was less than 1% for a whole range.

Figure 4 shows the pulse shape of a single channel readout of AMC. AMC has 32 levels of depth and is operated with 5-10 MHz and 5 MHz for writing and reading, respectively. An analog signal sampled by AMC is serialized in

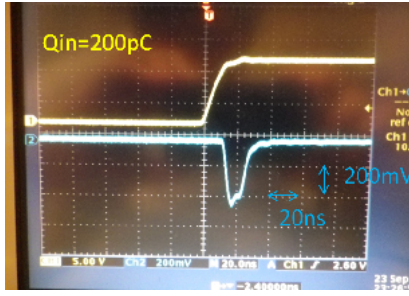


Figure 2. Transient response of the trigger output when an input charge is 200 pC. The upper line shows the input pulse. The lower line shows the pulse shape of the trigger output.

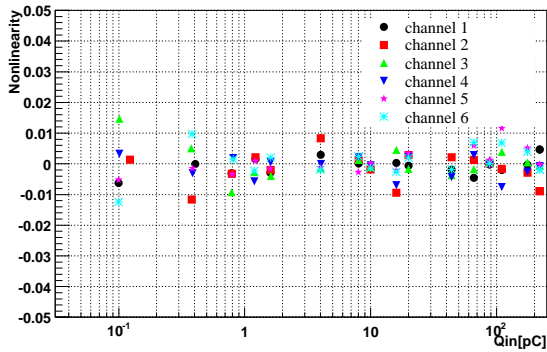


Figure 3. Channel dependence of nonlinearity in one chip at shaper output

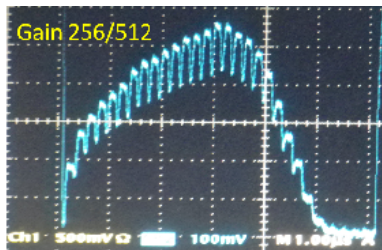


Figure 4. Transient response of a single channel AMC output. An input charge is 2 pC. Writing clock: 20 MHz, Readout clock: 5 MHz

each gain. The readout direction is opposite to the direction of writing. The pulse height at AMC decreased by factor of 3 compared with the output at the shaper. It indicates that a leakage of charges happens in writing or reading of AMC. Figure 5 shows the pulse height and nonlinearity at the AMC output. Nonlinearity was less than 1% in the whole range. However, the gains were lower than expected. It can be explained by a loss of a signal due to interference with the next channels when the signals from AMC are readout. This interference is caused by an insufficiency of the capacitance of the delay circuit preventing from simultaneous connection of 2 cells in AMC to the output. Although the simulated interference time is less than 0.5 ns, this interference must affect the lower gains.

4. Summary and Outlooks

The 6-channel prototype ASIC for FOCAL was fabricated and its basic performance was checked. Nonlinearity is within 1% up to 200 pC. A good time response which

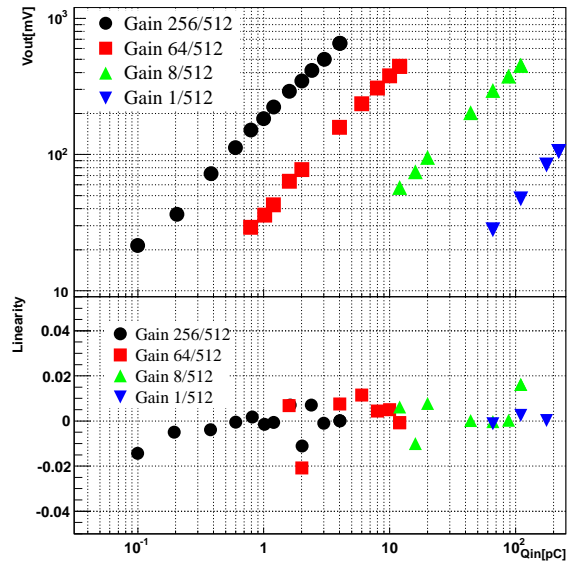


Figure 5. Upper panel: Pulse height at AMC output. Lower panel: Non-linearity at AMC output.

fulfills the requirements for a fast trigger generation is also obtained. AMC operation was checked and gain at AMC output is lower than that of shaper output due to interference between neighboring cells in analog memory.

As a next plan, more detailed studies such as noise performance and input bias current dependence will be executed. Overall performance with FOCAL will be checked.

References

- [1] A. Adare *et al.*, arXiv:1105.3928.
- [2] L.D. McLerran and R. Venugopalan, Phys. Rev. D **49** (1994) 2233.
- [3] Y. Hori *et al.*, J. Phys. Conf. Ser. **293** 012029 (2011).
- [4] K. Koli *et al.*, Helsinki University of Technology Electronic Circuit Design Laboratory Report **30**, Espoo 2000
- [5] S. Hayashi *et al.*, CNS Annual Report 2011 53.
- [6] <http://openit.kek.jp/>

The design and development of SOI pixel detector for radiation monitor

Y. Sekiguchi, H. Hamagaki, T. Gunji, Y. Arai^a, T. Imamura^b, T. Ohmoto^b, and A. Iwata^b

Center for Nuclear Study, Graduate School of Science, University of Tokyo

^aKEK

^bA-R-Tec Corp.

1. Introduction

We have developed a prototype of SOI pixel (SOIPIX) for radiation monitor, called RADPIX, with the silicon-on-insulator (SOI) pixel CMOS technology. SOIPIXs are monolithic pixel detectors which include a thin CMOS readout array (5 μm), a buried oxide layer (insulator; 200 nm), and a thick high-resistivity Si-sensor (FZ n-type; 500 μm) vertically on a single chip [1] (see Fig.1). RADPIX aims to count the rate of the radiation and to visualize the hit pattern in real time. From the hit pattern, one can estimate the radiative source such as beta-ray, γ -ray, α -ray, and so on. RADPIX has two characteristics, one of which is that it has the leakage compensation circuit in each pixel, and the other is that both analog and digital output can be read for each pixels. The design of the RADPIX and the simulation result are described in this report.

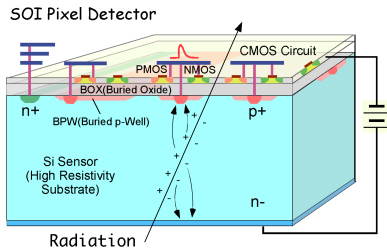


Figure 1. Cross sectional view of the SOI pixel detector

2. Design of RADPIX

2.1. chip specifications

RADPIX was fabricated in 0.2 μm CMOS fully depleted (FD-)SOI pixel process by Lapis Semiconductor Co. Ltd. [2]. It is 2.9 mm \times 2.9 mm in size and consists of 32 \times 32 pixels. The pixel size is 40 μm \times 40 μm , so the effective sensing area is 1.28 mm \times 1.28 mm. The microscope photo of RADPIX and block diagram are shown in Fig. 2. For the sake of comparison and evaluation, the chip contains four different types of test element group (TEG) pixels, a simple source follower (SF) type and three charge sensitive amplifier (CSA) types.

2.2. Pixel Circuit

Figure 3 shows the schematic of the pixel circuit of SF type (upper) and CSA type (bottom) pixels. For the simple SF type, the signal is processed through source follower from the sensor node. The signal goes into comparator to generate digital and is stored in the store capacitor. A NMOS device (M1) connected to the sensor node is used as for the comparator reset and also as the leakage compensation device. In other words, M1 is used in saturation region during the reset term and in weak inversion region during the exposure term by modulating the gate voltage. The SF type is very simple and unique structure providing both continuous reset and leakage current compensation. The pixel size of 40 μm \times 40 μm has about 7 pA leakage current at room temperature. To reduce transistor threshold voltage

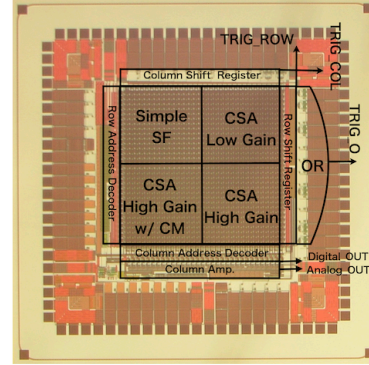


Figure 2. RADPIX chip photograph and block diagram. The chip size is 2.9 mm \times 2.9 mm.

variability and noise, a transistor of $L=10\ \mu\text{m}$ and $W=1\ \mu\text{m}$ is used for M1. The CSA type employs the Krummenacher feedback [3]. It has been used in many applications for X-ray imaging and particle tracking detector systems. There are three different types of CSA, Low gain (5 fF feedback capacitor), High gain (1 fF feedback capacitor), and High gain with current mirror (CM). We used a short transistor width of M1' and M2' (0.5 μm) to reduce the equivalence resistance and a long transistor of M3 to reduce noise. The feedback structure used the transistor in weak inversion and the drain current is very sensitive to the variability of the gate voltage. For the high gain with CM type, the bias voltage is made in each pixel with CM to reduce the variability in the pixel-by-pixel. Two inverter-chopper type comparators are used to detect signal level and generate a digital output. The reason for using two inverter stage is to get a sharp threshold. This comparator contains a cascade of inverter stages which is essentially a bistable multivibrator [4]. The comparator output is latched with SR latch circuit and also delayed to store the analog signal.

2.3. Simulation result

Figure 4 shows the output voltages as a function of the number of input electrons for the simple SF type and the low gain and high gain CSA type. The gain of the simple SF type is expected to be about 10 $\mu\text{V}/\text{electron}$, that of the low gain CSA is 30 $\mu\text{V}/\text{electron}$, and that of the high gain CSA type is 100 $\mu\text{V}/\text{electron}$ at the SF/CSA output node. Figure 5 shows the frequency response of the circuit for the SF/CSA output node, the comparator input node, the store node, and the analog output node in pixel. The 3 dB bandwidth of the simple SF type is 7 MHz, that of the low gain CSA is 70 kHz, and that of the high gain CSA is 48 kHz. Because RADPIX indicates the low-count-rate readout, it is preferable to suppress the variability transistor threshold or the noise than to pursue the readout speed. At the SF/CSA output node, the noise of SF output for the simple SF type is 1.4 mV. The noise of CSA output for the low gain type and the high gain type are 1.4 mV and 2.8 mV, respectively. The

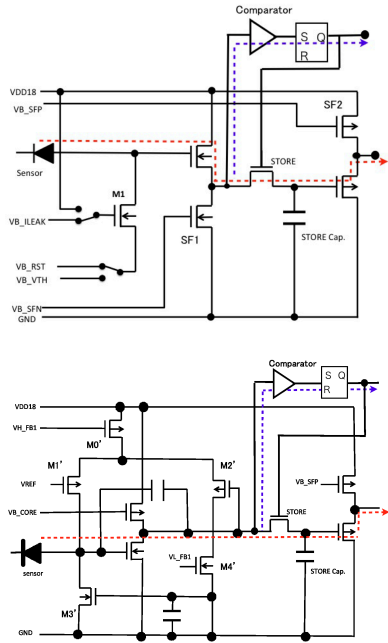


Figure 3. Upper: The Pixel circuitry of RADPIX for the simple SF circuit. Bottom: That for the CSP circuit. Blue and red lines show the digital and the analog process, respectively.

comparator input node seems to have large noise at low frequency because this simulation does not include body floating effect elements (Fig. 6). These results shown in Fig.4-6 are simulated with normal threshold NMOS (PMOS) transistor and at room temperature.

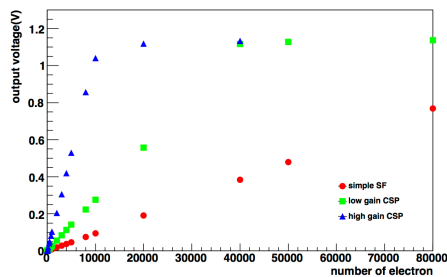


Figure 4. The output voltage as a function of the number of input electrons.

3. Summary and outlook

We have developed a prototype of SOIPIX for radiation monitor, called RADPIX. The Simple SF type and three CSA types have been fabricated in this chip.

We will evaluate the basic performance of the chip, such as gain and noise. The spectra with X-ray and cluster analysis will also be measured.

References

- [1] Y. Arai *et al.*, Nucl. Instrum. Methods sect. A **636** Suppl. 1 (2011) S31-S36.
- [2] Lapis Semiconductor Co. Ltd. <http://www.lapis-semi.com/en/>.
- [3] F. Krummenacher, Nucl. Instrum. Meth., vol. 305, pp. 527-532, 1991.
- [4] R. Gregorian and G. C. Temes, Analog MOS Integrated

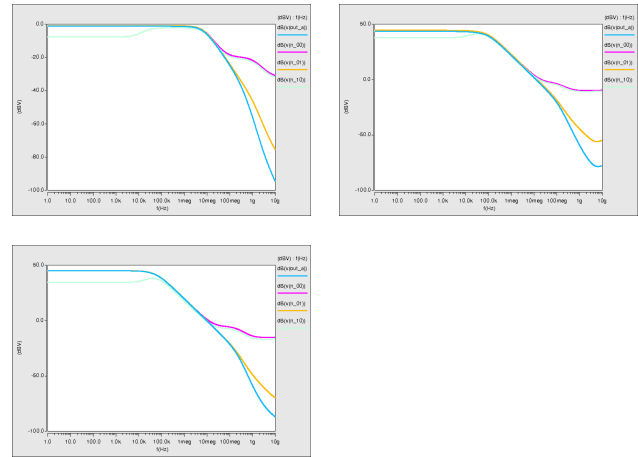


Figure 5. Frequency response of circuit: the simple SF (upper left), the low gain CSA (upper right), and the high gain CSA (bottom).

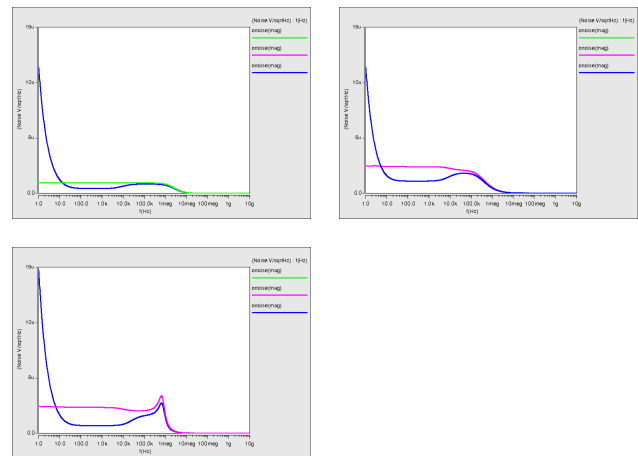


Figure 6. Noise value as a function of the frequency: the simple SF (upper left), the low gain CSA (upper right), and the high gain CSA (bottom).

Circuits for Signal Processing. Hoboken: A Wiley-Interscience Publication, 1986, pp. 425-437.

Performance evaluation of CAT through the measurement of $d(^{14}\text{O},d)$ reaction

S. Ota, H. Tokieda, A. Corsi^a, M. Dozno^b, J. Gibelin^c, T. Gunji, H. Hamagaki, T. Kawabata^d, S. Kawase, S. Kubono^b, Y. Kubota, C.S. Lee, Y. Maeda^e, H. Matsubara^b, Y. Matsuda^d, S. Michimasa, T. Nakao, T. Nishi^f, A. Obertelli^a, K. Okochi^f, H. Otsu^b, T. Ryan, C. Santamaria^a, M. Sasano^b, M. Takaki, Y. Tanaka^f, T. Uesaka^b, K. Yako, H. Yamaguchi, J. Zenihiro^b, E. Takada^g

Center for Nuclear Study, Graduate School of Science, University of Tokyo

^a *Service de Physique Nucléaire (SPhN), CEA-Saclay*

^b *Nishina Center for Accelerator-Based Science, RIKEN*

^c *LPC^d Department of Physics, Kyoto University*

^e *Department of Applied Physics, Miyazaki University*

^f *Department of Physics, the University of Tokyo*

^g *HIMAC, NIRS*

The supernova nucleosynthesis is one of the attractive subjects of nuclear astrophysics. In the supernova nucleosynthesis various nuclei from the iron-group to the uranium are produced in the very short period. In this process the electron capture rates are important parameter [1]. To extract the electron capture rates, we need the Gamow-Teller transition strength (B(GT)) distribution, especially of the iron-group nuclei. The nuclear reactions of (n,p)-type charge exchange can provide us the distribution up to highly excited region where β -decay can not access, while the measurement of β -decay gives the absolute value of B(GT) to the low-lying states below the electron capture threshold. As a (n,p)-type reaction we try to utilize $(d,^2\text{He})$ reaction because of its selectivity.

Another attractive subject is the equation-of-state (EoS) of nuclear matter [2]. In the EoS there are some parameters such as incompressibility and symmetry energy. The incompressibility of 230 MeV was deduced for symmetric nuclear matter from the systematics of excitation energy of Isoscalar Giant Monopole Resonance (GMR). On the other hand, there is little information on the symmetry energy. The measurements of GMR and/or dipole resonances in the neutron-rich nuclei are desired.

In these studies, we need to deduce spectra up to highly excited states and to measure the forward-angle scattering in center-of-mass frame. The highly excited states populated via charge-exchange reactions or inelastic scattering decay mainly by particle emission sometimes followed by gamma-ray emission. In the invariant-mass spectroscopy we need to measure all the particles and also gamma rays. On the other hand, in the missing-mass spectroscopy we need to measure only one or two recoiled particles. However, particles recoiled to the angle corresponding to the forward angle in center-of-mass frame have very small kinematic energy below 1 MeV/u. In order to measure such low-energy recoiled particles in the reaction, we are developing an gaseous active target.

The structure of the active target was described in the previous report [4]. The property of GEM with deuterium gas is reported in the ref. [5]. In this paper, we report the measurement of $d(^{14}\text{O},d)$ performed at HIMAC and the measured performance.

We performed the pilot experiment with ^{14}O beam after the modifications to solve the discharge problems and to improve the throughput of readout system and the event reconstruction. The primary beam of ^{16}O at 290 MeV/u



Figure 1. Photo of experimental setup at SB2 course in HIMAC facility.

bombarded a Be target and the secondary beam of ^{14}O at 100 MeV/u was produced and selected using two dipole magnets and an energy degrader at F1 at SB2 course in HIMAC facility. The angles and positions of incident particles and outgoing particles were measured with multi wire drift chambers (MWDC) located upstream and downstream of CAT. The momentum of outgoing particle were analyzed by the dipole magnet and the outgoing angle and position were measured with another set of two MWDCs. The time reference for those MWDC was measured with the plastic scintillator hodoscope located at the end of beam line. Figure 1 shows the photo of the setup at SB2 course in HIMAC facility.

The size of the secondary beam was not small enough to make the trigger with TPC itself if we use the OR of the self-trigger generated by flash ADCs for TPC. We modified the trigger for the TPC and used the anti-coincidence method to reject the beam event at the side regions of readout pads. Then the trigger rate was improved by three-times less than simple OR of self-triggers and the acquisition rate of 800 events per spill was achieved with a newly-developed parallel data processing system.

The typical hit pattern and pulse shape are displayed in Fig. 2 and Fig. 3. Figure 2 shows the hit pattern in the plane of readout pad. Each triangle is one readout pad. The length of the side of triangle is 5 mm and 10 mm for small and large pad, respectively. The beam travels from bottom to top

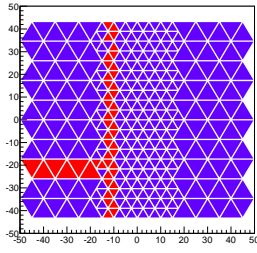


Figure 2. Typical hit pattern in one event. Beam particle go through the center and the recoiled particle can be seen in the side region.

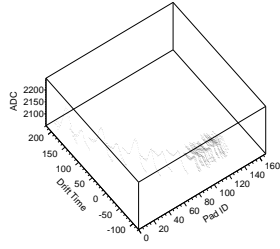


Figure 3. Pulse shape of each pad in the same event in Fig. 2.

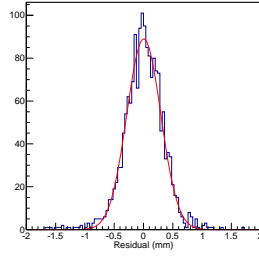


Figure 4. Residual distribution for one position. No restriction on the incident position and angle is applied.

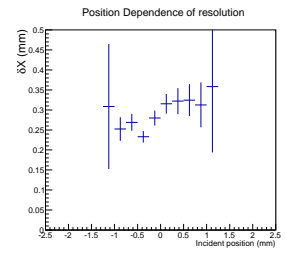


Figure 5. Position dependence of the position resolution.

and a sideways trajectory is clearly seen, which corresponds to the recoiled particle. Figure 3 shows the pulse shapes with relative timing in the pads fired in the event displayed in Fig. 2. From the id of 0 to 80, the pulse shapes for the recoiled particles are displayed. The small id corresponds to the far side from the beam trajectory. The increase of energy deposition can be seen, which may correspond to the brag curve.

We deduced the energy and position resolutions for incident particles in the side region of active area, where we used the regular triangular pad the length of whose side is 10 mm. The energy loss of those particles are 8 keV/mm, corresponding to that of 2-MeV/u deuteron. The energy resolution was estimated for a pair of the pads by comparing the energy loss in one pad with the average in the other pads. The typical energy resolution was 14%. Assuming the energy resolution mainly depends on the initial charge produced by the ionization process, it is expected to be 3.4%. This discrepancy may come from the attachment and/or the diffusion of the produced electrons along the long drift path or the resolution of GEM. We will perform an offline test with α particles in order to clarify this discrepancy.

The position was deduced using the charge division method as described in the Ref. [3]. The position resolution depends on the incident position (and also angle but here we neglect this for simplicity) and is described as $\delta l^2 = \frac{L^2}{k^3} \left\{ -\left(q - \frac{k}{2}\right)^2 + \frac{k^2}{4} \right\}$, where l is the position along the side of triangle, L is the length of the side of triangle, k is the total number of electrons collected in two pads, and q is that in one pad. The maximum (in worst case) position resolution is estimated to be $\frac{L}{2} \frac{1}{\sqrt{k}}$ and is at the center of pads. Using the energy resolution of 14%, the estimated maximum position resolution is 350 μm . The position resolution was estimated as the residual of one position to the track deduced from the other positions. The typical residual distribution is shown in Fig. 4. The distribution is a Gaussian shape and its standard deviation is 300 μm . This is almost the same as the expected one. (Note that the position we discuss here is the projection of l .)

In Fig. 5, the incident-position dependence of the position resolution is shown. The obtained dependence is almost flat in the region we measured while the expected distribution is parabolic as described above. We could not measure the edge region such as below -1.5 mm and above 1.5 mm, because the effective gain of GEMs was not enough to measure the pulse shape in such a region at the experiment. We need another measurement including the

edge region.

The analysis on the TPC and the other detectors is in progress.

In order to measure more forward angle scattering we are developing the low-pressure operation of CAT and we are investigating the basic property of Thick GEM with low-pressure deuterium gas [6]. We also plan to perform a test experiment of low-pressure operation in Autumn 2013.

References

- [1] K. Langanke and G. Martinez-Pinedo, Phys. Lett. B **436** (1998) 19-24.
- [2] E. Kahn *et al.*, Phys. Rev. C **87**, (2013), 064311.
- [3] R. Akimoto, Master Thesis.
- [4] S. Ota *et al.*, CNS Annual Report 2011, (2013), 70-71.
- [5] T. Tokieda *et al.*, in this report.
- [6] C.S. Lee, Master Thesis; C.S. Lee *et al.*, in this report.

Measurements of Gas Gain of Gas Electron Multiplier with 1-atm Deuterium Gas

H. Tokieda, S. Ota, M. Dozono^a, C. S. Lee, and T. Uesaka^a

Center for Nuclear Study, Graduate School of Science, University of Tokyo
^aRIKEN (The Institute of Physical and Chemical Research)

1. Introduction

We are developing the CNS active target (CAT). As a multiplier of the CAT, a gas electron multiplier (GEM) is employed. The CAT is intended for the missing-mass spectroscopy in inverse kinematics by using the (d,d'), ($d,^2\text{He}$) reaction. The counter gas of the CAT is deuterium (D_2) gas. It is described about the development of the CAT in the report by S. Ota *et al* [1].

The GEM used in the measurements was a CNS-GEM (for details, see, e.g., Ref. [2]). It was 100- μm thick and consisted of an insulator Liquid Crystal Polymer (LCP) and thin copper electrodes. The pitch and diameter of the holes were 140 μm and 70 μm , respectively. The area of the GEM is 100 \times 100 mm^2 . Gas-gain measurements were carried out with a double- or triple-layer GEM mounted in a chamber. We used D_2 gas as the counter gas at 1 atm. The required gas gain is approximately 10^4 .

Our purpose is to search on what the gain of the GEM depends. We measured the electric-field dependence in regions. The region between a mesh and GEM, between GEMs and between the GEM and a pad are called a drift, transfer and induction region, respectively as shown in Figure 1. This report describes the gain measurement of the GEM and the electric-field dependence in the drift, transfer and induction region with deuterium (D_2) gas at 1 atm.

2. Measurements and Results

2.1. Offline source measurement

Figure 1 shows a schematic view of the setup with the double-GEM layer mounted in the chamber. As shown in this figure, an α -ray source was put for the drift region. The distance between the α -ray source and a pad is 15 cm.

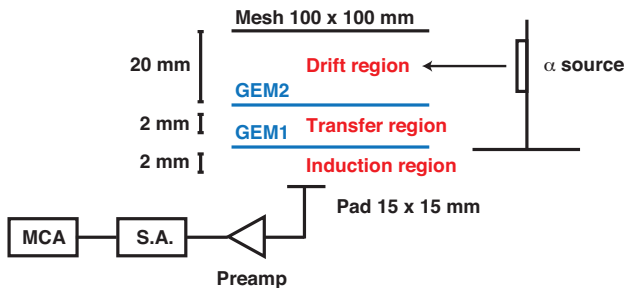


Figure 1. A schematic view of the setup for the double-GEM layer.

The distances between the mesh and top GEM and between the bottom GEM and pad are 20 mm and 2 mm, respectively. The distance between GEMs is 2 mm. The areas of the mesh and pad are 100 \times 100 mm^2 and 15 \times 15 mm^2 , respectively. The HV applied to the mesh, GEM and pad are supplied from independent HV-sources. The signal was read out from the pad and input to a preamplifier (*RPA-211*) and shaping amplifier (*S.A.*, *ORTEC 572A*). The data were recoded by the MCA (*SMTX MCA-5105Lite*)

with self-trigger.

We measured the electric-field dependence in the drift, transfer and induction region. Figure 2, 3 and 4 show these results of the drift, transfer and induction region, respectively.

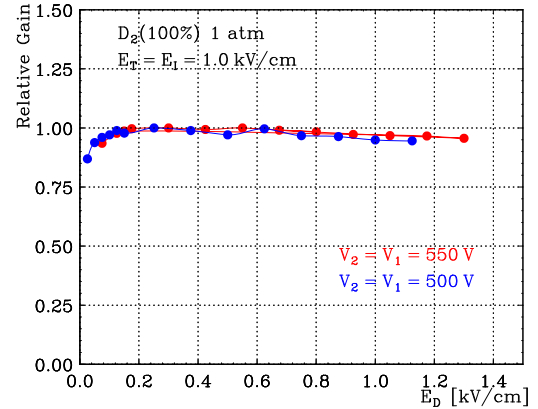


Figure 2. The result of the electric-field dependence in the drift region. The horizontal axis indicates the electric field of the drift region, and the vertical axis indicates the relative gain.

The horizontal axis indicates the electric field of each region, and the vertical axis indicates relative gains. The normalization of relative gains is arbitrary. Here, the electric fields in the drift, transfer and induction region are denoted by E_D , E_T and E_I , respectively. The voltages of GEM1 and GEM2 are denoted by V_1 and V_2 , respectively. We measured until discharges start.

In the measurement, the electric field of other regions were fixed to be 1.0 kV/cm. The V_1 and V_2 were fixed to be 500 V or 550 V. For instance, in the measurement of the drift region, the electric field of the transfer and induction region were fixed to be 1.0 kV/cm.

Figure 2 shows the relative gain becomes saturated around 0.15 kV/cm. At the high electric-field of the drift region, the relative gain slightly reduces due to the absorption of field lines on the upper GEM2 electrode.

As shown in Figure 3, the relative gain increases and becomes saturated at around 2.5 kV/cm in the transfer region.

In Figure 4 the relative gain increases up to about 3 kV/cm of the induction field. At the range from 3 kV/cm to 6 kV/cm, the increasing rate of the relative gain becomes small, because the collected electron is almost constant. For more than 6 kV/cm, the relative gain further increases again because of avalanches in the region between the GEM1 and pad.

We also measured with P-10 gas for the comparison. As shown in Figure 3, the electric-field dependence in the transfer region of D_2 gas shows a similar trend as that of P-10 gas. As can be seen in Ref. [3] [4], the electric-field dependence in the drift and induction region of the D_2 gas also have the same tendency as that of the commonly-used

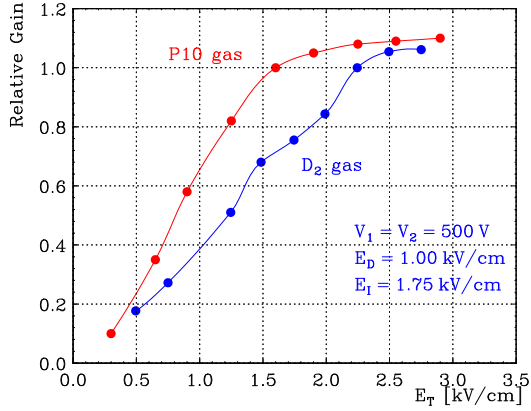


Figure 3. The result of the electric-field dependence in the transfer region. The horizontal axis indicates the electric field of the transfer region, and the vertical axis indicates the relative gain.

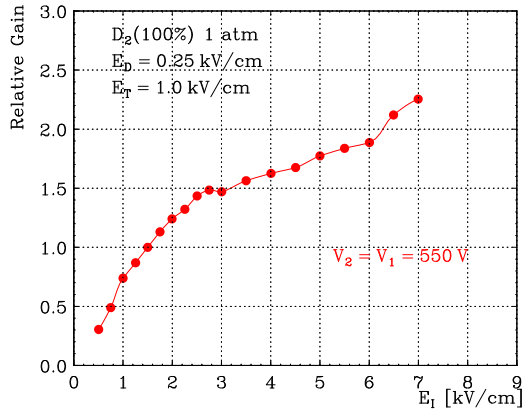


Figure 4. The result of the electric-field dependence in the induction region. The horizontal axis indicates the electric field of the induction region, and the vertical axis indicates the relative gain.

gas as a counter gas.

2.2. Online beam measurement

In February 2013, we carried out the online beam measurement with the $d(^{14}\text{O},d)$ reaction at 100 MeV/u in HIMAC. The CAT was operated with three layers of GEMs. Pulse shapes of the signals were recorded using a 50-MHz sampling flash ADC (V1740, CAEN) and the trigger of data acquisition was the logical OR of self-triggers generated by the FADC.

In this measurement, the typical charge taken by the FADC for the ^{14}O beam at 100 MeV/u was roughly 300 fC. Then, the absolute gain, which is the obtained charge divided by the charge of primary ionization-electrons, was about 2000 for three layers of GEMs. This value was four times smaller than the expected value based on results of the source measurement.

3. Discussion

As seen above, the electric-field dependence of D_2 gas has the same tendency as that of the other counter gas. However, the absolute gain of D_2 gas is much smaller than that of $\text{He} + \text{CO}_2$ (10%) gas [5]. When the Townsend coefficient is about 700, the needed voltage of the GEM of D_2 gas and $\text{He} + \text{CO}_2$ (10%) gas are 600 V and 500 V, respec-

tively [6] [7]. Then, the absolute gain of D_2 gas and $\text{He} + \text{CO}_2$ (10%) gas are about 15 and 1500, respectively [5]. This reason is still not clear, but it seems that the gain reduced due to the contamination such as a moisture during the measurement of D_2 gas. Therefore, to accomplish the required gain, we should measure more parameters of the moisture, temperature and pressure.

4. Summary

In summary, we measured the gain of the GEM and its electric-field dependence in drift, transfer and induction region with D_2 gas at 1 atm. The results show that the electric-field dependence in any region of the D_2 gas has the same tendency as that of the commonly-used counter gas. And we also carried out the online beam measurement with the $d(^{14}\text{O},d)$ reaction at 100 MeV/u in HIMAC. Then, the absolute gain was about 2000 for three layers of GEMs. This value was four times smaller than the expected value.

To accomplish the required gas gain, the development and analysis are currently in progress.

References

- [1] S. Ota *et al.*: CNS-REP 2012.
- [2] Y. L. Yamaguchi *et al.*: CNS-REP-69(2005) 83–84.
- [3] J. Benlloch *et al.* Nucl. Instr. and Meth. A **419**(1998) 410–417.
- [4] S. Bachmann *et al.* Nucl. Instr. and Meth. A **438**(1999) 376–408.
- [5] R. Akimoto: Master Thesis (2010).
- [6] D.J. Bachmann *et al.* Phys. Rev. **104**(1956) 273.
- [7] R. Vein's, Garfield, a Gaseous-Detector Simulation Program, <http://consult.cern.ch/writeup/garfield/>

Properties of Thick-GEM in Low Pressure Deuterium for Low Pressure Gaseous Active Target

C. S. Lee, S. Ota, H. Tokieda and T. Uesaka^a

Center for Nuclear Study, Graduate School of Science, University of Tokyo

^aRIKEN Nishina Center for Accelerator Based Science

1. Introduction

Incompressibility is an important parameter in the equation of state (EOS) of nuclear matter. It can be extracted via the systematic measurement of the incompressibility of nuclei. To extract the incompressibility of neutron rich nuclei experimentally, we plan to measure deutron inelastic scatterings on exotic nuclei such as Ni and Sn isotopes in inverse kinematics. In order to measure the low-energy deutron scattered in this reaction, we are developing a GEM-TPC based gaseous active target, CNS Active Target (CAT). The track length of the low energy particle depends on the density of the gas, or its pressure at a certain temperature. We need to optimize the gas pressure in order to measure lower-energy particles. It is necessary to make the range of low energy particles longer by lowering the gas pressure to track precisely those particles. Usually, so-called thick-GEMs (THGEMs) are used in a low-pressure condition to achieve an adequate signal gain.

In this report, basic properties of 400- μm -thick GEM in low-pressure deuterium gas were investigated. Not only electric field over pressure (E/P) dependence of gas gain but also electric fields of drift, transfer, induction region dependences were investigated. The gain stability over time was also tested.

2. Experimental Setup and Measurement

2.1. Gas Supply System

A schematic view of gas supply system which has been used is shown in Figure 1. A gas pressure regulator and a needle valve are employed for the gas flow. R1 is a regulator, V1~3 are normal valves and V4 is a needle valve for gas flow. The oxygen contamination in the chamber and the leakage of hydrogen are monitored.

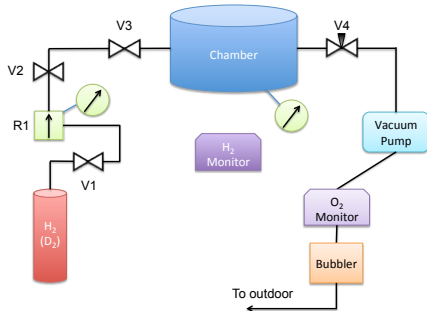


Figure 1. A schematic view of the gas supply system.

2.2. Geometrical Setup and Readout System

Geometrical setup and readout system is shown in Figure 2. Thick-GEMs, described in this report, geometries of 400 μm -thick, 300 μm -diameter, and 700 μm -pitch and they are without insulator rims. They were manufactured by REPIC company, Japan. A charge sensitive pre-amplifier RPA-211 and ORTEC 571 shaping amplifier were employed. Each spectrum had been recorded by MCA,

Kromek 102.

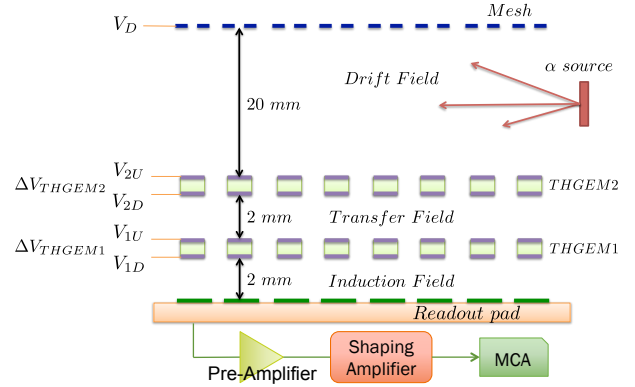


Figure 2. A schematic view of geometrical setup and readout system.

2.3. Effective Gas Gain

Electrons produced by an incident particle drift towards the GEM and are multiplied as they pass through the holes of the GEM. Part of these electrons drift towards the anode and the collected charges are amplified by the preamplifier.

The measured charge depends not only on the absolute gain of GEMs but also the collection efficiency at GEMs, readout pad and the transmission between them; hence, the effective gas gain [1] is employed instead of the absolute gas gain to analyze the data. The effective gas gain G_{eff} is derived from the equation

$$G_{\text{eff}} = \frac{Q_{\text{pads}}}{q_e \cdot \Delta E / W_i} \quad (1)$$

where G_{eff} is the effective gas gain of GEM, ΔE is the energy loss of particle, W_i is mean energy for ion-electron pair creation of certain gas, q_e , the elementary charge and Q_{pads} is the collected charges on the readout pad. We measured the G_{eff} as a function of E_{GEM}/P , E_D , E_T and E_I , where E_{GEM} , E_D , E_T and E_I are the electric field of GEM, drift field, transfer field, and induction field, respectively. The gain stability was also measured.

3. Results and Discussion

Effective gas gain G_{eff} in low-pressure deuterium gas for double THGEMs had been investigated. To have a sufficient gas gain, we have to employ multiple GEMs and we used double thick-GEMs. The gas gain curve up to around 1000 was obtained. Electric fields were fixed as $E_D = E_T = E_I = 1$ kV/cm/atm. The result shows different gas gain at the same E_{THGEM}/p value for various pressures (Figure 3). Therefore, the effective gas gain of GEMs may not be estimated by considering only E_{THGEM}/p value.

Dependences of each electric field were also measured. For these measurements, other electric field strengths were fixed to 1 kV/cm/atm, except the variable electric field

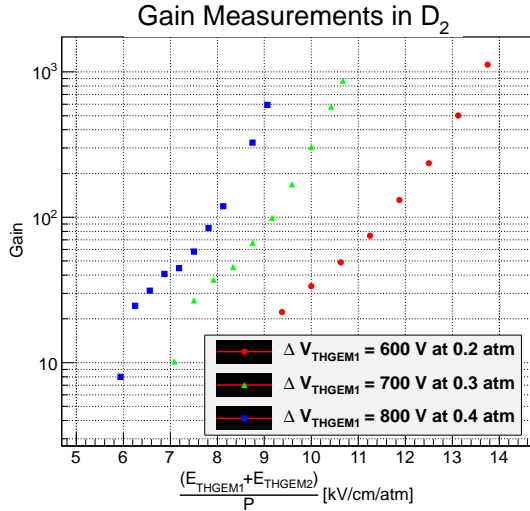


Figure 3. V_{GEM} dependence of effective gas gain G_{eff} at 0.2, 0.3 and 0.4 atm D_2 . $E_{THGEM1(2)}$ is the electric field strength in the center hole of THGEM1(2). Each electric field strength was $E_D = E_T = E_I = 1$ kV/cm/atm, respectively.

strength. G_{eff} increases linearly with E_D at a weak electric field region under 0.5 kV/cm/atm. After it reached the maximum value of this setup at around 1 kV/cm/atm, G_{eff} decreases gradually (Figure 4). This tendency is explained by the distribution of the electric field line [1]. G_{eff} increases linearly with E_T at a weak electric field region under 1 kV/cm/atm. After it reached the maximum value of this setup at around 2 kV/cm/atm, it plateaus at maximum transfer efficiency (Figure 5). G_{eff} increases almost linearly with E_I up to $E_I = 10$ kV/cm/atm (Figure 6). The extra increase around 12 kV/cm/atm is expected to be involved with a parallel plate multiplication between bottom electrode of GEM and readout pad as described in [1].

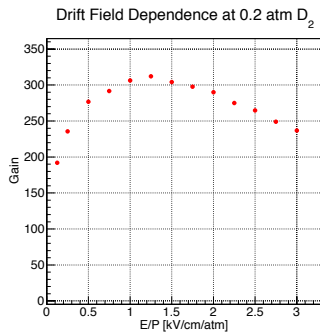


Figure 4. Drift field dependence of effective gas gain G_{eff} at 0.2 atm D_2 .

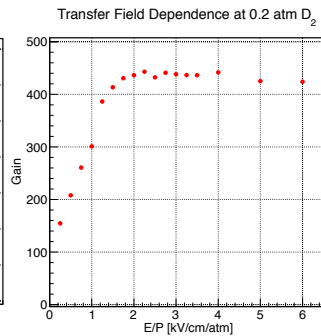


Figure 5. Transfer field dependence of effective gas gain G_{eff} at 0.2 atm D_2 .

Time dependence of effective gas gain of THGEM was investigated for gas gain stability of THGEMs with hydrogen gas. Basically, there are few chemical differences between hydrogen and deuterium, except the density. G_{eff} in 0.2 atm hydrogen gas for double THGEMs had been investigated for 22 hours (Figure 7). ΔV_{THGEM} was 500 V with $E_D = 1$ kV/cm/atm, $E_T = 2$ kV/cm/atm and $E_I = 2.5$ kV/cm/atm.

The result shows that G_{eff} is maintained well for 22 hours. There was a fluctuation of G_{eff} up to 10% with no pressure difference between the beginning and end of the measure-

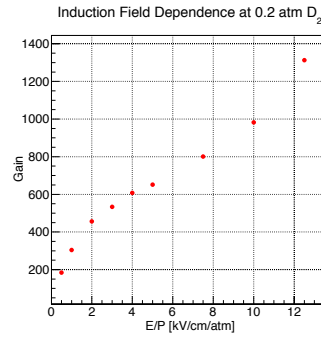


Figure 6. Induction field dependence of effective gas gain G_{eff} at 0.2 atm D_2 .

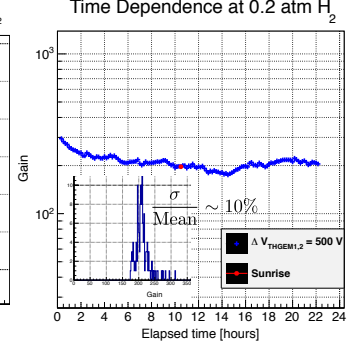


Figure 7. Time dependence of effective gas gain at 0.2 atm H_2 .

ment. For a longer time dependence at a higher gas gain with measuring the gas pressure and temperature variation will be investigated in the near future.

References

- [1] S. Bachmann *et al.*, Nucl. Instr. and Meth. A **438** (1999) 376.
- [2] C. K. Sharem *et al.*, Nucl. Instr. and Meth. A **558** (2006) 468.
- [3] C. K. Sharem *et al.*, Nucl. Instr. and Meth. A **558** (2006) 475.
- [4] K. Yamaguchi *et al.*, Nucl. Instr. and Meth. A **623** (2010) 135.

Algorithms for Active Target Data Analysis

D. Kahl, T. Hashimoto^a, S. Kubono^b, S. Ota, and H. Yamaguchi

Center for Nuclear Study, Graduate School of Science, University of Tokyo

^a*Research Center for Nuclear Physics, Osaka University*

^b*RIKEN (The Institute of Physical and Chemical Research)*

Several nuclear astrophysics experiments using an active target were carried out at CRIB in the last three years, and some are also planned. We performed measurements of $^{18}\text{Ne}+\alpha$ [1] and $^{30}\text{S}+\alpha$ [2] in 2010, $^{22}\text{Mg}+\alpha$ [3] in 2011, and are preparing for a measurement of the β -delayed α -decay of ^{16}N in 2013. The active target uses gas electron multiplier foils (GEMs) and backgammon geometry readout pads, which we call the GEM-MSTPC. Data are recorded to disk by a flash ADC, which digitizes the pulse shape of the deposited charge as a function of time for each pad. The energy loss of an ion is proportional to the deposited charge in a pad, its horizontal position is determined by comparison of the charge deposited at the left and right side of the backgammon, the vertical position is determined from the electron drift time, and the depth is simply determined by the sequential pad number. In this way, we can reconstruct an ion's trajectory in three dimensions. However, analyzing this wealth of data is non-trivial, and a significant amount of research time has been dedicated to creating a suitable analysis program, called CRABAT and released as free software [4] under the GNU General Public License version 3.

For the reaction experiments, the trigger is determined by coincidence between the beam monitors (PPACs) and silicon strip detectors (SSDs), where as for the decay experiment, the active target operates in a self-triggering mode. Once a trigger is received, the flash ADC begins sampling all the active target channels at a set frequency, typically 50 MHz. However, these samples are not retained until the sampled value exceeds a user-defined threshold in order to avoid recording excessive baseline data to disk. Once a sample from a given channel exceeds its threshold setting, the previous five samples are also kept for evaluation of the baseline, the time is recorded, and the flash ADC will continue to save all subsequent samples until the signal falls back below the threshold setting. In this way, the pulse shape from the preamplifier is digitized with some obvious advantages: the pulse shape can be analyzed, one can integrate the full charge deposition rather than merely using the peak deposited charge, and multiple pulses separated by a short time can be recorded without loss via dead time.

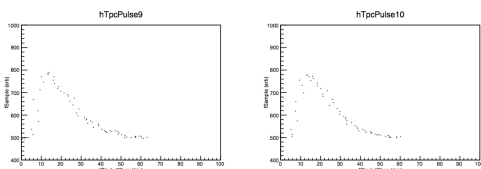


Figure 1. Comparison of two active target pulses under the same conditions. The pulse in the left panel was found by the simple peak finder, whereas the pulse on the right was not found. Nothing is apparently different between the intrinsic pulse shapes, but significant jitter is observed in both pulses.

In order to analyze the data, the first and most important

step is finding peaks within the flash ADC data. Naïvely, a peak is simply defined as a sample whose value is larger than neighboring samples. In this approach, beginning with the j^{th} sample, it is determined if the present sample is greater than each of $\pm j$ neighboring samples, and such samples are designated as peaks; subsequently, the baseline value is subtracted from the sample to derive its true height. The user should optimize the value of j . Unfortunately, jitter in the signal significantly complicates this approach. While the intrinsic pulse shape is smooth, a series of samples digitizing the pulse may show small fluctuations in height, as evident in Figure 1. Thus, if j is chosen to be very small, for example $j = 1$, many false peaks are identified by the algorithm, for example in the rising or falling shoulders of the peak, or in the tail as the peak settles back to the baseline value. Conversely, if j is chosen to be larger, for example $j = 5$, the likelihood of the algorithm finding a true peak diminishes, because it is unlikely that a single sample will be greater than all of $2j$ samples, in this instance 10 other samples. This manner of missing a true peak might be because the intrinsic peak value of the pulse occurred in between samples, but it, too, is mainly a result of the signal jitter. As j increases, the probability also increases for one of the $2j$ samples the present sample is compared against to be larger than the present sample, and yet that sample is also not larger than all its neighboring samples. Figure 1 shows a comparison of two pulses, one that the algorithm could find and another which was missed. Sampling at 50 MHz, it was found that the peak finding was optimized for $j = 3$ (equivalent to looking for peaks in a 140 ns window), yet from a manual analysis of 500 pulses from the same channel, it was found that 20% of the peaks were false positives, and about 20% of true peaks were missed; such a large margin of error is clearly unacceptable.

As these difficulties in locating peaks arise mainly from signal jitter, the obvious solution is to rebin the samples during the peak finding algorithm, and use a moving average to locate the peak position, smoothing out these fluctuations. The algorithm was optimized when the rebinning was set to 4 and $j = 2$; in this case, j refers to the rebinned samples, and thus the window for a peak is 400 ns. Once a peak is located, the algorithm checks the original data (which has not been rebinned), and designates the largest of those four samples within the rebinned peak location as the true peak. Manually checking the method again against 500 pulses from the same channel revealed no missed peaks and no false positives; although we do not expect the algorithm is 100% accurate, its efficiency appears better than 99%. The optimized parameters were found equally efficient for both heavy and light ions of various energies. A comparison of the pad multiplicities using these two different algorithms is shown in Figure 2, indicating a vast improvement.

Integration of the deposited charge in a pad is not only simple but useful. The integration is performed by summing the values of each sample pulse after subtracting the

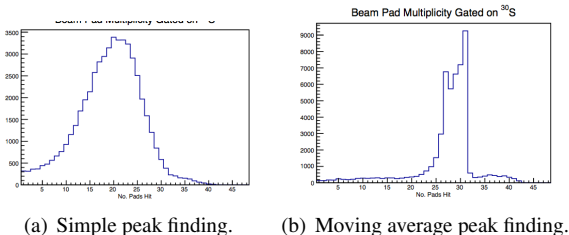


Figure 2. Multiplicity for the number of pads hit by the beam during the ^{30}S experiment. Although there are 48 pads, only about 31 of them operated correctly, thus we should expect a multiplicity typically near 31. The left panel (a) shows the case using the simple peak finding algorithm, while the right panel (b) shows the case with the moving average algorithm. It is obvious the moving average peak finder gives much more consistent results over a large number of events.

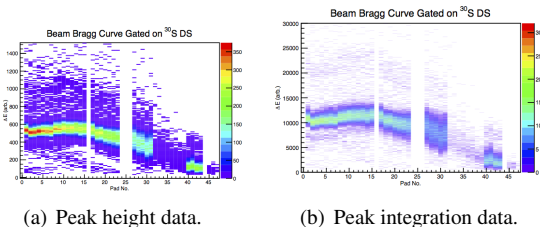


Figure 3. Bragg curves for the ^{30}S beam for the downscaled beam data (no SSD event). Although the Bragg curve appears prominently in both cases, a subtle difference emerges. In the left panel (a), there is no clear pattern for the data outside the Bragg curve. However, in the right panel (b), a second Bragg curve emerges at exactly twice the height of the first; this second Bragg curve represents the situation when two ions are injected within a very short interval from one another.

baseline. Although the algorithm can recognize the instance of multiple separate peaks in the same pulse, it cannot de-convolute them yet; for most of our experiments, the event rate is low enough that the instance of such events is less than 1% and they can be discarded. A comparison of Bragg curves from the peak height data and integrated peak data indicates an interesting feature, as shown in Figure 3. Suppose two identical ions are injected to the active target within a very short interval from one another. In this case, the active target pulse will appear not as two separate pulses, but as one larger pulse. The exact timing of their overlap will allow the pulse height to vary from one which is nearly the same as a single pulse to about two times this value. In the case that the pulse is integrated, however, the pulse will always indicate twice as much charge was deposited as for the case of one ion. Thus, peak integration allows us to easily reject pileup events, which is more difficult otherwise, for instance requiring a sophisticated pulse shape analysis algorithm.

The program also supports typical analysis features. Histogramming is handled by ROOT. An efficient algorithm for matching the raw left and right channel backgammon data to the correct pad, as well as checking that the timing data of the two pulses are consistent with the same event, exists. Runtime options allow the user to select and isolate data types and analysis methods, minimizing compu-

tational time. If executing the analysis over multiple runs, the program executes the analysis of each run as a separate process for each available core. Whenever possible, experiment specific parameters and conditions are controlled outside the main analysis code to increase portability.

Two main features are still lacking and under development. The first is an algorithm to determine the vertex in the case of a scattering or reaction experiment. For the beam and heavy recoil, sequential pairs of linear fits will be performed in the X vs. Z and Y vs. Z data, in order to determine the unique pad where χ^2 is minimized for both fits; a simple prototype for this algorithm has been tested. The second feature is to add online analysis capability, since at present the program can only be called on a closed run data file which has already been converted into a ROOT tree. Along with online capability, we plan to extend the graphical user interface to be more friendly to inexperienced users who are mainly concerned to verify proper experimental operating conditions without needing to know the details of the analysis code.

References

- [1] T. Hashimoto, *et al.* American Institute of Physics Conference Series **1484** (2012) 454-456.
- [2] D. Kahl, A. A. Chen, S. Kubono, T. Hashimoto, *et al.* Proceedings of Science **NIC XII** (2012) 201:1-5.
- [3] N. N. Duy, *et al.* Center for Nuclear Study Annual Report 2011 **CNS-REP-90** (2013) 9-10.
- [4] <https://github.com/goatface/crabat>

Ion-optical study of SHARAQ for high-resolution spectroscopy

S. Michimasa, M. Takaki, M. Dozono^a, T. Nishi^b, S. Go, H. Baba^a, A. Stolz^c, S. Ota, K. Yako, H. Matsubara^a, H. Miya, H. Tokieda, S. Kasase, K. Kisamori, R. Yokoyama, T. Fujii, Y. Kubota, C.S. Lee, M. Kobayashi, T. Kawabata^d, T. Baba^d, M. Tsumura^d, R.G.T. Zegers^c, E. Ideguchi^e, H. Takeda^a, Y. Yanagisawa^a, T. Kubo^a, N. Inabe^a, N. Fukuda^a, D. Kameda^a, H. Suzuki^a, Y. Shimizu^a, H. Sato^a, T. Ichihara^a, H. Sakai^a, T. Uesaka^a, S. Shimoura
for the SHARAQ collaboration.

Center for Nuclear Study, Graduate School of Science, University of Tokyo

^aRIKEN Nishina Center

^bDepartment of Physics, University of Tokyo

^cNSCL, Michigan State University

^dDepartment of Physics, Kyoto University

^eRCNP, Osaka University

The SHARAQ spectrometer and High-resolution beamline [1] were constructed to realize high-resolution nuclear spectroscopy with RI-induced reactions. The beam transport to the SHARAQ spectrometer has the following options for each experimental design: 1. Dispersion matching (DM) transport [2]; 2. High-resolution achromatic (HRA) transport [3]; 3. Large-acceptance achromatic (LAA) transport. At present, we have already provided the DM and HRA beams for physics experiments. In these beam transport modes, the DM is designated for high momentum-resolution spectroscopy of RI-induced two-body reactions. The momentum resolution of the DM is designated to be $p/\delta p = 15000$, but the achieved value had been $p/\delta p = 1800$ in FWHM before the present study. This beam study aimed at improving the momentum resolution of the DM transport, and practiced the new procedure to tune quickly the DM transport. We also stored the time-of-flight data between BigRIPS F3 focus and the final focal plane of the spectrometer (S2) by using a cocktail beam of light $A/Z = 2$ nuclei. We report here results of the beam study.

The DM mode is designed to achieve the ion optics where the position and angle at the S2 focus are independent from the beam momenta. The mode is suitable to measure precisely transfer momenta in a reaction induced by momentum-spread RI beam. The momentum resolution and angular resolution of the total system were respectively evaluated to be $p/\Delta p = 15000$ and 1 mrad by a first-order ion-optical calculation. The designed trajectory of the DM mode from the BigRIPS F3 focus to the SHARAQ S2 focus is shown in Fig. 1. In the DM mode, the momentum spread of the beam was ion-optically corrected although the spread in the HA transport is corrected by data analysis. Accordingly tracking detectors installed on the beamline can be reduced. As the result, we can realize high-resolution measurements by reducing a multiple scattering and an energy straggling from the online materials. The hit position and angle at F3 are only necessary to perform missing-mass spectroscopy. The information is used to determine incident angles to the secondary target and to evaluate shifts of the S2 hit position derived from the F3 hit position.

Whenever the DM mode is adopted to an experiment, the transport was necessary to be tuned before the physics measurement. So far, the procedure for the DM optics is that the SHARAQ spectrometer was firstly tuned by the HA mode and the beamline optics was changed to the DM mode. To reduce the tuning time of the DM mode, we developed the

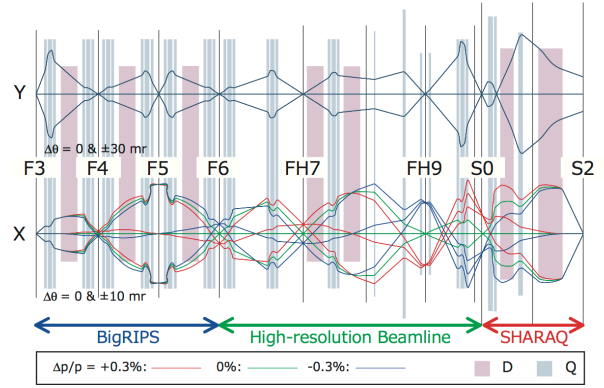


Figure 1. Beam trajectories of Dispersion-Matching (DM) transport of the High-resolution beamline and SHARAQ spectrometer.

new procedure which skips the tuning of HA mode. The procedure has a concept that the DM trajectory not only of the beamline and but also of the spectrometer are tuned in upstream-to-downstream sequence. This new procedure was very effective to save the beam tuning time and consequently we reduced 1/3 of the amount of time (4 hours) from the previous procedure.

In the study of the new tuning procedure, we obtained ion-optical data by using the $A/Z = 2$ nuclei fragmented from ^{18}O . In the DM transport, beam-momentum dependences in horizontal position and angle at S2 were designed to be vanished. The features of the beam were successfully demonstrated in Figs. 2 (a) and (b), which respectively show the lateral and angular dispersion matchings between the beamline and SHARAQ. Consequently we confirmed agreements between the measurement and the computational evaluation.

In Fig. 2(c), the thin histogram shows the horizontal spot size at S2. The width of this histogram (2.6 mm FWHM) included the effects of multiple scattering in tracking detectors on the beamline, which was estimated to be 1.3 mm (FWHM). Therefore, the achieved width of the SHARAQ system was evaluated to be 2.3 mm (FWHM), which corresponds to the resolving power of $p/\delta p = 3000$. This is due to the improvement of lateral dispersion matching between the beamline and spectrometer, and was considered to be the result of iterative tuning in the present procedure. However, this width still suffered from different

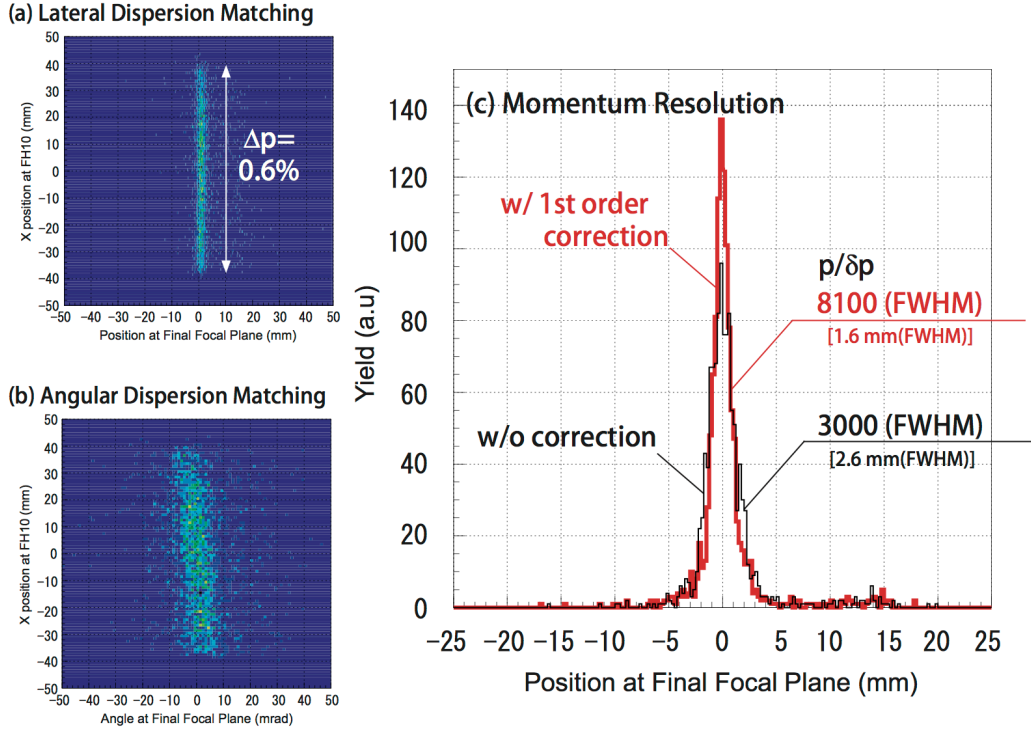


Figure 2. Beam properties in the DM transport of SHARAQ. Figs. (a) and (b) show lateral and angular momentum matchings at the S2. Fig. (c) shows achieved resolving powers without and with corrections by the beam information at F3.

trajectories at BigRIPS-F3, where the beam spot size and angular spread were horizontally 3.9 mm and 14.8 mrad in FWHM, respectively. Consequently, we successfully achieved the resolving power of $p/\delta p = 8100$ by correcting horizontal shifts at S2 calculated from beam trajectories measured at F3 and the first-order transport matrix elements from F3 to S2. The improvement indicated by a thick line in Fig. 2(c). Data analyses of higher-order matrix elements and of the transport matrix connecting to TOF between F3 and S2 are now in progress.

References

- [1] T. Uesaka, *et al.*, Prog. Theor. Exp. Phys., 03C007 (2012).
- [2] T. Kawabata *et al.*, Nucl. Instr. Meth. B **266**, 4201 (2008).
- [3] S. Michimasa *et al.*, RIKEN Accel. Prog. Rep. **45**, 136 (2012).

Polarized proton target in SHARAQ04 experiment

T.L. Tang, S.H. Hwang^a, T. Kawahara^b, T. Wakui^c, S. Sakaguchi^d, S. Kawase, T. Uesaka^e

Center for Nuclear Study, Graduate School of Science, University of Tokyo

^a*Advanced Science Research Center, Japan Atomic Energy Agency*

^b*Department of Physics, Toho University*

^c*Cyclotron and Radioisotope Center, Tohoku University*

^d*Department of Physics, Kyushu University*

^e*RIKEN (The Institute of Physical and Chemical Research)*

In order to identify the total angular momentum of a nuclear state, orbital angular momentum and spin have to be determined. The orbital angular momentum is deduced by angular distribution and the spin is deduced by the asymmetry of the distribution. The spin asymmetry is produced by a polarized proton target in SHARAQ04 experiment. This experiment was performed in RIKEN RIBF on June, 2012. This report explains the conditions of polarized proton target.

The advantage of this polarized proton target are two fold. It can be operated under a small magnetic field (64 mT in this experiment) that allows low energy recoil particles to exit the magnetic field instead of trapped inside. It can also be operated at rather high temperature (-160 °C in SHARAQ04 experiment) that makes it more easy to operate.

The principle of proton polarization is based on Hartman-Hahn theory [1]. The theory states that when the ESR (electron spin resonance) frequency in rotating frame is matched the nuclear Larmor frequency, the electron polarization can be transferred to nuclear spin or via visa. This condition is called Hartman-Hahn condition:

$$(\Omega_S - \omega_{\mu w})^2 + \Omega_{\mu w}^2 = \Omega_I^2 \quad (1)$$

where Ω_S is the ESR frequency, $\omega_{\mu w}$ is the microwave frequency, $\Omega_{\mu w}$ is the equivalent frequency of microwave's magnetic field in rotating frame and Ω_I is the nuclear Larmor frequency.

The target crystal was made of naphthalene (C₁₀H₈) doped with 0.05 mol% of pentacene (C₂₂H₁₄), which is the polarization agent. The proton polarization takes 4 major steps [2]. 1) The electrons are excited from the singlet ground state by laser irradiation to excited single states, then go to excited triplet states by inter-system crossing. 2) Any 2 states of the triplet states forms an effective electron polarization. This polarization can be transferred to proton spin when Hartman-Hahn condition is reached. 3) A magnetic field sweeps through the ESR (electron spin resonance between the 2 states) spectrum adiabatically to enhance the electron magnetization. 4) The proton polarization diffuses to surrounding protons by spin-spin interaction. In addition, the crystal was cooled down to -160 °C to reduce the thermal depolarization. Therefore, the polarized proton target system had laser, static magnetic field, cooling system (with vacuum), microwave and sweeping magnetic field. The condition is listed in Table 1.

The target crystal and associated devices (crystal holder, NMR coil, loop gap resonator, microwave antenna, field sweep coil) were placed inside a cooling chamber. LN₂ gas was used to keep the temperature inside the chamber around -160 °C. The temperature of the chamber was monitored by a Pt-100 resistance thermometer that located on

Table 1. Polarization condition

Magnetic field [mT]	64.2 ~ 65.6
Vacuum [mbar]	7×10^{-2}
Temperature [°C]	-160
Laser wavelength [nm]	514.5
Laser 1 power [W]	10.7
Laser 2 power [W]	11.1
Chopper frequency [kHz]	3.5
Laser pulse width [ns]	83.9
Microwave frequency [GHz]	2.695
Microwave power [W]	2.6
Microwave pulse width [ns]	15.9
Field sweep [mT]	±3
Field sweep gate width [ns]	16.5
Field sweep phase	0/180#

Spin-up or spin-down

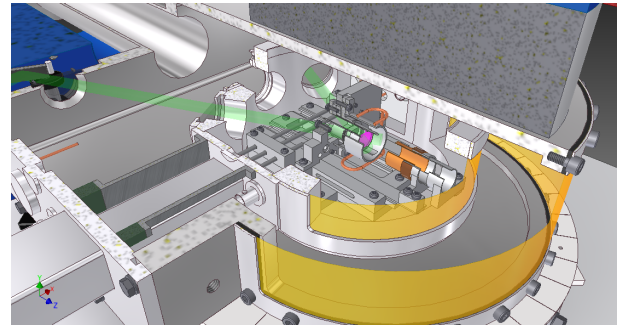


Figure 1. Computer model of target system. The pink disk is the target crystal. The transparent green is the laser ray. The yellow films are 256 μm Kapton film. The loop gap resonator is the orange cylinder. The brown cylinder is NMR coil. The cables and wires are not shown.

the top of the crystal holder. It was regulated and stabilized by a PID (proportion-integrate-differential) controller which was controlling the nitrogen gas flow. The cooling chamber was put inside a larger vacuum chamber. In order to let recoil or scattered particles exit the chambers for detection, both chambers have an 150° and 170° arc windows, each was covered by a 256 μm Kapton film. The vacuum chamber served 2 purposes: 1) as a connector to connect the beam pipe and 2) as a thermal insulator to keep the cooling chamber in low temperature. The magnetic field was monitored by a Hall probe that was placed between the vacuum chamber and lower magnetic pole. The loop gap resonator [3](LGR) served as a microwave cavity while letting recoil particles pass through. A computer model of the target system is shown in Figure 1.

The measurement of the polarization was done by 2 methods - NMR (nuclear magnetic resonance) detection

and proton-proton elastic scattering. NMR method provided a quick way to monitor the magnitude of polarization through out the experiment. However, NMR signal only gives a relative magnitude of polarization due to lack of reference for calibration. The absolute magnitude of polarization can be determined by proton-proton elastic scattering. A 4~5 degree NMR pulse was used that it will not affect the polarization significantly while obtaining the NMR signal. The condition of NMR setting is shown in Table 2. The NMR signal strength is shown in Figure 2.

Frequency [MHz]	2.73878
Level#	55 ~ 60
Gain [dB]	20
Pulse width [μ s]	2.6
Low pass filter [kHz]	90
Phases [deg]	90

It is related to the output power.

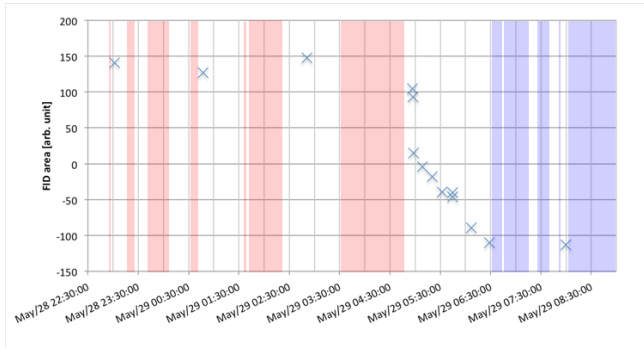


Figure 2. The NMR signal strength during elastic scattering. The scattering data is shaded (red = spin-up, blue = spin down)

An inconvenience of using NMR is that the NMR coil strongly interference with the LGR when they are overlapped, that the resonance frequency of the microwave or the impedance of NMR changes significantly. When protons were polarizing, the LGR was inserted and covered the crystal while the NMR coil was moved away from the LGR. When measuring the NMR signal, the NMR coil was inserted and LGR was moved away.

The proton-proton elastic scattering with a polarized target results cross section asymmetry on left and right distribution. The yield of left/right detector is:

$$Y_{L/R}^{\uparrow/\downarrow}(\theta) = N_t N_b \lambda \varepsilon_{L/R} \sigma(\theta) \Delta\Omega (1 \pm A_y(\theta) P_{\uparrow/\downarrow}) \quad (2)$$

where N_t and N_b are the number of target and beam particle, λ is the DAQ live time, ε is the detector efficiency, σ is the cross section, $\Delta\Omega$ is the detector acceptance, A_y is the analyzing power (which is well known) and P is the polarization of the target.

The total run time for elastic scattering is 280 min, in which 165 min for spin-up and 115 min for spin down (Figure 2). The systematic error can be canceled by spin-up and spin-down measurement. The recoil or scattered proton was detected and tracked by 2 MWDC (Multi-Wire Drift Chamber) [4] located on left and right. The acceptance of the MWDC covered 50° from 20° to 70° forward angle. The elastic scattering restricted the opening angle of the 2

recoil/scattered proton ranging from 86.3° to 90° . Figure 3 shows the opening angle obtained by all runs. The broadening of the peak is due to angular resolution from detection and multi-scattering when protons traveling in air. The background can be eliminated by requiring the conservation of total energy that the total energy of recoil/scattered protons should be equal to incident protons. The data is still under analysis.

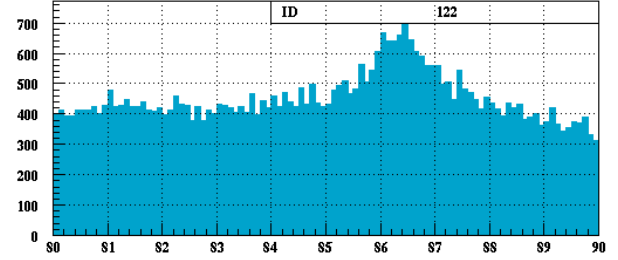


Figure 3. Opening angle of recoil/scattered proton. X-axis is angle in degree. Y-axis is number of count. Bin size is 0.1 degree.

References

- [1] S.R. Hartmann and E.L. Hahn, Phys. Rev. **128**, 2042 (1962).
- [2] W. Th. Wenckebach, Dynamic Nuclear Polarization using Strong Microwave Field (2012)
- [3] B.T. Ghim, G.A. Rinard, R.W. Quine, S.S. Eaton, G.R. Eaton, Jour. Mag. Reson. A, **120** (1996), p. 72
- [4] H. Okamura et al., Nucl. Instr. and Meth. A, **406** (1998), p. 78

Performance test of high-granularity neutron detector with beams in CYRIC

Y. Kubota, M. Sasano^a, T. Uesaka^a, M. Dozono^a, M. Itoh^b, S. Kawase, M. Kobayashi, C. S. Lee, H. Matsubara^a, H. Miya, S. Ota, K. Sekiguchi^c, T. Taguchi^c, T. L. Tang, H. Tokieda and T. Wakui^b

Center for Nuclear Study, Graduate School of Science, University of Tokyo

^a*RIKEN Nishina Center for Accelerator-Based Science*

^b*Cyclotron and Radioisotope Center (CYRIC), Tohoku University*

^c*Department of Physics, Tohoku University*

1. Introduction

Nucleon-knockout (p, pN) reactions at intermediate energies (200–300 MeV) provide a powerful probe of single particle nature of nuclei [1]. Exclusive measurements of the (p, pN) reactions allow one to determine the separation energies, becoming one of hot topics in studies of unstable nuclei.

The first goal of our (p, pN) studies is to measure the energy spectra on oxygen isotopes of $^{14-24}\text{O}$ at the RIBF. We have performed an experiment on these isotopes. The detail of the experiment and the analysis on the ($p, 2p$) channel is described in Ref. [2].

In the present study, in order to improve the resolution of the separation energy in (p, pn) measurement, we have developed a prototype neutron detector with a high position resolution better than 3 mm to measure neutrons with kinetic energies ranging from 50 to 200 MeV. The opening angle θ between the ejectile with the beam-projectile origin and knocked-out nucleon predominantly determines the separation energies S . The resolution in the separation energy (ΔS) can be approximately written as $\Delta S = 0.3 \text{ (MeV/mrad)} \times \Delta\theta \text{ (mrad)}$ on oxygen isotopes. If the neutron detector located at 2 m apart from the target, the separation energy resolution of $\Delta S = 1 \text{ MeV}$ requires the position resolution of 5 mm in the direction of opening angle, which enables us to distinguish neighboring single particle states.

2. Prototype detector

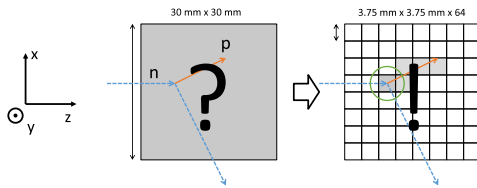


Figure 1. An idea to improve the position resolution. Blue dashed lines and red solid lines show trajectories of incident neutrons and scattered protons.

Figure 1 shows the schematic view of the newly-designed detector to improve the position resolution dramatically. A proton scattered by an incident neutron deposits its energy as passing through the scintillator and the scintillation photons are generated along the trajectory of the scattered proton. By segmenting this scintillator to an array of 64 scintillators, we can see the trajectory as the hit pattern. By analyzing the hit pattern, the reaction point can be determined within the size of a segment and the uncertainty of position can be improved from 30 mm to 3.75 mm by a factor of 8.

Figure 2 shows the photo of the prototype detector, which has a total effective volume of $30.0 \times 30.0 \times 1000 \text{ mm}^3$ con-

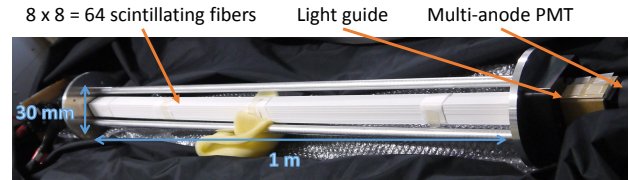


Figure 2. A photograph of the prototype detector, consisting of the neutron detection part comprised of 64 plastic scintillation fibers, the two multi-anode PMTs for reading out the scintillation light from the both ends of each fiber, through optical fibers.

sisting of 64 scintillating fibers ($3.75 \times 3.75 \times 1000 \text{ mm}^3$). Scintillation photons generated in each fiber are transported via pitch conversion fibers with a diameter of 2 mm having no scintillation ability, to the photo-cathode planes of the multi-anode PMT (Hamamatsu H7546B). We use dynode signal for determining the reaction timing and the reaction position along the y -direction, as well as anode signals for the hit pattern analysis on (x, z) -plane.

3. Experiment

A test experiment of the prototype detector consisting of two measurements was performed in November 2012 at the Cyclotron and Radioisotope Center (CYRIC), Tohoku University. In the first measurement, a faint proton beam accelerated up to the energy of 70 MeV by the 930-type azimuthally-varying-field cyclotron was used for characterizing the time resolution (Δt), the position resolution along the y -direction (Δy) and the proportion of the effective volume in the total volume of scintillators (P_{eff}). In the second measurement, monoenergetic neutron beams at 68 and 50 MeV produced through the $^7\text{Li}(p, n)^7\text{Be(g.s.} + 0.43 \text{ MeV)}$ and $^{12}\text{C}(p, n)^{12}\text{N(g.s.)}$ reactions at the 0 degree, respectively, are used for characterizing the position resolution along the (x, z) -direction (Δx) and the detection efficiency (ϵ). Natural Li and C targets were used and their thickness were 0.18 and 0.27 g/cm^2 , respectively. The intensity of the proton beam was about 10 nA and the rate of neutrons bombarding the detector was typically 10^6 particles per second.

Figure 3 shows the setup of all the detectors used in the second measurement. A 13-mm-thick plastic scintillator (labeled as PL1) was used for vetoing charged-particle. A 100-mm-thick plastic scintillator (PL2) covering the same solid angle as the prototype detector, was used for calibrating the detection efficiency. A 3-mm-thick plastic scintillator (PL3) was used as a trigger of multi-wire drift chambers (MWDCs); the MWDCs are used for tracking of protons scattered by incident neutrons in the prototype detector.

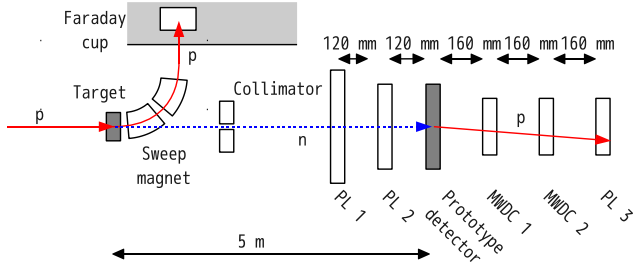


Figure 3. A schematic view of the setup for neutron measurement.

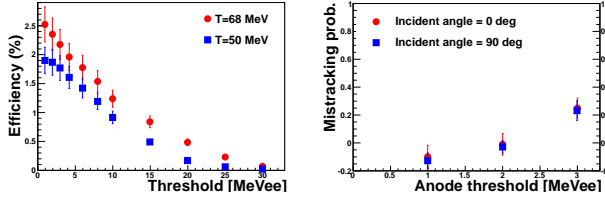


Figure 4. The left and the right panels show the detection efficiency curve and the mistracking probability, respectively. In the left panel, two different marks show the different kinetic energy of incident neutron.

4. Results

The left panel of Fig. 4 shows the detection efficiency as a function of a dynode threshold. The detection efficiency of $\varepsilon = 2.5\%$ was achieved for 68-MeV neutron with a dynode threshold of 1 MeV_{ee} . This value is about 30% smaller than that of conventional detector having same thickness of 30 mm. This depression comes from the ineffective area such as cladding, light shielding and gaps surrounding each scintillating fiber. It is sufficient to perform the (p, pn) experiment.

The right panel of Fig. 4 shows the mistracking probability as a function of an anode threshold. This value was derived from the detection efficiencies of each fibers assuming a toy model that the mistracking always occurs neighboring fibers and its probabilities along the x -direction and z -direction are the same. As a result, its influence on the position resolution Δx can be ignored when we set anode threshold around 1 MeV_{ee} .

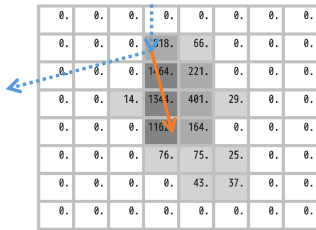


Figure 5. Example of hit pattern. 8×8 numbers indicate the light output in each segment.

Figure 5 shows a hit pattern of anodes of the PMT in the unit of QDC channels for a typical neutron-detection event. In this event, the fiber where the reaction due to the incident neutron can be easily identified, implying that the uncertainty of the neutron detection position, ± 1.8 mm, can be achieved. The detailed analysis for establishing the method of the hit-position reconstruction is under progress.

Table 1 shows the result of the performance test. The

Table 1. Summary of the items characterizing the performance of the prototype detector, the requirements on the items to achieve $\Delta S = 1$ MeV with the detector position of 2 m apart from the target, and their results. Resolutions are written in a full-width at half-maximum.

Items	Requirements	Results
Detection efficiency ε	–	2.5%
Position resolution Δx	5 mm	2.6 mm
Position resolution Δy	70 mm	55 mm
Timing resolution Δt	700 ps	300 ps
Effective volume P_{eff}	–	70%

requirements for achieving the separation energy resolution of $\Delta S = 1$ MeV is fully satisfied.

5. Summary and outlook

We constructed the prototype detector with high position resolution for intermediate-energy neutrons consisting of scintillating fibers and multi-anode PMTs. The test experiment using 70-MeV proton and 68- and 50-MeV neutron was performed in CYRIC for characterizing its performance. The result shown in Table 1 satisfies the requirement for the separation energy resolution of $\Delta S = 1$ MeV when the detector is located 2 m apart from the target.

Due to the limitation of the accelerator, the performance was characterized only in the energy region of 50–70 MeV and there is no data in the energy region of 70–200 MeV, which is the most important for (p, pn) measurement. We are planning to perform the further experiment in the energy region of 100–200 MeV in autumn (2013) at Research Center for Nuclear Physics, Osaka University.

References

- [1] G. Jacob and TH. A. J. Maris, Rev. of Mod. Phys. **45**, 6 (1973).
- [2] S. Kawase *et al.*, “Spectroscopy of single-particle states in oxygen isotopes via the (p, pN) reaction with polarized protons”, in this Report.

Beam simulation of AVF cyclotron injection line for efficient beam transportation

S. Watanabe, Y. Ohshiro, S. Yamaka, H. Yamaguchi, S. Shimoura, Y. Kotaka^a, M. Kase^a,
K. Hatanaka^b, A. Goto^c, W. Yotaka^d, T. Mitsumoto^e

Center for Nuclear Study, Graduate School of Science, University of Tokyo

^aRIKEN (The Institute of Physical and Chemical Research)

^bRCNP Osaka Univ. ^cNIRS Chiba ^dJAERI Takasaki ^eSHI Osaka

Introduction

A 14 GHz electron cyclotron resonance ion source, called HyperECR, has been installed to provide the beam to the RIKEN-AVF cyclotron [1] through a beam injection line, called LEBT. Its performance was made improved and now it can provide high current beams. The beam injection efficiency however, is not yet stabilized, and varies from several percents to 30 percents, depending on the ion species. We first briefly discuss the beam property of the present ion source studied using the simulation code IGUN [2] [3]. The second, measured beam transport efficiency is compared with the calculated one by using the code WinAGILE [4]. Also description will be made on utility programs such as a data convertor, called point file generator.

1. Procedure of beam simulation

Figure 1 illustrates the flow chart of beam simulation. Detailed descriptions of each category are provided in the following.

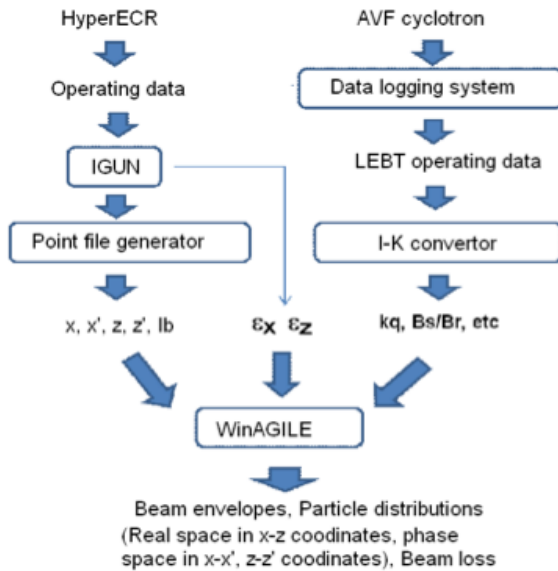


Figure 1. Schematic flow chart of the beam simulation of the AVF cyclotron injection line.

2. Point file generator

Computation code IGUN is used to simulate extraction of positive ions from a plasma. In this program, a beam orbit is calculated in the electric field generated by the plasma electrode, extraction electrode and focusing-electrode. Figure 2 shows some calculation results. As the initial parameters of the calculation, a beam current of $85\mu\text{A}$, an extraction voltage of 9995 Volt, and an einzel lens voltage of -600

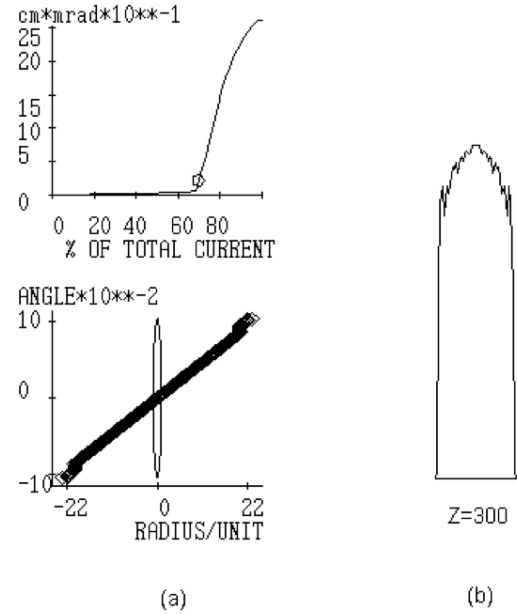


Figure 2. calculated fractional emittance (a) and the profile image (b) of $^{20}\text{Ne}^{7+}$ at the exit of the ion source.

volt were used. Obtained rms emittance is $2.61\text{ cm}\cdot\text{mRad}$, which means an emittance area of $156.6\pi\text{ mm}\cdot\text{mRad}$. If the beam current is increased, the profile becomes ragged and the fractional emittance is increased. The results from the calculations using the code IGUN are recorded in the output files, such as `**out` and `**trj`. The output file `**out` contains the twiss parameters such as $\alpha_{x,z}=-1.38$ and $\beta_{x,z}=0.62\text{ m}$. This twiss parameters will be used in the calculation of beam envelopes as shown in Figure 5. The output file, `**trj`, is transformed to a particle information file, called point file. The particle information means 2 coordinates (x, z) and 2 directions (x', z') of the particles. The point file is taken into the WinAGILE to do the particle tracking.

Figure 3 shows an example of task flow of the particle tracking, called I-knowledge base. A point file generator reads the IGUN output file called `hyper_e9.trj`, and generates a point file. The point file called `hyper_e9.pnt`, is composed of lines of 4-dimensional data i.e. ray number, x, x', z, z' . These information contained in the point file are the initial parameters for WinAGILE to make calculation of the particle distribution.

In Figure 4, examples of the calculated particle distribution are shown. Particle distribution of $^7\text{Li}^{2+}$ is shown in (a) at the start point of the beam transport line, and in (b) at

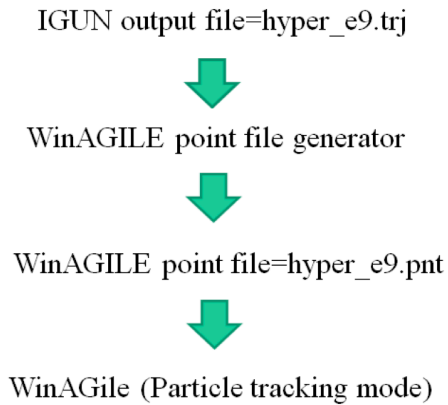


Figure 3. Task flow of the particle tracking.

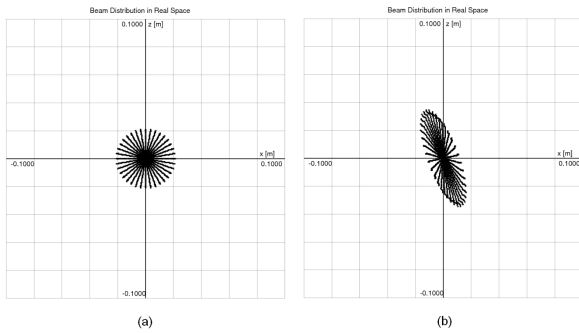


Figure 4. Calculated particle distributions of ${}^7\text{Li}^{2+}$ in x - z coordinate. Horizontal and vertical scales are 20 mm/div, respectively.

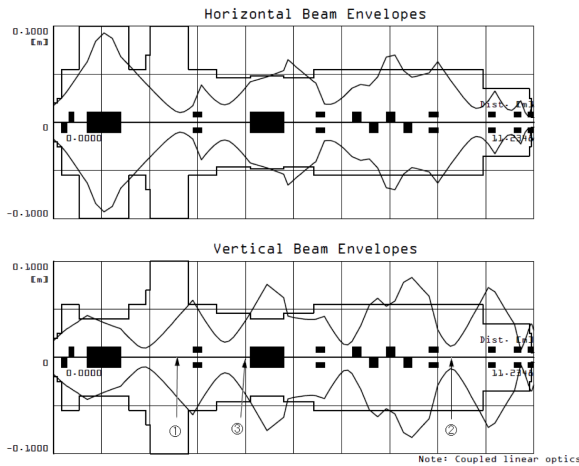


Figure 5. Beam envelopes of ${}^{20}\text{Ne}^{7+}$. Left-side axis represents start point of the LEBT. Right-axis represents median plane of the AVF cyclotron. Symbols ①, ② and ③ denote I10, I36 and KBr, respectively.

the KBr viewer.

A position of the KBr viewer is found in Fig. 5.

3. I-K convertor

The WinAGILE is an interactive program dedicated to alternating-gradient lattice design of synchrotron rings and transfer lines. An I-K convertor transforms an excitation

current of the magnetic elements to the WinAGILE parameter. Figure 5 shows calculated beam envelopes of ${}^{20}\text{Ne}^{7+}$. In Fig.5, a start line of beam envelopes denotes the exit of the ion source. Assumed beam emittance (2.23σ) is $100 \pi\cdot\text{mm}\cdot\text{mRad}$. A transport efficiency is defined as the ratio of I10 and I36. I10 and I36 mean the values of ion currents at the locations indicated in Fig. 5. I10 is located at a focal point of the magnetic mass analyzer. I36 is located at an exit of solenoid magnet, named S5. The KBr viewer is located at an entrance of the vertical bending magnet. The most particle loss occurs at the wall surface of beam chamber of the transport line. So, the beam loss is dependent on the emittance of the beam extracted from the ion source. Result of particle tracking shows $I36/I10=0.76$ using assumed beam emittance of $100 \pi\cdot\text{mm}\cdot\text{mRad}$. Measured transmission of the beam from the HyperECR was 0.67, when measured emittance of the one was $156.6 \pi\cdot\text{mm}\cdot\text{mRad}$. When using the measured emittance as the initial condition of the particle-tracking, the transmission of 0.67 was gotten. In order to achieve the transmission larger than 0.76, recommended beam emittance of the HyperECR is $100 \pi\cdot\text{mm}\cdot\text{mRad}$. We are now studying the one to make the small emittance.

4. Conclusion

A beam injection efficiency of the LEBT has been studied. In this study, we prepared the I-knowledge base for the orbit calculation of the ion source, the I-K convertor for calculating the orbit of the beam transport system. Preliminary study shows that measured results of beam transport efficiency well agree with the numerical calculation. It will become possible in near future to make precise comparison of the measured data with the simulated ones.

References

- [1] Y. Ohshiro, S. Yamaka, S. Watanabe, H. Muto and S. Kubono. "Production of stable metallic ion beams of Hyper ECR ion source" Annual Report 2011.
- [2] R.Becker, Rev. Sci. Instrum. 63 (4), April 1992
- [3] R.Becker, Proc. EBIS Symposium, Tokyo. 2004
- [4] P.J.BRYANT, <http://nicewww.cern.ch/~bryant>. WinAgile: Windows Alternating Gradient Interactive Lattice dEsign.
- [5] J.W.Stetson et al, Proc. of 2005 PAC, Knoxville, Tennessee, 2281-2283

Development of intense ^7Be and ^{22}Na beam for wear diagnostics application

A. Yoshida, A. Nakao, T. Kambara, R. Uemoto^a, H. Uno^a, H. Yamaguchi^b, T. Nakao^b, and D. Kahl^a

RIKEN Nishina Center for Accelerator-Based Science (RNC)

^a*S.H.I. Examination and Inspection (SHIEI) Ltd.*

^b*Center for Nuclear Study (CNS), University of Tokyo*

The industrial cooperation team in RNC and SHIEI Ltd. are developing a new method for wear diagnostics of industrial material using RI beams as tracers. RI nuclei are implanted in a near surface of the machine parts within depth of 100 μm , and its wear-loss is evaluated by the decrease in the measured radioactivity. Continuous γ -ray detection from the outside of the machine enables real-time diagnostics of wear in running machines. For this purpose, RI nuclei having appropriately long lifetime are desired. At present, we can provide an intense ^{22}Na ($T_{1/2} = 2.6\text{y}$) beam at RIPS separator [1] using a fragmentation reaction of ^{23}Na . As the produced ^{22}Na beam has an adequate energy of 26.6 MeV/u, it enables to implant in atmosphere and to control the depth profile easily. However, the RI beam production at RIPS needs the RRC cyclotron whose beam time scheduling is very tight. The beam production cost using RRC and RIPS is expensive, also. These two drawbacks were practical issues of developing and promoting industrial applications using RI beams.

On the other hand, CRIB group has developed a cryogenic gas target system [2] and reported production of intense ^7Be ($T_{1/2} = 53\text{d}$) and ^{22}Na beams using the system. The RI beam energy produced by CRIB is low as 4 MeV/u, approximately. Accordingly, it becomes difficult to implant in atmosphere environment. But from the point of view of beam cost and beam-time flexibility, the low energy RI beam production at CRIB using the compact AVF cyclotron independently is favorable. With the aim to utilize these intense RI beams for the wear diagnostics, beam studies managed by the industrial cooperation team collaborating with the CRIB group was performed.

The ^7Be beam was produced via $p(^7\text{Li}, ^7\text{Be})n$ reaction. A primary beam of $^7\text{Li}^{2+}$ with the energy of 5.7 MeV/u and intensity of 1.2 particle μA ($\text{p}\mu\text{A}$) was introduced to the cryogenic gas target. The H_2 target gas was confined in a gas cell (8 cm long and 2 cm in diameter) sealed by 2.5- μm -thick Havar foils. The H_2 gas at a pressure of 760 Torr was cooled by liquid N_2 in a vessel at 90 K and circulated to the gas cell at a rate of 55 slm . The primary beam was focused on a Havar foil placed at entrance of the gas cell with the spot size of 1 mm in diameter. The calculated energy loss in the gas target was 1.0 and 4.6 W at the entrance Havar foil and the target gas, respectively. The target was very stable during this experiment. The produced ^7Be beam was introduced to the F2 focal plane without degrader foil at F1. In order to enable ^7Be implantation under air pressure condition, the vacuum chamber at F2 was modified so that a vacuum-separation foil could be attached. First, under a vacuum condition, the profiles of secondary beams were measured at F2 using a PPAC and a silicon detector. The energy and radius of the $^7\text{Be}^{4+}$ beam was 28.7 MeV (4.1 MeV/u) and $\sigma = 6.1$ mm, respectively, with a momentum slit of $\pm 3.1\%$ (± 50 mm) at F1. The calculated range of this ^7Be beam into an aluminum material is 67 μm . A contaminant nuclide of $^7\text{Li}^{3+}$ was observed with a fraction of

20 % and energy of 18.8 MeV. Secondly, a Kapton vacuum-separation foil (50 μm thick and 5 cm in diameter) was assembled, and He gas at 1 atm was filled in the F2 chamber. The distance from the foil to the irradiation position was 14 cm. The ^7Li contaminant was stopped in the He gas, completely. The remainder of the ^7Be beam was 100 % in purity and its peak energy was 13.5 MeV, with a width of $\sigma = 1.6$ MeV. The intensity of the ^7Be beam was 1.9×10^8 pps obtained by the following γ -ray measurement, which reproduced the reported value in the Ref. 2.

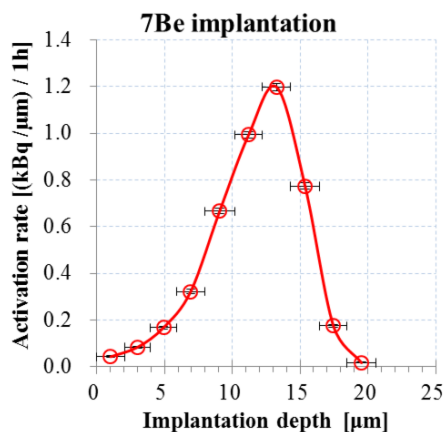


Figure 1. Implantation-depth profile of ^7Be beam into aluminum material under He gas of 1 atm environment.

In order to control the implantation depth near to the surface, a rotating energy degrader was introduced. An 8- μm -thick aluminum foil was set on the beam path at 50° (corresponding to a thickness of 10.4 μm) and 90° , alternatively, relative to the beam axis with a time fraction of 5:1. To investigate the implantation-depth profile of ^7Be , a stack of 2- μm -thick aluminum foils with a diameter of 16 mm were irradiated. After irradiation, the stack was disassembled and the intensity of the γ ray ($E_\gamma = 478$ keV) was measured using a Ge detector. The obtained implantation-depth profiles are shown in Figure 1. In this figure, the vertical axis is in the unit of (kBq/ μm)/1h irradiation with a full primary beam intensity of 1.2 $\text{p}\mu\text{A}$. X-error bars indicate the thickness of each foil. We achieved the total activity rate of 10 kBq/1h, approximately.

The ^{22}Na beam was produced via the $p(^{22}\text{Ne}, ^{22}\text{Na})n$ reaction. A primary beam of $^{22}\text{Ne}^{7+}$ with energy of 6.1 MeV/u and intensity of 0.3 $\text{p}\mu\text{A}$ was introduced to the cryogenic gas target. The H_2 gas at a pressure of 400 Torr was cooled as 90 K and circulated to the gas cell at a rate of 70 slm . The calculated energy loss in the gas target was 2.2 and 5.3 W at the entrance Havar foil of 2.5 μm in thickness and at the target gas, respectively. The target was very stable during this experiment. The produced ^{22}Na beam was introduced to the F2 focal plane without degrader foil at F1. To investigate optimum parameters for ^{22}Na beam,

RI beam		CRIB		RIPS
		${}^7\text{Be}$	${}^{22}\text{Na}$	${}^{22}\text{Na}$
Energy	MeV/u	4.1	3.69	26.6
Intensity	cps	1.9×10^8	3.1×10^7	1.5×10^8
Purity		80%	78%	100%
Activation rate	kBq/1h	~ 10	~ 0.9	~ 5
Irradiation environment		He 1 atm	Vacuum	Air 1 atm
max. Range in Al	μm	67	38	685
Primary beam		${}^7\text{Li}^{2+}$	${}^{22}\text{Ne}^{7+}$	${}^{23}\text{Na}^{11+}$
Energy	MeV/u	5.7	6.1	63.4
Intensity	μA	~ 1.0	~ 0.3	~ 1.0
Target		H_2 760 Torr	H_2 400 Torr	Be 1.5 mm

Table 1. Available RI beams for wear diagnostics.

the magnetic rigidity of CRIB separator was scanned in the range of 0.53 - 0.59 Tm. Contaminant nuclei of ${}^{19}\text{F}^{9+}$ (stable) and ${}^{22}\text{Ne}^{10+}$ (primary beam) were observed. The ${}^{22}\text{Na}$ beam had two components with different charge state as $q=10+$ and $11+$. Because the ${}^{22}\text{Na}^{10+}$ component had fudge ${}^{22}\text{Ne}^{10+}$ contamination, we have searched an optimum magnetic rigidity for ${}^{22}\text{Na}^{11+}$ beam. At the optimum condition, the energy and radius of the ${}^{22}\text{Na}^{11+}$ beam was 81.2 MeV (3.7 MeV/u) and $\sigma = 1.6$ mm, respectively, with a momentum slit of $\pm 3.1\%$ (± 50 mm) at F1. The ${}^{22}\text{Na}$ beam was 78 % in purity. The intensity was 3.1×10^7 pps obtained by the following γ -ray measurement. This beam study was performed under a vacuum condition at F2 irradiation chamber. The implantation-depth profile was measured using the same method mentioned above, observing the γ ray ($E_\gamma = 1274$ keV) from ${}^{22}\text{Na}$. The obtained profile is shown in Figure 2, here the activation rate indicates (kBq/ μm)/1h irradiation with a full primary beam intensity of 0.3 μA . We achieved the total activity rate of 0.9 kBq/1h, approximately.

References

- [1] T. Kambara *et al.*, AIP Conference Proceedings **1412** (2011) 423-429.
- [2] H. Yamaguchi *et al.*, Nucl. Instrum. Methods, Sect. A **589** (2008) 150-156.

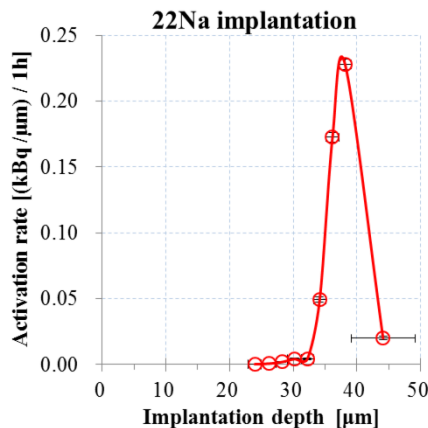


Figure 2. Implantation-depth profile of ${}^{22}\text{Na}$ beam into aluminum material under vacuum environment.

The obtained results of these beam studies are summarized in the Table 1 including the result of ${}^{22}\text{Na}$ production in RIPS. For the case of ${}^{22}\text{Na}$ beam, the total activation rate using RIPS was 5 kBq/1h irradiation, which is 5 times larger intensity than CRIB. However, this difference is nearly compensated with the difference of beam production cost between RIPS+RRC and CRIB+AVF.

Radioactive Beam Production of ^{44}Ti

H. Ishiyama^a, H. Yamaguchi, Y.X. Watanabe^a, D. Kahl, Y. Hirayama^a, T. Nakao, N. Imai^a,
Y.H. Kim^a, M. Mukai^a, M. Oyaizu^a, H. Miyatake^a, S.C. Jeong^a, Y. Wakabayashi^b, T. Hashimoto^c,
P. Lee^d, G.W. Kim^e, and T. Komatsubara^f

Center for Nuclear Study, Graduate School of Science, University of Tokyo

^a*Institute for Particles and Nuclear Studies, High Energy Accelerator Research Organization*

^b*RIKEN Nishina Center for Accelerator-Based Science*

^c*Research Center for Nuclear Physics, Osaka University*

^d*Department of Physics, Chung-Ang University*

^e*Department of Physics, Ewha Womans University*

^f*Department of Physics, Tsukuba University*

The ^{44}Ti ($T_{1/2} = 59$ yr) nuclide has recently been observed as live radioactivity by γ -ray astronomy from the Cas A supernova (SN) remnant. The observed ^{44}Ti yield is larger by a factor of 2-10 than those calculated in current SN models. The ^{44}Ti yield strongly depends not only on current SN models but also on the astrophysical reaction rates in SN nucleosynthesis. The sensitivity study for the reactions concerned suggests that several key reactions can largely affect the ^{44}Ti yield, and the $^{44}\text{Ti}(\alpha, p)^{47}\text{V}$ reaction has the highest sensitivity for the yield of ^{44}Ti , which directly destroys ^{44}Ti . Although the direct measurement of $^{44}\text{Ti}(\alpha, p)^{47}\text{V}$ cross sections was performed in the energy range from center-of-mass energy $E_{\text{cm}} = 5.7$ to 9 MeV at the Argonne National Laboratory [1], this measurement did not cover the astrophysically interesting energy regime of $E_{\text{cm}} = 4 - 6.1$ MeV, corresponding to the Gamow peak temperature of $T_9(10^9 \text{ K}) = 2.2 - 4.2$. Thus, we have proposed the direct measurement of the cross sections of $^{44}\text{Ti}(\alpha, p)^{47}\text{V}$ in the energy regime of astrophysical interest.

fore, in order to perform these measurements, we have attempted to produce a ^{44}Ti radioactive nuclear beam at CRIB.

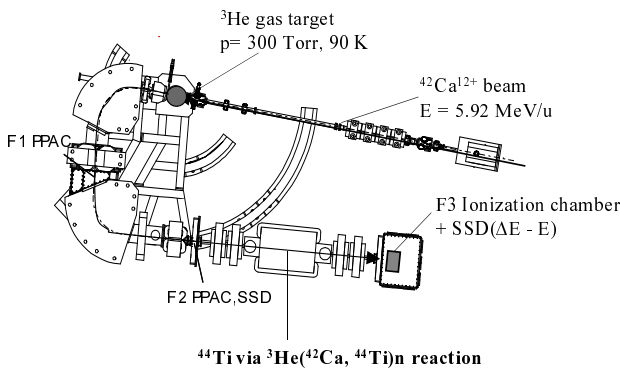


Figure 1. Experimental setup for ^{44}Ti beam production at CRIB.

Further, a compound nucleus of the $^{44}\text{Ti} + \alpha$ system is ^{48}Cr , in which $^{40}\text{Ca} + \alpha + \alpha$ three-cluster states were predicted to exist in almost the same energy regime of astrophysical interest [2]; however these states have not thus far been observed. These states can be accessible by the measurement of $^{44}\text{Ti}(\alpha, \alpha)$ resonant elastic scatterings. There-

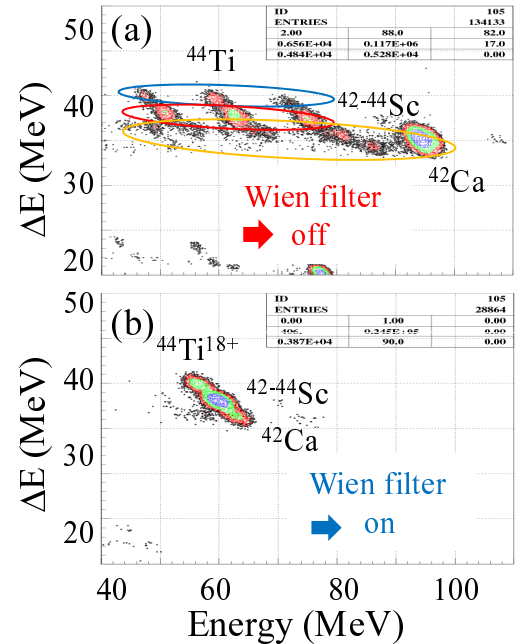


Figure 2. ΔE - E plots at F3 of CRIB. The measurements shown in panels of (a) and (b) were obtained when the Wien filter was off with the CRIB optical parameters at $A/q = 44/17+$ and $E = 110$ MeV, and when the filter on at $A/q = 44/18+$ and $E = 110$ MeV, respectively. In Fig. 2 (a), those circles indicate ^{44}Ti , $^{42-44}\text{Sc}$, and ^{42}Ca with different charge states, respectively. Particle identification was carried out by obtaining the ΔE differences based on the elastic-scattered ^{42}Ca particles and from expected possible products from the production reaction.

The experimental setup for ^{44}Ti beam production at CRIB is shown in Fig. 1. The production reaction for ^{44}Ti was selected to be the $^3\text{He}(^{42}\text{Ca}, ^{44}\text{Ti})n$ reaction. The energy of the $^{42}\text{Ca}^{12+}$ primary beam was set at 5.92 MeV/u, which is the maximum value available at the AVF cyclotron. The pressure of the ^3He gas target with 2.5- μm -thick Havar

windows was set to be 300 Torr at 90 K. The length of the ^3He gas target was 8 cm. The ^{44}Ti beam, in principle, can be separated from ^{42}Ca and other contaminants by using the in-flight separation technique at CRIB. In order to measure the intensity and purity of the ^{44}Ti beam, an ionization chamber (IC) and a solid-state Si detector (SSD) were placed at F3 (final focal plane) of CRIB, which can provide energy loss (ΔE) and residual energy (E) for particle identification.

Figure 2 shows the ΔE - E plots obtained from the IC + SSD at F3. The ^{42}Ca beam intensity was about 1 pnA. As shown in Fig. 2 (a), when the Wien filter was not on, several contaminants, particularly ^{42}Ca with the highest intensity, were observed. When the Wien-filter was on (Fig.2 (b)), most of these contaminants were removed. As the result, the observed intensity for ^{44}Ti was 130 – 350 pps (depending on the charge states)/1 pnA ^{42}Ca , corresponding to $0.9 - 2 \times 10^4$ pps/70 pnA ^{42}Ca , which is the maximum beam current for the ^3He gas target, and the beam purity was about 15%. A ^{44}Ti beam can now be generated with sufficient intensity to perform the abovementioned measurements. The particle identification for the beam contaminants can be performed using ΔE - E (TOF) measurements, in which the ΔE differences between different particles are the same as in Fig. 2 (b). After the construction of a new ionization chamber for ΔE measurement, which will be installed immediately in front of a secondary target (^4He), we plan to perform the abovementioned measurements.

References

- [1] A.A. Sonzogni *et al.*, Phys. Rev. Lett. **84** (2000) 1651.
- [2] P. Descouvemont, Nucl. Phys. A **709** (2002) 275.

Plasma Spectroscopy for Hyper-ECR Ion Source

Hideshi Muto^a, Yukimitsu Ohshiro^b, Shoichi Yamaka^b, Shin-ichi Watanabe^b, Michihiro Oyaizu^c, Shigeru Kubono^{b,c,d}, Hidetoshi Yamaguchi^b, Masayuki Kase^c, Toshiyuki Hattori^e and Susumu Shimoura^b

^a Center of general education, Tokyo University of Science, Suwa, 5000-1 Toyohira, Chino Nagano 391-0292, Japan

^b Center for Nuclear Study, University of Tokyo, 2-1 Hirosawa, Wako Saitama 351-0198, Japan

^c RIKEN Nishina Center for Accelerator-Based Science, Wako Saitama 351-0198, Japan

^d Institute of Modern Physics, Chinese Academy of Sciences, Nanchang Road 509, Lanzhou 730000, China

^e Heavy Ion Cancer Therapy Center, National Institute of Radiological Sciences, 4-9-1 Anagawa, Inage Chiba 263-855, Japan

Recently, we started to observe optical line spectra from ECR plasma using a grating monochromator with a photomultiplier [1]. The light intensity of line spectrum from the ECR plasma had a strong correlation with ion beam intensity measured by a magnetic mass analyzer. This correlation is a significant information for beam tuning because it allows the extraction of the desired ion species from the ECR plasma. Separation of ion species of the same charge to mass ratio with an electromagnetic mass analyzer is known to be an exceptionally complex process, but this research gives new insights into its simplification.

A Hyper-ECR ion source has succeeded in producing intense beams of highly charged ions [2, 3, 4, 5]. During beam tuning charge distribution of ions extracted from ECR plasma has been measured by a magnetic beam analyzer and a Faraday cup. Then, the ion beam intensity selected by the magnetic beam analyzer was maximized in order to reach the highest possible efficiency. In the process of production of multi-charged ion beams accidental appearance of the same M/Q species occur in the ECR plasma, and their separation by a magnetic beam analyzer is impossible. If optical line spectrum from our desired ions is detected, identification of the presence of the ions in the ECR plasma becomes possible. Therefore, we tried to tune the beam by watching the voltage signal of light intensity from photomultiplier combined with a monochromator.

At the Hyper ECR ion source there is a quartz window at the straight section of a beam analyzer of the Hyper-ECR ion source. A grating monochromator (JASCO CT-25C) was set outside of the quartz window connecting with a photomultiplier (Photosensor module H11462-031, Hamamatsu Photonics) as shown in Fig. 1. The monochromator is set on the source axis at the extraction side. Distance from ECR plasma to the entrance slit of the monochromator is about 1.5 m. Beam resolution of the grating is 0.1 nm (FWHM). L-37 and R-64 filters are used for preventing both second and third order light signals.

Figure 2 shows the optical line spectrum of the Hyper-ECR plasma under operation of He^{2+} ion beam. Light intensity of He II line spectrum was observed at $\lambda = 468.5$ nm ($n=3-4$). He II line complex was observed as reported often in the literature [6, 7]. Wavelengths of the lines were determined from NIST Atomic Spectra Database [8]. The ion source was tuned for the production of the He^{2+} ions. Beam intensity of the He^{2+} was set at $300 \mu\text{A}$. Multi-charged ions of residual gases such as Nitrogen and Oxygen were also observed. He II ($\lambda = 468.5$ nm) spectrum was clearly separated from other line spectra. Figure 3 shows light intensity of He II line spectrum as a function of ana-

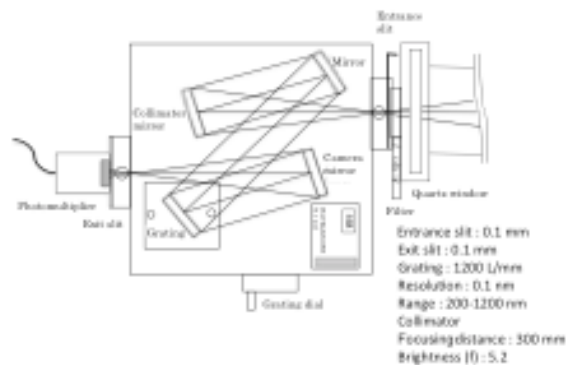


Figure 1. Schematic diagram of the grating monochromator with photomultiplier.

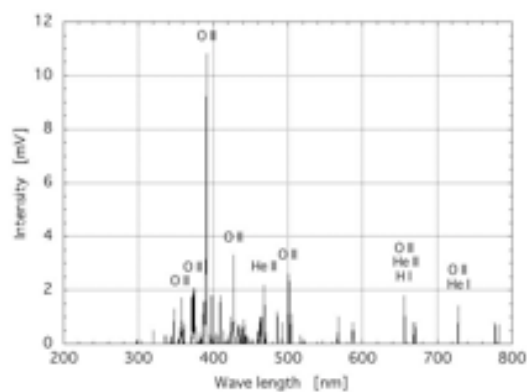


Figure 2. Optical line spectrum of the Hyper-ECR ion source under He^{2+} beam operation.

lyzed He^{2+} beam intensity. The beam intensity was tuned by controlling He gas flow rate. RF power was fixed at about 100 W. With the rising of the He^{2+} beam current, the light intensity of the He II spectrum also increased. This result clearly shows a linear correlation of these two values. Oxygen line spectrum was also observed during tuning of the multi-charged ion beams. Figure 4 shows light intensity of O VII ($\lambda = 824.176$ nm) line spectrum as a function of analyzed O^{7+} beam intensity. Wavelength of Oxygen line spectrum was determined from NIST Database and higher light intensity lines were experimentally selected from these reference lines [8]. In this experiment the gas flow rate was

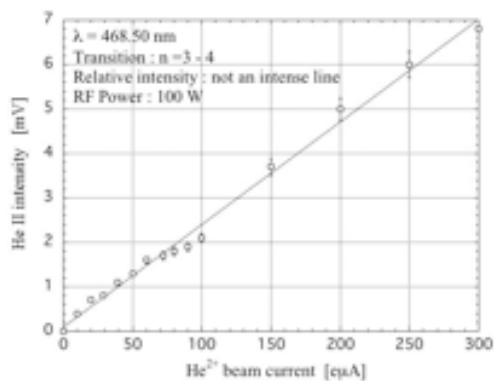


Figure 3. Strength of He II line spectrum as a function of analyzed He²⁺ beam intensity.

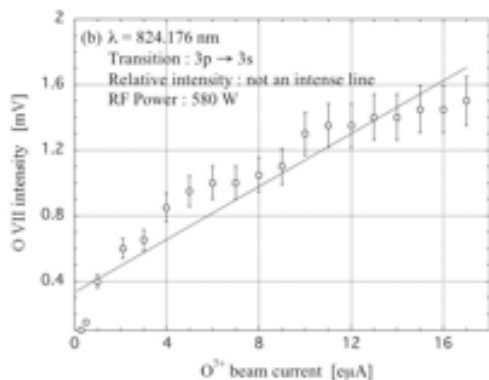


Figure 4. Light intensity of O VII line spectrum as a function of analyzed O⁷⁺ beam intensity. Wavelength of the observed line spectrum, observed transition, its relative intensity and operating RF power were shown in each figures.

controlled with the purpose of receiving an exact beam intensity. This result shows a strong correlation between light intensity and beam current in the same way as with the Helium beam, although these figures have deviation from linear relation. These results show that the light intensity signal from the photomultiplier is an essential information for the beam tuning operation.

Plasma spectroscopy was proved to be useful for ion source tuning. By this method, the observation of the existence of desired beam species in the plasma has been simplified. Also, tuning of the ion source without interrupting beam time by watching the light intensity signal of photomultiplier was successfully conducted.

References

- [1] H. Muto *et al.*, Rev. of Sci. Instr. 84 (2013) 073304.
- [2] Y. Ohshiro *et al.*, RIKEN Accel. Prog. Rep. 35 (2002) 256-257.
- [3] Y. Ohshiro *et al.*, RIKEN Accel. Prog. Rep. 36 (2003) 279-280.
- [4] Y. Ohshiro, S. Yamaka, S. Watanabe, RIKEN Accel. Prog. Rep. 38 (2005) 253.
- [5] Y. Ohshiro, S. Yamaka, S. Watanabe, RIKEN Accel. Prog. Rep. 39 (2003) 231-232.
- [6] H.P. Larson and R.W. Stanley, J. Opt. Soc. Am. 57

(1967) 1439.

[7] E.G. Kessler, Jr, Phys. Rev. A7 (1973) 408.

[8] NIST Atomic Spectra Database,
<http://www.nist.gov/pml/data/asd.cfm>

Theoretical Nuclear Physics

Rotational stabilization in exotic and heavy nuclear synthesis

Yoritaka Iwata

Center for Nuclear Study, Graduate School of Science, The University of Tokyo

1. Introduction

Let low energy heavy-ion collisions be collisions between heavy-ions with incident energies about a few MeV per nucleon in the center-of-mass frame. In the theoretical research of low energy heavy-ion collisions, one of the most important purposes is to predict the formation of both new chemical elements and new isotopes, as well as proposing a new method for producing them. Exotic and heavy nuclear synthesis has especially attracted attention with a focus on the understanding of nuclei located around the “island of stability”. In such a heavy synthesis the competition between long-range Coulomb force and short-range nuclear force is essential. For this purpose it is necessary to reduce the Coulomb repulsion by introducing the rotational motion of the composite nucleus in the collision dynamics. Indeed, the binding energy decreases due to the Coulomb effect, so that its reduction in a strongly deformed rotating system contributes to increase the binding energies of nuclear systems.

In this report the role of rotation in nuclear synthesis is discussed with the emphasis on the stabilization of the composite nucleus arising from its rotational motion. A rather new concept for the synthesis of exotic and heavy nuclei utilizing three-nucleus simultaneous collisions is reviewed following Ref [1]. Consequently two experimental setups making use of rotational stabilization are suggested.

2. Key concepts

2.1. Exotic nuclear synthesis

The most important guiding principle for producing exotic nuclei is to suppress the fast charge equilibration, which can be controlled by changing the incident energy (cf. the upper-energy limit formula for the fast charge equilibration) [2]. In particular exotic nuclear synthesis is realized by introducing relatively higher energies more than 5 to 10 MeV per nucleon. While higher energies are thus preferred for exotic nuclear synthesis, the energy should not be so high for producing heavy nuclei.

2.2. Heavy nuclear synthesis

One of the most decisive factors for producing heavy nuclei is the Coulomb repulsion, which is controlled by introducing rotation to the composite nucleus [1]. Here it is worth noting that the nonzero centrifugal force arising from the rotational motion brings about an iso-volumetric change to stretch a composite nucleus, in which the axial symmetry of the composite nucleus with respect to the rotational axis is broken, where the rotation plays the role of restoring the broken symmetry. Accordingly a thin and long composite nucleus appears due to the centrifugal force.

2.3. Rotational stabilization

The competition between the Coulomb force and nuclear force is essential to exotic and heavy nuclear synthesis. In this situation the centrifugal force modifies the balance between them. As shown in Fig. 1 the width of the nuclear potential increases depending on the quantized rotational energy (amplitude of centrifugal force), but the depth of nuclear potential is not so sensitive to it. This property is

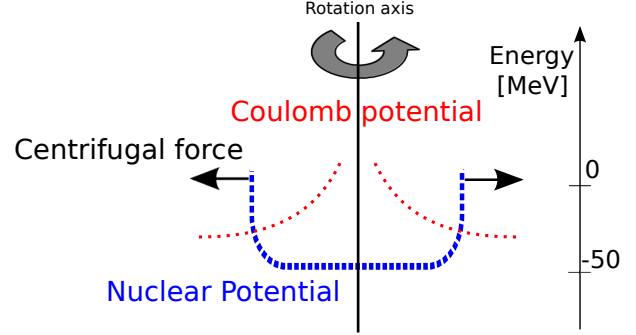


Figure 1. Illustration of the competition between nuclear, Coulomb and centrifugal forces in three-nucleus collisions in which the axially symmetric compound nucleus is assumed to be rotating. The nuclear force forms a potential basin (blue dashed curve) confining the nuclei. The Coulomb potential (red dotted curve), which is shown as it acts for the binary system (the systems being separated at a plane including and being parallel to the rotation axis), forms a repulsive potential. The centrifugal force (whose effect is shown by two symmetric black arrows) acts if rotation appears.

related to the saturation property of nuclear density. The width of the nuclear potential has a maximum value depending on the A and Z numbers of the composite nucleus; indeed, a composite nucleus breaks into two pieces if the width is larger than the maximum value. One stability criterion is whether nuclear and Coulomb potentials have a crossing point in negative energy region in Fig. 1 or not. The negative valued crossing point tends to take lower values for nuclear potentials with a larger width. Such a rough picture simply tells us the effect of the centrifugal force, which should be quantitatively examined in a microscopic framework such as (time-dependent) density functional theory.

3. Three-nucleus collisions

3.1. Stability of spherically-shaped composite nucleus

The appearance of a nonzero centrifugal force promotes the formation of multi-spherical shaped composite nuclei (for multi-spherical shaped nuclei, see Panel (a) of Fig. 4 of Ref. [1]). The exchange of stability from single-spherical to multi-spherical shapes is understood by the competition between the surface tension and the Coulomb repulsion. In Eq. (6) of Ref. [1], based on the liquid drop model, the value:

$$A_{\text{crit}}(A, Z, n) = \frac{850(A/Z)^2 n^2 2^n}{(184n - 575)2^n + 239n + 575} \quad (1)$$

is suggested to understand that competition, where n is the number of connected spherical shapes (see Panel (a) of Fig. 4). Eq. (1) means that states with $n = 1$ are less stable compared to a certain state with $n \geq 2$ if $A > A_{\text{crit}}(A, Z, n)$ is satisfied. Equation (1) is the generalization

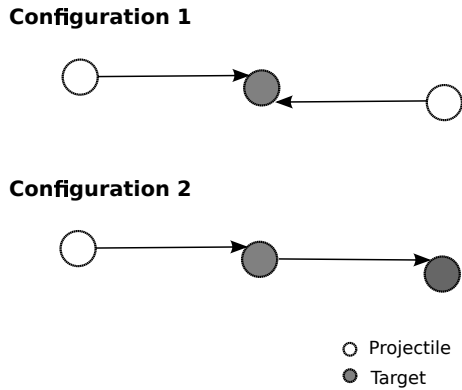


Figure 2. Two configurations of three-nucleus collisions. Two projectile nuclei are designed to collide with target nucleus (at one point) in configuration 1, while one projectile nucleus is designed to experience a sequential collision with two generally different target nuclei (at two different points) in configuration 2.

of the fissility/clusterizability into two fragments/clusters ($A = Z^2/49.2$) to the fissility into n fragments/clusters.

One method of realizing rotating composite nuclei is three-nucleus simultaneous collisions (Configuration 1 of Fig. 2). In such three-nucleus simultaneous collisions the rotational energy is controlled by the projectile energy. Here we define the simultaneous collisions by collisions within 33.3×10^{-22} s, which corresponds to the typical duration of low-energy heavy-ion reactions.

Three-nucleus simultaneous collisions leading to rotating composite nuclei with connected three-spherical shapes have been shown to produce thin and long final nuclei [1]. Furthermore the rotation has been confirmed to reduce the internal Coulomb instability [1], which is advantageous to heavy nuclear synthesis. Consequently three-nucleus simultaneous collisions are useful for the production of heavy nuclei.

3.2. Two configurations for experimental setup

Three-nucleus collisions are realized in some dense situations expected to be realized in the universe. Two configurations for three-nucleus collisions, which are feasible in experimental facilities on earth, are suggested in Fig. 2. The three nucleus simultaneous collisions can be more exactly realized in Configuration 1 than Configuration 2. Indeed, let the projectile be accelerated to x % of the speed of light, the time interval of the two collisions for Configuration 2 is estimated to be $d/(x \times 0.333) 10^{-7}$ s, where d m is the distance between the first and the second targets. Strictly speaking, three-nucleus simultaneous collisions are realized only in the case of Configuration 1. On the other hand, the expected cross sections for three-nucleus collisions are much larger in Configuration 2 than Configuration 1. In addition the rotational motion is more efficiently introduced for Configuration 1 than Configuration 2. However Configuration 2 is still attractive because of the considerably large cross section.

4. Conclusion

The exotic and heavy nuclear synthesis has been shown to be determined mostly by the incident energy and the Coulomb force. In particular, by introducing rotational mo-

tion intentionally, the Coulomb energy is controlled by the incident energy in case of Configuration 1 of Fig. 2. Three nucleus simultaneous collisions have been confirmed to be useful to the formation of thin and long structures, and therefore the formation of exotic and heavy nuclei. Here is a complicated situation in terms of controlling incident energy; first, higher energies (more than 5 to 10 MeV per nucleon) are preferred for exotic nuclear synthesis; second, energy should not be so high for heavy nuclear synthesis; third, the incident energy can be neither too high nor too low in order to reduce the Coulomb repulsion by utilizing rotation. Consequently the rotational stabilization of thin and long structures enables us to have exotic and heavy nuclear synthesis, from clustering of light nuclei to superheavy synthesis aiming at nuclei located around the island of stability [1, 3].

This work was supported by EMMI of the Helmholtz Alliance, and by HPCI Strategic Programs for Innovative Research (SPIRE) Field 5 "The origin of matter and the universe". The author thanks Prof. J. A. Maruhn for reading the manuscript carefully.

References

- [1] Y. Iwata, K. Iida, and N. Itagaki, *Phys. Rev. C* **87** (2013) 014609.
- [2] Y. Iwata, T. Otsuka, T. Ichikawa and N. Itagaki, *Phys. Rev. Lett.* **104** (2010) 252501.
- [3] Y. Iwata, T. Ichikawa, N. Itagaki, J. A. Maruhn, and T. Otsuka, in preparation.

E1 strength in calcium isotopes in view of shell-model calculations

N. Shimizu^a, Y. Utsuno^{a,b}, S. Ebata^c, M. Honma^d, T. Mizusaki^e, and T. Otsuka^{a,f,g}

^a Center for Nuclear Study, Graduate School of Science, University of Tokyo

^b Advanced Science Research Center, Japan Atomic Energy Agency

^c Meme Media Laboratory, Hokkaido University

^d Center for Mathematical Sciences, University of Aizu

^e Institute of Natural Sciences, Senshu University

^f Department of Physics, University of Tokyo

^g National Superconducting Cyclotron Laboratory, Michigan State University

1. Introduction

The giant dipole resonance (GDR) is observed experimentally by measuring photoabsorption cross section, and is intensively studied theoretically by various models, including random phase approximation with density functional theory and its variants (e.g. [1,2]). On the other hand, a small number of studies have been done about GDR in view of shell-model calculation [4, 3]. In this report, we report the study of the E1 excitations utilizing large-scale shell-model calculation aiming at a microscopic description of such collective excitation.

2. Method

We perform large-scale shell-model calculations of neutron-rich calcium isotopes. The model space consists of three major shells of harmonic oscillator, namely *sd*, *pf* and *sdg* shells. The excitation energy of each configuration is restricted to $1\hbar\omega$ or $3\hbar\omega$, where ω is a harmonic-oscillator frequency. The interaction of this model space is constructed combined with the trustworthy USD interaction for *sd*-shell [5], GXPF1B interaction for *pf*-shell [6], and Monopole-based universal interaction (VMU) [7] for the other component of the model space. It is a natural extension of the SDPF-MU interaction [8] and is successful to describe 3_1^- levels of calcium isotopes [9].

The E1 operator is defined as

$$\mathcal{O}_\mu^{(1)} = e \frac{N}{A} \sum_i^Z r_i Y_\mu^{(1)}(r_i) - e \frac{Z}{A} \sum_i^N r_i Y_\mu^{(1)}(r_i), \quad (1)$$

where e , r , and Y denote the electric charge, radius, and spherical harmonics. In this definition, the contamination of the spurious center-of-mass motion is subtracted from the isovector transition operator. Moreover, Lawson method is used to remove its contamination in the shell-model wave function [10].

The photoabsorption cross section is evaluated as

$$\sigma(E) = \sum_i \frac{16\pi^3}{9\hbar c} E_i B(E1; 0_1^+ \rightarrow 1_i^-) \delta(E - E_i) \quad (2)$$

$$B(E1; 0_1^+ \rightarrow 1_i^-) = \left| \langle 0_1^+ || \mathcal{O}^{(1)} || 1_i^- \rangle \right|^2, \quad (3)$$

where E_i is the excitation energy of 1_i^- state.

3. Results and discussions

Figure 1 shows the shell-model results of the photoabsorption cross section comparing with the experimental value [11]. The green dashed line in Fig. 1 shows the result with $1\hbar\omega$ model space. Because the ground 0_1^+ state

has positive parity, it is calculated with $0\hbar\omega$ model space, or within *pf* shell. The excited 1^- states consist of $1\hbar\omega$ configurations, in other words, one-particle excitation from *sd* shell to *pf* shell or that from *pf* shell to *sdg* shell is allowed. We adopt the strength function of the Lanczos algorithm [12] to obtain photoabsorption cross section. The discrete strength is smoothed out by the Lorentz distribution, the width of which is taken as $\Gamma = 1\text{MeV}$.

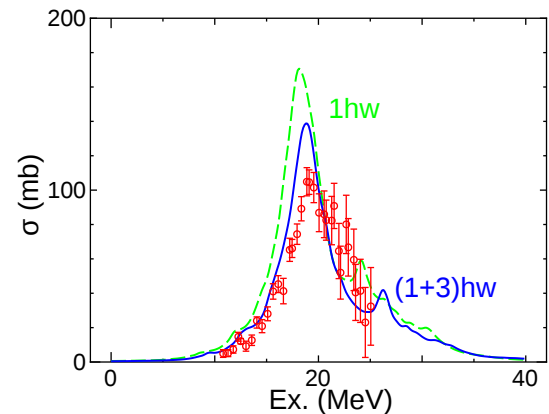


Figure 1. (Color online) Photoabsorption cross section of ^{48}Ca against excitation energy. The green dashed (blue solid) line denotes the shell-model result with $1\hbar\omega$ ($(1+3)\hbar\omega$) model space. The red circles with error bars are given by the experiment [11].

The result with $1\hbar\omega$ model space reproduces the experimental peak energy successfully. However, the peak height is rather overestimated. We also performed the shell model calculation up to $3\hbar\omega$ excitations in *sd-pf-sdg* shells. In this case, the ground state was calculated up to $2\hbar\omega$ excitations. The result is shown as the blue solid line in Fig. 1. While the M -scheme dimension of $1\hbar\omega$ model space is rather modest, 2.8×10^6 , the dimension of $(1+3)\hbar\omega$ space reaches 7.9×10^9 . We succeeded in performing such huge numerical calculations by utilizing state-of-the-art massive parallel computers, specifically, FX10 supercomputer at the University of Tokyo and BX9000 supercomputer at Japan Atomic Energy Agency. We utilized the shell-model code *KSHELL*, which was developed especially for massive parallel computation [13]. It is demonstrated that the contribution of $3\hbar\omega$ configuration suppresses the peak height and gives the reasonable agreement with the experimental value. The similar tendency is also seen in the cases of ^{42}Ca and ^{44}Ca . Further analysis is in progress.

4. Acknowledgments

This work has been supported by a Grant-in-Aid for Scientific Research (23244049) from JSPS, the HPCI Strategic Program from MEXT, and the CNS-RIKEN joint project for large-scale nuclear structure calculations. N.S. acknowledges Toshio Suzuki for fruitful discussions.

References

- [1] I. Stetcu, A. Bulgac, P. N. Magierski, and K. J. Roche, *Phys. Rev. C* **84**, 051309(R) (2011).
- [2] T. Inakura, T. Nakatsukasa, and K. Yabana, *Phys. Rev. C* **84**, 021302(R) (2011).
- [3] R. Schwengner *et al.*, *Phys. Rev. C* **81**, 054315 (2010).
- [4] H. Sagawa and T. Suzuki, *Phys. Rev. C* **59**, 3116 (1999).
- [5] B. A. Brown and B. H. Wildenthal, *Annu. Rev. Nucl. Part. Sci.* **38**, 29 (1988).
- [6] M. Honma, T. Otsuka and T. Mizusaki, *RIKEN Accel. Prog. Rep.* **41**, 32 (2008).
- [7] T. Otsuka, T. Suzuki, M. Honma, Y. Utsuno, N. Tsunoda, K. Tsukiyama, and M. H.-Jensen, *Phys. Rev. Lett.* **104**, 012501 (2010).
- [8] Y. Utsuno, T. Otsuka, B. A. Brown, M. Honma, T. Mizusaki, and N. Shimizu, *Phys. Rev. C* **86**, 051301(R) (2012).
- [9] Y. Utsuno *et al.*, in preparation.
- [10] D. H. Gloeckner and R. D. Lawson, *Phys. Lett.* **53B**, 313 (1974).
- [11] G. J. O’Keefe, M. N. Thompson, Y. I. Assafiri, and P. E. Pywell, *Nucl. Phys. A* **469**, 239, (1987).
- [12] R. R. Whitehead, in “Moment Methods in Many Fermion Systems”, edited by B.J. Dalton, S.M. Grimes, J.D. Vary, and S. A. Williams (Plenum, New York, 1980), p. 235.
- [13] N. Shimizu, *et al.*, code *KSHELL*, unpublished.

The behavior of PDR and $E1$ polarizability with respect to neutron skin-thickness

S. Ebata and T. Nakatsukasa^a

Meme Media Laboratory, Hokkaido University

^a*RIKEN Nishina Center*

To define a neutron-skin thickness is a very important topic in nuclear physics. The neutron-skin thickness is the difference between neutron and proton density distributions, and it will be connected with nuclear symmetry energy intimately. In neutron-rich nuclei far from stability line, the appearance of large neutron-skin is expected. To understand the structure of unstable nuclei, and also nuclear matter property from finite nuclear system, it is important to investigate the character of skin thickness.

The low-lying electric dipole ($E1$) mode is known as a characteristic excited state of neutron-rich nuclei, which is often called Pygmy dipole resonance (PDR). The PDR are sometimes explained as a neutron-skin mode, because neutron-rich unstable nuclei have neutron-skin or halo structure in their ground state [1]. Some previous studies indicate that there is a linear relation between the sum of PDR strength and neutron-skin thickness [2, 3]. On the other hand, it is reported that the correlation between PDR and the skin is small from a covariance analysis [4]. Furthermore, Ref. [4] indicates that the $E1$ polarizability is much more correlated to the neutron skin than PDR. Both previous studies are performed in the limited region, i.e., Sn isotopes and $Z < 40$, with only one interaction parameter [2, 3], and special nuclei: ^{132}Sn , ^{208}Pb [4]. In this report, we discuss the behavior of PDR and $E1$ polarizability with respect to neutron-skin thickness in wide mass region including neutron-rich, unstable, deformed and heavy nuclei.

To study nuclear dynamics in wide mass region, we had proposed the canonical-basis time-dependent Hartree-Fock-Bogoliubov (Cb-TDHFB) theory [5]. And we performed this method in the three-dimensional coordinate-space representation, where any type of deformation can be handled and is treated the pairing correlation in the Bardeen-Cooper-Schrieffer (BCS)-like approximation. The Cb-TDHFB equations can be derived from the full TDHFB equation. They are written as

$$i\hbar\dot{\phi}_l(r,t) = (\hat{h}[\rho(t)] - \eta_l(t))\phi_l(r,t), \quad (1)$$

$$i\hbar\dot{\rho}_l(t) = \Delta_l^*(t)\kappa_l(t) - \Delta_l(t)\kappa_l^*(t), \quad (2)$$

$$i\hbar\dot{\kappa}_l(t) = (\eta_l(t) + \eta_{\bar{l}}(t))\kappa_l(t) + \Delta_l(t)(2\rho_l(t) - 1), \quad (3)$$

where $\phi_l(r,t)$ means the canonical basis. $u_l(t)$ and $v_l(t)$ correspond to the time-dependent BCS factors. $\rho_l(t) = |v_l^2(t)|$ and $\kappa_l(t) = u_l(t)v_l(t)$ are occupation- and pair-probability. $\Delta_l(t)$ indicates the pair potential. We have gauge freedom which is fixed by choosing the time-dependent function, $\eta_l(t) \equiv \langle \phi_l(t) | \hat{h} | \phi_l(t) \rangle + i\hbar \langle \frac{\partial \phi_l}{\partial t} | \phi_l(t) \rangle$. Equations (1) - (3) conserve the orthonormality of the canonical basis, the average of particle number and the total energy in real time. Details of the Cb-TDHFB equations and the adopted energy functionals are given in Ref. [5].

We carried out a systematic investigation of $E1$ strength from light to heavy isotopes with a Skyrme energy functional for the particle-hole channel. We solved the Cb-TDHFB equations in real time and computed the linear response of the nucleus. For the linear-response calcu-

lation, we add an external field $\hat{V}_{\text{ext}}(r,t) \equiv -k\hat{F}\delta(t)$ to the HF+BCS or HF ground state, where \hat{F} is a one-body operator and k is an arbitrary small parameter. In this study, we selected the $E1$ operator, $\hat{F}_{E1} = (N/A)\sum_p \hat{r}_p - (Z/A)\sum_n \hat{r}_n$, here $r = (x,y,z)$. We obtained the strength function $S(E1;E)$ through the Fourier transformation of the time-dependent expectation value of \hat{F}_{E1} .

To show the availability of Cb-TDHFB for heavy deformed superfluid nuclei, Fig. 1 shows the photo nuclear reaction cross section of ^{172}Yb . The black symbols show the experimental data [6], and the lines show the results computed using the SkM* Skyrme parameter set. In this calculation, the ground state of ^{172}Yb shows prolate deformation ($\beta = 0.32$), and both neutrons and protons are in the superfluid phase ($\Delta_n = 0.76, \Delta_p = 0.55$ MeV). In the present work, we employ a schematic pairing functional [5]. Our results can reproduce experimental data very well. We in-

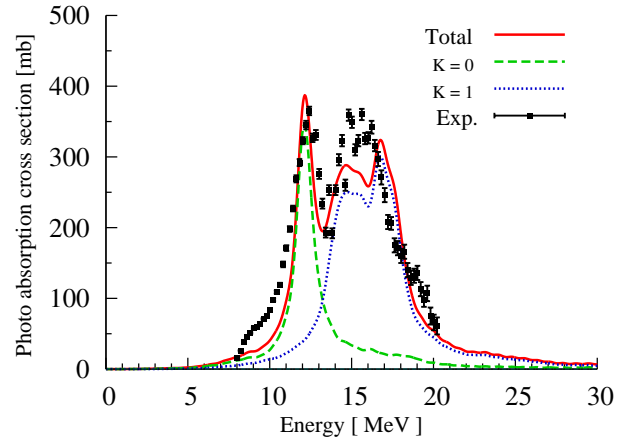


Figure 1. Photo nuclear reaction cross section of ^{172}Yb . Black symbols show the experimental data [6]. Solid line shows the total cross section, which can be decomposed into $K=0$ and $K=1$. The Skyrme functional of the SkM* parameter set and the smoothing parameter $\Gamma = 1$ MeV are used.

vestigated the $E1$ strength using this linear response calculation for about 350 isotopes.

To quantify the PDR, we used the following ratio;

$$\frac{m_1(E_c)}{m_1} \equiv \frac{\int^{E_c} E \times S(E1;E)dE}{\int^{E_T} E \times S(E1;E)dE}, \quad (4)$$

where we adopt the cutoff energy $E_c = 10$ MeV and the total energy $E_T = 100$ MeV in the present calculation. We regard the strength below the E_c as PDR strength. The $E1$ polarizability α_D is defined using $E1$ strength as,

$$\alpha_D \equiv 2 \int^{E_T} \frac{S(E1;E)}{E} dE. \quad (5)$$

Figure 2 shows the PDR ratio defined by Eq.(4) for even-even isotopes with $Z = 32 - 50$, as a function of neutron-skin thickness which is defined by the difference between root mean square radii of neutron and proton. In both panels, open circles and triangles indicate the isotopes with $N=50$ and 82 , respectively. We can see the linear relation between

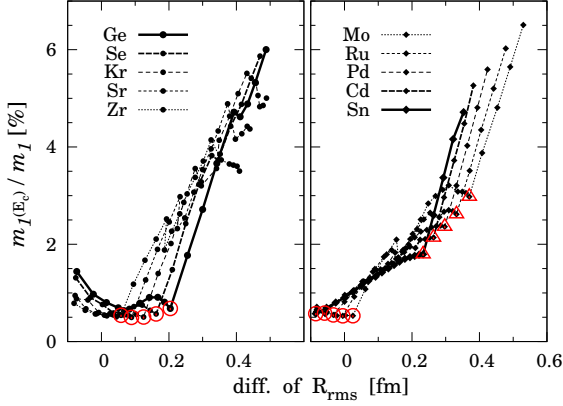


Figure 2. PDR ratio defined by Eq.(4), as a function of N -skin thickness from Ge to Sn isotopes. Open circle and triangle symbols indicate the isotope with $N=50$ and 82 , respectively.

the PDR ratio and the neutron-skin thickness for each isotopic chain for $N > 50$, although including deformed nuclei. The slope of the linear correlation becomes small as the proton number approaches $Z=50$. The slope for Sn isotope from $N=50$ to 82 is about half of that for Ge isotope. The gradient of linear relation, however, becomes large again $N > 82$ which is similar to that for Ge isotopes.

Figure 3 shows the $E1$ polarizability α_D as a function of neutron-skin thickness for Sn isotopes. Circles (squares) are obtained with the SkM* (SkI3) Skyrme energy functional. Open symbols in Fig.3 are computed from the $E1$ strength excluding the PDR part;

$$\tilde{\alpha}_D \equiv 2 \int_{E_c}^{E_T} \frac{S(E1; E)}{E} dE. \quad (6)$$

We can see that the α_D is strongly correlated with the skin-thickness, although the contribution of the PDR becomes large in both results over $N=82$, which can be seen in the difference between α_D and $\tilde{\alpha}_D$. The magnification of the difference is corresponding to the jump of PDR ratio at $N=82$ in Fig.2. The correlation between α_D and the skin thickness is more stable for change of the neutron number than the case of PDR, and the change of interaction also.

We carried out the systematic investigation of the $E1$ strength using the Cb-TDHFB in three-dimensional space which can describe nuclear dynamics with deformation effects while treating pair correlation in a BCS-like approximation. We investigate the behavior of the PDR and α_D as a function of neutron-skin thickness. In the PDR ratio case, the linear relations appear in each isotopes but partially, the correlation has a strong neutron-number dependence. The correlation becomes strong in more unstable nuclei which have $N > 50$ and > 82 in Ge and Sn isotopes, respectively. In contrast, the relation between α_D and neutron-skin is stable for the change of neutron number and energy functional. Our results, however, indicate that the covariance of α_D and the skin in a change of interaction will have neutron number dependence, especially $N > 84$. If we use the PDR and α_D to probe the property of neutron-skin, we should understand their characteristic particle-number dependence.

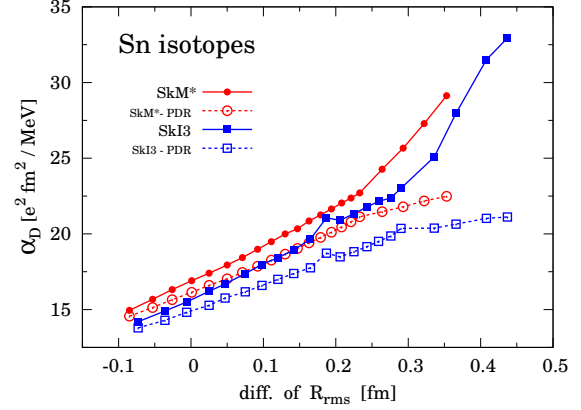


Figure 3. $E1$ polarizability defined by Eq.(5), and neutron-skin thickness for Sn isotopes with $N = 50 - 90$. Circles (squares) with solid lines indicate results with SkM* (SkI3) parameter set. Open symbols are evaluated by Eq.(6)

Currently, we are investigating the relation between α_D and other physical quantities (particle numbers, symmetry energy slope, etc.). We will apply the Cb-TDHFB to investigation of other excitation modes (monopole, quadrupole, etc.) and heavy-ion collision dynamics.

This contribution was done when the author was a member of Center for Nuclear Study, University of Tokyo.

References

- [1] I. Tanihata, *et al.*: *Phys. Rev. Lett.* **55** (1985) 2676.
- [2] J. Piekarewicz: *Phys. Rev. C* **73** (2006) 044325.
- [3] T. Inakura, *et al.*: *Phys. Rev. C* **84** (2011) 021302.
- [4] P.-G. Reinhard and W. Nazarewicz: *Phys. Rev. C* **81** (2010) 051303(R).
- [5] S. Ebata *et al.*: *Phys. Rev. C* **82** (2010) 034306.
- [6] A. M. Goryachev and G. N. Zalesnyy: *Vopr. Teor. Yad. Fiz.* **5** (1976) 42.

Shape transitions in exotic Si and S isotopes and tensor-force-driven Jahn-Teller effect

Y. Utsuno^{a,b}, T. Otsuka^{c,b,d,e}, B. A. Brown^{d,e}, M. Honma^f, T. Mizusaki^g, and N. Shimizu^b

^aAdvanced Science Research Center, Japan Atomic Energy Agency

^bCenter for Nuclear Study, Graduate School of Science, University of Tokyo

^cDepartment of Physics, University of Tokyo

^dDepartment of Physics and Astronomy, Michigan State University

^eNational Superconducting Cyclotron Laboratory, Michigan State University

^fCenter for Mathematical Sciences, University of Aizu

^gInstitute for Natural Sciences, Senshu University

1. Introduction

The tensor force is regarded as one of the main sources which cause the evolution of shell structure (i.e., shell evolution) [1]. Although single-particle evolutions in various regions are obtained in accordance with experiment by including the tensor force, the effect of the tensor-force driven shell evolution on many-body properties has not been investigated in detail. The aim of this study (the work published in [2]) is to show (i) a clear evidence for the evolution of the spin-orbit splitting and (ii) an onset of deformation, both of which are due to the tensor force. For (i), fragmentation of single-particle states must be calculated. For (ii), deformation degree of freedom must be included. In this study, we carry out a large-scale shell-model calculation for describing those properties, with a new effective interaction including a proper tensor force.

2. SDPF-MU interaction

In this study, taking the full sd - pf shell as the valence shell, we focus on the nuclear structure evolving from $N = 20$ to 28, where the $0f_{7/2}$ orbit is mainly occupied. The evolution of the proton sd shell is of particular interest, which is dominated by the two-body interaction that connects between the sd shell and the pf shell. For this part of interaction, we adopt a refined version of the V_{MU} interaction [3]. The refined V_{MU} interaction consists of the tensor force of the $\pi + \rho$ meson exchange potential, the spin-orbit force of the M3Y interaction [4], and the central force of a density (or center-of-mass coordinate) dependent Gaussian. The difference from the original V_{MU} is the inclusion of the two-body spin-orbit interaction and the introduction of the density dependence for the central force. The latter is aimed at better agreement of the monopole matrix elements between V_{MU} and the GXPF1 interaction that is adopted as a reference interaction. As for the effective interaction for the sd shell and that for the pf shell, we take the USD interaction [5] and the GXPF1B interaction [6], respectively. The sd - pf shell interaction thus constructed is named SDPF-MU interaction.

The SDPF-MU interaction is characterized as an interaction that has a reasonable strength of the tensor force, complying with the Renormalization Persistency [3, 7]. In other words, the shell evolution due to the tensor force [1] can be examined from comparison between experiment and theory.

3. Evolution of the spin-orbit splitting due to the tensor force

The tensor force can be distinguished from other components in terms of the effect of the spin-orbit splitting. Namely, the tensor force causes a sharp reduction or en-

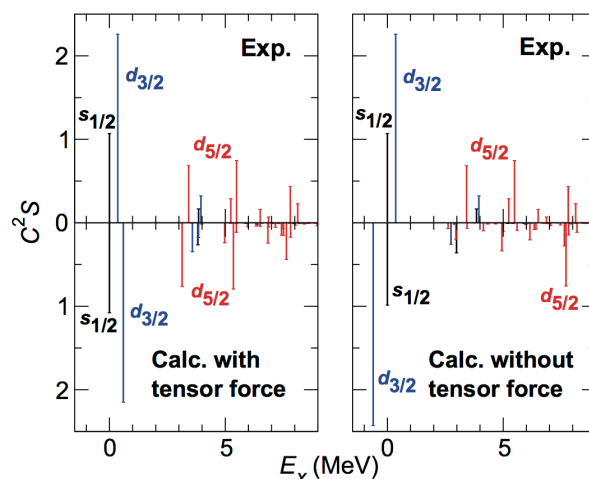


Figure 1. Spectroscopic factors for one-proton removal from ^{48}Ca compared between experiment (upper) and theory (lower). The experimental data are taken from [8]. The lower left and lower right panels show the calculations with and without the tensor force in the cross-shell interaction, respectively.

largement of the spin-orbit splitting in filling up a $j_>$ or $j_<$ orbit, whereas other components give much weaker effects. Hence, direct observation of the spin-orbit splitting is a key to probe the tensor-force driven shell evolution. The distribution of spectroscopic factors provides a good testing ground for this purpose.

Figure 1 shows the distribution of spectroscopic factors for one-proton removal from ^{48}Ca . Following the mechanism of [1], the tensor force reduces the spin-orbit splitting in ^{48}Ca from that in ^{40}Ca . The shell-model calculation with the full tensor force reproduces the distribution of spectroscopic factors very well, indicating a reasonable spin-orbit splitting (~ 5 MeV) described by the SDPF-MU interaction. On the other hand, if the tensor force is removed from the cross-shell interaction, the proton spin-orbit splitting is kept to be ~ 7 MeV, causing large discrepancy between experiment and theory. It is noted that both calculations give the same single-hole states for ^{40}Ca , the positions of which are in agreement with experimental centroids. Thus, the evolution of the spin-orbit splitting due to the tensor force is clearly demonstrated.

4. Large deformation in ^{42}Si due to the tensor force

Next, we have examined the effect of the tensor force on collectivity. Figure 2 displays the energy levels and the $B(E2)$ values for neutron-rich Si and S isotopes. It is shown

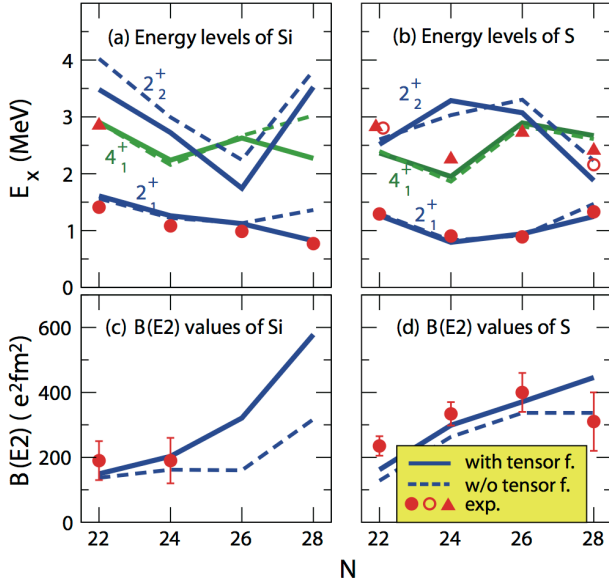


Figure 2. (a), (b) Energy levels and (c), (d) $B(E2; 0_1^+ \rightarrow 2_1^+)$ value of Si and S isotopes compared between experiment (symbols) and theory (lines). The solid and dashed lines stand for the shell-model calculation with and without the tensor force, respectively.

that the shell-model calculation with the SDPF-MU interaction gives very good agreement with experiment. It is interesting to compare between calculations with and without the tensor force. Although both the calculations give rather similar values for S isotopes, the tensor force plays a crucial role in the location of the 2_1^+ level in ^{42}Si . The low 2^+ level in ^{42}Si is a consequence of the development of deformation as illustrated in Fig. 3. The tensor force works to shift the shapes of Si isotopes toward larger oblate deformation as a whole, and this effect is most prominent for the $N = 28$ nucleus ^{42}Si .

The development of deformation is explained with the shell evolution. As demonstrated in the last section, the proton spin-orbit splitting is reduced by the tensor force. As a result, the proton $0d_{5/2}$ orbit is closer to the $1s_{1/2}$ orbit. Once those two orbits are coming close enough, the $0d_{5/2}$ orbit does not necessarily form a good subshell closure and a deformation can occur due to a mixing between $0d_{5/2}$ and $1s_{1/2}$. This mixing favors an oblate deformation for Si isotopes rather than a prolate deformation as discussed in more details in [2] using a simple $Q \cdot Q$ residual interaction. This onset of deformation is analogous to the Jahn-Teller effect in which deformation is induced by near-degeneracy of single-particle orbits. Since the near-degeneracy is due to the tensor force in the present case, we name the onset of deformation in ^{42}Si "tensor-force-driven Jahn-Teller effect."

References

- [1] T. Otsuka *et al.*, Phys. Rev. Lett. **95** (2005) 232502.
- [2] Y. Utsuno *et al.*, Phys. Rev. C **86** (2012) 051301(R).
- [3] T. Otsuka *et al.*, Phys. Rev. Lett. **104** (2010) 012501.
- [4] G. Bertsch *et al.*, Nucl. Phys. A **284** (1977) 399.
- [5] B. A. Brown and B. H. Wildenthal, Annu. Rev. Nucl. Part. Sci **38** (1988) 29.
- [6] M. Honma *et al.*, RIKEN Accelerator Progress Report **41** (2008) 32.

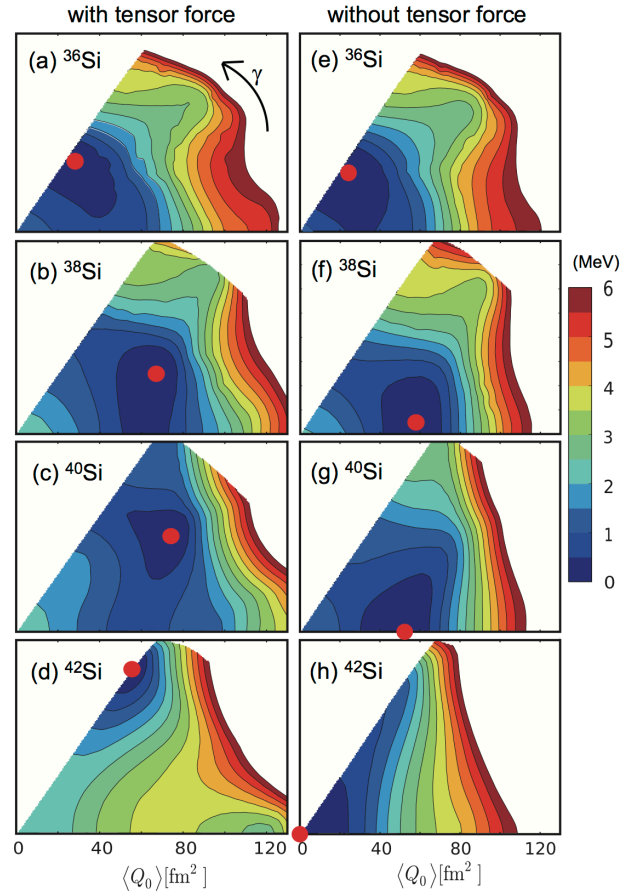


Figure 3. Potential energy surfaces of Si isotopes compared between effective interactions with and without the tensor force.

- [7] N. Tsunoda *et al.*, Phys. Rev. C **84** (2011) 044322.
- [8] G. J. Kramer *et al.*, Nucl. Phys. A **679** (2001) 267.

Shell-model calculation of the high-spin states in neutron-rich Cr isotopes

T. Togashi^a, N. Shimizu^a, Y. Utsuno^{a,b} and T. Otsuka^{a,c}

^aCenter for Nuclear Study, Graduate School of Science, University of Tokyo

^bAdvanced Science Research Center, Japan Atomic Energy Agency

^cDepartment of Physics, University of Tokyo

The recent development of experimental measurement for the properties of neutron-rich nuclei has motivated the construction of novel effective interactions in the region far from the valley of stability as the basic theoretical interest. For the medium-mass fp -shell nuclei, the recently developed GXPF1A [1] has succeeded to describe the low-lying states with high accuracy in the shell-model calculations for the fp -shell model space. However, the observation in some odd-mass neutron-rich chromium (Cr) nuclei [2, 3, 4] reveals that the excitation energy of $9/2_1^+$ state drops down considerably with increasing neutron number, which cannot be explained by GXPF1A [5] and indicates that the model space should be expanded at least to the higher gds shell including the intruder $1g_{9/2}$ orbit. Furthermore, the high spin states in ^{55}Cr and ^{57}Cr have been measured as the rotational bands of $9/2_1^+$ state [2, 3]. The study of high-spin states in the even-even Cr isotopes is also expected to gain information about the excitation of single-particle orbit and the collectivity. Therefore, to describe both of low-lying and high-spin states in Cr isotopes, we examine the effective Hamiltonian in the expanded $fp + gds$ -shell model space.

In this report, we applied the shell-model calculation for the $fp + gds$ -shell model space to the Cr isotopes, $^{53-59}\text{Cr}$. For full $fp + gds$ -shell model space, the dimension of Hamiltonian matrix is over the order of 10^{10} to be current limitation of the direct diagonalization by the Lanczos method [6]. Hence, in order to decrease the dimension of Hamiltonian matrix below the order of 10^{10} and adopt the important orbits, we truncated the configuration for the gds shell that one neutron is allowed to occupy the $1g_{9/2}$ or $2d_{5/2}$ orbit, which means that only the $1p-1h$ excitation to the gds shell occurs in unnatural parity states. We diagonalized the Hamiltonian matrix in full fp -shell model space and the above truncation with the M scheme by using MShell64 [7]. We applied the prescription of Gloeckner and Lawson [8] with the parameter $\beta_{c.m.}\hbar\omega/A = 10$ MeV to remove the spurious center-of-mass motion induced by the excitation from a fp -shell orbit to the $1g_{9/2}$ or $2d_{5/2}$ orbit. We examined the Hamiltonian composed of GXPF1A for the fp shell and V_{MU} [9], which has the tensor force as the $\pi+\rho$ meson exchange force and the central force of a simple Gaussian form so as to reproduce monopole properties of the shell-model interactions in sd and fp shells, for the gds shell and the cross part between fp and gds shells. V_{MU} in this work has density dependence similar to the one in Ref. [10].

In the above Hamiltonian, the bare single-particle energies (bspe) of the $1g_{9/2}$ and $2d_{5/2}$ orbits are undetermined. We determined these bare single-particle energies as $1g_{9/2}$ bspe = $2d_{5/2}$ bspe = 0.881 MeV by considering the splitting between $1g_{9/2}$ and $2d_{5/2}$ orbits in the effective single-particle energies (ESPEs) and fitting the excitation energies of $9/2_1^+$ state in odd-mass neutron-rich Cr isotopes in the followings.

Figure 1 shows the ESPEs of each neutron orbit in

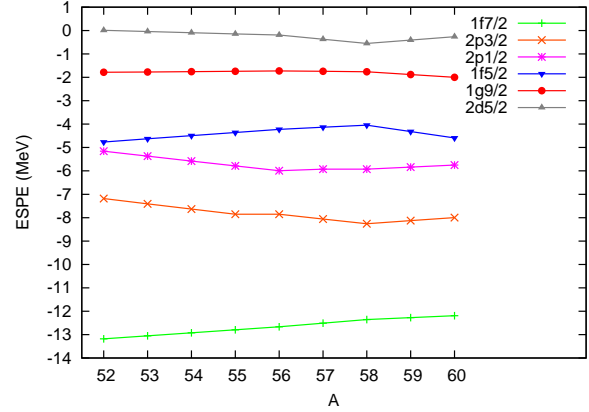


Figure 1. Effective single-particle energies (ESPEs) of the neutron for Cr ($Z=24$) isotopes calculated with GXPF1A + V_{MU} .

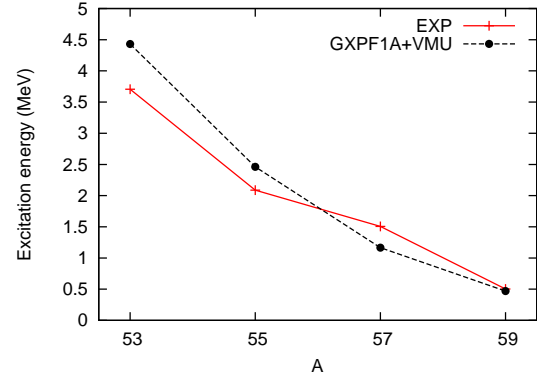


Figure 2. The plot of excitation energies of $9/2_1^+$ state in odd-mass $^{53-59}\text{Cr}$. The red solid and black dashed lines represent the experimental data and this theoretical results, respectively. The experimental data of ^{53}Cr and $^{55-59}\text{Cr}$ are taken from Refs. [11] and [2, 3, 4], respectively.

$^{52-60}\text{Cr}$ isotopes. We adopted the $1g_{9/2}$ bspe equal to the $2d_{5/2}$ one since the splitting between $1g_{9/2}$ and $2d_{5/2}$ orbits becomes around 1.8 MeV whose value is analogous to the gds -shell ls splitting on top of ^{48}Ca [12]. These values were determined by using the excitation energies of $9/2_1^+$ state in the next.

Figure 2 shows the experimental and theoretical excitation energies of $9/2_1^+$ state in odd-mass $^{53-59}\text{Cr}$. We tuned the $1g_{9/2}$ bspe (= $2d_{5/2}$ bspe) to be the best fitting to the excitation energies of $9/2_1^+$ state in $^{55,57,59}\text{Cr}$. The theoretical excitation energies of $9/2_1^+$ state are entirely reproduced but its tendency of change with increasing neutron number is not similar to the experimental data around ^{57}Cr . Since the ground $3/2_1^-$ state in ^{57}Cr lies above the $5/2_1^-$ state in the fp -shell calculation by using GXPF1A [5] and it means to be underbound, the fp -shell effective interaction may be needed to be adjusted.

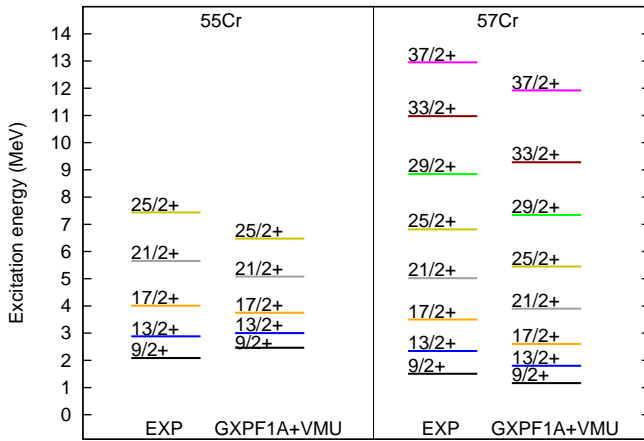


Figure 3. Positive-parity level schemes of ^{55}Cr in the left panel and ^{57}Cr in the right one. The experimental data in the left and this theoretical results in the right are compared in each panel. The experimental data of $^{55,57}\text{Cr}$ are taken from Refs. [2, 3], respectively.

Figure 3 shows the experimental and theoretical level schemes of positive parity states in ^{55}Cr and ^{57}Cr . The theoretical intervals of energy levels in the states below $J=25/2$ are smaller than experimental ones, while its intervals in the higher-spin states are restored to the moderate agreement with the experiment. That indicates that the moments of inertia in the states below $J=25/2$ become larger than the nature due to the larger deformation derived from the effective interaction at this stage.

Figure 4 shows the experimental and theoretical level schemes of negative parity states in ^{56}Cr and ^{58}Cr . Similar to the positive parity states of odd-mass Cr nuclei, the theoretical intervals of the low-spin energy levels are smaller than the experiment but they seem not to be as large deficiency as those of odd-mass Cr nuclei. In these calculations, the staggering signatures are predicted in addition to the experimental candidates. In ^{56}Cr , the low-spin states of 3_1^- , 4_1^- , and 5_1^- are predicted around the 7_1^- state, while another theoretical calculation [13] predicts the 3_1^- state below 3.0 MeV. In ^{58}Cr , the experimental 7^- candidate is predicted as the first excited 7_2^- state and the lower-spin states than 5^- , the 3_1^- and 4_1^- states, lie above the 5_1^- state.

As perspective, to improve the energy levels in these results, we attempt to adjust the two-body matrix elements of this Hamiltonian and calculate by using other effective interactions.

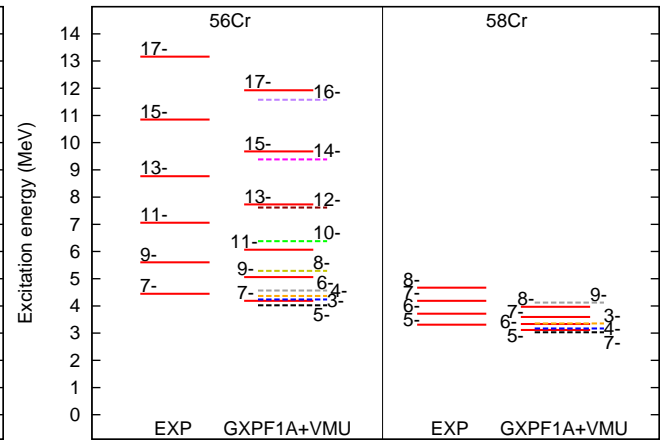


Figure 4. Negative-parity level schemes of ^{56}Cr in the left panel and ^{58}Cr in the right one. The experimental data in the left and this theoretical results in the right are compared in each panel. The experimental data of $^{56,58}\text{Cr}$ are taken from Ref. [5]. In the theoretical results, the solid and dashed lines represent the states corresponding to the experiment and the theoretical predicted ones, respectively.

- [8] D.H. Gloeckner and R.D. Lawson, Phys. Lett. **53B** (1974) 313.
- [9] T. Otsuka *et al.*, Phys. Rev. Lett. **104** (2010) 012501.
- [10] B.A. Brown, W.A. Richter, R.E. Julies and B.H. Wildenthal, Ann. Phys. **182** (1988) 191.
- [11] National Nuclear Data Center (NNDC), information extracted from the NuDat2 database, <http://www.nndc.bnl.gov/nudat2/>.
- [12] A. Bohr and B.R. Mottelson, Nuclear Structure vol. 2.
- [13] K. Kaneko, Y. Sun, M. Hasegawa and T. Mizusaki, Phys. Rev. C **78** (2008) 064312.

References

- [1] M. Honma, T. Otsuka, B.A. Brown and T. Mizusaki, Eur. Phys. J. A **25**, s01 (2005) 499.
- [2] D.E. Appelbe *et al.*, Phys. Rev. C **67** (2003) 034309.
- [3] A.N. Deacon *et al.*, Phys. Lett. B **622** (2005) 151.
- [4] S.J. Freeman *et al.*, Phys. Rev. C **69** (2004) 064301.
- [5] S. Zhu *et al.*, Phys. Rev. C **74** (2006) 064315.
- [6] N. Shimizu *et al.*, Prog. Theor. Exp. Phys. **2012** (2012) 01A205.
- [7] T. Mizusaki, N. Shimizu, Y. Utsuno and M. Honma, private communications.

Cluster structure in Monte Carlo shell model

T. Yoshida^a, N. Shimizu^a, T. Abe^b and T. Otsuka^{a, b, c}

^a Center for Nuclear Study, Graduate School of Science, University of Tokyo

^b Department of Physics, University of Tokyo

^c National Superconducting Cyclotron Laboratory

1. Introduction

The shell model calculation enables us to take all relevant degrees of freedom of nucleon motion into account when the particles are set to be in the valence shell on top of the core nucleus. For the lightest part of the nuclear chart (mass number lower than $A = 14$), shell model calculations without assuming an inert core can be performed. The model space without the core is important for the accurate prediction of the properties on light nuclei.

On the other hand, α cluster configuration exists in light nuclei, which has an important role at the α -breakup-threshold-energy region [1]. Recently, *ab initio* calculations have been started for this region. One example is the Green's function Monte Carlo (GFMC) [2] approach and another is the lattice effective field theory [3]. In their analyses of $A = 8$ and 12 nuclei, the two and three- α -cluster shapes emerge in *a priori*. It is important to confirm the existence of the cluster configuration by calculating the density distribution of ${}^8\text{Be}$ from shell-model side. However, it is difficult to discuss α -cluster configuration in view of intrinsic shape utilizing shell model calculations. This is because the single-particle orbit of the shell model is expanded around the one center of the harmonic oscillator potential.

Recently, the size of the model space which is tractable in the shell model calculation has been increased due to the development of parallel computers and methodology of shell model calculations. Therefore, it is natural to expect that α -cluster configurations are included in the single-particle orbit of the shell model if the model space is large enough. In fact, the deformation and cluster-like shape for Li isotopes have been investigated by using no core full configuration (NCFC) approach [4]. Another approach is the Monte Carlo shell model (MCSM) [5] method which has been applied to the various nuclei by using the recent parallel computer with sophisticated energy-minimum search where the conjugate gradient method and energy-variance extrapolation [6, 7, 8] are combined. The MCSM is expected to be applicable toward the large region of the nuclear chart both with and without the inert core (no-core MCSM).

2. Formulation

In this section, we show how to obtain the intrinsic structure for ${}^8\text{Be}$. In order to investigate the cluster-like state, it is important to extract the intrinsic state from the wave function whose angular momentum is a good quantum number in the no-core MCSM. In the no-core-MCSM calculation, the wave function is projected to the state which has a good angular momentum quantum, J . We use a Slater determinant, $|\phi_n\rangle$, to describe a basis state which is defined as

$$|\phi_n\rangle = \prod_{\alpha=1}^{N_p} \sum_{i=1}^{N_{sp}} c_i^\dagger D_{i\alpha}^{(n)} |-\rangle, \quad (1)$$

where $|-\rangle$ is a vacuum state and c_i^\dagger 's are creation operators of the single-particle orbit, i . It is specified by coefficients

of the harmonic oscillator state. The resultant wave function is given by a superposition of the angular-momentum-projected Slater determinants,

$$|\Psi\rangle = P_{MK}^{J\pi} |\Phi\rangle, \quad |\Phi\rangle = \sum_{n=1}^{N_b} f_n |\phi_n\rangle. \quad (2)$$

In this study, we use the values, $\pi = +$, $J = 0$, $M = 0$ and therefore K -quantum number, $K = 0$. The coefficients f_n 's are determined by diagonalizing the Hamiltonian matrix, $\langle \phi_i | H | \phi_j \rangle$. In the no-core-MCSM procedure, we tune the value of $D^{(n)}$ for each Slater determinant by the conjugate gradient method in order to minimize the expectation value of the Hamiltonian with J -projected wave functions. Here, we use the JISP16 NN interaction which reproduces NN scattering data and properties of deuteron and other light nuclei [9]. In this J -projected wave function, the cluster-like structure is difficult to be visualized. To analyse the wave function in detail, we go back to the wave function before the angular momentum projection, $|\Phi\rangle$, which is the linear combination of the unprojected basis states. However, this state is not considered as an intrinsic state because the principal axis of a basis state, $|\phi_i\rangle$, is not necessarily in the same direction with that of other basis states. The directions are rather randomly distributed after the energy-minimum search in MCSM procedure. As a result, the intrinsic structure such as cluster configurations may be hidden. In order to extract the wave function of the intrinsic state, we rotate each basis state so that its diagonalized Q-moment is aligned along the z -axis, following the concept of the intrinsic state in the GFMC [2]. The intrinsic wave function $|\Phi^{\text{intr}}\rangle$ is defined as

$$|\Phi^{\text{intr}}\rangle \equiv \sum_n f_n R(\Omega_n) |\phi_n\rangle = \sum_n f_n |\phi_n^R\rangle, \quad (3)$$

with the transformed basis state $|\phi_n^R\rangle$. Here, $R(\Omega_n)$ is the rotation operator with an Euler angle Ω_n , which is determined by the condition, $\langle \phi_n^R | Q_{i,j} | \phi_n^R \rangle = \delta_{i,j} q_i$, where $Q_{i,j(=x,y,z)}$ are the operators of Q-moment. We note that this state, $|\Phi^{\text{intr}}\rangle$, exactly has the same energy after the angular momentum projection. After that, it is probable that these aligned basis states have large overlap with each other and make a distinct principal axis toward the z -axis when the condition $q_z > q_y > q_x$ is set. The intrinsic density is obtained by the expectation value of the one-body-density operator,

$$\rho^{\text{intr}}(r) = \langle \Phi^{\text{intr}} | \sum_i \delta(r - r_i) | \Phi^{\text{intr}} \rangle, \quad (4)$$

where r_i denotes the position of the i -th nucleon.

3. Result

Figure 1 shows the proton densities for the 0^+ ground state of ${}^8\text{Be}$. Here, the densities of the wave function Φ (before alignment) are shown in the left panel. The intrinsic

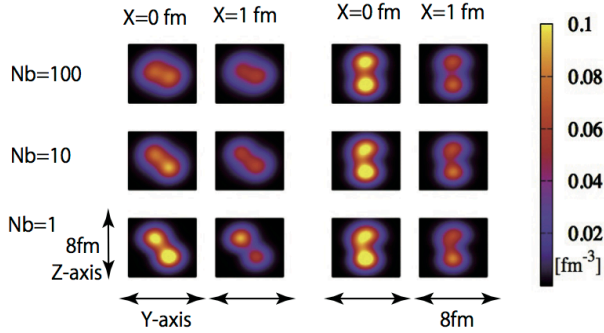


Figure 1. The densities of the 0^+ ground state for ^8Be are shown. The number of basis states is $N_b = 1, 10$ and 100 (lower, middle and upper, respectively). The model space and harmonic oscillator energy are $N_{shell}=4$ and $\hbar\omega=20$ MeV, respectively. The left and right panel correspond to the before and after the alignment, respectively.

densities of the wave function Φ^{intr} are shown in the right panel. As shown in the results of $N_b = 1$, a clear deformation and its neck structure to be called dumbbell shape appear. We can see that as the number of the Slater determinants (N_b) increases, the densities before alignment becomes vaguer because of the mixture of different directions of principal axes of the basis states. On the other hand, the intrinsic densities have clearer dumbbell-like structure for each N_b . In addition, the density distribution of the intrinsic state is almost unchanged with respect to N_b . This result indicates the appearance of cluster structure. Since the number of particles appeared in the density distribution for opposite sides of the principal axis are almost the same, this state can be considered as two α clusters. This result is similar to that of the GFMC [2]. We perform the same analysis for the ground state of ^{10}Be . We depict the densities as shown in Fig. 2. The valence-neutron density is estimated by subtracting the proton density from the neutron density. We find that the valence neutrons are located mainly around the node of ^8Be -like core. This picture is consistent with the behavior of π -orbit in the molecular orbital model of ^{10}Be .

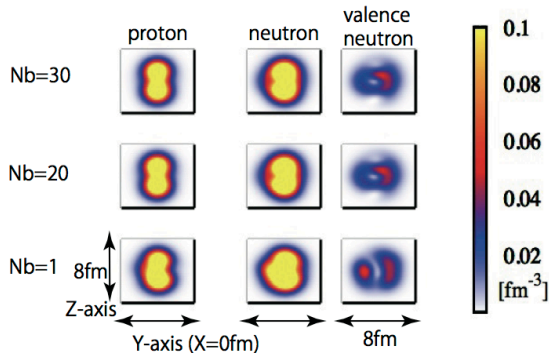


Figure 2. The densities of the 0^+ ground state for ^{10}Be are shown. The model space and harmonic oscillator energy are $N_{shell}=4$ and $\hbar\omega=25$ MeV, respectively.

4. Summary

We analyse the density distribution of the 0^+ ground state of $^{8,10}\text{Be}$. We use the method by which one can extract the intrinsic structure from the wave function in the no-core MCSM. We show that the neck shape indicating the two α clusters emerges within a relatively small number of the harmonic oscillator quanta. We notice that the shape which

appears in the no-core MCSM has the similar property in the GFMC in terms of the density. In the analysis for the 0^+ ground state of ^{10}Be , we see the two- α -cluster shape and π -orbit-like configuration of the valence neutrons. This corresponds to the result of the α cluster model. However, it is necessary to clarify whether the present analysis is valid with larger model spaces, with Coulomb interaction and without contamination of spurious center of mass motion as a future study.

Acknowledgements

This work has been supported by the SPIRE Field 5 from MEXT, and the CNS-RIKEN joint project for large-scale nuclear structure calculations. The numerical calculations were performed on the T2K Open Supercomputers at the University of Tokyo and Tsukuba University.

References

- [1] Fujiwara Y, Horiuchi H, Ikeda K, Kamimura M, Katō K, Suzuki Y and Uegaki E 1980 Prog. Theor. Phys. Suppl. **68** 29
- [2] Wiringa R B, Pieper S C, Carlson J and Pandharipande V R 2000 Phys. Rev. C **62** 014001
- [3] Epelbaum E, Krebs H, Lee D and Meißner U 2011 Phys. Rev. Lett **106** 192501
- [4] Cockrell C, Vary J P and Maris P 2012 Phys. Rev. C **86** 034325
- [5] Abe T, Maris P, Otsuka T, Shimizu N, Utsuno Y and Vary J P 2012 Phys. Rev. C **86** 054301
- [6] Otsuka T, Honma M, Mizusaki T, Shimizu N and Utsuno Y 2001 Prog. Part. Nucl. Phys. **47** 319
- [7] Shimizu N, Abe T, Tsunoda Y, Utsuno Y, Yoshida T, Mizusaki T, Honma M and Otsuka T 2012 Prog. Theor. Exp. Phys. **2012** 01A205
- [8] Abe T, Maris P, Otsuka T, Shimizu N, Tsunoda Y, Utsuno Y, Vary J P and Yoshida T contribution to the CCP2012 proceedings
- [9] Shirokov A M, Vary J P, Mazur A I, Zaytsev S A and Weber T A 2005 Phys. Lett. B **621** 96

Other Activities

Laboratory Exercise for Undergraduate Students

S. Ota, K. Yako, M. Niikura^a, M. Kobayashi, K. Matsui^a, H. Sakurai^{a,b} and S. Shimoura

Center for Nuclear Study, Graduate School of Science, University of Tokyo

^a*Department of Physics, University of Tokyo*

^b*RIKEN Nishina Center*

Nuclear scattering experiments were performed as a laboratory exercise for undergraduate students of the University of Tokyo. This program was aiming at providing undergraduate students with an opportunity to learn how to study subatomic physics by using an ion beam from an accelerator. In 2012, 30 students attended this program.

The four beam times were scheduled in the second semester for third-year students, and 8 students participated in each beam time. The experiment was performed at the RIBF using a 26-MeV alpha beam accelerated in the AVF cyclotron. The alpha beam extracted from the AVF cyclotron was transported to the E7B beam line in the E7 experimental hall. The scattering chamber has two separate target ports which enable us to perform two independent experiments. In each beam time, the students were divided into two groups and took one of the following two subjects:

1. Measurement of elastic scattering of incident alpha particle with ^{197}Au , to learn how to determine nuclear size.
2. Measurement of gamma rays emitted from the cascade decay of highly excited ^{154}Gd and ^{184}Os , to learn on the nuclear deformation.

Before the experiment, the students took a course on the basic handling of the semiconductor detectors and electronic circuits at the Hongo campus, and attended a radiation safety lecture at RIKEN. They also joined a tour to the RI beam factory at RIKEN.

In the $\alpha+^{197}\text{Au}$ measurement, the Au target with a thickness of 1.42 mg/cm², and α particles scattered from the Au target were detected by a silicon PIN-diode located 11 cm away from the target. A collimator with a diameter of 6 mm was attached on the silicon detector. The energy spectrum of the scattered α particles was recorded by a multi-channel analyzer (MCA) system. The beam was stopped by a Faraday cup in the scattering chamber. The cross section for the alpha elastic scattering was measured in the angular range of $\theta_{\text{lab}} = 25-160^\circ$.

The measured cross section was compared with the calculated cross section for the Rutherford scattering. The cross section was also analyzed by the potential model calculation, and the radius of the gold nucleus was discussed. Some students obtained the radius of 10 fm by using a classical model where the trajectory of the α particle in the nuclear potential is obtained using the Runge-Kutta method. Others tried to understand the scattering process by calculating the angular distribution using the distorted wave Born approximation method with a Coulomb wave function and a realistic nuclear potential.

In the measurement of gamma rays, excited states in ^{154}Gd and ^{184}Os nuclei were populated by the $^{152}\text{Sm}(\alpha,2n)$ and $^{182}\text{W}(\alpha,2n)$ reactions, respectively. The gamma rays emitted from the cascade decay of the rotational bands were measured by a high-purity germanium detector located 50

cm away from the target. The energies of the gamma rays were recorded by the MCA system. The gain and the efficiency of the detector system had been calibrated with standard gamma-ray sources of ^{22}Na , ^{60}Co , ^{133}Ba , and ^{137}Cs . The gamma rays from the $12+\rightarrow 10+$ and $10+\rightarrow 8+$ decay in ^{154}Gd and ^{184}Os were successfully identified. Based on the energies of the gamma rays, the moment of inertia and the deformation parameters of the excited states were discussed by using a classical rigid rotor model and a irrotational fluid model. The students found that the reality lies between the two extreme models. The initial population among the levels in the rotational band was also discussed by taking the effect of the internal conversion into account.

We believe this program was very impressive for the students. It was the first time for most of the students to use large experimental equipments. They learned basic things about the experimental nuclear physics and how to extract physics from the data. The authors would like to thank Dr. Y. Uwamino, the CNS accelerator group, and the RIBF cyclotron crew for their helpful effort in the present program.

Appendices

**Symposium, Workshop, Seminar, PAC and
External Review**

CNS Reports

Publication List

Talks and Presentations

Personnel

Symposium, Workshop, Seminar, PAC and External Review

A. Symposium

1. International Symposium “Exotic Nuclear Structure From Nucleons” (ENSFN2012)

Oct. 1012, 2012, University of Tokyo, Japan

Recent achievement and perspectives in the structure of Exotic nuclei were discussed from the viewpoint of the nuclear force. This symposium was supported by Riken Nishina Center and CNS.

Organizes: T. Abe (Univ. Tokyo), M. Honma (Aizu, chair), N. Itagaki (YITP, Kyoto) T. Mizusaki (Senshu), T. Nakatsukasa (RNC), H. Sakurai (Tokyo/RNC), N. Shimizu (CNS, scientific secretary), S. Shimoura (CNS), Y. Utsuno (JAEA/CNS; scientific secretary)

2. 4th International Conference on “Collective Motion in Nuclei under Extreme Conditions” (COMEX4)

Oct. 2226, 2012, Hayama, Japan

The COMEX conferences are a continuation of the series of topical conferences on Giant Resonances, started in 1979. The scope of COMEX4 includes the related topics of collective excitations in stable and unstable nuclei. Decay studies from highly excited states, cluster and exotic shapes of nuclei, and applications in astrophysics are also the scope of this conference.

Local Organizers: Y. Fujita (RCNP, Co-chair), S. Shimoura (CNS, Co-chair), N. Aoi (RCNP), T. Nakamura (TIT), A. Tamii (RCNP), K. Yako (CNS), M. Yamagami (Aizu), H. Otsu (RIKEN), S. Ota(CNS)

B. Workshop

1. 1st Visiting NAOJ Fellow Workshop, “Element Genesis and Cosmic Chemical Evolution: r-process perspective”

Oct. 1719, 2012, RIKEN, Wako, Saitama, Japan.

This international workshop was hosted by NAOJ and RIKEN, and co-hosted by CNS and KEK. It was focusing on the r-process to work together with a variety of researchers from theory, observation and experiment, to develop a comprehensive picture of the evolution of the universe through the discussion about the cosmic origin of elements and their recycling process, the first generation of astronomical objects, galaxy formation and dynamically driven chemical evolution, formation of solar system, and the origin of life.

2. 6th LACM-TORIJIN-JUSTIPEN workshop

Oct.31Nov. 2, 2012, Oak Ridge National Laboratory, USA.

15 researchers participated from Japan. The workshop was hosted by JUSTIPEN and TORIJIN.

C. CNS Seminar

1. “Separation of Pygmy Dipole Resonance and M1 Resonance in ^{90}Zr ”,
C. Iwamoto (Konan University), Jun. 29th, 2012.
2. “Theoretical Situation on Pygmy Dipole Resonances”,
T. Inakura (Riken Nishina Center), Jun. 29th, 2012.
3. “Isomer (p, n) Reaction as a New Experimental Means”,
H. Sakai (Riken Nishina Center), Jul. 13rd, 2012.
4. “Photonuclear Reactions and Related Topics – from PDR to Nucleosynthesis”,
H. Utsunomiya (Konan University / CNS), Sep. 26, 2012.

D. Program Advisory Committee for Nuclear-Physics Experiments at RI Beam Factory

1. The 11th NP-PAC meeting

Date: June 18-19, 2012

Place: Conference room, 2F RIBF building

F. External Review

1. The second external review meeting.

Date: March, 8-9, 2013

Place: Room 338, 3F Science-1st building, Hongo Campus and Seminar room, 3F, CNS, Wako Campus

The second external review meeting was held in order to review the scientific activities, administration, education, and future plans. The review went well, and the CNS activities were evaluated quite high by the committee. The committee report was publicized in May, 2013.

CNS Reports

#89 “Alpha-resonance structure in ^{11}C studied via resonant scattering of $^7\text{Be} + \alpha$ and $^7\text{Be}(\alpha, p)$ reaction”

H. Yamaguchi, D. Kahl, Y. Wakabayashi, S. Kubono, T. Hashimoto, S. Hayakawa, T. Kawabata, N. Iwasa, T. Teranishi, Y.K. Kwon, D.N. Binh, L.H. Khiem, and N.N. Duy”

#90 “CNS Annual Report 2011”, Edited by S. Ota, March, 2013

Publication List

A. Original Papers

1. J. Chen, A.A. Chen, A.M. Amthor, D. Bazin, A.D. Becerril, A. Gade, D. Galaviz, T. Glasmacher, D. Kahl, G. Lorusso, M. Matos, C.V. Ouellet, J. Pereira, H. Schatz, K. Smith, B. Wales, D. Weisshaar, R.G.T. Zegers: “ ^{26}Si excited states via one-neutron removal from a ^{27}Si radioactive ion beam”, *Phys. Rev. C* **85** (2012) 045809.
2. G.L. Zhang, C.L. Zhang, H.Q. Zhang, C.J. Lin, D.Y. Pang, X.K. Wu, H.M. Jia, G.P. An, Z.D. Wu, X.X. Xu, F. Yang, Z.H. Liu, S. Kubono, H. Yamaguchi, S. Hayakawa, D.N. Binh, Y.K. Kwon, N. Iwasa, M. Mazzocco, M. La Commara, M. Romoli, C. Signorini: “Quasi-elastic scattering of the proton drip line nucleus ^{17}F on ^{12}C at 60 MeV”, *Eur. Phys. J. A* **48** (2012) 65.
3. L. Lamia, C. Spitaleri, V. Burjan, N. Carlin, S. Cherubini, V. Crucillà, M. Gameiro Munhoz, M. Gimenez Del Santo, M. Gulino, Z. Hons, G.G. Kiss, V. Kroha, S. Kubono, M. La Cognata, C. Li, J. Mrazek, A. Mukhamedzhanov, R.G. Pizzone, S.M.R. Puglia, Q. Wen, G.G. Rapisarda, C. Rolfs, S. Romano, M.L. Sergi, E. Somorjai, F.A. Souza, A. Szanto de Toledo, G. Tabacaru, A. Tumino, Y. Wakabayashi, H. Yamaguchi and S-H. Zhou: “New measurement of the $^{11}\text{B}(p,\alpha_0)^8\text{Be}$ bare-nucleus $S(E)$ factor via the Trojan horse method”, *J. Phys. G: Nucl. Part. Phys.* **39** (2012) 015106.
4. B. Guo, J. Su, Z.H. Li, Y.B. Wang, S.Q. Yan, Y.J. Li, N.C. Shu, Y.L. Han, X.X. Bai, Y.S. Chen, W.P. Liu, H. Yamaguchi, D.N. Binh, T. Hashimoto, S. Hayakawa, D. Kahl, S. Kubono, J.J. He, J. Hu, S.W. Xu, N. Iwasa, and N. Kume: “Determination of the astrophysical $^{12}\text{N}(p,\gamma)^{13}\text{O}$ reaction rate from the $^2\text{H}(^{12}\text{N},^{13}\text{O})n$ reaction and its astrophysical implications”, *Phys. Rev. C* **87** (2013) 015803.
5. H. Yamaguchi, D. Kahl, Y. Wakabayashi, S. Kubono, T. Hashimoto, S. Hayakawa, T. Kawabata, N. Iwasa, T. Teranishi, Y.K. Kwon, D.N. Binh, L.H. Khiem and N.N. Duy: “Alpha-resonance structure in ^{11}C studied via resonant scattering of $^7\text{Be}+\alpha$ and $^7\text{Be}(\alpha, p)$ reaction”, *Phys. Rev. C* **87** (2013) 034303 .
6. K. Miki, H. Sakai, T. Uesaka, H. Baba, C.L. Bai, G.P.A. Berg, N. Fukuda, D. Kameda, T. Kawabata, S. Kawase, T. Kubo, S. Michimasa, H. Miya, S. Noji, T. Ohnishi, S. Ota, A. Saito, Y. Sasamoto, H. Sagawa, M. Sasano, S. Shimoura, H. Takeda, H. Tokieda, K. Yako, Y. Yanagisawa, R.G.T. Zegers: “Identification of the β^+ Isovector Spin Monopole Resonance via the ^{208}Pb and $^{90}\text{Zr}(t,^3\text{He})$ Reactions at 300 MeV/u”, *Phys. Rev. Lett.* **108** (2012) 262503.
7. S. Takeuchi, M. Matsushita, N. Aoi, P. Doornenbal, K. Li, T. Motobayashi, H. Scheit, D. Steppenbeck, H. Wang, H. Baba, D. Bazin, L. Caceres, H. Crawford, P. Fallon, R. Gernhauser, J. Gibelin, S. Go, S. Grevy, C. Hinke, C. R. Hoffman, R. Hughes, E. Ideguchi, D. Jenkins, N. Kobayashi, Y. Kondo, R. Krucken, T. Le Bleis, J. Lee, G. Lee, A. Matta, S. Michimasa, T. Nakamura, S. Ota, M. Petri, T. Sako, H. Sakurai, S. Shimoura, K. Steiger, K. Takahashi, M. Takechi, Y. Togano, R. Winkler, K. Yoneda “Well Developed Deformation in ^{42}Si ”, *Phys. Rev. Lett.* **109** (2012) 182501.
8. Y. Togano, Y. Yamada, N. Iwasa, K. Yamada, T. Motobayashi, N. Aoi, H. Baba, S. Bishop, X. Cai, P. Doornenbal, D. Fang, T. Furukawa, K. Ieki, T. Kawabata, S. Kanno, N. Kobayashi, Y. Kondo, T. Kuboki, N. Kume, K. Kurita, M. Kurokawa, Y.G. Ma, Y. Matsuo, H. Murakami, M. Matsushita, T. Nakamura, K. Okada, S. Ota, Y. Satou, S. Shimoura, R. Shioda, K. N. Tanaka, S. Takeuchi, W. Tian, H. Wang, J. Wang, K. Yoneda “Hindered Proton Collectivity in $^{28}_{16}\text{S}_{12}$: Possible Magic Number at $Z = 16$ ”, *Phys. Rev. Lett.* **108** (2012) 222501.
9. K. Tshoo, Y. Satou, H. Bhang, S. Choi, T. Nakamura, Y. Kondo, S. Deguchi, Y. Kawada, N. Kobayashi, Y. Nakayama, K. N. Tanaka, N. Tanaka, N. Aoi, M. Ishihara, T. Motobayashi, H. Otsu, H. Sakurai, S. Takeuchi, Y. Togano, K. Yoneda, Z. H. Li, F. Delaunay, J. Gibelin, F.M. Marques, N.A. Orr, T. Honda, M. Matsushita, T. Kobayashi, Y. Miyashita, T. Sumikama, K. Yoshinaga, S. Shimoura, D. Sohler, T. Zheng, Z.X. Cao “N=16 Spherical Shell Closure in ^{24}O ”, *Phys. Rev. Lett.* **102** (2012) 022501.
10. D. Steppenbeck, R.V.F. Janssens, S.J. Freeman, M.P. Carpenter, P. Chowdhury, A.N. Deacon, M. Honma, H. Jin, T. Lauritsen, C.J. Lister, J. Meng, J. Peng, D. Seweryniak, J.F. Smith, Y. Sun, S.L. Tabor, B.J. Varley, Y.-C. Yang, S.Q. Zhang, P.W. Zhao, S. Zhu: “Magnetic rotation and quasicollective structures in ^{58}Fe : Influence of the $\nu g_{9/2}$ orbital”, *Phys. Rev. C* **85** (2012) 044316.
11. Y. Akamatsu, H. Hamagaki, T. Hatsuda, T. Hirano: “Low-mass dilepton production through transport process in quark-gluon plasma”, *Phys. Rev. C* **85** (2012) 054903.
12. B. Abelev *et al.*, for the ALICE Collaboration: “Heavy flavour decay muon production at forward rapidity in protonproton collisions at $\sqrt{s} = 7 \text{ TeV}$ ”, *Phys. Lett. B* **708** (2012) 265.

13. B. Abelev *et al.*, for the ALICE Collaboration: “Measurement of Event Background Fluctuations for Charged Particle Jet Reconstruction in Pb-Pb collisions at $\sqrt{s_{NN}} = 2.76$ TeV”, JHEP **03** (2012) 053.
14. B. Abelev *et al.*, for the ALICE Collaboration: “Light vector meson production in pp collisions at $\sqrt{s} = 7$ TeV”, Phys. Lett. B **710** (2012) 557–568
15. B. Abelev *et al.*, for the ALICE Collaboration: “ J/ψ Production as a Function of Charged Particle Multiplicity in pp Collisions at $\sqrt{s} = 7$ TeV”, Phys. Lett. B **712** (2012) 165–175
16. B. Abelev *et al.*, for the ALICE Collaboration: “Multi-strange baryon production in pp collisions at $\sqrt{s} = 7$ TeV with ALICE”, Phys. Lett. B **712** (2012) 309.
17. B. Abelev *et al.*, for the ALICE Collaboration: “Underlying Event measurements in pp collisions at $\sqrt{s} = 0.9$ and 7 TeV with the ALICE experiment at the LHC”, JHEP **1207** (2012) 116.
18. B. Abelev *et al.*, for the ALICE Collaboration: “Measurement of charm production at central rapidity in proton-proton collisions at $\sqrt{s} = 2.76$ TeV”, JHEP **1207** (2012) 191.
19. B. Abelev *et al.*, for the ALICE Collaboration: “ J/ψ suppression at forward rapidity in Pb-Pb collisions at $\sqrt{s_{NN}} = 2.76$ TeV”, Phys. Rev. Lett. **109** (2012) 072301.
20. B. Abelev *et al.*, for the ALICE Collaboration: “Transverse sphericity of primary charged particles in minimum bias proton-proton collisions at $\sqrt{s} = 0.9, 2.76$ and 7 TeV”, Eur. Phys. J. C **72** (2012) 2124.
21. B. Abelev *et al.*, for the ALICE Collaboration: “Production of muons from heavy flavour decays at forward rapidity in pp and Pb–Pb collisions at $\sqrt{s_{NN}} = 2.76$ TeV”, Phys. Rev. Lett. **109** (2012) 112301.
22. B. Abelev *et al.*, for the ALICE Collaboration: “Suppression of high transverse momentum prompt D mesons in central Pb–Pb collisions at $\sqrt{s_{NN}} = 2.76$ TeV”, JHEP **9** (2012) 112.
23. B. Abelev *et al.*, for the ALICE Collaboration: “Neutral pion and eta meson production in proton-proton collisions at $\sqrt{s} = 0.9$ TeV and 7 TeV”, Phys. Lett. B **717** (2012) 162–172.
24. B. Abelev *et al.*, for the ALICE Collaboration: “ K_0^s - K_0^s correlations in 7 TeV pp collisions from the LHC ALICE experiment”, Phys. Lett. B **717** (2012) 151–161.
25. B. Abelev *et al.*, for the ALICE Collaboration: “Production of $K^*(892)^0$ and $\phi(1020)$ in pp collisions at $\sqrt{s} = 7$ TeV”, Eur. Phys. J. C **72** (2012) 2183.
26. B. Abelev *et al.*, for the ALICE Collaboration: “Rapidity and transverse momentum dependence of inclusive J/ψ production in pp collisions at $\sqrt{s} = 7$ TeV”, Phys. Lett. B **718** (2012) 692698.
27. B. Abelev *et al.*, for the ALICE Collaboration: “ D_s meson production at central rapidity in proton–proton collisions at $\sqrt{s} = 7$ TeV”, Phys. Lett. B **718** (2012) 279–294.
28. A. Adare *et al.*, for the PHENIX Collaboration: “Cold-nuclear-matter effects on heavy-quark production in d+Au collisions at $\sqrt{s_{NN}} = 200$ GeV”, Phys. Rev. Lett. **109** (2012) 242301.
29. A. Adare *et al.*, for the PHENIX Collaboration: “ J/ψ suppression at forward rapidity in Au+Au collisions at $\sqrt{s_{NN}} = 39$ and 62.4 GeV”, Phys. Rev. C **86** (2012) 064901.
30. A. Adare *et al.*, for the PHENIX Collaboration: “Measurement of Transverse Single-Spin Asymmetries for J/ψ Production in Polarized p+p Collisions at $\sqrt{s} = 200$ GeV (and Erratum)”, Phys. Rev. D **86** (2012) 099904.
31. A. Adare *et al.*, for the PHENIX Collaboration: “Cross Sections and Double Helicity Asymmetries of Mid-Rapidity Inclusive Charged Hadrons in p+p at $\sqrt{s} = 62.4$ GeV”, Phys. Rev. D **86** (2012) 092006.
32. A. Adare *et al.*, for the PHENIX Collaboration: “Measurement of Direct Photons in Au+Au Collisions at $\sqrt{s_{NN}} = 200$ GeV”, Phys. Rev. Lett. **109** (2012) 152302.
33. A. Adare *et al.*, for the PHENIX Collaboration: “Evolution of π^0 suppression in Au+Au collisions from $\sqrt{s_{NN}} = 39$ to 200 GeV”, Phys. Rev. Lett. **109** (2012) 152301.
34. A. Adare *et al.*, for the PHENIX Collaboration: “Observation of direct-photon collective flow in Au+Au collisions at $\sqrt{s_{NN}} = 200$ GeV”, Phys. Rev. Lett. **109** (2012) 122302.
35. A. Adare *et al.*, for the PHENIX Collaboration: “Nuclear-Modification Factor for Open-Heavy-Flavor Production at Forward Rapidity in Cu+Cu Collisions at $\sqrt{s_{NN}} = 200$ GeV”, Phys. Rev. C **86** (2012) 024909.

36. A. Adare *et al.*, for the PHENIX Collaboration: “Deviation from quark-number scaling of the anisotropy parameter v_2 of pions, kaons, and protons in Au+Au collisions at $\sqrt{s_{NN}} = 200$ GeV”, *Phys. Rev. C* **85** (2012) 064914.
37. A. Adare *et al.*, for the PHENIX Collaboration: “Ground and excited charmonium state production in p+p collisions at $\sqrt{s} = 200$ GeV”, *Phys. Rev. D* **85** (2012) 092004.
38. J.D. Holt, T. Otsuka, A. Schwenk and T. Suzuki, “Three-body forces and shell structure in calcium isotopes”, *J. Phys.* **G39**, 085111 (2012).
39. T. Suzuki, T. Yoshida, T. Kajino, T. Otsuka: “Beta Decays of isotones with neutron magic number of N=126 and r-process nucleosynthesis”, *Phys. Rev. C* **85**, 015802 (2012).
40. E.S. Diffenderfer, L.T. Baby, D. Santiago-Gonzalez, N. Ahsan, A. Rojas, A. Volya, I. Wiedenhover, A.H. Wuosmaa, M.P. Carpenter, R.V.F. Janssens, C.J. Lister, M. Devlin, D.G. Sarantites, L.G. Sobotka, Y. Utsuno, and M. Horoi: “High-spin spectrum of ^{24}Mg studied through multiparticle angular correlations”, *Phys. Rev. C* **85**, 034311-1-17 (2012).
41. J. Kotila, K. Nomura, L. Guo, N. Shimizu, and T. Otsuka : “Shape phase transitions in the interacting boson model: Phenomenological versus microscopic descriptions”, *Phys. Rev. C* **85**, 054309 (2012).
42. N. Shimizu, Y. Utsuno, T. Mizusaki, M. Honma, Y. Tsunoda, and T. Otsuka : “Variational procedure for nuclear shell-model calculations and energy-variance extrapolation”, *Phys. Rev. C* **85**, 054301, (2012).
43. Y. Utsuno, T. Mizusaki, B.A. Brown, M. Honma, T. Mizusaki and N. Shimizu : “Shape transitions in exotic Si and S isotopes and tensor-force-driven Jahn-Teller effect”, *Phys. Rev. C* **86** 051301(R), (2012).
44. Liu Lang, Takaharu Otsuka, Noritaka Shimizu, Yutaka Utsuno, and Robert Roth : “No-core Monte Carlo shell model calculation for ^{10}Be and ^{12}Be low-lying spectra”, *Phys. Rev. C* **86**, 014302 (2012).
45. C. Bauer, T. Behrens, V. Bildstein, A. Blazhev, B. Bruyneel, J. Butterworth, E. Clement, L. Coquard, J. L. Egidio, A. Ekstrom, C. R. Fitzpatrick, C. Fransen, R. Gernhauser, D. Habs, H. Hess, J. Leske, T. Kroll, R. Krucken, R. Lutter, P. Marley, T. Moller, T. Otsuka, N. Patronis, A. Petts, N. Pietralla, T.R. Rodriguez, N. Shimizu, C. Stahl, I. Stefanescu, T. Stora, P.G. Thirolf, D. Voulot, J. van de Walle, N. Warr, F. Wenander, and A. Wiens : “Prolate shape of ^{140}Ba from a first combined Doppler-shift and Coulomb-excitation measurement at the REX-ISOLDE facility”, *Phys. Rev. C* **86**, 034310 (2012)
46. K. Nomura, R. Rodriguez-Guzman, L. M. Robledo, and N. Shimizu : “Shape coexistence in Lead isotopes in the interacting boson model with Gogny energy density functional”, *Phys. Rev. C* **86**, 034322 (2012).
47. T. Abe, P. Maris, T. Otsuka, N. Shimizu, Y. Utsuno, and J.P. Vary : “Benchmarks of the ab initio FCI, MCSM and NCFC methods”, *Phys. Rev. C* **86**, 054301 (2012).
48. N. Shimizu, T. Abe, Y. Tsunoda, Y. Utsuno, T. Yoshida, T. Mizusaki, M. Honma, and T. Otsuka : “New generation of the Monte Carlo shell model for the K computer era”, *Prog. Theor. Exp. Phys.* **bf** 2012(1), 01A205 (2012).
49. K. Nomura, N. Shimizu, D. Vretenar, T. Niksic, and T. Otsuka : “Robust regularity in γ -soft nuclei and its microscopic realization”, *Phys. Rev. Lett.* **108**, 132501 (2012).
50. K. Shimada, H. Ueno, G. Neyens, K. Asahi, D.L. Balabanski, J.M. Daugas, M. Depuydt, M.De Rydt, L. Gaudefroy, S. Grevy, Y. Hasama, Y. Ichikawa, D. Kameda, P. Morel, T. Nagatomo, L. Perrot, Ch. Stodel, J.-C. Thomas, Y. Utsuno, W. Vanderheijden, N. Vermeulen, P. Vingerhoets, E. Yagi, K. Yoshida and A. Yoshimi: “Erosion of N=20 shell in ^{33}Al investigated through the ground-state electric quadrupole moment”, *Phys. Lett. B* **714**, 246-250 (2012).
51. Y. Utsuno, N. Shimizu, T. Otsuka and T. Abe: “Efficient computation of Hamiltonian matrix elements between non-orthogonal Slater determinants”, *Comp. Phys. Comm.* **184**, 102 (2013).

B. Proceedings

1. T. Uesaka, H. Matsubara, K. Miki, S. Noji, H. Sakai, Y. Sasamoto, S. Shimoura, M. Takaki, K. Yako, for the SHARAQ Collaboration: “New Experimental Studies of Nuclear Spin-Isospin Responses”, *Proc. of Frontier Issues in Physics of Exotic Nuclei (YKIS2011)*, *Prog. Theor. Phys. Suppl.* **196** (2012) 150–157
2. S. Ebata, T. Nakatsukasa, T. Inakura: “Cb-TDHF calculation for the low-lying E1 strength of heavy nuclei around the r-process path”, *Proc. of Frontier Issues in Physics of Exotic Nuclei (YKIS2011)*, *Prog. Theor. Phys. Suppl.* **196** (2012) 316–321

3. E. Ideguchi, S. Ota, T. Morikawa, M. Oshima, M. Koizumi, Y. Toh, A. Kimura, H. Harada, K. Furutaka, S. Nakamura, F. Kitatani, Y. Hatsukawa, T. Shizuma, M. Sugawara, Y. X. Watanabe, Y. Hirayama, M. Oi: “Superdeformed Band in Asymmetric N ζ Z Nucleus, Ar-40 and High-Spin States in A=30 similar to 40 Nuclei”, Proc. of Frontier Issues in Physics of Exotic Nuclei (YKIS2011), Prog. Theor. Phys. Suppl. **196** (2012) 427–432
4. Y. Utsuno, T. Otsuka, B.A. Brown, M. Honma, T. Mizusaki, and N. Shimizu: “Shell evolution around and beyond N=28 studied with large-scale shell- model calculations”, Proc. of Frontier Issues in Physics of Exotic Nuclei (YKIS2011), Prog. Theor. Phys. Suppl. **196** (2012) 304–309
5. Shigeru Kubono, Binh N Dam, S. Hayakawa, H. Hashimoto, D. Kahl, H. Yamaguchi, Y. Wakabayashi, T. Teranishi, N. Iwasa, T. Komatsubara, S. Kato, A. Chen, S. Cherubini, S.H. Choi, I.S. Hahn, J.J. He, Hong Khiem Le, C.S. Lee, Y.K. Kwon, S. Wanajo, H.-T. Janka: “Alpha-Cluster Dominance in the alpha Process in Explosive Hydrogen Burning”, Progress of Theoretical Physics Supplement **196** (2012) 346–351.
6. S. Hayakawa, S. Kubono, D. Kahl, H. Yamaguchi, D.N. Binh, T. Hashimoto, Y. Wakabayashi, J.J. He, N. Iwasa, S. Kato, T. Komatsubara, Y.K. Kwon, T. Teranishi, S. Wanajo: “Direct measurement of the $^{11}\text{C}(\alpha, p)^{14}\text{N}$ reaction at CRIB: a path from pp-chain to CNO”, Exotic Nuclei and Nuclear/Particle Astrophysics (IV) From Nuclei to Stars, AIP Conf. Proc. **1498** (2012) 339–343.
7. Y.B. Wang, B. Guo, S.J. Jin, Z.H. Li, D.N. Binh, H. Hashimoto, S. Hayakawa, J.J. He, J. Hu, N. Iwasa, D.M. Kahl, S. Kubono, N. Kume, E.T. Li, Y.J. Li, X. Liu, J. Su, S.W. Xu, H. Yamaguchi, S.Q. Yan, S. Zeng, X.X. Bai, G. Lian, B.X. Wang, W.P. Liu: “Indirect measurements of reactions in hot p-p chain and CNO cycles”, *Origin of Matter and Evolution of Galaxies 2011*, AIP Conf. Proc. **1484** (2012) 19–24
8. D.N. Binh, S. Kubono, H. Yamaguchi, S. Hayakawa, T. Hashimoto, D. Kahl, T. Teranishi, N. Iwasa, S. Kato, L.H. Khiem, N.T. Tho, Y. Wakabayashi: “Measurement of $^{21}\text{Na}(\alpha, p)^{24}\text{Mg}$ stellar reaction using a ^{21}Na RI-beam”, *Origin of Matter and Evolution of Galaxies 2011*, AIP Conf. Proc. **1484** (2012) 25–30
9. T. Otsuka, T. Suzuki: “Nuclear forces, exotic nuclei and stellar evolution”, *Origin of Matter and Evolution of Galaxies 2011*, AIP Conf. Proc. **1484** (2012) 45–46
10. T. Nakatsukasa, T. Inakura, P. Avogadro, S. Ebata, K. Sato, K. Yabana: “Linear-response calculation in the time-dependent density functional theory”, *Origin of Matter and Evolution of Galaxies 2011*, AIP Conf. Proc. **1484** (2012) 142–149
11. T. Sumikama, K. Yoshinaga, H. Watanabe, S. Nishimura, Y. Miyashita, K. Yamaguchi, K. Sugimoto, J. Chiba, Z. Li, H. Baba, J.S. Berryman, N. Blasi, A. Bracco, F. Camera, P. Doornenbal, S. Go, T. Hashimoto, S. Hayakawa, C. Hinke, E. Ideguchi, T. Isobe, Y. Ito, D. G. Jenkins, Y. Kawada, N. Kobayashi, Y. Kondo, R. Krucken, S. Kubono, G. Lorusso, T. Nakano, M. Kurata-Nishimura, A. Odahara, H.J. Ong, S. Ota, Z. Podolyak, H. Sakurai, H. Scheit, K. Steiger, D. Steppenbeck, S. Takano, A. Takashima, K. Tajiri, T. Teranishi, Y. Wakabayashi, P.M. Walker, O. Wieland, H. Yamaguchi: “Search for spin-orbit-force reduction at $^{106,108}\text{Zr}$ around r-process path”, *Origin of Matter and Evolution of Galaxies 2011*, AIP Conf. Proc. **1484** (2012) 156–160
12. S. Kubono, D.N. Binh, S. Hayakawa, T. Hashimoto, D.M. Kahl, H. Yamaguchi, Y. Wakabayashi, T. Teranishi, N. Iwasa, T. Komatsubara, S. Kato, A. Chen, S. Cherubini, S.H. Choi, I.S. Hahn, J.J. He, L.H. Khiem, C.S. Lee, Y.K. Kwon, S. Wanajo, H.-T. Janka: “Experimental challenge to nuclear physics problems in the nu p-process”, *Origin of Matter and Evolution of Galaxies 2011*, AIP Conf. Proc. **1484** (2012) 189–196
13. S. Nishimura and RIBF Decay Collaboration: “Beta-decay spectroscopy relevant to the r-process nucleosynthesis”, *Origin of Matter and Evolution of Galaxies 2011*, AIP Conf. Proc. **1484** (2012) 209–216
14. H. Yamaguchi, D. Kahl, J. Hu, S. Kubono, S. Hayakawa, T. Hashimoto: “Alpha-induced reaction studies using low-energy RI beams at CRIB”, *Origin of Matter and Evolution of Galaxies 2011*, AIP Conf. Proc. **1484** (2012) 225–231.
15. J.J. He, L.Y. Zhang, S.W. Xu, S.Z. Chen, J. Hu, P. Ma, R.F. Chen, H. Yamaguchi, S. Kubono, T. Hashimoto, D. Kahl, S. Hayakawa, Y. Wakabayashi, Y. Togano, H.W. Wang, W.D. Tian, B. Guo, T. Teranishi, N. Iwasa, T. Yamada, T. Komatsubara: “Study of resonant scattering of $^{21}\text{Na} + p$ relevant to astrophysical $^{18}\text{Ne}(\alpha, p)^{21}\text{Na}$ reaction”, *Origin of Matter and Evolution of Galaxies 2011*, AIP Conf. Proc. **1484** (2012) 240–245
16. S. Shimoura: “Spin-Isospin responses via charge exchange reactions of RI beams at SHARAQ”, *Origin of Matter and Evolution of Galaxies 2011*, AIP Conf. Proc. **1484** (2012) 253–256
17. S. Cherubini, M. Gulino, G.G. Rapisarda, C. Spitaleri, M.L. Cognata, L. Lamia, S. Kubono, H. Yamaguchi, S. Hayakawa, Y. Wakabayashi, N. Iwasa, S. Kato, H. Komatsubara, T. Teranishi, A. Coc, N.D. Sereville, F. Hammache: “Trojan Horse Method and RIBs: The $^{18}\text{F}(p, \alpha)^{15}\text{O}$ reaction at astrophysical energies”, *Origin of Matter and Evolution of Galaxies 2011*, AIP Conf. Proc. **1484** (2012) 293–300

18. H.S. Jung, C.S. Lee, Y.K. Kwon, J.Y. Moon, J.H. Lee, C.C. Yun, S. Kubono, H. Yamaguchi, T. Hashimoto, D. Kahl, S. Hayakawa, S. Choi, M.J. Kim, Y.H. Kim, Y.K. Kim, J.S. Park, E.J. Kim, C.-B. Moon, T. Teranishi, Y. Wakabayashi, N. Iwasa, T. Yamada, Y. Togano, S. Kato, S. Cherubini, G.G. Rapisarda: “Study of proton resonance structure in ^{27}P via resonant elastic scattering of $^{26}\text{Si} + p$ ”, *Origin of Matter and Evolution of Galaxies 2011*, AIP Conf. Proc. **1484** (2012) 307–312
19. T. Suzuki, T. Yoshida, T. Kajino, T. Otsuka: “First-forbidden transitions in N=126 isotones and r-process nucleosynthesis”, *Origin of Matter and Evolution of Galaxies 2011*, AIP Conf. Proc. **1484** (2012) 363–364
20. Y.K. Kwon, C.S. Lee, H.S. Jung, J.Y. Moon, J.H. Lee, C.C. Yun, S. Kubono, H. Yamaguchi, T. Hashimoto, D. Kahl, S. Hayakawa, S. Choi, M.J. Kim, Y.H. Kim, Y.K. Kim, J.S. Park, E.J. Kim, C.-B. Moon, T. Teranishi, Y. Wakabayashi, N. Iwasa, T. Yamada, Y. Togano, S. Kato, S. Cherubini, G. G. Rapisarda: “Measurement of $^{25}\text{Al} + p$ resonant elastic scattering for studying the $^{25}\text{Al}(p, \gamma)^{26}\text{Si}$ ”, *Origin of Matter and Evolution of Galaxies 2011*, AIP Conf. Proc. **1484** (2012) 365–368
21. T. Yoshida, N. Itagaki and K. Katō: “Symplectic structure and transition properties of ^{12}C ”, *Origin of Matter and Evolution of Galaxies 2011*, AIP Conf. Proc. **1484**, (2012) 424–426
22. S. Ebata, T. Nakatsukasa, T. Inakura: “Systematic study of low-lying E1 strength using the time-dependent mean field theory”, *Origin of Matter and Evolution of Galaxies 2011*, AIP Conf. Proc. **1484** (2012) 427–429
23. S. Hayakawa, S. Kubono, D. Kahl, H. Yamaguchi, Dam N. Binh, T. Hashimoto, Y. Wakabayashi, J.J. He, N. Iwasa, S. Kato, T. Komatsubara, Y.K. Kwon, T. Teranishi, S. Wanajo : “Direct measurement of the breakout reaction $^{11}\text{C}(\alpha, p)^{14}\text{N}$ in explosive hydrogen-burning process”, *Origin of Matter and Evolution of Galaxies 2011*, AIP Conf. Proc. **1484** (2012) 445–447.
24. T. Hashimoto, S. Kubono, H. Yamaguchi, S. Hayakawa, D.M. Kahl, S. Ota, S. Michimasa, H. Tokieda, H. Ishiyama, Y. X. Watanabe, Y. Hirayama, N. Imai, H. Miyatake, S. C. Jeong, K. Yamaguchi, I. Arai, T. Komatsubara, T. Fukuda, Y. Mizoi, S. K. Das, N. Iwasa, T. Yamada, A.A. Chen, J.J. He: “Direct measurement of the $^{18}\text{Ne}(\alpha, p)^{21}\text{Na}$ reaction”, *Origin of Matter and Evolution of Galaxies 2011*, AIP Conf. Proc. **1484** (2012) 454–456.
25. H. Yamaguchi, D. Kahl, T. Nakao, and S. Kubono: “Recent astrophysical studies at the low-energy RI beam separator CRIB”, *Proceedings of Science NIC XII* (2012) 244:1–6.
26. H. S. Jung, C. S. Lee, J. Y. Moon, Y. K. Kwon, J. H. Lee, C. C. Yun, S. Kubono, H. Yamaguchi, and D. Kahl: “Experimental study of resonant states in ^{26}Si and ^{27}P via elastic scattering of $^{25}\text{Al}+p$ and $^{26}\text{Si}+p$ ”, *Proceedings of Science NIC XII* (2012) 200:1–6.
27. D. Kahl, A. A. Chen, S. Kubono, T. Hashimoto, D. N. Binh, J. Chen, S. Cherubini, N. N. Duy, S. Hayakawa, N. Iwasa, H. S. Jung, S. Kato, Y. K. Kwon, S. Michimasa, S. Nishimura, S. Ota, K. Setoodehnia, T. Teranishi, H. Tokieda, T. Yamada, H. Yamaguchi, C. C. Yun, and L. Y. Zhang: “Measurement of the $^{30}\text{S} + \alpha$ system for type I X-ray bursts”, *Proceedings of Science NIC XII* (2012) 201:1–5.
28. L. Y. Zhang, J. J. He, S. W. Xu, H. Yamaguchi, S. Kubono, Y. Wakabayashi, S. Z. Chen, J. Hu, P. Ma, Y. Togano, T. Hashimoto, D. Kahl, T. Teranishi, R. F. Chen, H. W. Wang, W. D. Tian, B. Guo, S. Hayakawa, N. Iwasa, T. Yamada, and T. Komatsubara: “Experimental Study of the Key $^{18}\text{Ne}(\alpha, p)^{21}\text{Na}$ reaction”, *Proceedings of Science NIC XII* (2012) 186:1–5.
29. H. Hamagaki: “High Energy Density QCD – Experimental Overview –”, *Proc. of the 41th International Symposium on Multiparticle Dynamics (ISMD 2011)*, Sep. 26–30, 2011, Miyajima, Hiroshima, Japan, *Prog. Theor. Phys. Suppl.* **193** (2012) 79–88.
30. Y. Akamatsu, H. Hamagaki, T. Hatsuda, T. Hirano: “Can transport peak explain the low-mass enhancement of dileptons at RHIC?”, *Proc. of the 22nd International Conference on ON Ultra Relativistic Nucleus-Nucleus Collisions (QM 2011)*, May 23–28, 2011, Annecy, France, *J. Phys. G* **38** (2011) 124184.
31. A. Yoshikawaa, T. Tamagawaa, T. Iwahashia, F. Asamia, Y. Takeuchia, A. Hayatoc, H. Hamagaki, T. Gunji, R. Akimoto, A. Nukariya, S. Hayashi, K. Ueno, A. Ochi, R. Oliveira: “Development of Resistive Electrode Gas Electron Multiplier (RE-GEM)”, *2nd International Conference on Micro Pattern Gaseous Detectors (MPGD2011)*, Aug. 29–Sep. 1, 2011, Maiko, Kobe, Japan, *JINST* **7** (2012) C06006.
32. S. Hayashi, H. Hamagaki, T. Gunji, M. Tanaka, H. Ikeda: “Development of a Wide-Dynamic Range Front-End ASIC for W + Si calorimeter”, *Proceedings of the 2012 IEEE Nuclear Science Symposium and Medical Imaging Conference*, Oct. 29–Nov. 3, 2012, Disneyland Hotel, Anaheim, USA, *Conference Record* (2012) 576–580.

33. Y. Sekiguchi, H. Tokieda, S. Ota, S. Michimasa, M. Dozono, T. Tamagawa, T. Gunji, H. Yamaguchi, H. Hamagaki, T. Tamagawa, T. Uesaka: "Performance of GEM with Deuterium Gas and GEM with Glass Insulator", at the 2012 IEEE Nuclear Science Symposium and Medical Imaging Conference, Oct. 29–Nov. 3, 2012, Disneyland Hotel, Anaheim, USA, Conference Record (2012) 1772–1774.
34. Y. Sekiguchi, T. Gunji, H. Hamagaki, S. Hayashi, Y. Hori "Development of W+Si Based Electromagnetic Calorimeter for the Upgrade of the LHC-ALICE Experiment", at the 2012 IEEE Nuclear Science Symposium and Medical Imaging Conference, Oct. 29–Nov. 3, 2012, Disneyland Hotel, Anaheim, USA, Conference Record (2012) 1854–1856.
35. T. Otsuka: "Interacting boson model and nucleons", Proc. of Beauty in Physics : Theory and Experiment in honor of Francesco Iachello on the occasion of his 70th birthday, AIP Conf. Proc. 1488, 445 (2012).
36. T. Nakatsukasa, S. Ebata, P. Avogadro, L. Guo, T. Inakura and K. Yoshida: "Density functional approaches to nuclear dynamics", Proc. of XXXV Symposium on Nuclear Physics, Journal of Physics Conf. Ser. 387, 012015 (2012).
37. S. Ebata, T. Nakatsukasa, T. Inakura: "Study of pygmy dipole resonance with a new time-dependent mean field theory", Proc. of Rutherford Centennial Conference on Nuclear Physics, Journal of Physics Conf. Ser. 381, 012104 (2012).
38. T. Yoshida, N. Itagaki and K. Katō : "Symplectic structure and transition properties of ^{12}C ", Proc. of The 11th. International Symposium on Origin of Matter and Evolution of the Galaxies(OMEG11), AIP Conf. Proc. 1484, 424 (2012).

C. Theses

1. T. Fujii: " α 非弾性散乱を用いた ^{32}Mg 近傍核の核分光", Master Thesis, the University of Tokyo, March 2013.
2. R. Yokoyama: "中性子過剰変形原子核における核異性体", Master Thesis, the University of Tokyo, March 2013.
3. Y. Kubota: "Development of a tracking-type neutron detector with high granularity for studying unstable nuclei", Master Thesis, the University of Tokyo, March 2013.
4. C.S. Lee: "Properties of Thick GEM in Low-Pressure Deuterium for Low-Pressure Gaseous Active Target", Master Thesis, the University of Tokyo, March 2013.
5. Y. Sekiguchi: "Development of SOI pixel detector for radiation monitor", Master Thesis, the University of Tokyo, March 2013.
6. S. Hayakawa: "Direct Measurement of the Breakout Reaction $^{11}\text{C}(\alpha, p)^{14}\text{N}$ in Explosive Hydrogen-Burning Process", Doctor Thesis, University of Tokyo, December 2012.
7. Y. Hori: "Mixed harmonic azimuthal correlations in $\sqrt{s_{NN}} = 2.76\text{TeV}$ Pb-Pb collisions measured by ALICE at LHC", Doctor Thesis, University of Tokyo, March 2013.

D. Other Publications

1. "Stellar Evolution, Nuclear Astrophysics, and Nucleogenesis", A.G.W. Cameron, edited by David Miles Kahl, Dover Publications, Mineola, NY. (2013).
2. T. Nakatsukasa and S. Ebata : "Canonical-basis time-dependent mean-field theory and linear response of superfluid nuclei", *Butsuri* **67**, No.4, 243-246 (2012).

Talks and Presentations

A. Conferences

1. S. Ota (Oral): “Possibility of forward angle measurement in use of CNS active target”, Towards forward angle inelastic scattering experiments at RIBF, Apr. 4, 2012, RIKEN, Saitama, Japan.
2. T. Otsuka (invited): “Novel structure of exotic nuclei and nuclear forces”, 14th National Conference on Nuclear Structure in China, Huzhou, China, April 12–14, 2012
3. T. Otsuka (invited): “Shell evolution in exotic nuclei”, Symposium for the 40th Anniversary of DNP of KPS, Daejeon, Korea, April 24–27, 2012
4. S. Shimoura (invited): “RI beam as probes for study of nuclear reaction and structure”, Symposium for the 40th Anniversary of DNP of KPS, Daejeon, Korea, April 24–27, 2012
5. T. Otsuka(invited): “Spin properties of effective two-body interaction extracted from three-body forces ”, EMMI Program The extreme matter physics of nuclei : from universal properties to neutron-rich extremens, GSI, Darmstadt, Germany, May 3 (April 16 – May 11), 2012
6. Y. Hori (Oral): “Mixed harmonic charge dependent azimuthal correlations in relativistic HIC”, 14th Heavy Ion Pub, May 5, 2012, the University of Hiroshima, Hiroshima, Japan.
7. T. Otsuka(invited): “Shell evolution in exotic nuclei”, Workshop on RI Physics Theory, Riviera Hotel, Daejeon, Korea, May 11–12, 2012
8. T. Otsuka(invited): “Shell evolution with tensor and three-body forces ”, 11th International Conference on Nucleus-Nucleus Collision, San Antonio, Texas, USA, May 27–June 1, 2012
9. T. Otsuka(invited): “Exotic nuclei and nuclear forces”, Nobel Symposium on Physics with Radioactive Beams, Goteborg, Sweden, June 10–15, 2012
10. T. Gunji (Oral): “Simulation Study of Ion Back Flow for the GEM-TPC upgrade for ALICE”, RD51 Mini-workshop, June 13–15, 2012, CERN, Switzerland.
11. Y. Utsuno (invited): “Monte Carlo shell model and its applications to exotic nuclei ”, International Workshop “Nuclear Theory in the Supercomputing Era,” Khabarovsk, Russia, June 18–22, 2012.
12. H. Yamaguchi: “CRIB – a low energy RI beam facility of CNS”, RIBF Users Meeting 2012, Jun 20–21, 2012, RIKEN, Wako, Saitama, Japan.
13. T. Otsuka: “Activity report of JUSTIPEN”, RIBF Users Meeting 2012, Jun 20–21, 2012, RIKEN, Wako, Saitama, Japan.
14. S. Shimoura: “Physics programs using SHARAQ spectrometer”, RIBF Users Meeting 2012, Jun 20–21, 2012, RIKEN, Wako, Saitama, Japan.
T. Otsuka(invited): “Rotating around atomic nuclei and my cup of models ”, Gelberg 90 Colloquium, IKP, Koeln, Germany, June 28, 2012
15. Y.L. Yamaguchi (Oral): “Direct Photons at RHIC”, Dynamics of Classical and Quantum Fields at RHIC/LHC, July 7th, 2012, RIKEN, Saitama, Japan.
16. H. Torii (Oral): “Photon at LHC”, Dynamics of Classical and Quantum Fields at RHIC/LHC, July 7th, 2012, RIKEN, Saitama, Japan.
T. Otsuka(invited): “Perspectives of Monte Carlo Shell Model”, International Symposium Nuclear Structure and Dynamics II Opatija, Croatia, July 9–13, 2012
17. S. Ota (Oral): “Charge exchange reactions, hadronic probe for neutrino-nucleus interactions,” 6th meeting of OMEG Institute on Element Genesis and Neutrinos, 25, Jul., 2012, RIKEN, Saitama, Japan.
18. S. Ota (Oral): “Capability of cns active target for the (d,p) reactions in inversekinematics”, RIBF ULIC mini-workshop on radiative neutron capture reactions for r-process, Jul. 26, 2012, RIKEN.
19. H. Yamaguchi (Poster): “Recent astrophysical studies at the low-energy RI beam separator CRIB”, XII International Symposium on Nuclei in the Cosmos (NIC-XII), Aug. 6–11, 2012, Cairns Convention Centre, Cairns, Australia.

20. D. Kahl (Poster): “Measurement of the $^{30}\text{S}+\alpha$ System for Type-I X-ray Bursts”, XII International Symposium on Nuclei in the Cosmos (NIC-XII), Aug. 6–11, 2012, Cairns Convention Centre, Cairns, Australia.
21. T. Gunji for the ALICE Collaboration (Poster): “A GEM-based Continuous Readout Scheme for the ALICE-TPC”, XXIII International Conference on Ultrarelativistic Nucleus-Nucleus collisions (QM2012), Aug. 13–18, 2012, Washington, D.C., USA.
22. T. Gunji for the ALICE Collaboration (Poster): “Development of W+Si-Pad/Micro-Pad based ElectroMagnetic Calormeter for the ALICE upgrade”, XXIII International Conference on Ultrarelativistic Nucleus-Nucleus collisions (QM2012), Aug. 13–18, 2012, Washington, D.C., USA.
23. T. Gunji for the ALICE Collaboration (Poster): “FoCAL - a high granurality electromagnetic calorimeter for forward direct photon measurements as an upgrade of ALICE”, XXIII International Conference on Ultrarelativistic Nucleus-Nucleus collisions (QM2012), Aug. 13–18, 2012, Washington, D.C., USA.
24. Y. Hori for the ALICE collaboration (Oral): “Mixed harmonic azimuthal correlations in $\sqrt{s_{NN}} = 2.76$ TeV Pb-Pb collisions measured with the ALICE experiment at the LHC”, XXIII International Conference on Ultrarelativistic Nucleus-Nucleus collisions (QM2012), Aug. 13–18, 2012, Washington, D.C., USA.
25. R. Akimoto for the PHENIX Collaboration (Poster): “Measurement of charm and bottom yields in Au+Au collisions at RHIC-PHENIX experiment”, XXIII International Conference on Ultrarelativistic Nucleus-Nucleus collisions (QM2012), Aug. 13–18, 2012, Washington, D.C., USA.
26. T. Otsuka(invited): “Three-body forces and neutron-rich exotic nuclei”, The 20th Internatinal IUPAP Conference on Few-Body Problems in Physics (FB20) Aug. 20-25, 2012, Fukuoka international Congress Center, Japan.
27. T. Yoshida, N. Shimizu, T. Abe and T. Otsuka: “Intrinsic structure of light nuclei in Monte Carlo Shell model calculation”, The 20th Internatinal IUPAP Conference on Few-Body Problems in Physics (FB20) Aug. 20-25, 2012, Fukuoka international Congress Center, Japan.
28. H. Matsubara, M. Takaki, T. Uesaka, S. Shimoura, N. Aoi, M. Dozono, T. Fujii, K. Hatanaka, T. Hashimoto, T. Kawabata, S. Kawase, K. Kisamori, Y. Kikuch, Y. Kubota, C.S. Lee, H.C. Lee, Y. Maeda, S. Michimasa, K. Miki, H. Miya, S. Noji, S. Ota, S. Sakaguchi, Y. Sasamoto, T. Suzuki, L.T. Tang, K. Takahisa, H. Tokieda, A. Tamii, K. Yako, Y. Yasuda, N. Yokota, R. Yokoyama, J. Zenihiro: “Spectroscopic measurement in ^9He and ^{12}Be ” The 20th Internatinal IUPAP Conference on Few-Body Problems in Physics (FB20) Aug. 20-25, 2012, Fukuoka international Congress Center, Japan.
29. S. Sakaguchi, Y. Iseri, T. Uesaka, M. Tanifuji, K. Amos, N. Aoi, E. Hiyama, Y. Ichikawa, S. Ishikawa, K. Itoh, M. Itoh, H. Iwasaki, S. Karataglidis, T. Kawabata, T. Kawahara, Y. Kondo, H. Kuboki, Y. Maeda, T. Nakamura, T. Nakao, H. Okamura, H. Sakai, Y. Sasamoto, M. Sasano, Y. Satou, K. Sekiguchi, Y. Shimizu, K. Suda, D. Suzuki, A. Tamii, T. Wakui, K. Yako, M. Yamaguchi: “Analyzing power in elastic scattering of polarized protons from neutron-rich helium isotopes”, The 20th Internatinal IUPAP Conference on Few-Body Problems in Physics (FB20) Aug. 20-25, 2012, Fukuoka international Congress Center, Japan.
30. Y. Utsuno (invited) : “Tensor-force driven shell evolution in correlated nuclei ”, International Symposium on Perspective in Isospin Physics – Role of non- central interactions in structure and dynamics of unstable nuclei, Wako, Japan, Aug. 27-28, 2012.
31. T. Otsuka(invited): “Nuclear Structure towards the driplines: understanding many-body forces and correlations”, Zakopane Conference on Nuclear Physics Extremes of the Nuclear Landscape, 47th in the series of Zakopane Schools of Physics, Zakopane, Poland, Aug. 27–Sep. 1, 2012
32. Y. Utsuno (invited): “Recent shell model results for exotic nuclei”, VIII Tours Symposium on Nuclear Physics and Astrophysics, Lenzkirch-Saig, Germany, September 2–7, 2012.
33. H. Torii (Oral): “ハードプローブ” 第 22 回 Heavy Ion Cafe+第 15 回 Heavy Ion Pub 合同研究会 2012 年 9 月 6 日、名古屋大学、名古屋市.
 Y. Hori for the ALICE collaboration (Oral): “Mixed harmonic azimuthal correlations in $\sqrt{s_{NN}} = 2.76$ TeV Pb-Pb collisions measured with the ALICE experiment at the LHC”, International Symposium on Multiparticle Dynamics 2012, Sep. 16–21, 2012, Kielce, Poland.
 T. Otsuka(invited): “Perspectives of Physics of Exotic Nuclei”, APCTP mini-workshop on nuclear structure, APCTP headquarter, Pohang, Korea, Sep. 21–22, 2012
34. M. Matsushita, N. Aoi, S. Takeuchi, P. Doornenbal, D. Steppenbeck, H. Wang : “Gamma-ray spectroscopy for medium mass nuclei”, 3rd RIBF discussion on “Gamma-Ray Spectroscopy of Medium-Mass Neutron-Rich Nuclei,” Sendai, Japan, Sep. 24, 2012.

35. Y. Utsuno (invited) : “Evolution of the shell structure probed by energy levels of exotic nuclei ”, 3rd RIBF discussion on “Gamma-Ray Spectroscopy of Medium-Mass Neutron-Rich Nuclei,” Sendai, Japan, Sep. 24, 2012.
36. T. Yoshida, N. Itagaki and K. Katō “Algebraic approach for cluster structure in ^{12}C and ^{16}O ”, 10th International Conference on Clustering Aspects of Nuclear Structure and Dynamics (CLUSTER12), Sept. 24–28, 2012, Debrecen, Hungary.
37. S. Shimoura (invited): “Charge exchange reactions of RI-beams”, The sixth International Symposium on Exotic Nuclei (EXON-2012), Oct. 1–6, 2012, Vladivostok, Russia.
38. Y. Utsuno (invited) : “Towards unified description of the shell evolution ”, Exotic Nuclear Structure From Nucleons (ENSFN2012), Oct.10-12, 2012, University of Tokyo, Japan.
39. N. Shimizu (invited), T. Abe, Y. Tsunoda, Y. Utsuno, T. Yoshida, T. Mizusaki, M. Honma and T. Otsuka : “History and future perspectives of the Monte Carlo shell model”, Exotic Nuclear Structure From Nucleons (ENSFN2012), Oct.10-12, 2012, University of Tokyo, Japan.
40. S. Ebata, T. Nakatsukasa, T. Inakura : ”Systematic investigation of E1 strength for the isotopes from $Z = 28$ to 50 ”, Exotic Nuclear Structure From Nucleons (ENSFN2012), Oct.10-12, 2012, University of Tokyo, Japan.
41. T. Yoshida, N. Shimizu, T. Abe and T. Otsuka: “Density profiles in the intrinsic frame of light nuclei obtained from Monte Carlo shell model calculation”, Exotic Nuclear Structure From Nucleons (ENSFN2012), Oct.10-12, 2012, University of Tokyo, Japan.
42. S. Shimoura (invited): “Physics opportunities using double-charge exchange reactions”, Exotic Nuclear Structure From Nucleons (ENSFN 2012), Oct. 10–12, 2012, University of Tokyo, Tokyo, Japan.
43. D. Steppenbeck, S. Takeuchi, N. Aoi, H. Baba, N. Fukuda, S. Go, P. Doornenbal, M. Honma, J. Lee, K. Matsui, M. Matsushita, S. Michimasa, T. Motobayashi, T. Otsuka, Y. Shiga, P.-A. Söderström, T. Sumikama, H. Suzuki, R. Taniuchi, J.J. Valiente-Dobón, H. Wang, K. Yoneda (Oral): “Investigating the strength of the $N = 34$ subshell closure in ^{54}Ca ”, Exotic Nuclear Structure From Nucleons (ENSFN 2012), Oct. 10–12, 2012, University of Tokyo, Tokyo, Japan.
44. T. Otsuka(invited), “New horizon of computational nuclear structure physics in the K computer era – A shell-model perspective –”, Conference on Computational Physics (CCP2012), Oct.14-18, 2012, Nichii Gakkan Kobe Port Island Center, Hyogo, Japan.
45. S. Ebata : “Simulation of heavy ion collision using time-dependent density functional theory including nuclear superfluidity”, Conference on Computational Physics (CCP2012), Oct.14-18, 2012, Nichii Gakkan Kobe Port Island Center, Hyogo, Japan.
46. T. Yoshida, N. Shimizu, T. Abe and T. Otsuka: “Cluster structure obtained from Monte Carlo shell model calculation ”, Conference on Computational Physics (CCP2012), Oct.14-18, 2012, Nichii Gakkan Kobe Port Island Center, Hyogo, Japan.
47. H. Yamaguchi (Oral): “Experimental studies on supernova nucleosynthesis in low-mass and proton-rich region”, 1st Visiting NAOJ Fellow Workshop Element Genesis and Cosmic Chemical Evolution: r-process perspective, Oct. 17–19, 2012, RIKEN, Wako, Saitama, Japan.
48. K. Yako, H. Sakai, Y. Kubota, H. Matsubara, S. Michimasa, K. Miki, H. Miya, M. Kurata-Nishimura, S. Noji, C.S. Lee, T. Ohnishi, S. Ota, H. Baba, M. Sasano, Y. Shimizu, S. Shimoura, M. Takaki, H. Takeda, T.L. Tang, H. Tokieda, T. Uesaka, Z.Y. Xu, R. Yokoyama, R.G.T. Zegers, T. Fujii, N. Inabe, S. Kawase, Y. Kikuchi, K. Kisamori, T.Kubo (Oral): “Measurement of $^{12}\text{Be}(p,n)^{12}\text{B}$ reaction at 200A MeV in inverse kinematics”, Collective Motions in nuclei under EXtreme conditions (COMEX4), Oct.22–26, 2012, Shonan Village Center, Kanagawa, Japan.
49. K. Kisamori et al., (Poster): “Missing-mass spectroscopy of the $4n$ system by exothermic double-charge exchange reaction $^4\text{He}(^8\text{He}, ^8\text{Be})4n$ ”, Collective Motions in nuclei under EXtreme conditions (COMEX4), Oct.22–26, 2012, Shonan Village Center, Kanagawa, Japan.
50. M. Takaki, H. Matsubara, T. Uesaka, S. Shimoura, N. Aoi, M. Dozono, T. Fujii, T. Hashimoto, K. Hatanaka, T. Kawabata, S. Kawase, K. Kisamori, C.S. Lee, J. Lee, T.L. Tang, Y. Maeda, S. Michimasa, K. Miki, H. Miya, S. Noji, S. Ota, S. Sakaguchi, M. Sasano, T. Suzuki, K. Takahisa, A. Tamii, H. Tokieda, K. Yako, N. Yokota, R. Yokoyama, J. Zenihiro (Poster): “Study of the ^{12}Be nucleus via the heavy-ion double-charge exchange $^{12}\text{C}(^{18}\text{O}, ^{18}\text{Ne})$ reaction”, Collective Motions in nuclei under EXtreme conditions (COMEX4), Oct.22–26, 2012, Shonan Village Center, Kanagawa, Japan.

51. H. Miya, S. Shimoura, K. Kisamori, H. Baba, T. Baba, M. Dozono, N. Fukuda, T. Fujii, S. Go, E. Ideguchi, N. Inabe, M. Ito, D. Kameda, T. Kawabata, S. Kawase, Y. Kikuchi, T. Kubo, Y. Kubota, M. Kobayashi, Y. Kondo, C. S. Lee, Y. Maeda, H. Matsubara, K. Miki, S. Michimasa, T. Nishi, M. Nishimura, S. Noji, S. Ota, S. Sakaguchi, H. Sakai, Y. Sasamoto, M. Sasano, H. Sato, Y. Shimizu, H. Suzuki, M. Takaki, H. Takeda, S. Takeuchi, A. Tamii, H. Tokieda, M. Tsumura, T. Uesaka, Y. Yanagisawa, K. Yako, R. Yokoyama, K. Yoshida, M. Assie, D. Beaumel, H. Fariouz, A. Stolz (Poster): “Study of spin-isospin response via exothermic charge exchange (^8He , ^8Li)”, Collective Motions in nuclei under EXtreme conditions (COMEX4), Oct.22–26, 2012, Shonan Village Center, Kanagawa, Japan.
52. S. Ebata, T. Nakatsukasa, T. Inakura : “Systematic study of low-lying E1 strength from light to heavy nuclei”, Collective Motions in nuclei under EXtreme conditions (COMEX4), Oct.22–26, 2012, Shonan Village Center, Kanagawa, Japan.
53. S. Hayashi, H. Hamagaki, T. Gunji, M. Tanaka, H. Ikeda (Oral): “Development of a Wide-Dynamic Range Front-End ASIC for W + Si calorimeter”, 2012 IEEE Nuclear Science Symposium and Medical Imaging Conference, Oct. 29–Nov. 3, 2012, Disneyland Hotel, Anaheim, USA.
54. Y. Sekiguchi, H. Tokieda, S. Ota, S. Michimasa, M. Dozono, T. Tamagawa, T. Gunji, H. Yamaguchi, H. Hamagaki, T. Tamagawa, T. Uesaka: “Performance of GEM with Deuterium Gas and GEM with Glass Insulator”, 2012 IEEE Nuclear Science Symposium and Medical Imaging Conference, Oct. 29–Nov. 3, 2012, Disneyland Hotel, Anaheim, USA.
55. Y. Sekiguchi, T. Gunji, H. Hamagaki, S. Hayashi, Y. Hori: “Development of W+Si Based Electromagnetic Calorimeter for the Upgrade of the LHC-ALICE Experiment”, 2012 IEEE Nuclear Science Symposium and Medical Imaging Conference, Oct. 29–Nov. 3, 2012, Disneyland Hotel, Anaheim, USA.
56. Y. Sekiguchi, H. Hamagaki, T. Gunji, Y. Arai, T. Imamura, T. Ohmoto, A. Iwata (Poster): “Development of SOI Pixel Sensor for Environmental Radiation Monitor”, 2012 IEEE Nuclear Science Symposium and Medical Imaging Conference, Oct. 29–Nov. 3, 2012, Disneyland Hotel, Anaheim, USA.
57. T. Otsuka (invited): “Advanced Monte Carlo Shell Model calculations and exotic nuclei around $Z=28$ ”, LACM-TORIJJIN-JUSTIPEN workshop, The 6th LACM-TORIJJIN-JUSTIPEN Workshop Oct. 31- Nov. 2, 2012, Oak Ridge National Laboratory.
58. T. Yoshida, N. Shimizu, T. Abe and T. Otsuka : “Study of intrinsic states for light nuclei in Monte Carlo shell model calculation”, The 6th LACM-TORIJJIN-JUSTIPEN Workshop Oct. 31- Nov. 2, 2012, Oak Ridge National Laboratory.
59. S. Shimoura (invited): “Charge exchange reactions of RI-beams”, The 6th LACM-TORIJJIN-JUSTIPEN Workshop Oct. 31- Nov. 2, 2012, Oak Ridge National Laboratory.
60. H. Yamaguchi (Oral): “Studying alpha-cluster structure using low-energy RI beams at CRIB”, RIKEN HPCI workshop on alpha-particle condensation, Nov. 13–19, 2012, RIKEN, Wako, Saitama, Japan.
61. T. Gunji for the ALICE Collaboration (Oral): “Future Perspectives of the ALICE Experiment and ALICE detector upgrades”, 4th Asian Triangle Heavy Ion conference (ATHIC2012), Nov. 14–17, 2012, Grand Hotel, Pusan, South Korea.
62. T. Nagaoka, T. Gunji, H. Hamagaki, T. Hatsuda, T. Hirano (Oral): “Sequential melting of quarkonia in quark-gluon fluid at RHIC and LHC”, 4th Asian Triangle Heavy Ion conference (ATHIC2012), Nov. 14–17, 2012, Grand Hotel, Pusan, South Korea.
63. T. Tsuji for the ALICE Collaboration (Oral): “Neutral pion measurements in Pb-Pb Collisions at $\sqrt{s_{NN}} = 2.76$ TeV with ALICE at the LHC”, 4th Asian Triangle Heavy Ion conference (ATHIC2012), Nov. 14–17, 2012, Grand Hotel, Pusan, South Korea.
64. R. Akimoto for the PHENIX Collaboration (Oral): “Measurement of charm and bottom contributions to electrons from heavy quark decay at RHIC-PHENIX experiment”, 5th International workshop on heavy quark production in heavy-ion collisions, Nov. 14–17, 2012, Utrecht University, Netherland.
65. H. Yamaguchi (invited): “Studying nuclear reactions with the low-energy RI beam separator CRIB”, 7th Italy-Japan symposium on Nuclear Physics, Nov. 20–23, University of Milano, Milano, Italy.
66. S. Shimoura (invited): “High-resolution missing-mass spectroscopy using intermediate-energy RI beams”, 7th Italy-Japan symposium on Nuclear Physics, Nov. 20–23, University of Milano, Milano, Italy.
67. T. Otsuka(invited): “An Overview of Exotic Nuclei and Nuclear Forces, and Monte Carlo Shell Model”, 7th Italy-Japan symposium on Nuclear Physics, Nov. 20–23, University of Milano, Milano, Italy.

68. Y. Utsuno (invited): “Shell evolution in neutron-rich calcium isotopes”, 7th Italy-Japan symposium on Nuclear Physics, Nov. 20–23, University of Milano, Milano, Italy.
69. H. Yamaguchi (Oral): “Recent developments and research projects at the low-energy RI beam facility CRIB”, 16th International Conference on Electromagnetic Isotope Separators and Techniques Related to their Applications (EMIS2012), Dec. 2–7, 2012, Kunibiki-Messe, Matsue, Japan.
70. T. Nakao (Poster): “Measurement of the $^{30}\text{S}+\alpha$ System Using an Active Target”, 16th International Conference on Electromagnetic Isotope Separators and Techniques Related to their Applications (EMIS2012), Dec. 2–7, 2012, Kunibiki-Messe, Matsue, Japan.
71. S. Michimasa, T. Uesaka, S. Ota, S. Shimoura, Y. Sasamoto, K. Miki, S. Noji, H. Miya, H. Tokieda, S. Kawase, K. Kisamori, M. Takaki, M. Dozono, T. Kawabata, Y. Kikuchi, Y. Kubota, H. Kurei, C.S. Lee, H. Matsubara, K. Yako, T. Nishi, N. Yamazaki, A. Yoshino, H. Sakai, T. Kubo, Y. Yanagisawa, H. Baba, G.P. Berg, P. Roussel-Chomaz, D. Bazin, for the SHARAQ collaboration (Oral): “SHARAQ spectrometer for high-resolution studies of RI-induced reactions” 16th International Conference on Electromagnetic Isotope Separators and Techniques Related to their Applications (EMIS2012), Dec. 2–7, 2012, Kunibiki-Messe, Matsue, Japan.
72. K. Yako, M. Kobayashi, S. Shimoura, M. Dozono, T. Fujii, S. Kawase, Y. Kikuchi, K. Kisamori, Y. Kubota, H. Matsubara, S. Michimasa, K. Miki, H. Miya, S. Noji, C.S. Lee, T. Ohnishi, S. Ota, H. Sakai, Y. Sasamoto, M. Sasano, M. Takaki, H. Tokieda, T. Uesaka, Z.Y. Xu, R. Yokoyama (Oral): “Development of WINDS for (p,n) measurements in inverse kinematics” 16th International Conference on Electromagnetic Isotope Separators and Techniques Related to their Applications (EMIS2012), Dec. 2–7, 2012, Kunibiki-Messe, Matsue, Japan.
73. S. Michimasa, M. Takaki, M. Dozono, S. Go, H. Baba, E. Ideguchi, K. Kisamori, H. Matsubara, H. Miya, S. Ota, H. Sakai, S. Shimoura, A. Stolz, T.L. Tang, H. Tokieda, T. Uesaka, R.G.T. Zegers (Poster): “Development of CVD diamond detector for time-of-flight measurements”, 16th International Conference on Electromagnetic Isotope Separators and Techniques Related to their Applications (EMIS2012), Dec. 2–7, 2012, Kunibiki-Messe, Matsue, Japan.
74. H. Miya, S. Shimoura, S. Ota, H. Matsubara, K. Miki, S. Kawase, T. Fujii, Y. Kubota, C. S. Lee, S. Michimasa, T. Uesaka (Poster): “Performance of Low-Pressure Multi-Wire Drift Chamber for High-Intensity RI Beams”, 16th International Conference on Electromagnetic Isotope Separators and Techniques Related to their Applications (EMIS2012), Dec. 2–7, 2012, Kunibiki-Messe, Matsue, Japan.
75. H. Hamagaki (Oral): “LHC ALICE 実験における GEM-TPC 計画について”, 9th MPGD workshop, Dec. 7–8, 2012, Nagasaki Institute of Applied Science, Nagasaki, Japan.
76. S. Ota (Oral): “Development of ActiveTarget GEM-TPC using Deuterium Gas”, 9th MPGD workshop, Dec. 7–8, 2012, Nagasaki Institute of Applied Science, Nagasaki, Japan.
77. Y. Utsuno (invited): “Manifestation of the shell evolution in energy levels of exotic nuclei”, RCNP International Workshop on Physics Opportunities Using Compton Suppressed Ge Clover Array (Clover12), Osaka, Japan, Dec. 7–8, 2012.
78. N. Shimizu: “New Generation of the Monte Carlo Shell Model for the K-Computer Era”, one-day workshop on “ab initio study of nuclear structure and reaction” RCNP, Osaka Univ., Japan, December 11, 2012.
79. T. Otsuka(invited): “Low-lying continuum states of drip-line Oxygen isotopes”, Resonance workshop, RIFP Kyoto, Japan, December 12–13, 2012
80. H. Torii (Oral): “重イオン衝突実験の展望”, ハドロンスクエア研究会、2013年1月31日、理化学研究所、和光市.
81. M. MATSUSHITA (talk): “In-beam Gamma-ray Spectroscopy of $^{38,40,42}\text{Si}$ ” SUNFLOWER - In-beam gamma and MINOS mini work shop, Feb. 20-21 2013, RIKEN Nishina Center, Japan.
82. S. Shimoura (invited): “The SHARAQ spectrometer and its physics opportunities”, NUSTAR Annual Meeting 2013, Feb.25 - Mar. 1, 2013, GSI, Germany.
83. T. Otsuka (invited), “Quest for signatures of tensor and other forces - A proposal for relativistic heavy-ion beam facility -”, NUSTAR Annual Meeting 2013, February 28 (25-March 1), 2013, GSI, Darmstadt, Germany.
84. H. Yamaguchi (oral): “Studying exotic alpha-cluster structure at CRIB”, RIKEN mini workshop “Experimental observation and theoretical analysis for a new cluster law beyond the Ikeda diagram”, Mar. 5–6, 2013, RIKEN, Wako, Japan.
85. T. Abe (oral) : “Lattice calculation by quantum Monte Carlo method in nonrelativistic quantum many-body systems” Second HPCI Strategic Program (Field2 and Field5) -quantum Monte Carlo calculation- May. 30, 2012, The Institute for Solid State Physics, University of Tokyo, Kashiwa, Japan.

86. T. Yoshida, N. Shimizu, T. Abe and T. Otsuka (oral): “Density of light nuclei obtained from Monte Carlo shell model”, HPCI Strategic Program Field 5 Symposium, Mar. 5–6, 2013, Fujisoft Akiba Plaza, Tokyo, Japan.
87. S. Ebata, T. Nakatsukasa, T. Inakura (oral): “Density functional approaches to nuclear dynamics”, HPCI Strategic Program Field 5 Symposium, Mar. 5–6, 2013, Fujisoft Akiba Plaza, Tokyo, Japan.
88. T. Otsuka (oral): “Ultra large-scale Simulations of quantum many-body systems for nuclear properties and its applications”, HPCI Strategic Program Field 5 Symposium, Mar. 5–6, 2013, Fujisoft Akiba Plaza, Tokyo, Japan.
89. Y. Utsuno (invited): “Shell evolution along the Sn isotopes”, 10th ASRC International Workshop “Nuclear Fission and Decay of Exotic Nuclei”, 2013.03.21 - 03.22, JAEA Nuclear Science Research Institute, Tokai, Japan.
90. S. Ebata, T. Nakatsukasa (oral): “Pairing effects in fusion phenomena utilizing a time-dependent mean field theory”, 10th ASRC International Workshop “Nuclear Fission and Decay of Exotic Nuclei”, 2013.03.21 - 03.22, JAEA Nuclear Science Research Institute, Tokai, Japan.

B. JPS Meetings

1. 川瀬頌一郎, 上坂友洋, 下浦享, 矢向謙太郎, 大田晋輔, 道正新一郎, 時枝紘史, 宮裕之, Tang Tsz Leung, 木佐森慶一, 高木基伸, 久保田悠樹, 李清秀, 横山輪, 藤井俊彦, 小林幹, 笹野匡紀, 錢廣十三, 松原礼明, 堂園昌伯, Jenny Lee, 酒井英行, 久保敏幸, 吉田光一, 稲辺尚人, 柳澤善行, 竹田浩之, 日下健祐, 福田直樹, 亀田大輔, 鈴木宏, 河原朋美, 涌井崇志, 坂口聡志, 野呂哲夫, 若狹智嗣, 安田淳平, 福永拓, 前田幸重, Wooyoung Kim, Sanghoon Hwang, Samvel Stepanyan, Alexandre Obertelli, Alfredo Galindo-Uribarri, Elizabeth Padilla-Rodal, “偏極陽子標的を用いた陽子ノックアウト反応による $14,22,24\text{O}$ のスピン軌道分離の研究”, 日本物理学会 2012 年秋期大会、2012 年 9 月 11 日–9 月 14 日、京都産業大学、京都。
2. 李清秀, 大田晋輔, 時枝紘史, 松原礼明, 堂園昌伯, 川瀬頌一郎, 道正新一郎, 久保田悠樹, 山口英斉, 酒向正己, 大津秀暁, 浜垣秀樹, 上坂友洋, 川畑貴裕, 久保野茂, 前田幸重, “アクティブターゲットにおける高エネルギー反跳粒子の測定”, 日本物理学会 2012 年秋期大会、2012 年 9 月 11 日–9 月 14 日、京都産業大学、京都。
3. H. Miya, S. Shimoura, K. Kisamori, H. Baba, T. Baba, M. Dozono, N. Fukuda, T. Fujii, S. Go, E. Ideguchi, N. Inabe, M. Ito, D. Kameda, T. Kawabata, S. Kawase, Y. Kikuchi, T. Kubo, Y. Kubota, M. Kobayashi, Y. Kondo, C. S. Lee, Y. Maeda, H. Matsubara, K. Miki, S. Michimasa, T. Nishi, M. Nishimura, S. Noji, S. Ota, S. Sakaguchi, H. Sakai, Y. Sasamoto, M. Sasano, H. Sato, Y. Shimizu, H. Suzuki, M. Takaki, H. Takeda, S. Takeuchi, A. Tamii, H. Tokieda, M. Tsumura, T. Uesaka, Y. Yanagisawa, K. Yako, R. Yokoyama, K. Yoshida, M. Assie, D. Beaumel, H. Fariouz, A. Stolz: “Study of spin-isospin response via exothermic charge exchange ($^8\text{He}, ^8\text{Li}\gamma$)”, at the JPS Autumn meeting, Sep. 11–14, 2012, Kyoto Sangyo University, Miura-gun, Kyoto, Japan.
4. M. Kobayashi, S. Shimoura, K. Yako, S. Ota, S. Kawase, K. Kisamori, Y. Kubota, M. Sasano, M. Takaki, M. Dozono, S. Michimasa, H. Miya and C.S. Lee (Oral): “Development of a system for (p, n) measurements in inverse kinematics”, at the JPS Autumn meeting, Sep. 11–14, 2012, Kyoto Sangyo University, Kyoto, Japan.
5. K. Kisamori, S. Shimoura, C. Lee, E. Ideguchi, N. Inabe, M. Ito, T. Uesaka, S. Ota, D. Kameda, T. Kawabata, S. Kawase, Y. Kikuchi, T. Kubo, Y. Kubota, S. Go, M. Kobayashi, Y. Kondo, S. Sakaguchi, H. Sakai, Y. Sasamoto, M. Sasano, H. Sato, Y. Shimizu, H. Suzuki, M. Takaki, A. Tamii, H. Takeda, S. Takeuchi, M. Tumura, H. Tokieda, T. Nishi, M. Nishimura, S. Noji, H. Baba, T. Baba, M. Dozono, N. Fukuda, T. Fujii, Y. Maeda, H. Matsubara, K. Miki, S. Michimasa, H. Miya, Y. Yanagisawa, K. Yako, R. Yokoyama, K. Yoshida, M. Assie, D. Beaumel, H. Fariouz, A. Stolz (Oral): “Missing mass spectroscopy of $4n$ system by exothermic double-charge exchange reaction $^4\text{He}(^8\text{He}, ^8\text{Be})4n$ ”, at the JPS Autumn meeting, Sep. 11–14, 2012, Kyoto Sangyo University, Kyoto, Japan.
6. S. Go, D. Kameda, T. Kubo, N. Inabe, N. Fukuda, H. Takeda, H. Suzuki, K. Yoshida, K. Kusaka, K. Tanaka, Y. Yanagisawa, M. Ohtake, T. Ohnishi, H. Sato, Y. Shimizu, H. Baba, M. Kurokawa, D. Nishimura, N. Iwasa, A. Chiba, H. Yamada, K. Ieki, D. Murai, E. Ideguchi, R. Yokoyama, T. Fujii, H. Nishibata, S. Momota, Y. Sato, J. Hwang, S. Kim, O.B. Tarasov, D.J. Morrissey, B.M. Sherrill, G. Simpson (Oral): “Isomers at $N=100$ in neutron rich region”, JPS Autumn meeting, Sep. 11–14, 2012, Kyoto Sangyo University, Kyoto, Japan.
7. 横山輪, 久保敏幸, 稲辺尚人, 福田直樹, 竹田浩之, 亀田大輔, 鈴木宏, 吉田光一, 日下健祐, 田中鐘信, 柳澤善行, 大竹政雄, 大西哲哉, 佐藤広海, 清水陽平, 馬場秀忠, 黒川明子, 西村太樹, 家城和夫, 村井大地, 井手口栄治, 郷慎太郎, 藤井俊彦, 岩佐直仁, 山田拓, 千葉鮎子, 百田佐多生, 西畑洗希, O.B. Tarasov, D.J. Morrissey, B.M. Sherrill, 佐藤義輝, Kim Sunji, Hwnag Jongwon, G. Simpson (Oral): “中性子過剰 $Z=60$ 近傍のアイソマー探索”, 日本物理学会 2012 年秋期大会、2012 年 9 月 11 日–9 月 14 日、京都産業大学、京都。
8. Y.L. Yamaguchi for the ALICE Collaboration (Oral, Invited): “LHC-ALICE 実験の初期成果から将来展望まで”, JPS Autumn Meeting, Sept. 11–14, 2012, Kyoto-Sangyo University, Kyoto, Japan.

9. R. Akimoto for the PHENIX Collaboration: “Measurement of electrons from charms and bottoms created in Au+Au collisions at $\sqrt{s_{NN}} = 200$ GeV at the RHIC-PHENIX experiment”, JPS Autumn meeting, Sep. 11–14, 2012, Kyoto Sangyo University, Kyoto, Japan.
10. T. Tsuji for the ALICE Collaboration: “ π^0 measurements on Pb-Pb collisions at $\sqrt{s_{NN}} = 2.76$ TeV with ALICE at the LHC”, JPS Autumn Meeting, Sep. 11–14, 2012, Kyoto-Sangyo university, Kyoto, Japan.
11. Y. Sekiguchi, H. Hamagaki, T. Gunji, Y. Arai, T. Imamura, T. Ohmoto, A. Iwata: “環境放射線センサーのための SOI ピクセル検出器の開発”, JPS Autumn Meeting, Sep. 11–14, 2012, Kyoto-Sangyo University, Kyoto, Japan
12. Y. Utsuno, N. Shimizu, M. Honma, T. Mizusaki, and T. Otsuka (oral): “Shell evolution in antimony isotopes”, at the JPS 2012 Fall Meeting, Kyoto, Japan, Sep. 11-14, 2012.
13. S. Ebata : “Application of Cb-TDHF to nuclear collision II”, at the JPS 2012 Autumn Meeting, Sep.11-14, 2012, Kyoto Sangyo Univ, Kyoto, Japan.
14. N. Shimizu, T. Mizusaki and K. Kaneko: “Extension of Monte Carlo method on nuclear shell model diagonalization”, at the JPS 2012 Autumn Meeting, Sep.11-14, 2012, Kyoto Sangyo Univ, Kyoto, Japan.
15. N. Shimizu: “Nuclear structure calculations aimed at K computer”, at the JPS 2012 Autumn Meeting, Sep.11-14, 2012, Kyoto Sangyo Univ, Kyoto, Japan.
16. T. Yoshida, N. Itagaki and K. Katō: “ Study of linear-chain structure of ^{16}O in alpha cluster model” , at the JPS 2012 Autumn Meeting, Sep.11-14, 2012, Kyoto Sangyo Univ, Kyoto, Japan.
17. Yokoyama R., Kubo T., Inabe N., Fukuda N., Takeda H., Kameda D., Suzuki H., Yoshida K., Kusaka K., Tanaka K., Yanagisawa Y., Otake M., Onishi T., Sato H., Shimizu Y., Baba H., Kurokawa M., Nishimura T., Ieki K., Murai D., Ideguchi E., Go. S., Fujii T., Iwasa N., Yamada T., Chiba A., Momota S., Nishibata H., Oleg B. T., Dave J. M., Sato Y., Kim S., Hwang J., Gray S., “中性子過剰 Tb 同位体の新アイソマーとその変形核構造”, the JPS Spring meeting, Mar. 26-29, 2013, Hiroshima University, Hiroshima, Japan
18. Go S., Kubo T., Inabe N., Fukuda N., Takeda H., Kameda D., Suzuki H., Yoshida K., Kusaka K., Tanaka K., Yanagisawa Y., Otake M., Onishi T., Sato H., Shimizu Y., Baba H., Kurokawa M., Nishimura T., Ieki K., Murai D., Ideguchi E., Yokoyama R., Fujii T., Iwasa N., Yamada T., Chiba A., Momota S., Nishibata H., Oleg B. T., Dave J. M., Sato Y., Kim S., Hwang J., Gray S., “中性子過剰変形領域における中性子数 100 のアイソマー”, the JPS Spring meeting, Mar. 26-29, 2013, Hiroshima University, Hiroshima, Japan
19. Fujii T., Ota S., Shimoura S., Aoi N., Takeshita E., Takeuchi S., Suzuki S., Baba H., Fukuchi T., Fukui T., Hashimoto K., Ideguchi E., Ieki K., Iwasa N., Iwasaki H., Kanno S., Konda Y., Kubo T., Kurita K., Minemura T., Michimasa S., Motobayashi T., Murakami T., Nakamura T., Niikura M., Okumura T., Onishi T., Shinohara M., Suzuki D., Suzuki K., Tamaki M., Tanaka K., Togano T., Wakabayashi Y., Yamada K., “ α 非弾性散乱を用いた ^{32}Mg 近傍核の核分光”, the JPS Spring meeting, Mar. 26-29, 2013, Hiroshima University, Hiroshima, Japan
20. Shimoura S., “RIPS における多種粒子測定”, the JPS Spring meeting, Mar. 26-29, 2013, Hiroshima University, Hiroshima, Japan
21. S. Ota, H. Tokieda, M. Dozono, T. Gunji, H. Hamagaki, T. Hashimoto, T. Kawabata, S. Kawase, S. Kubono, Y. Kubota, C.S. Lee, Y. Maeda, H. Matsubara, S. Michimasa, H. Otsu, M. Sako, T. Uesaka,” 重水素ガスアクティブ標的の性能評価”, the JPS Spring meeting, Mar. 26-29, 2013, Hiroshima University, Hiroshima, Japan
22. Y. Kubota, M. Sasano, T. Uesaka, C.S. Lee, M. Itho, S. Ota, S. Kawase, M. Kobayashi, T. Taguchi, T. Leung, M. Dozono, H. Tokieda, H. Matsubara, H. Miya, and T. Wakui, “不安定核研究のための高粒度 中性子検出器の開発”, the JPS Spring meeting, Mar. 26-29, 2013, Hiroshima University, Hiroshima, Japan
23. C.S. Lee, S. Ota, H. Tokieda and T. Uesaka, “低圧重水素中における厚い GEM の基礎特性”, the JPS Spring meeting, Mar. 26-29, 2013, Hiroshima University, Hiroshima, Japan
24. Y. Sekiguchi, H. Hamagaki, T. Gunji, Y. Arai, T. Imamura, T. Omoto, A. Iwata, “SOI ピクセル技術を用いた環境放射線モニターの基本動作評価” the JPS Spring meeting, Mar. 26-29, 2013, Hiroshima University, Hiroshima, Japan
25. Y. Hori, H. Hamagaki, T. Gunji, K. Murase, T. Hirano “Directed flow and Mixed harmonic azimuthal correlations in Relativistic Heavy-Ion Collisions at the LHC energy” the JPS Spring meeting, Mar. 26-29, 2013, Hiroshima University, Hiroshima, Japan
26. S. Hayashi, H. Hamagaki, T. Gunji, S. Tanaka, H. Ikeda “LHC-ALICE における前方方向カロリメータ用読み出し ASIC の性能評価”, the JPS Spring meeting, Mar. 26-29, 2013, Hiroshima University, Hiroshima, Japan

27. K. Terasaki, H. Hamagaki, T. Gunji, Y. Yamaguchi, “Development of Thick COBRA GEM for Ion Back Flow Suppression”, the JPS Spring meeting, Mar. 26-29, 2013, Hiroshima University, Hiroshima, Japan
28. Y. Utsuno, T. Otsuka, N. Shimizu, T. Mizusaki, and M. Honma (oral): “Energy levels and shell evolution for neutron-rich Ca isotopes” JPS 2013 Spring Meeting, Mar. 26–29, 2013, Hiroshima Univ., Hiroshima, Japan.
29. T. Yoshida, N. Shimizu, T. Abe and T. Otsuka (oral): “Study of light-nuclei density measured from body-fixed frame in Monte Carlo shell model”, JPS 2013 Spring Meeting, Mar. 26–29, 2013, Hiroshima Univ., Hiroshima, Japan.
30. S. Ebata, T. Nakatsukasa, T. Inakura (oral): “Systematic study of low-lying E1 mode”, JPS 2013 Spring Meeting, Mar. 26–29, 2013, Hiroshima Univ., Hiroshima, Japan.
31. S. Ebata (oral): “Approaches to nuclear dynamics by time dependent mean field theory”, JPS 2013 Spring Meeting, Mar. 26–29, 2013, Hiroshima Univ., Hiroshima, Japan.
32. N. Shimizu, Y. Utsuno, S. Ebata, M. Honma, T. Mizusaki, and T. Otsuka (oral) : “Study of E1 excitation for neutron-rich Ca isotopes”, JPS 2013 Spring Meeting, Mar. 27, 2013, Hiroshima Univ, Hiroshima, Japan.

C. Lectures

1. S. Shimoura: “Physics of Exotic Nuclei”, Kyoto University, July 25-27, 2012
2. T. Otsuka (invited) : “Perspectives of Physics of Exotic Nuclei”, 11th CNS Summer School, Sep. 4 (Aug. 29–Sep. 4), 2012, Riken, Wako and Hongo, Japan.

D. Seminars

1. H. Yamaguchi (oral): “Studying nuclear reactions with the low-energy RI beam separator CRIB”, Nuclear Physics Seminar at INFN-LNS, Nov. 15, 2012, INFN-LNS, Catania, Italy.
2. S. Ota : “CNS Active Target for deuterium induced reactions with high intensity unstable beam at 100-300 MeV/u”, Nov. 5, 2012, IPNO, Orsay, France
3. S. Ota : “CNS Active Target for deuterium induced reactions with high intensity unstable beam at 100-300 MeV/u”, Nov. 9, 2012, GANIL, Caen, France
4. S. Ota : “CNS Active Target for deuterium induced reactions with high intensity unstable beam at 100-300 MeV/u”, Nov. 15, 2012, SPhN-IRFU, Saclay, France

Personnel

Director

OTSUKA, Takaharu *Professor, Department of Physics,
Graduate School of Science*

Scientific Staff

SHIMOURA, Susumu *Professor*
HAMAGAKI, Hideki *Professor*
YAKO, Kentaro (May, 2012~) *Associate Professor*
SHIMIZU, Noritaka *Associate Professor*
IDEGUCHI, Eiji (~Apr, 2012) *Lecturer*
YAMAGUCHI, Hidetoshi *Lecturer*
MICHIMASA, Shin'ichiro *Assistant Professor*
GUNJI, Taku *Assistant Professor*
OTA, Shinsuke *Assistant Professor*

Guest Professors

UTSUNOMIYA, Hiroaki *Konan University*
UTSUNO, Yutaka *JAEA*

Technical Staff

OHSHIRO, Yukimitsu *YAMAZAKI, Norio*

Technical Assistants

YAMAKA, Shoichi
YOSHIMURA, Kazuyuki
WATANABE, Shin'ichi
YOSHINO, Rho

NINOMIYA, Hideaki
KUREI, Hiroshi
TANAKA, Masahiko

Post Doctoral Associates

TORII, Hirayuki
YAMAGUCHI, Yorito
NAKAO, Taro
KAHL, David

YOSHIDA, Tohru
STEPPENBECK, David
EBATA Shuichiro
MATSUSHITA, Masahumi

Graduate Students

TAKAHARA, Akihisa
HORI, Yasuto
TOKIEDA Hiroshi
TANG, Tsz Leung
TUJI, Tomoya
TAKAKI, Motonobu
YOKOYAMA, Rin
SEKIGUCHI, Yuko
LEE, CheongSoo
TERASAKI, Kouhei

AKIMOTO, Roji
MIYA, Hiroyuki
KAWASE, Shoichiro
GO, Shintaro
KISAMORI, Keiichi
HAYASHI, Shin'ichi
FUJII, Toshihiko
KUBOTA, Yuki
KOBAYASHI, Motoki
KOBAYASHI, Kazuma

Administration Staff

ASAKAWA, Yuko (~ Dec, 2012)
YAMAMOTO, Ikuko
ENDO, Takako
YOSHIMURA, Hiroshi (Dec, 2012~)

KISHI, Yukino
ITAGAKI, Toshiko
SOMA, Yuko

Committees

Steering Committee

AIHARA, Hiroaki	<i>Department of Physics, Graduate School of Science, UT</i>
HOSHINO, Masahiro	<i>Department of Earth and Planetary Science, Graduate School of Science, UT</i>
MIYASHITA, Seiji	<i>Department of Physics, Graduate School of Science, UT</i>
OTSUKA, Takaharu	<i>Department of Physics, Graduate School of Science, UT</i>
SHIMOURA, Susumu	<i>Center for Nuclear Study, Graduate School of Science, UT</i>
HAMAGAKI, Hideki	<i>Center for Nuclear Study, Graduate School of Science, UT</i>
GONOKAMI, Makoto	<i>Department of Physics, Graduate School of Science, UT</i>
NAGAMIYA, Shoji	<i>J-PARC Center, KEK and JAEA</i>
SAKURAI, Hiroyoshi	<i>Department of Physics, Graduate School of Science, UT</i>
KOBAYASHI, Tomio	<i>International Center for Elementary Particle Physics, UT</i>
TAKAHASHI, Hiroyuki	<i>Department of Nuclear Engineering and Management, Graduate School of Engineering, UT</i>

